Final Report

Investigation of Generation, Acceleration, Transport and Final Focusing of High-Intensity Heavy Ion Beams from Sources to Targets

Grant No. DE-FG02-01ER54662

Grant Period:
September 1, 2001 – May 31, 2006

Submitted to
Dr. Francis Thio
Office of Fusion Energy Sciences
Office of Science
U.S. Department of Energy
19901 Germantown Road
Germantown, MD 20874-1290

Submitted by
Dr. Chiping Chen
Principal Research Scientist
Waves and Beams Division
Plasma Science and Fusion Center
Massachusetts Institute of Technology
Cambridge, Massachusetts 02139

Telephone: (617) 253-8506
Fax: (617) 253-6078
Email: chenc@psfc.mit.edu

October 26, 2006

Table of Contents

Executive Summary

1 Derivation of RMS Envelope Equations and Study of RMS Envelope Dynamics for High-Intensity Heavy Ion Beams in a Small-Aperture Alternating-Gradient (AG) Focusing Transport Systems

2 Identification of a New Mechanism for Chaotic Particle Motion, Halo Formation, and Beam Loss in High-Intensity Heavy Ion Beams in a Small-Aperture Alternating-Gradient (AG) Focusing Transport Systems

3 Development of Elliptic Beam Theory

4 Studies of Physics Issues in the Neutralization Transport Experiment (NTX)

References

Appendices A-K: Selected Publications

Appendix A "Image-charge effects on the envelope dynamics of an unbunched intense charged-particle beam," B. L. Qian, J. Zhou, and C. Chen, Phys. Rev. ST Accel Beams **6**, 014201 (2003)

Appendix B "Chaotic particle motion and beam halo formation induced by image-charge effects in a small-aperture alternating-gradient focusing system," J. Zhou, B. L. Qian, and C. Chen, Phys. Plasmas **10**, 4203 (2003)

Appendix C "Parametric Study of Parametric Studies of Image-Charge Effects on an Intense Beam in a Small-Aperture Alternating-Gradient Focusing System," J. Zhou and C. Chen, Nucl. Instrum. Methods Phys. Res. **A544**, 493 (2005)

Appendix D "Theory and Simulation of Non-Relativistic Elliptic Beam Formation with Child-Langmuir Flow Characteristics," R. Bhatt and C. Chen, Phys. Rev. ST – Accel and Beams 8, 014201 (2005)

Appendix E "Final Focus System for High Intensity Beams," E. Henestroza, S. Eylon, P. K. Roy, et al., Phys. Rev. ST – Accel. Beams **8**, 052801 (2005)

Appendix F "Three-Dimensioanl Theory and Simulation of Large-Aspect Ratio Ellipse-Shaped Charged-Particle Beam Gun," R. Bhatt, T. Bemis, and C. Chen, Proc. 2005 Part. Accel. Conf., p 3372 – **First Prize for Outstanding Technical Paper by Student**

Appendix G "Three-Dimensional Theory and Simulation of Non-Relativistic Elliptic Electron and Ion Beam Generation," R. Bhatt, T. Bemis, and C. Chen, IEEE Trans. Plasma Sci. **34**, 187 (2006) - **Invited Paper**

Appendix H "Cold-Fluid Theory of Equilibrium and Stability of a High-Intensity Periodically Twisted Ellipse-Shaped Charged-Particle Beam," J. Zhou, R. Bhatt and C. Chen, Phys. Rev. ST – Accel. Beams **9**, 034401 (2006)

Appendix K "Generation, Transport and Focusing of High-Brightness Heavy Ion Beams," E. Henestroza, Ph.D. Thesis, Massachusetts Institute of Technology, 2006.

Executive Summary

Under the auspices of the research grant (Chen, 2001), the research group has made significant contributions in a number of important areas in the HIF and HEDP research, including:

(a) Derivation of rms envelope equations and study of rms envelope dynamics for high-intensity heavy ion beams in a small-aperture AG focusing transport systems (Qian, Zhou and Chen, 2003a and 2003b);

(b) Identification of a new mechanism for chaotic particle motion, halo formation, and beam loss in high-intensity heavy ion beams in a small-aperture AG focusing systems (Zhou, Qian and Chen, 2003; Zhou, Qian and Chen, *et al*., 2003; Zhou and Chen, 2005; Zhou, 2006);

(c) Development of elliptic beam theory (Bhatt, Chen and Zhou, 2004; Bhatt and Chen, 2005; Bhatt, 2006; Bhatt, Bemis, and Chen, 2005 and 2006; Zhou, 2006; Zhou, Bhatt, and Chen 2006);

(d) Study of Physics Issues in the Neutralization Transport Experiment (NTX) (Zhou, Qian and Chen, *et al*., 2003; Henestroza, Eylon, Roy, *et al*., 2005; Henestroza, 2006).

All of these contributions have been made possible through rigorous collaboration with the Inertial Fusion Energy Science (IFES) community, especially the Virtual National Laboratory for HIF.

1. Derivation of rms envelope equations and study of rms envelope dynamics fo high-intensity heavy ion beams in a small-aperture alternating-gradient (AG) focusing transport systems (Qian, Zhou and Chen, 2003a and 2003b)

Under the auspices of the present research grant (Chen, 2001), we studied an unbunched elliptical beam propagating in an alternating-gradient focusing field and a cylindrical metal pipe with radius R, as shown in Fig. 1.1 (Qian, Zhou and Chen, 2003a and 2003b). The beam has an envelope $a(s)$ in the x-direction and an envelope $b(s)$ in the y-direction. The root-mean-squared envelope equations including all higher-order image-charge effects from the cylindrical conducting pipe were derived and analyzed. Higher-order image-charge effects were expressed in terms of so-called multiple moment factors in the rms beam envelope equations, which were

then evaluated. In particular, the self-electric and self-magnetic fields were calculated for an unbunched beam with elliptic symmetry and an arbitrary transverse dependence in the self-similar beam density model.

Numerical results showed that for vacuum phase advance s_v $90°$, the image-charge effects on the matched and slightly mismatched beam envelopes are negligibly small, at all orders, for all beams with arbitrary beam density profiles (including hollow density profiles measured recently in the heavy ion injector experiment at Lawrence Berkeley National Laboratory) as well as for arbitrary small apertures (including beams with large aspect ratios).

As shown in Fig. 1.2, the matched beam envelope functions $a(s)$ and $b(s)$ for a hollow beam are plotted for a periodic step-function lattice with filling factor $h = 0.5$, normalized beam perveance $KS/e = 10.0$, emittances $e_x = e_y = e$, and vacuum phase advance $s_v = 80.0°$, which corresponds to those in the High-Current Experiment (HCX) at LBNL (Seidl, Bieniosek, Celata, *et al*., 2001) for two cases: free space and with a cylindrical conducting pipe of $a_{max}/R = 81.3\%$.

Furthermore, the main unstable region for the envelope evolution with image-charge effects, which occurs for $90° < s_v < 270°$, depending on the value of the normalized beam intensity SK/e, is found to be narrower than its counterpart without image-charge effects. Figure 1.3 is a plot of SK/e versus s_v, showing the unstable regions of the slightly mismatched beam envelopes for uniform beam with $h = 0.5$ in three cases: (a) free space, (b) $a_{\max}/R = 0.75$, and (c) $a_{\max}/R = 0.90$. Although the lower boundaries for the three cases nearly coincide, there is an observable difference between their upper boundaries.

In this study, the beam centroid was assumed to be on axis. Once it is off-axis, however, it will couple to the rms envelope oscillations, which requires further investigation.

2. Identification of a new mechanism for chaotic particle motion, halo formation, and beam loss in high-intensity heavy ion beams in a small-aperture alternating-gradient (AG) focusing systems (Zhou, Qian and Chen, 2003; Zhou, Qian, Chen, *et al*., 2003; Zhou and Chen, 2005; Zhou 2006)

Under the auspices of the research grant (Chen, 2001), we used a test-particle model to

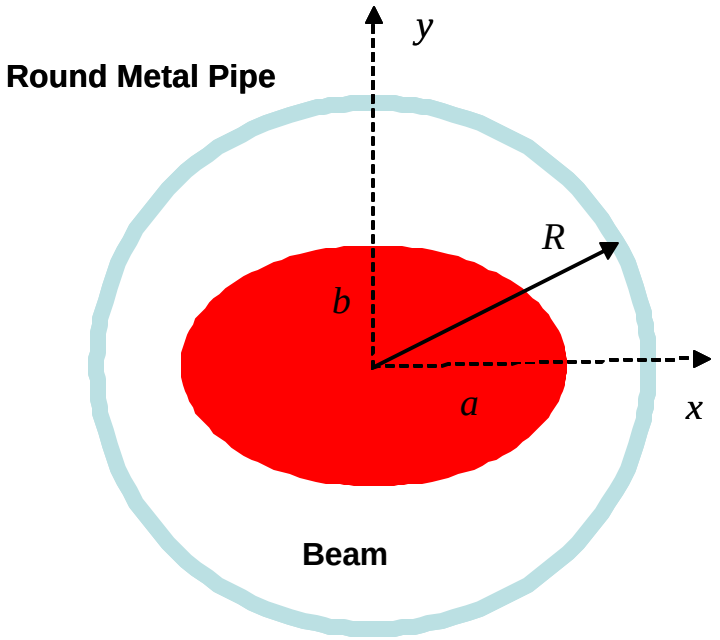

Figure 1.1 Elliptical unbunched charged-particle beam in a cylindrical conducting pipe.

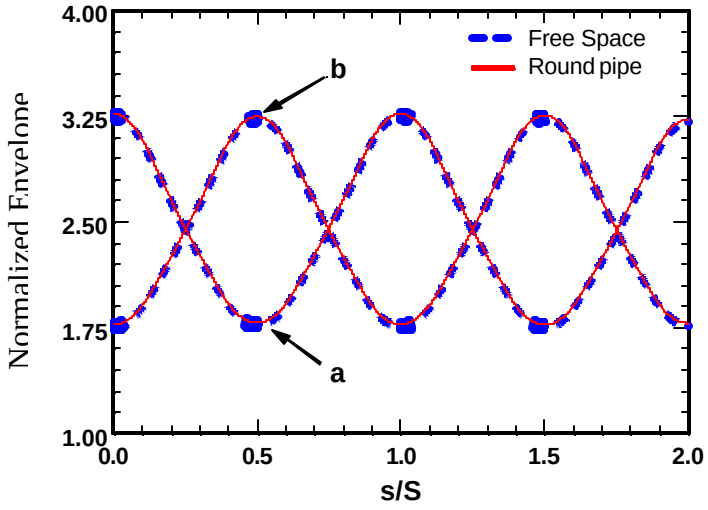

Figure 1.2 The normalized envelope functions $a/\sqrt{eS}$ and $b/\sqrt{eS}$ for $s_u = 80^0$, $\hat{K} = 10$, $h = 0.5$, $\hat{R} = 4.0$ for a hollow beam (from Qian, Zhou and Chen, 2003a).

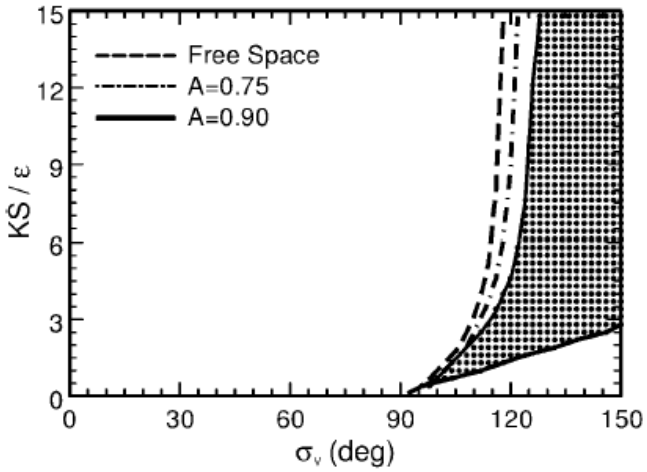

Figure 1.3 Plot of the unstable regions in the dimensionless parameter space for the beam envelope evolution with $h = 0.5$ for three cases corresponding to (a) free space, (b) $A = a_{\max}/R = 0.75$, and (c) $A = a_{\max}/R = 0.90$. The shaded region is the unstable region for the beam envelope evolution with image-charge effects and $A = a_{\max}/R = 0.90$ (from Qian, Zhou and Chen, 2003a).

investigate the halo formation and chaos induced by the image-charge effects in such small aperture alternating-gradient focusing transport systems (Zhou, Qian and Chen, 2003), which is a new mechanism for chaotic particle motion and halo formation in intense charged-particle beams.

In particular, an analytical expression for the scalar potential of this elliptic beam in a round pipe was obtained for the Kapchinskij-Vladimirskij (KV) distribution for an rms-matched continuous intense charged-particle beam propagating in the longitudinal direction though an alternating-gradient quadrupole magnetic field with axial periodicity length S in a perfectly conducting round pipe R. The fields induced by the image charges were shown to be nonlinear. Therefore, the particle orbits are non-integrable, and can become chaotic.

Numerical simulation results showed that the particles can escape from the beam core to form halos in several periods and strike the wall after tens of periods due to the image charge effects when the beam maximum envelope a fills the pipe radius up to 86%. In the simulation we used a periodic step-function lattice with filling factor $h = 0.5$, normalized beam perveance

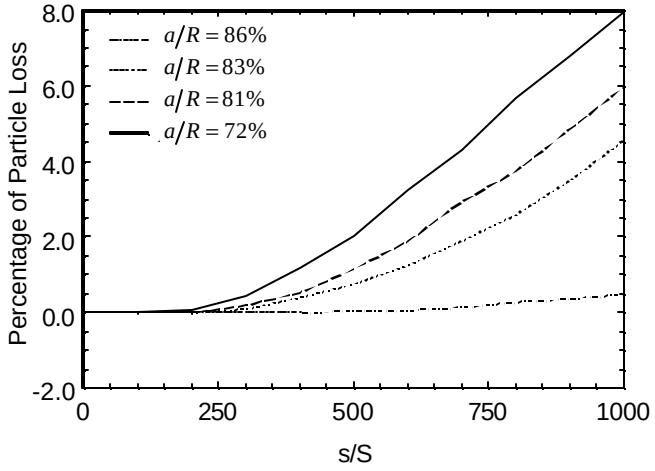

Figure 2.1 Plots of the percentage of particles striking the conductor wall as a function of propagation distance for $h = 0.5$, $KS/e_x = 10.0$, $e_x = e_y = e$, $s_v = 80°$ and several choices of R. Here, 10,000 test particles with the KV distribution initially are used in the simulations (from Zhou, Qian and Chen, et al., 2003).

$KS/e = 10.0$, emittances $e_x = e_y = e$, and vacuum phase advance $s_v = 80.0°$, which corresponds to those in the High-Current Experiment (HCX) at LBNL (Seidl, Bieniosek, Celata, *et al*., 2001). Furthermore, the beam loss was computed as a function of propagation distance for four choices of the pipe radius with $a/R =$ 86%, 83%, 81%, and 72%, as shown in Fig. 2.1.

Our results, obtained for the ideal KV distribution, represent the beam loss one may observe for a uniform density beam in a long (>100 periods) focusing system such as the planned Integrated Research Experiment (IRE) for heavy ion fusion. They also suggest that in short (2 to 30 periods) systems such as the existing Neutralized Transport Experiment (NTX) (Yu, Henestroza, Eylon, Roy, *et al*., 2005; Henestroza, 2006) and High-Current Experiment (HCX) (Seidl, Bieniosek, Celata, *et al*., 2001), imperfections such as charge-density fluctuations, mismatch, and focusing field nonlinearity and error may play a more important role than image charge effects on beam halo production (Zhou, Qian, Chen, *et al*., 2003).

We also performed parametric studies of image-charge effects on inducing chaotic particle motion, beam halo formation and beam loss, which will help us to identify the operating regime

in which beam loss is minimum. Detailed results of this investigation were published (Zhou and Chen, 2005).

3. Development of elliptic beam theory (Bhatt, Chen and Zhou, 2004; Bhatt and Chen, 2005; Bhatt, 2006; Bhatt, Bemis and Chen, 2005 and 2006; Zhou, 2006; Zhou, Bhatt and Chen, 2006)

Under the auspices of the research grant (Chen, 2001), a theory of non-relativistic, laminar, elliptic beam formation was developed (Bhatt, Chen and Zhou, 2004; Bhatt and Chen 2005; Bhatt, 2006; Bhatt, Bemis and Chen, 2005 and 2006). The beam was shown to have the Child-Langmuir form (Child, 1911; Langmuir, 1923). An analytic expression for the electrostatic potential outside the beam was derived. Equipotentials corresponding to electrode surfaces were computed numerically. The effectiveness of the electric field formed by the electrodes in focusing and preserving the elliptic Child-Langmuir beam was verified via 3D ray-tracing simulations.

As an example, we computed the potential outside a 10:1:8.7 space-charge-limited elliptical diode of semi-major axis $a = 10b$, semi-minor axis b, and length $d = 8.7b$. Equipotentials corresponding to $= 0$ and $= {}_d$ are shown in Figs. 3.1(a) and 2.3.2(b), respectively, for several values of z. The level contours are roughly elliptical in shape, and the $= {}_d$ surface is more steeply inclined to the beam than the $= 0$ surface, as expected from the 2D theory (Pierce, 1954). The aspect ratio of a/b=10 is chosen here to illustrate the theory, although a typical heavy ion beam in the AG focusing system only has an aspect ratio of 1.5 approximately.

We verified our theory by a 3D space-charge emission simulation using OMNITRAK (OmniTrak Software, Field Precisions, Albuquerque, New Mexico), a commercially available ray-tracing code. Simulation results are shown in Fig. 3.2 for the same geometry as in Fig. 3.1. Neumann boundaries were used for the symmetry planes of the beam as well as for the outer boundaries of the simulation region, which is shown in Fig. 3.2 along with computed equipotentials and particle trajectories projected to the $x = 0$ and $y = 0$ planes.

The beam produced by the simulation is essentially parallel, laminar, uniform density Child-Langmuir flow. Beam laminarity is often characterized by the rms beam emittances

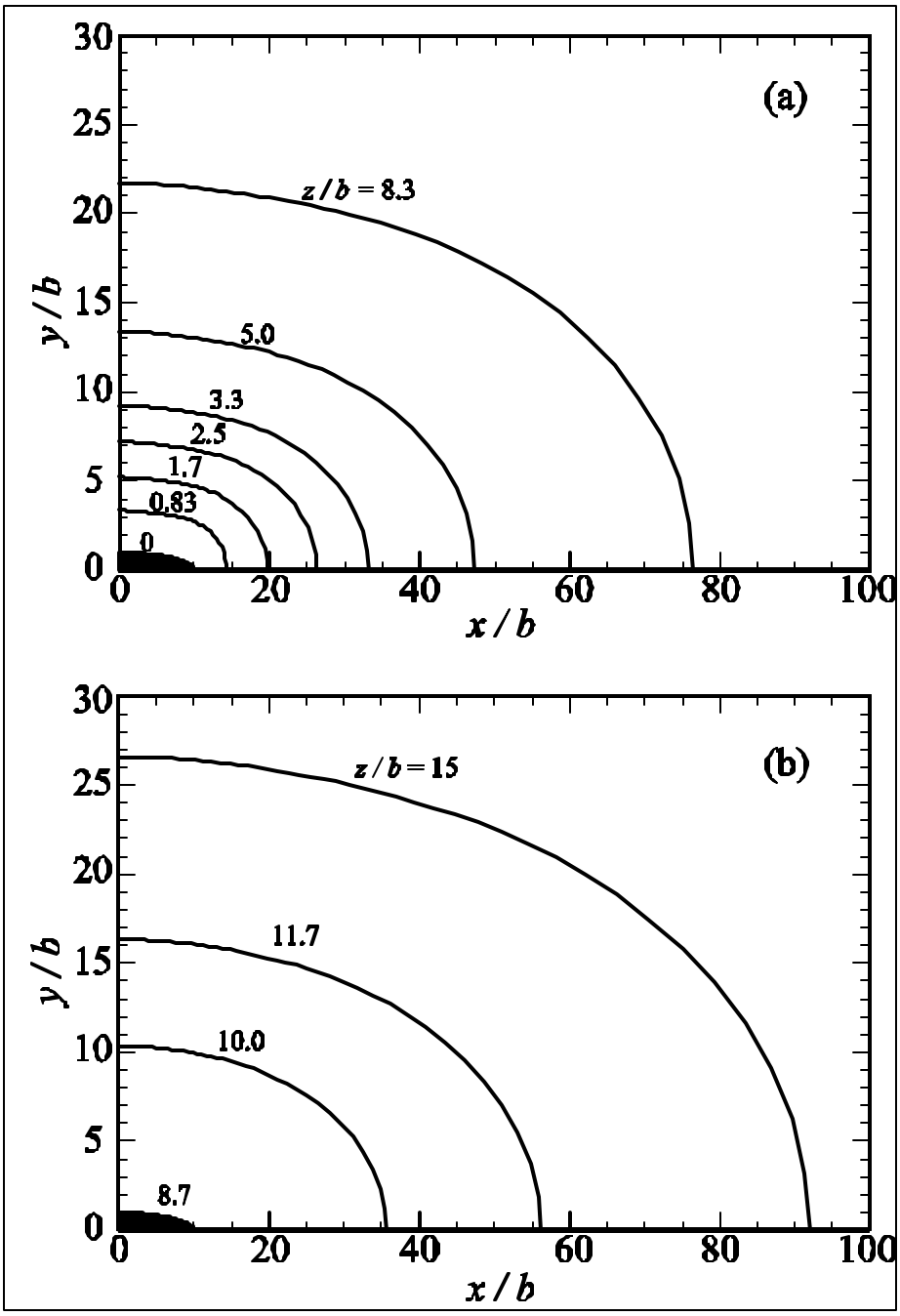

Figure 3.1: Level curves of (a) $\quad = 0$ and (b) $\quad = \ _d$ surfaces for a 10: 1:8.7 space-charge-limited elliptical diode of semi-major radius $10b$, semi-minor radius b, and length $8.7b$. The beam fills the shaded area, which is intersected by the $\quad = 0$ surface at $z = 0$ and the $\quad = \ _d$ surface at $z = 8.7b$ (from Bhatt and Chen, 2005).

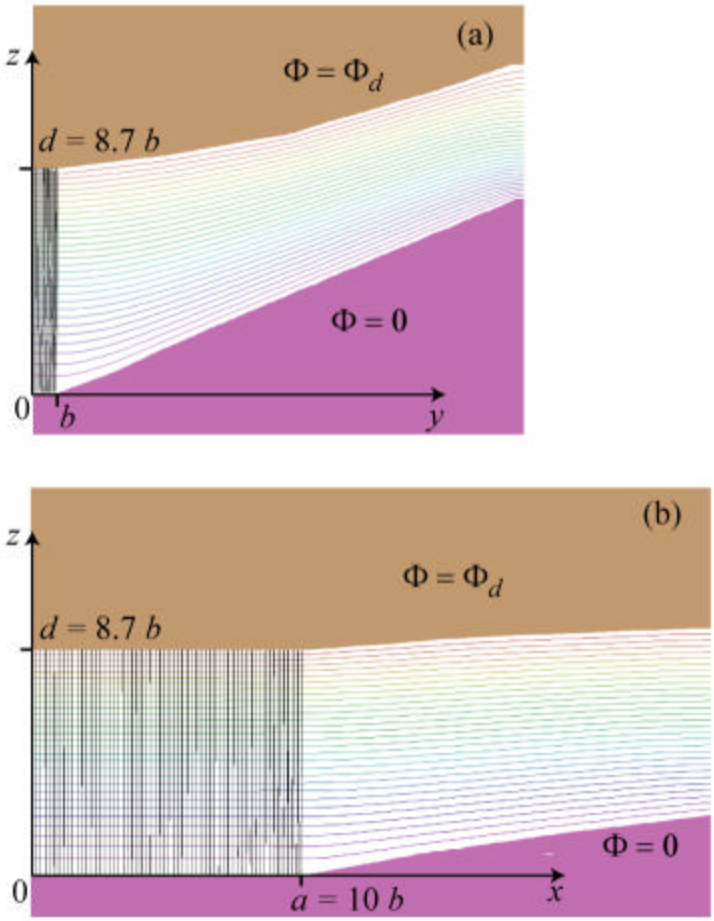

Figure 3.2: (Color online) A 3D OMNITRAK simulation of space-charge-limited Child-Langmuir flow using the 10:1:8.7 elliptical diode geometry shown in Fig. 2.3.1. Particle trajectories and equipotentials are shown in (a) the $x = 0$ plane and (b) the $y = 0$ plane (from Bhatt and Chen, 2005).

$e_x \quad \left(\left\langle x^2\right\rangle\left\langle x'^2\right\rangle \quad \left\langle xx'\right\rangle^2\right)^{1/2}$ and $e_y \quad \left(\left\langle y^2\right\rangle\left\langle y'^2\right\rangle \quad \left\langle yy'\right\rangle^2\right)^{1/2}$, where the averages of transverse particle position (x, y) and divergence $(x', y') \quad (dx/dz, dy/dz)$ are taken over a slice of the beam at $z = d$. For a uniform density elliptic beam, these emittances can be related to effective beam temperatures (Lawson, 1988) by the relations $e_x = a\left(kT_{eff,x}/8q_{\ d}\right)^{1/2}$ and $e_y = b\left(kT_{eff,y}/8q_{\ d}\right)^{1/2}$. If we use the parameters of our earlier examples, a 10:1:8.7 elliptical electron or ion diode with $_d = 5.0\,\text{kV}$, $d = 5.2\,\text{mm}$, $a = 6.0\,\text{mm}$, and $b = 0.6\,\text{mm}$, the OMNITRAK simulation shown in Fig. 3.2 predicts the effective beam temperatures $T_{eff,x} = 6.7 \quad 10^{\ 4}\,\text{eV}$ and $T_{eff,y} = 8.1 \quad 10^{\ 3}\,\text{eV}$. These temperatures are negligible compared to a typical thermionic electron or ion diode temperature of ~0.1 eV, implying that the emittance of an elliptical diode constructed using the above prescription will approach the theoretical limits imposed by finite emitter temperature.

We also developed a cold-fluid equilibrium theory of a periodically twisted elliptic beam. Detailed results were published (Zhou, 2006; Zhou, Bhatt and Chen, 2006). The combination of the elliptic beam gun theory and the elliptic beam propagation theory will enable researchers to design very high-brightness electron and ions for particle accelerator applications, high-energy density physics research, and/or heavy ion fusion.

4. Study of physics issues in the Neutralization Transport Experiment (Zhou, Qian, Chen, *et al*., 2003; Henestroza, Eylon, Roy, *et al*., 2005; Henestroza, 2006)

Under the auspices of the research grant (Chen, 2001), we used the test-particle model to analyze the Neutralized Transport Experiment (NTX) at LBNL (Henentroza, Eylon, Roy, *et al*., 2005). Results showed that there is no halo formation in the simulation for this short channel. However, the nonlinear forces induced by image charges create slight S-shaped and non-elliptic distributions in (x,x') and (y,y'), respectively. The orientation of S-shaped and non-elliptic distribution in (x,x') from the test-particle calculation differs from that measured experimentally (Zhou, Qian, Chen, *et al*., 2003). The cause for the discrepancy remains to be resolved.

One of the graduate students supported in part by this research grant led the theoretical, computational, and experimental studies of a final focus system of heavy ion beams (Henestroza, Eylon, Roy, et al, 2005) , and completed his doctoral thesis in 2006 (Henestroza 2006).

References

Bhatt, R.J, 2006, Ph.D. Thesis, Massachusetts Institute of Technology.

Bhatt, R., and C. Chen, 2005, Phys. Rev. ST – Accel. Beams **8**, 014201.

Bhatt, R. T. Bemis, and C. Chen, 2005, Proc. 2005 Part. Accel. Conf., p. 3372 – ***First Price for Outstanding Technical Paper by Student***

Bhatt, R., T. Bemis, and C. Chen, 2006, IEEE Trans. Plasma Sci. **34**, 187 – ***Invited Paper***

Bhatt, R., C. Chen, J. Zhou, 2004, Proc. 2004 European Part. Accel. Conf., p. 1494.

Chen, C., 2001, "Investigation of Generation, Acceleration, Transport and Final Focusing of Intense Heavy Ion Beams from Sources to Targets," Department of Energy, Office of Fusion Energy Science, Grant No. DE Grant No. DE-FG02-01-ER54662, Chiping Chen, Principal Investigator.

Child, C.D., 1911, Phys. Rev. 32, 492.

Henestroza, E., 2006 Ph.D. Thesis, Massachusetts Institute of Technology.

Henestroza, E., S. Eylon, P. K. Roy, *et al*., 2005, Phys. Rev. ST – Accel. Beams **8**, 052801.

Langmuir, I., 1923, Phys. Rev. **21**, 419.

Lawson, J.D., 1988, *Physics of Charged Particle Beams* (Clarendon Press, Oxford), p.210.

Pierce, J. R.,1954, *Theory and Design of Electron Beams*, 2nd ed. (D. Van Nostrand Company, Princeton, New Jersey).

Qian, B.L., J. Zhou, and C. Chen, 2003a, Phys. Rev. ST – Accel. Beams **6**, 014201.

Qian, B.L., J. Zhou, and C. Chen, 2003b, Proc. 2003 Part. Accel. Conf., p. 3302.

Seidl, P.A., F.M. Bieniosek, C.M. Celata, *et al*., 2001, Nucl. Instrum. Methods Phys. Res. **A464**, 369.

Zhou, J., 2006, Ph.D. Thesis, Massachusetts Institute of Technology.

Zhou, J. and C. Chen, 2005, Nucl. Instrum Methods Phys. Res. **A544**, 493.

Zhou, J., B. L. Qian, and C. Chen, 2003, Phys. Plasmas **10**, 4203.

Zhou, J., B. L. Qian, C. Chen, E. Henestroza, S. Eylon, and S. Yu, 2003, Proc. 2003 Part. Accel. Conf., p. 2646.

Image-charge effects on the envelope dynamics of an unbunched intense charged-particle beam

B. L. Qian,* J. Zhou, and C. Chen

Plasma Science and Fusion Center, Massachusetts Institute of Technology, Cambridge, Massachusetts 02139

(Received 5 August 2002; published 6 January 2003)

The root-mean-squared (rms) envelope equations are derived and analyzed for an unbunched intense charged-particle beam in an alternating-gradient focusing field and a cylindrical conducting pipe. All higher-order image-charge effects from the cylindrical pipe are expressed in terms of so-called multiple moment factors in the rms beam envelope equations, and the multiple moment factors are evaluated. Numerical results show that for vacuum phase advance $\sigma_v < 90°$, the image-charge effects on the matched and slightly mismatched beam envelopes are negligibly small, at all orders, for all beams with arbitrary beam density profiles (including hollow density profiles) as well as for arbitrary small apertures (including beams with large aspect ratios). However, the main unstable region for the envelope evolution with image-charge effects, which occurs for $90° < \sigma_v < 270°$, depending on the value of the normalized beam intensity SK/ε, is found to be narrower than its counterpart without image-charge effects.

DOI: 10.1103/PhysRevSTAB.6.014201 PACS numbers: 41.85.Ja, 41.75.–i

I. INTRODUCTION

High-intensity accelerators with alternating-gradient focusing systems have many applications in basic scientific research and nuclear physics. These applications include heavy ion fusion [1,2], nuclear waste treatment [3], and spallation neutron source [4]. In the research and development of high-intensity accelerators, a key issue is to minimize the aperture of the transport system for intense charged-particle beams, while preventing the beams from developing large-amplitude charge density and velocity fluctuations as well as subsequent emittance growth and halo formation [4–15]. In order to understand the collective behavior of charged-particle beams, it is important to examine the beam envelope evolution under the influence of both the beam space charge and the image charges induced on the conducting walls of accelerator structures.

Intense charged-particle beams in alternating-gradient focusing systems have been investigated since the late 1950s. One of the earliest works on the beam envelope equations can be found in Ref. [16], in which the well-known two-dimensional (2D) Kapchinskij-Vladimirskij (KV) equations were derived for a uniform beam density in free space. In 1965, Lapostolle [17] gave the three-dimensional (3D) envelope equations for a uniform beam density in free space, and his results could be applicable for bunched beams. In 1971, Sacherer [18] and Lapostolle [19] extended the previous 2D and 3D results to the arbitrary beam density cases in free space. Sacherer's 2D results, which describe the root-mean-squared (rms) beam envelopes for all elliptical beams with arbitrary beam densities, assume the same form of the KV equations.

Recently, Allen and Reiser [20,21] extended Sacherer's 2D results to include the image-charge effects due to the cylindrical conducting pipe. They analyzed the *first-order* image-charge effects. Their results showed that the first-order image-charge effects do not affect the beam envelope evolution until the beam is very close to the wall of the cylindrical conducting pipe. The expressions for the first-order image-charge contributions in the rms beam envelope equations in [20,21] were identical to those obtained in an earlier paper by Lee, Close, and Smith [22].

In general, there are two approaches in treating the density distribution of a nonequilibrium beam. One approach uses a rigorous normal-mode analysis (i.e., small-signal theory) [23,24] to describe the density evolution in a charged-particle beam. The normal-mode analysis is useful for understanding the collective oscillations and instabilities in the beam. The other approach makes use of the assumption of a self-similar beam density distribution [7–9,11,17–21]. While the self-similar beam density distribution is not rigorous and, in general, not self-consistent, it has proven to be a useful model in the many previous derivations of rms beam envelope equations [7–9,11,17–21]. The rms beam envelope equations based on the self-similar model are very useful in the design of beam optics. Although the beam density usually does not remain in the prescribed self-similar form, the rms envelope equations still give a quite accurate description of an intense beam, provided the actual beam emittances, which can be either measured in the beam experiment or computed in the self-consistent simulation, are used (see, for example, Ref. [25]).

In this paper, we extend Allen and Reiser's 2D envelope equations to include all higher-order image-charge effects from the cylindrical conducting pipe. In particular, the self-electric and self-magnetic fields are calculated for an unbunched beam with elliptic symmetry and an

arbitrary transverse dependence in the self-similar beam density model [7–9,11,17–21]. The rms envelope equations are derived, including all higher-order image-charge effects, from the cylindrical conducting pipe. Numerical results show that for vacuum phase advance $\sigma_v < 90°$, the image-charge effects on the matched and slightly mismatched beam envelopes are negligibly small, at all orders, for all beams with arbitrary beam density profiles (including hollow density profiles measured recently in the heavy ion injector experiment at Lawrence Berkeley National Laboratory [26]) as well as for arbitrary small apertures (including beams with large aspect ratios). However, the main unstable region for the envelope with image-charge effects, which occurs for $90° < \sigma_v < 270°$, depending on the value of the normalized beam intensity SK/ε, is found to be narrower than its counterpart without image-charge effects [11].

The organization of the present paper is as follows. In Sec. II, 2D envelope equations are derived, including all higher-order image-charge effects. In Sec. III, the multiple moment factors in the envelope equations are evaluated. In Sec. IV, the higher-order image-charge effects on the matched beam envelopes are investigated by numerically solving the 2D envelope equations for arbitrary beam densities, including a hollow beam density profile, in a cylindrical conducting pipe. In Sec. V, the image-charge effects on the slightly mismatched beams and beam envelope instability are numerically analyzed. Conclusions are presented in Sec. VI.

II. BEAM ENVELOPE EQUATIONS WITH IMAGE-CHARGE EFFECTS

We consider an unbunched elliptical beam propagating in an alternating-gradient focusing field and a cylindrical metal pipe with radius R, as shown in Fig. 1. The beam has an envelope $a(s)$ in the x direction and an envelope $b(s)$ in the y direction, where $s = z$. The beam drift velocity in the z direction is $v_z \approx \beta_b c$, where c is the speed of light in vacuum. In the present analysis, we assume that the beam centroid motion is stable and on the z axis, and ignore the beam centroid motion. Following the analysis of Sacherer [18], we express the beam density in a self-similar beam model as

$$n(x, y, s) = n\left(\frac{x^2}{a^2} + \frac{y^2}{b^2}\right). \tag{1}$$

The general rms envelope equations can be expressed as [18]

$$\frac{d^2\tilde{x}}{ds^2} + \kappa_q(s)\tilde{x} + \frac{K}{2qN_b\tilde{x}}\left\langle x\frac{\partial\phi}{\partial x}\right\rangle = \frac{1}{\tilde{x}^3}\left(\frac{\varepsilon_x}{4}\right)^2 \tag{2}$$

and

$$\frac{d^2\tilde{y}}{ds^2} - \kappa_q(s)\tilde{y} + \frac{K}{2qN_b\tilde{y}}\left\langle y\frac{\partial\phi}{\partial y}\right\rangle = \frac{1}{\tilde{y}^3}\left(\frac{\varepsilon_y}{4}\right)^2. \tag{3}$$

In Eqs. (2) and (3), $\langle\rangle$ denotes the moment operator with respect to the particle beam distribution; $\tilde{x} = \sqrt{\langle x^2\rangle}$ and $\tilde{y} = \sqrt{\langle y^2\rangle}$ are the rms envelopes in the x and y directions, respectively;

$$\varepsilon_x = 4[\langle x^2\rangle\langle(dx/ds)^2\rangle - \langle x(dx/ds)\rangle^2]^{1/2}, \tag{4}$$

and

$$\varepsilon_y = 4[\langle y^2\rangle\langle(dy/ds)^2\rangle - \langle y(dy/ds)\rangle^2]^{1/2} \tag{5}$$

are 4 times the beam rms emittances in the x and y directions, respectively; $s = c\beta_b t$ is the axial distance; ϕ is the potential distribution generated by the beam space charge including image-charge effects of the cylindrical conducting pipe; $\kappa_q(s) = qB_q'(s)/(\gamma_b m\beta_b c)$ is the focusing parameter of the alternating-gradient focusing system; $\vec{B}^q = B_q'(s)(y\hat{x} + x\hat{y})$ is the alternating-gradient quadrupole magnetic field with $B_q'(s) = B_q'(s + S)$, where S is the period of the field, m and q are the rest mass and charge of the particle, respectively; $K = 2q^2N_b/\gamma^3 m\beta_b^2 c^2$ is the generalized beam perveance; $N_b = \int_{-\infty}^{\infty}\int_{-\infty}^{\infty} n(x, y, s)dxdy$ is the number of charged particle per unit length along the z direction; $\gamma = (1 - \beta_b^2)^{-1/2}$ is the relativistic factor of the beam.

In order to derive an explicit expression for the potential ϕ, we solve Poisson's equation

$$\frac{1}{r}\frac{\partial}{\partial r}\left(r\frac{\partial\phi}{\partial r}\right) + \frac{1}{r^2}\frac{\partial^2\phi}{\partial\theta^2} = -4\pi qn\left(\frac{x^2}{a^2} + \frac{y^2}{b^2}\right) \tag{6}$$

under the paraxial approximation with the boundary condition $\phi|_{r=R} = 0$. Here (r, θ, z) is the corresponding cylindrical coordinate system. Using Green's function technique, it is readily shown that the solution to Eq. (6) can be expressed as

$$\phi = \phi^{\text{free}} + \phi^{\text{image}}, \tag{7}$$

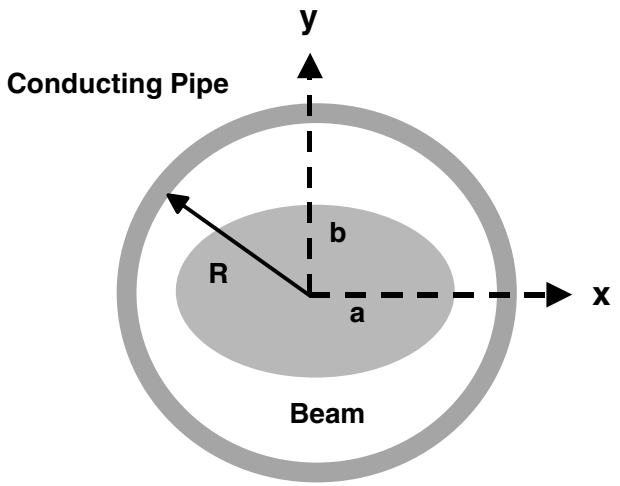

FIG. 1. Elliptical unbunched charged-particle beam in a cylindrical conducting pipe.

where

$$\phi^{\text{free}} = -\pi abq \int_0^\infty \frac{du}{\sqrt{(a^2+u)(b^2+u)}} \int_0^T n(T')dT' \tag{8}$$

is the free-space contribution of the beam,

$$\phi^{\text{image}} = 2q \int_0^\infty \int_0^{2\pi} \ln\left(\frac{R}{r'}\right) n\left(\frac{r'^2\cos^2\theta'}{a^2} + \frac{r'^2\sin^2\theta'}{b^2}\right) r' dr' d\theta' - 2q \sum_{m=1}^{\infty} \int_0^\infty \int_0^{2\pi} \frac{1}{m}\left(\frac{r'r}{R^2}\right)^m \cos[m(\theta-\theta')] n\left(\frac{r'^2\cos^2\theta'}{a^2} + \frac{r'^2\sin^2\theta'}{b^2}\right) r' dr' d\theta' \tag{9}$$

is the image-charge contribution from the cylindrical metal pipe, and the function T is defined by

$$T = \frac{x^2}{a^2+u} + \frac{y^2}{b^2+u}. \tag{10}$$

The space-charge terms in the envelope equations can be simplified by using Eqs. (7)–(10). The results are

$$\left\langle x\frac{\partial\phi}{\partial x}\right\rangle = N_b q(I_x^{\text{free}} + I_x^{\text{image}}), \tag{11}$$

and

$$\left\langle y\frac{\partial\phi}{\partial y}\right\rangle = N_b q(I_y^{\text{free}} + I_y^{\text{image}}), \tag{12}$$

where

$$I_x^{\text{free}} = -\frac{\tilde{x}}{\tilde{x}+\tilde{y}} \tag{13}$$

and

$$I_y^{\text{free}} = -\frac{\tilde{y}}{\tilde{x}+\tilde{y}} \tag{14}$$

are the space-charge contributions in free space [18], and

$$I_x^{\text{image}} = -\sum_{l=1}^{\infty} \frac{\tilde{x}^2(\tilde{x}^2-\tilde{y}^2)^{2l-1}}{R^{4l}} 4^{2l} N_l \tag{15}$$

and

$$I_y^{\text{image}} = -\sum_{l=1}^{\infty} \frac{\tilde{y}^2(\tilde{y}^2-\tilde{x}^2)^{2l-1}}{R^{4l}} 4^{2l} N_l \tag{16}$$

are the image-charge contributions from the cylindrical conducting pipe. Here,

$$N_l = 2\left(\frac{(2l)!}{4^l(l!)^2}\right)^2 \frac{[\int_0^\infty 2\pi abn(\hat{r}^2)\hat{r}^{2l+1}d\hat{r}]^2[\int_0^\infty 2n(\hat{r}^2)\hat{r}d\hat{r}]^{2l}}{N_b^2[4\int_0^\infty n(\hat{r}^2)\hat{r}^3 d\hat{r}]^{2l}} \tag{17}$$

is a multiple moment factor related to the beam density profile.

Substituting Eqs. (11)–(17) into Eqs. (2) and (3), we obtain the envelope equations of the following form:

$$\frac{d^2X}{ds^2} + \kappa_q(s)X - 2K\left[\frac{1}{X+Y} + \sum_{l=1}^{\infty} \frac{X(X^2-Y^2)^{2l-1}}{R^{4l}} N_l\right] = \frac{\varepsilon_x^2}{X^3} \tag{18}$$

and

$$\frac{d^2Y}{ds^2} - \kappa_q(s)Y - 2K\left[\frac{1}{X+Y} + \sum_{l=1}^{\infty} \frac{Y(Y^2-X^2)^{2l-1}}{R^{4l}} N_l\right] = \frac{\varepsilon_y^2}{Y^3}, \tag{19}$$

where $X = 2\tilde{x}$ and $Y = 2\tilde{y}$.

Unlike the previous results obtained by Allen and Reiser [20,21], which include only the $l = 1$ contribution, the present envelope Eqs. (18) and (19) are complete, including both the $l = 1$ contribution and all of the higher-order image-charge effects with $l \geq 2$.

III. EVALUATION OF MULTIPLE MOMENT FACTORS

The multiple moment factor N_l contains the information about the higher-order image-charge effects in the envelope equations (18) and (19). We can assess these effects by evaluating N_l as a function of l. In particular, we consider the following parabolic density profile [11]:

$$n = \begin{cases} n_0 + \delta n_0\left[1 - 3\left(\frac{x^2}{a^2}+\frac{y^2}{b^2}\right)^2\right], & \frac{x^2}{a^2}+\frac{y^2}{b^2} \leq 1, \\ 0, & \frac{x^2}{a^2}+\frac{y^2}{b^2} > 1, \end{cases} \tag{20}$$

where

$$N_b = \int_{-\infty}^{\infty}\int_{-\infty}^{\infty} ndxdy = \pi abn_0 = \text{const}, \tag{21}$$

and δn_0 is independent of x and y and satisfies $-n_0 \leq \delta n_0 \leq n_0/2$.

In Eq. (20), $\delta n_0 = 0$ means that the beam density is a constant across the beam profile, $\delta n_0 > 0$ indicates that the beam density decreases monotonically from the center of profile to its edge and represents a Gaussian-like beam profile, and $\delta n_0 < 0$ implies that the beam density increases monotonically from the center of beam profile to its edge and represents a hollow beam profile such as that observed in the heavy ion injector experiment at LBNL [26].

Using Eq. (20) and the moment definition, we can obtain the simplified expressions of envelopes X and Y. They are written in the form of

$$X^2 = a^2\left(1 - \frac{1}{2}g\right) \tag{22}$$

and

$$Y^2 = b^2\left(1 - \frac{1}{2}g\right). \tag{23}$$

In addition, substituting Eqs. (20) and (21) into Eq. (17), we obtain

$$N_l = 2\left(\frac{(2l)!}{4^l(l!)^2}\right)^2\left(\frac{1}{l - 0.5g}\right)^{2l}\left(\frac{1 - 2gl/(l+3)}{l+1}\right)^2, \tag{24}$$

where

$$g = \frac{\delta n_0}{n_0}. \tag{25}$$

Note in Eq. (24) that $N_1 = 1/8 = 0.125$ is independent of the factor g.

Figure 2 shows a plot of N_l as a function of l for three cases corresponding to $g = 0$, 0.5, and -0.5. In Fig. 2, $N_1 = 0.125$ for all three cases, as expected. For $l \geq 2$, however, the value of N_l decreases with increasing l and depends strongly on the factor g (i.e., on the choice of the density profile). In addition, for a given value of $l > 1$, N_l increases with g; that is, the value of N_l is lower at $g = -0.5$ than at $g = 0.5$. However, this does not necessarily mean that the image-charge effects of a hollow beam are weaker than those of a solid beam because the beam envelopes X and Y given by Eqs. (22) and (23) increase considerably with decreasing g. The physics of image-charge effects is contained in X and Y. Obviously, the values of X and Y are higher at $g = -0.5$ than at $g = 0.5$, which implies that the image-charge effects of a hollow beam are stronger than those of a solid beam.

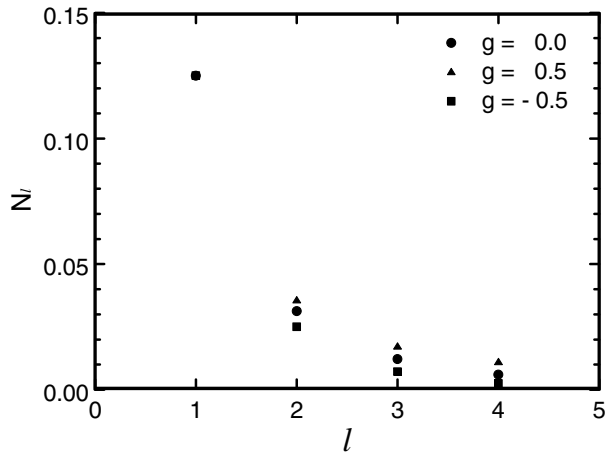

FIG. 2. The dimensionless multiple moment factor N_l versus l for several densities with $g = 0$, 0.5, and -0.5.

IV. IMAGE-CHARGE EFFECTS ON RMS MATCHED BEAMS

In this section, we investigate numerically the image-charge effects on a matched beam using the analytical results obtained in Sec. II, and show that for vacuum phase advance $\sigma_v < 90°$, the higher-order image-charge effects on the matched beam envelopes are negligibly small for all beams with arbitrary beam density profiles (including hollow density profiles) as well as for arbitrary small apertures (including beams with large aspect ratios). We pay special attention to a hollow beam observed in a recent heavy ion beam experiment [26].

For present purposes, we assume that the rms emittances ε_x and ε_y are constant, i.e., $\varepsilon_x = \varepsilon_y = \varepsilon$, and that the beam density profile is given in Eq. (20). We also assume that the alternating-gradient transport system is presented a step-function lattice (in Fig. 3) defined by [11]

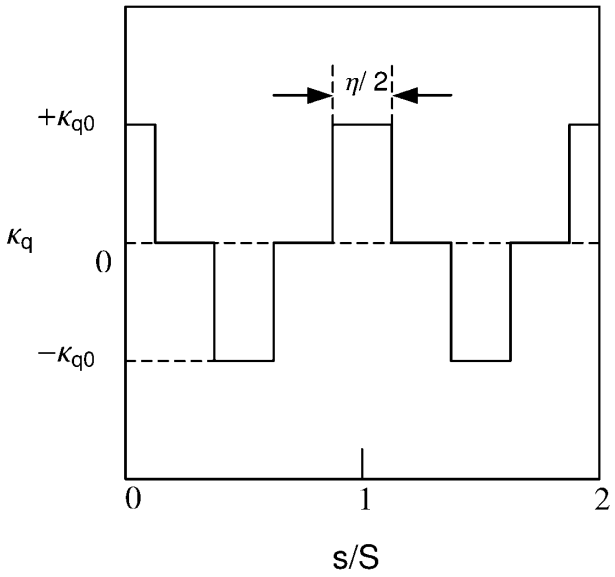

FIG. 3. Plot of the normalized step-function lattice $\kappa_q(s)$ versus normalized propagating distance s/S for $\eta = 0.5$.

$$\kappa_q(s) = \begin{cases} +\kappa_{q0}, & 0 \le s/S < 0.25\eta, \\ 0, & 0.25\eta \le s/S < 0.5(1-0.5\eta), \\ -\kappa_{q0}, & 0.5(1-0.5\eta) \le s/S < 0.5(1+0.5\eta), \\ 0, & 0.5(1+0.5\eta) \le s/S < 0.5(2-0.5\eta), \\ +\kappa_{q0}, & 0.5(2-0.5\eta) \le s/S < 1, \end{cases} \tag{26}$$

where κ_{q0} is a constant and η $(0 < \eta < 1)$ is the filling factor. The strength of the alternating-gradient focusing field can be measured in terms of the vacuum phase advance σ_v. For step-function lattice defined in Eq. (26), the vacuum phase advance σ_v satisfies [11]

$$\cos\sigma_v = \cosh\varphi_1(\cos\varphi_1 - \varphi_2\sin\varphi_1) + \varphi_2\sinh\varphi_1(\cos\varphi_1 - 0.5\varphi_2\sin\varphi_1), \tag{27}$$

where

$$\varphi_1 = 0.5S\eta\sqrt{\kappa_{q0}} \tag{28}$$

and

$$\varphi_2 = \frac{1-\eta}{\eta}\varphi_1. \tag{29}$$

In the numerical analysis of the beam envelope equations (18) and (19), it is convenient to use the dimensionless parameters and normalized variables defined by $\hat{s} = s/S$, $\tilde{a} = X/\sqrt{S\varepsilon}$, $\tilde{b} = Y/\sqrt{S\varepsilon}$, $\hat{K} = KS/\varepsilon$, $\hat{R} = R/\sqrt{S\varepsilon}$, and $\tilde{\kappa}_q(s) = S^2\kappa_q(s)$. For example, Fig. 4 shows the matched beam envelope functions $\tilde{a}(s) = \tilde{a}(s+S)$ and $\tilde{b}(s) = \tilde{b}(s+S)$ for $\sigma_v = 80^0$, $\hat{K} = 10$, $\eta = 0.5$, $g = -0.5$ for beam propagation in free space as well as in a cylindrical conducting pipe with $\hat{R} = 4.0$. It is evident in Fig. 4 that the image-charge effects, including the contributions from all orders, are negligibly small for a hollow beam whose maximum envelopes are very close to the wall of the cylindrical pipe ($\tilde{a}_{\max} = \tilde{b}_{\max} \approx 3.25$ and $\hat{R} = 4.0$).

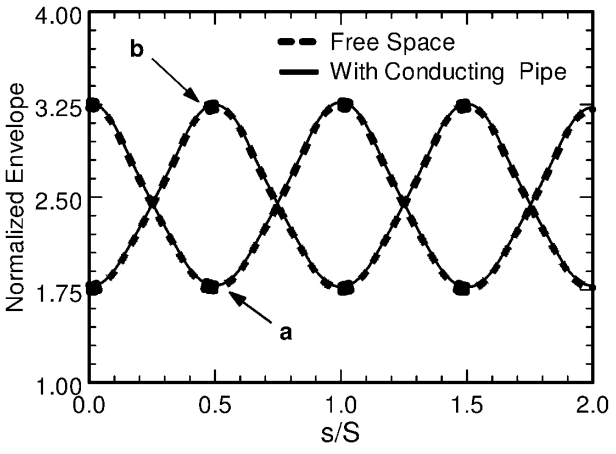

FIG. 4. Plot of the normalized envelope functions $\tilde{a}$ and $\tilde{b}$ versus normalized propagating distance s/S for $\sigma_v = 80^0$, $\hat{K} = 10$, $g = -0.5$, $\eta = 0.5$, and $\hat{R} = 4.0$.

We have carried out comprehensive numerical studies of the image-charge effects on the matched envelope functions for different beam density profiles, including beams with large aspect ratios. The numerical results show that for vacuum phase advance $\sigma_v < 90°$, the total image-charge effects, including higher-order ones, do not affect significantly the matched beam envelopes for arbitrary beam density profiles and arbitrarily small apertures (conducting pipes).

V. IMAGE-CHARGE EFFECTS ON SLIGHTLY MISMATCHED BEAMS AND ENVELOPE INSTABILITIES

In a real device, it is almost impossible to obtain a precisely matched beam because there exist some perturbations on the beam propagation. These perturbations may cause beam envelope instabilities, and the unstable beam envelopes may result in particle beam losses. A perturbation on the matched beam results in a mismatched beam in the alternating-gradient focusing system. The beam envelope instability has already been investigated in free space [11–15]. However, the image-charge effects of the cylindrical conducting pipe on the mismatched beams and the beam envelope instability have not been studied until the present paper. In this section, the envelope equations (18) and (19) are solved, assuming $\varepsilon_x = \varepsilon_y = \varepsilon$, for slightly mismatched beams to find the unstable regions in the parameter space.

In order to obtain slightly mismatched beam envelopes, following the method employed in Ref. [11], the initial conditions for $\tilde{a}(s)$ and $\tilde{b}(s)$ at $s = 0$ are chosen to be

$$\tilde{a}(0) = \tilde{a}_0(1+\delta) \tag{30}$$

and

$$\tilde{b}(0) = \tilde{b}_0(1-\delta), \tag{31}$$

where $\tilde{a}_0$ and $\tilde{b}_0$ are the matched beam envelopes at $s = 0$, and δ is chosen to be in the region of $0 \le |\delta| \le 0.01$. Here, δ represents the perturbations caused by the noise in the beam. Therefore, the initial perturbation to the matched beam envelope is assumed to be as small as 1%. In the numerical calculations, the particle beams are allowed to propagate over 40 periods. Further increasing the number of the propagation periods does not affect the determination of the unstable regions. In order to determine the unstable regions for beam envelopes, we run the envelope code and observe if the beam envelopes are stable or unstable for given parameters, instead of calculating the eigenvalues of the transfer matrix.

Figure 5 is a plot of $\hat{K} = KS/\varepsilon$ versus σ_v, showing the unstable regions of the slightly mismatched beam envelopes for $\eta = 0.5$ and $g = 0$ for three cases

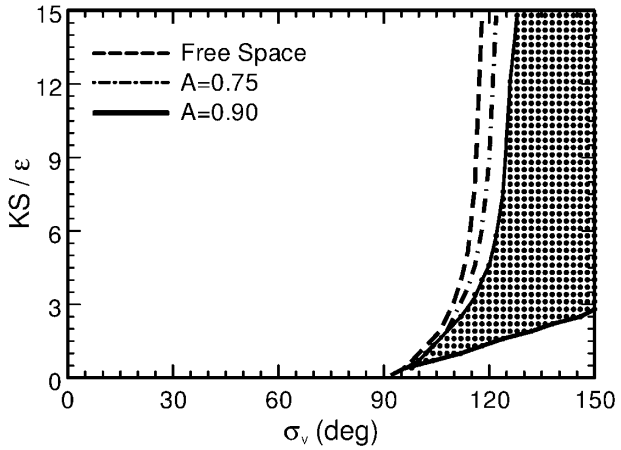

FIG. 5. Plot of the unstable regions in the dimensionless parameter space for the beam envelope evolution with $\eta = 0.5$ and $g = 0$ for three cases corresponding to (a) $R = \infty$ (free space), (b) $A = \tilde{a}_0/\hat{R} = 0.75$, and (c) $A = \tilde{a}_0/\hat{R} = 0.90$. Here, the shaded region is the unstable region for the beam envelope evolution with image-charge effects and $A = \tilde{a}_0/\hat{R} = 0.90$.

corresponding to (a) $R = \infty$ (free space), (b) $A = \tilde{a}_0/\hat{R} = 0.75$ (with cylindrical conducting pipe), and (c) $A = \tilde{a}_0/\hat{R} = 0.90$ (with cylindrical conducting pipe). As can be seen from Fig. 5, the unstable regions for all three cases start around $\sigma_v = 90°$. The solid lines indicate the boundary of the unstable region with image-charge effects from the cylindrical pipe for $A = \tilde{a}_0/\hat{R} = 0.90$, whereas the dashed lines represent the boundary of unstable region without image-charge effects in free space. The unstable region with image-charge effects for $A = \tilde{a}_0/\hat{R} = 0.90$ is shaded in Fig. 5. Although the lower boundaries for the three cases almost coincide, there is an observable difference between their upper boundaries.

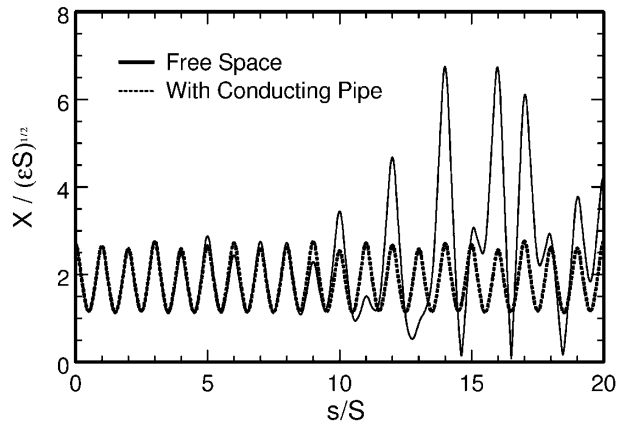

FIG. 6. Oscillations of the normalized beam envelope $\tilde{a} = X/\sqrt{S\varepsilon}$ for both free-space and cylindrical conducting pipe cases with $\hat{K} = 10.0$, $\sigma_v = 120°$, and $A = \tilde{a}_0/\hat{R} = 0.9$, corresponding to a point in Fig. 5 where the envelopes in free space are unstable but the envelopes in cylindrical conducting pipe are stable.

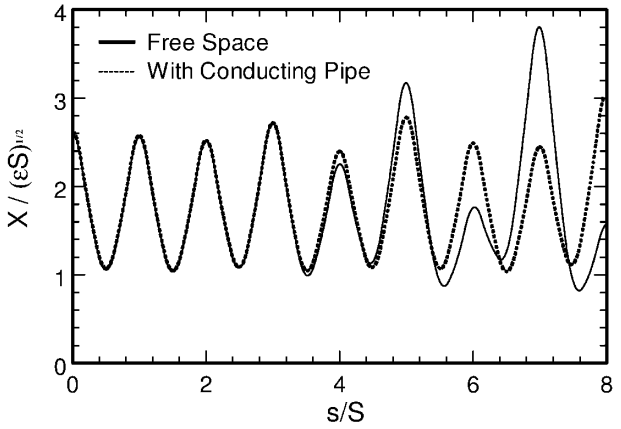

FIG. 7. Oscillations of the normalized beam envelope $\tilde{a} = X/\sqrt{S\varepsilon}$ for both free-space and cylindrical conducting pipe cases at $\hat{K} = 10.0$, $\sigma_v = 130°$, and $A = \tilde{a}_0/\hat{R} = 0.9$, corresponding to a point in Fig. 5 where the envelopes are unstable in both free space and cylindrical pipe.

The unstable region for cylindrical pipe case (i.e., with image-charge effects) is obviously narrower than that in the free-space situation (i.e., without image-charge effects).

Figure 6 shows the oscillations of $\tilde{a} = X/\sqrt{S\varepsilon}$ for both free-space and cylindrical conducting pipe cases at $\hat{K} = 10.0$, $\sigma_v = 120°$, and $A = \tilde{a}_0/\hat{R} = 0.9$, which corresponds to a point in Fig. 5 where the envelopes in free space are unstable but the envelopes in cylindrical conducting pipe are stable. Figure 7 shows the oscillations of $\tilde{a} = X/\sqrt{S\varepsilon}$ for both free-space and cylindrical conducting pipe cases at $\hat{K} = 10.0$, $\sigma_v = 130°$, and $A = \tilde{a}_0/\hat{R} = 0.9$, which corresponds to a point in Fig. 5 where the envelopes are unstable in both free space and cylindrical conducting pipe. Figure 7 indicates that the unstable growth rate of the beam envelopes in free space is greater than that in cylindrical pipe. The results for free space agree with those obtained by Qian and Davidson in Ref. [11], in which they showed an unstable region for $90° < \sigma_v < 170°$. It should be mentioned that the unstable regions are not sensitive to both η and g for the case of a cylindrical conducting pipe, which is similar to the fact that the instability in the free-space case is insensitive to η as noted by Qian and Davidson [11].

VI. CONCLUSIONS

In this paper, rms envelope equations were derived and analyzed for unbunched intense charged-particle beams in an alternating-gradient focusing field and a cylindrical metal pipe. All higher-order image-charge effects from the cylindrical pipe were expressed in terms of so-called multiple moment factors in the rms beam envelope equations, and the multiple moment factors were evaluated. Numerical results showed that for vacuum phase advance $\sigma_v < 90°$, the image-charge effects on the matched and slightly mismatched beam envelopes are negligibly

small, at all orders, for all beams with arbitrary beam density profiles (including hollow density profiles) as well as for arbitrary small apertures (including beams with large aspect ratios). However, the main unstable region for the envelope evolution with image-charge effects, which occurs for $90° < \sigma_v < 270°$, depending on the value of the normalized beam intensity SK/ε, was found to be narrower than its counterpart without image-charge effects.

ACKNOWLEDGMENTS

This research was supported by the U.S. Department of Energy, Office of Fusion Energy Science, Grant No. DE-FG02-01ER54662, and Division of High-Energy Physics, Grant No. DE-FG02-95ER40919.

*Permanent address: Department of Applied Physics, National University of Defense Technology, Changsha 410073, Hunan, People's Republic of China.

[1] E. P. Lee and J. Hovingh, Fusion Technol. **15**, 369 (1989).
[2] R. W. Müller, in *Nuclear Fusion by Inertial Confinement: A Comprehensive Treatise*, edited by G. Velarde, Y. Ronen, and J. M. Martínez-Val (Chemical Rubber Co., Boca Raton, FL, 1993), Chap. 17, pp. 437–453.
[3] R. A. Jameson, in *Advanced Accelerator Concepts*, edited by J. S. Wurtele, AIP Conf. Proc. No. 279 (AIP, New York, 1993), p. 969.
[4] See, e.g., *Space-Charge Dominated Beams and Applications of High-Brightness Beams*, edited by S. Y. Lee, AIP Conf. Proc. No. 377 (AIP, New York, 1996).
[5] F. M. Bieniosek, J. W. Kwan, E. Henestroza, and C. Kim, Nucl. Instrum. Methods Phys. Res., Sect. A **464**, 592 (2001).
[6] C. Chen and R. C. Davidson, Phys. Rev. Lett. **72**, 2195 (1994).
[7] Q. Qian, R. C. Davidson, and C. Chen, Phys. Plasmas **2**, 2674 (1995).
[8] Q. Qian, R. C. Davidson, and C. Chen, Phys. Plasmas **1**, 1328 (1994).
[9] R. C. Davidson and Q. Qian, Phys. Plasmas **1**, 3104 (1994).
[10] M. Reiser, *Theory and Design of Charged-Particle Beams* (Wiley, New York, 1994).
[11] Q. Qian and R. C. Davidson, Phys. Rev. E **53**, 5349 (1996).
[12] I. Hofmann, L. Laslett, L. Smith, and I. Haber, Part. Accel. **13**, 145 (1983).
[13] J. Stuckmeier, J. Klabunde, and M. Reiser, Part. Accel. **15**, 47 (1984).
[14] R. Pakter and F. B. Rizzato, Phys. Rev. Lett. **87**, 044801 (2001).
[15] R. Pakter and F. B. Rizzato, Phys. Rev. E **65**, 056503 (2002).
[16] I. M. Kapchinskij and V. V. Vladimirskij, in *Proceedings of the International Conference on High-Energy Accelerators and Instrumentation* (CERN, Geneva, 1959), p. 274.
[17] P. Lapostolle, CERN Report No. AR/Int SG/65-15, 1965.
[18] F. J. Sacherer, IEEE Trans. Nucl. Sci. **18**, 1105 (1971).
[19] P. Lapostolle, IEEE Trans. Nucl. Sci. **18**, 1101 (1971).
[20] C. K. Allen and M. Reiser, Phys. Rev. E **54**, 2884 (1996).
[21] C. K. Allen, Ph.D. thesis, University of Maryland, 1996.
[22] E. P. Lee, E. Close, and L. Smith, in *Proceedings of the 1987 IEEE Particle Accelerator Conference*, edited by E. R. Lindstorm and L. S. Taylor (IEEE, New York, 1987), p. 1126.
[23] R. L. Gluckstern, in *Proceedings of the 1970 Proton Linear Accelerator Conference*, edited by M. R. Tracy (National Accelerator Laboratory, Batavia, IL, 1971), p. 811.
[24] S. M. Lund and R. C. Davidson, Phys. Plasmas **5**, 3028 (1998).
[25] R. Pakter and C. Chen, IEEE Trans. Plasma Sci. **28**, 502 (2000).
[26] S. Yu, S. Eylon, E. Henestroza, and D. Grote, in *Space-Charge Dominated Beams and Applications of High-Brightness Beams* (Ref. [4]).

Chaotic particle motion and beam halo formation induced by image-charge effects in a small-aperture alternating-gradient focusing system

Jing Zhou,[a] B. L. Qian, and Chiping Chen
Plasma Science and Fusion Center, Massachusetts Institute of Technology, Cambridge, Massachusetts 02139

(Received 10 July 2003; accepted 5 September 2003)

It is shown with a test-particle model that image-charge effects induce a new mechanism for chaotic particle motion and halo formation in an intense charged-particle beam propagating through an alternating-gradient focusing channel with a small aperture, circular, perfectly conducting pipe. This mechanism occurs for a well-matched beam with the Kapchinskij–Vladimirskij distribution. The percentage of beam loss to the conductor wall is calculated as a function of propagating distance and aperture size. © *2003 American Institute of Physics.* [DOI: 10.1063/1.1622388]

Alternating-gradient accelerators have wide applications in basic scientific research, medicine and industrial processing. Many accelerators that are being constructed or proposed for basic scientific research such as heavy ion fusion accelerators and spallation neutron sources are required to handle high average power and high brightness beams. An important aspect in the design of periodically focused beams in such accelerators and klystrons for the next linear collider (NLC) is to prevent the beams from developing halos and chaos which may cause beam losses to the conducting walls of the accelerating structures.[1–7] The problem of halo formation and beam losses is of a serious concern in the design of small-aperture focusing transport systems[8,9] that are often required in order to keep accelerator costs manageable.

Two key mechanisms for halo formation have been studied using analytical models[1–3] and self-consistent simulations with particle-in-cell (PIC)[4–7] and Green's function techniques. It has been shown in the test-particle model that chaotic particle motion and halo formation occur when the root-mean-squared (rms) beam envelopes have a sufficient large mismatch in a constant focusing channel[1] or when the beam density is sufficiently nonuniform in an alternative-gradient focusing channel.[3] Until the present analysis, however, most published analytical results on beam halo formation have been based on free-space models in which wall effects on halo formation have been ignored.

In this Letter, we report a new mechanism for chaotic particle motion and halo formation in intense charged-particle beams. In particular, use is made of a test-particle model to investigate the dynamics of rms matched intense charged particle beams propagating through an alternating-gradient quadrupole magnetic field and a small aperture. The elliptical cross section of the beam and the circular cross section of the pipe are incorporated. While the present model allows for nonuniform beams with elliptic symmetry, the effects of image charges on halo formation are illustrated with a uniform (Kapchinskij–Vladimirskij, KV) beam distribution.[10] It is shown that the image-charge-induced fields are nonlinear, and that they induce chaotic particle motion and halo formation. While it has been recognized recently that image-charge effects have negligibly small influence on the rms beam envelope dynamics[11] for vacuum phase advance less than 90°, our results show that image-charge effects play an important role in halo formation and cause significant beam losses as the aperture decreases.

We consider an rms-matched continuous intense charged-particle beam propagating in the longitudinal direction through an alternating-gradient quadrupole magnetic field with axial periodicity length S in a perfectly conducting round pipe with radius R. The beam density is assumed to be $n=n(x^2/a^2+y^2/b^2)$. An analytical expression for the scalar potential can be obtained for the assumed density profile,

$$\phi=-\pi abq\int_0^\infty \frac{ds}{\sqrt{(a^2+s)(b^2+s)}}\int_0^T n(T)dT + \pi abq\left[\int_0^\infty \frac{ds}{\sqrt{(a^2+s)(b^2+s)}}\int_0^{T_1} n(T_1)dT_1 - 2\ln\left(\frac{R}{r}\right)\int_0^\infty n(T_1)dT_1\right], \tag{1}$$

where $T=x^2/(a^2+s)+y^2/(b^2+s)$, $T_1=x_1^2/(a^2+s)+y_1^2/(b^2+s)$, $r=(x^2+y^2)^{1/2}$, $x_1=R^2x/(x^2+y^2)$, and $y_1=R^2y/(x^2+y^2)$.

For the KV beam, the periodic beam envelope functions $a(s)=a(s+S)$ and $b(s)=b(s+S)$ obey[11]

$$\frac{d^2a}{ds^2}+\kappa_q(s)a-2K\left[\frac{1}{a+b}+\sum_{l=1}^{\infty}\frac{a(a^2-b^2)^{2l-1}}{R^{4l}}N_l\right]=\frac{\epsilon_x^2}{a^3} \tag{2}$$

and

$$\frac{d^2b}{ds^2}-\kappa_q(s)b-2K\left[\frac{1}{a+b}+\sum_{l=1}^{\infty}\frac{b(b^2-a^2)^{2l-1}}{R^{4l}}N_l\right]=\frac{\epsilon_y^2}{b^3}, \tag{3}$$

where $N_l=(2/\pi)[\Gamma(l+\frac{1}{2})/\Gamma(l+2)]^2$ with $\Gamma(x)$ being the standard gamma function, $\epsilon_x=4\epsilon_{x\,\mathrm{rms}}$ and $\epsilon_y=4\epsilon_{y\,\mathrm{rms}}$ are 4 times the beam rms emittances in the x and y directions,

[a]Electronic mail: jea_zhou@mit.edu

respectively, $s=\beta_b ct$ is the axial coordinate, the periodic function $\kappa_q(s)=\kappa_q(s+S)=(q/\gamma_b m\beta_b c)(\partial B_x^q/\partial y)$ describes the quadrupole focusing field, $N_b=\pi ab\int_0^\infty n(u)du$ is the number of particles per unit axial length, $K=2q^2N_b/(\gamma^3 m\beta_b^2 c^2)$ is the generalized beam perveance, $\phi(x,y,s)$ and $\beta_b\phi(x,y,s)$ are the scalar and axial vector potentials associated with the space charge and current of the intense charged particle beam, respectively, q and m are the particle charge and rest mass, respectively, c is the speed of light in vacuum, $\beta_b c$ is the average axial beam velocity, and $\gamma_b=(1-\beta_b^2)^{-1/2}$ is the relativistic mass factor.

In the paraxial approximation, the transverse equations of motion for an individual test particle can be expressed as[12]

$$\frac{d^2x}{ds^2}+\kappa_q(s)x+\frac{q}{\gamma_b^3 m\beta_b^2 c^2}\frac{\partial\phi}{\partial x}=0, \tag{4}$$

$$\frac{d^2y}{ds^2}-\kappa_q(s)y+\frac{q}{\gamma_b^3 m\beta_b^2 c^2}\frac{\partial\phi}{\partial y}=0. \tag{5}$$

It is important to specify initial conditions for the test-particle motion that are consistent with the assumed beam density, which is accomplished by the particular choice of an initial distribution function[3] at $s=s_0$, i.e., $f_b(x,y,x',y',s_0)=N_b\delta(W-1)/\pi^2\epsilon_x\epsilon_y$, where $x'=dx/ds$, and W is the variable defined by $W=x^2/a^2+(ax'-xa')^2/\epsilon_x^2+y^2/b^2+(by'-yb')^2/\epsilon_y^2$. Here, a, a', b, and b' denote the "initial" values at $s=s_0$. The dynamical Eqs. (4) and (5) completely describe the model.

A test-particle simulation module is added to the existing two-dimensional periodically focused beam (PFB2D) code for studies of the test-particle dynamics described in Eqs. (4) and (5), where an analytical expression for ϕ is derived for a uniform density beam. The code uses the standard IMSL Runge–Kutta integration routine. For the results discussed below, a maximum accumulative relative error of 10^{-4} which is weighted true error taken over all dynamical variables and all steps from $s=0$ to the end of this computation, is used to give sufficiently accurate results in the simulations.

For the KV beam distribution,[10] as the pipe radius goes to infinity, the image charge fields vanish. Therefore, in the free-space case, the self-fields have a linear dependence on x and y within the beam boundary $x^2/a^2+y^2/b^2=1$. The equations of motion reduce to uncoupled Hill's equations, and the particle orbits are confined within the beam envelope, provided the latter is stable.

As the pipe radius gets close to the beam envelope, the fields become nonlinear due to the image charge on the pipe. The particle orbits are nonintegrable, and can become chaotic. Equations (4) and (5) are solved numerically, where the periodic $a(s)$ and $b(s)$ are obtained numerically from the envelope Eqs. (2) and (3). We have benchmarked our numerical results against the published results for the free-space case in Ref. 3. In the free space case, all the particles with $W(s=0)\leqslant 1$ are regular and their W's are constant.

The best way to illustrate the image charge effects on inducing chaotic particle motion and halo formation is by plotting the range of W for various initial conditions, instead of using the usual Poincaré surface-of-section plot.[3] In Fig. 1

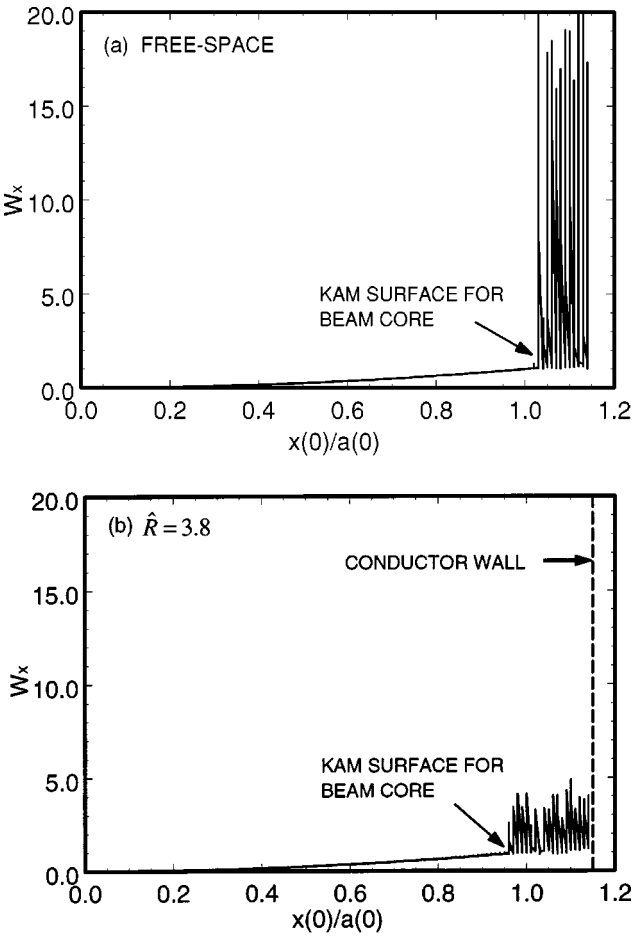

FIG. 1. Plots of the range of W_x for test particles propagating over 2000 lattice periods for two cases (a) free space $\hat{R}=\infty$ and (b) $\hat{R}=3.8$. The system parameters are chosen to be $\eta=0.5$, $KS/\epsilon_x=10.0$, $\epsilon_x=\epsilon_y=\epsilon$, and $\sigma_v=80°$. The 115 test particles are loaded uniformly at $s=0$ between the interval $0\leqslant W_x\leqslant 1.15$ along the x' axis in phase space.

the range of transverse energy $W_x=x^2/a^2+(ax'-xa')^2/\epsilon^2$ is plotted for test particles propagating over 2000 lattice periods for two cases (a) free space ($\hat{R}\equiv R/\sqrt{\epsilon S}=\infty$) and (b) $\hat{R}=3.8$. In the simulations, we use a periodic step-function lattice with filling factor η [see Eq. (26) in Ref. 11]. The system parameters are $\eta=0.5$, $KS/\epsilon_x=10.0$, $\epsilon_x=\epsilon_y=\epsilon$, and vacuum phase advance $\sigma_v=80.0°$, which correspond to those in the High-Current Experiment (HCX) at Lawrence Berkeley National Laboratory (LBNL).[9] For these parameters, the maximum value of the normalized envelope is $a(0)/\sqrt{\epsilon S}\cong 3.25$. The 115 test particles are loaded uniformly at $s=0$ between the interval $0\leqslant W_x\leqslant 1.15$ along the x' axis. Because all of the test particles have $(y(0),y'(0))=0$ initially, their trajectories remain in the (x,x') plane of the phase space. As shown in Fig. 1(a), the outermost Kolmogorov–Amold–Moser (KAM) surface for the beam core in the free space case is located at $x/a=1.03$ which is slightly outside the beam boundary. There is a continuum of KAM surfaces for $x(0)/a(0)\leqslant 1.03$, where W_x is conserved. The particles inside the beam core have regular motion and cannot escape to form a halo. As the pipe radius R decreases, the conductor wall intersects the chaotic sea. Furthermore, the image force induced by the conductor wall becomes im-

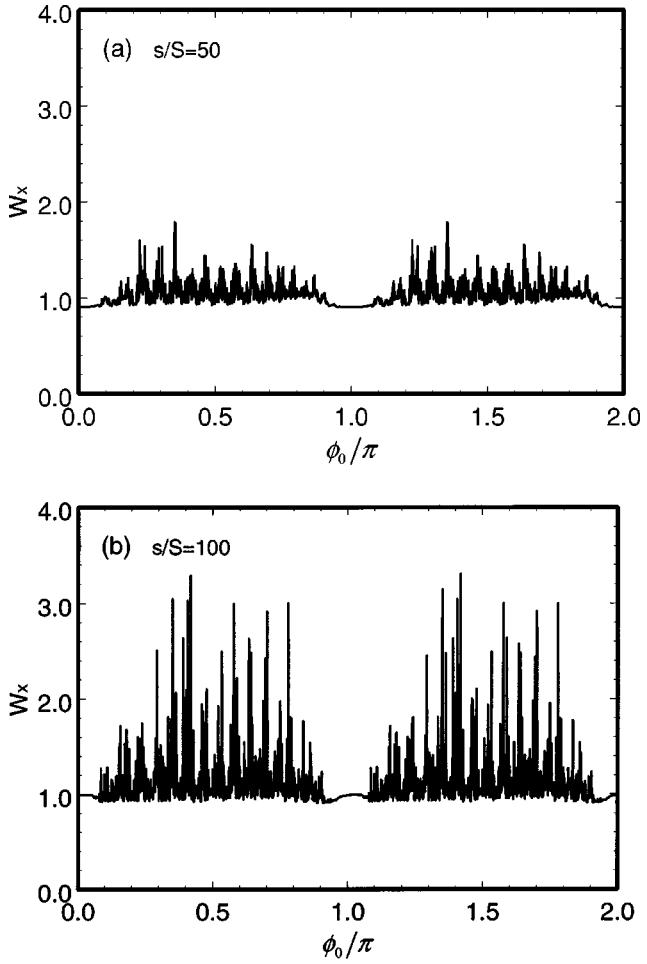

FIG. 2. Plots of W_x for 2000 test particles with the same system parameters as in Fig. 1(b) at two axial locations (a) $s/S=50$ and (b) $s/S=100$. The test particles are initially loaded uniformly with phase ϕ_0 ranging from 0 to 2π on the beam boundary $W_x(0)=(x(0)/a(0))^2+(a(0)x'(0)/\epsilon)^2=1$ in the phase space.

portant and the KAM surface for the beam core moves into the beam interior, reaching $x/a=0.96$, as shown in Fig. 1(b) for $\hat{R}=3.8$. In this case some particles inside the beam core will escape to form a halo and eventually strike the wall.

The locations and evolution of the chaotic particles are illustrated in Fig. 2, where the transverse energy W_x is plotted for 2000 test particles loaded at $s=0$ on the beam boundary $W_x(0)=1$ in the phase space with the initial phases $\phi_0=\tan^{-1}[(S/\epsilon)^{1/2}a(0)x'(0)/x(0)]$ uniformly distributed from 0 to 2π for the same system parameters as in Fig. 1(b). Those test particles with initial phases in the intervals $0\leqslant\phi_0\leqslant0.1\pi$, $0.9\pi\leqslant\phi_0\leqslant1.1\pi$, and $1.9\pi\leqslant\phi_0\leqslant2\pi$ are regular and remain inside the beam with $W_x\cong1$. The other test particles are chaotic and gain energy. Some of the chaotic particles in Fig. 2 strike the wall after tens of periods. An example of such a chaotic particle is illustrated in comparison with a core particle in Fig. 3, where W_x is plotted as a function of s for two test particles with initial phases (a) $\phi_0/\pi=0$ and (b) $\phi_0/\pi=0.35$, which correspond to a halo particle and a core particle, respectively.

Finally, the beam loss is computed as a function of propagation distance and pipe radius. As an example, the

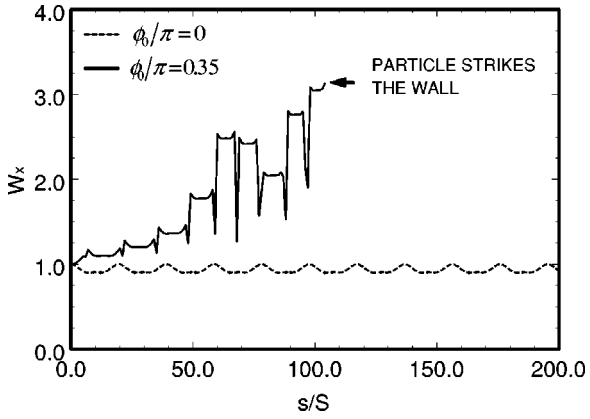

FIG. 3. Plots of W_x vs s for two test particles with initial phases (a) $\phi_0/\pi=0$ and (b) $\phi_0/\pi=0.35$ for the same system parameters as in Fig. 1(b).

results are shown in Fig. 4 for $\eta=0.5$, $KS/\epsilon_x=10.0$, $\epsilon_x=\epsilon_y=\epsilon$, $\sigma_v=80°$, and four choices of the pipe radius with $\hat{R}=3.8$, 3.9, 4.0, and 4.5. The critical value of $\hat{R}$ for the outermost KAM surface adjacent to the beam core to penetrate the beam is estimated to be $\hat{R}=5.5$. The beam loss rate increases with the decreasing pipe radius, where the image effects play a more important role in the total space charge force. When the maximum beam envelope fills 86% of the pipe, the beam loss reaches 8% at $s=1000S$. Although the results shown in Fig. 4 are based on the test-particle calculations, they provide order of magnitude estimates for the actual beam losses, which are being studied using self-consistent simulations.

The results of this paper, which are rigorous to the lowest order, are useful to benchmark PIC and other self-consistent studies of beam halo formation and beam loss, which are known to have noise problems[13] and disagreement with the experimental measurements.[6,7] Because our results are obtained for ideal KV distribution, they are not a quantitative measure of the beam loss in a real experiment. However, they do provide an indication of the amount of such beam loss for a uniform density beam in a long (>100 peri-

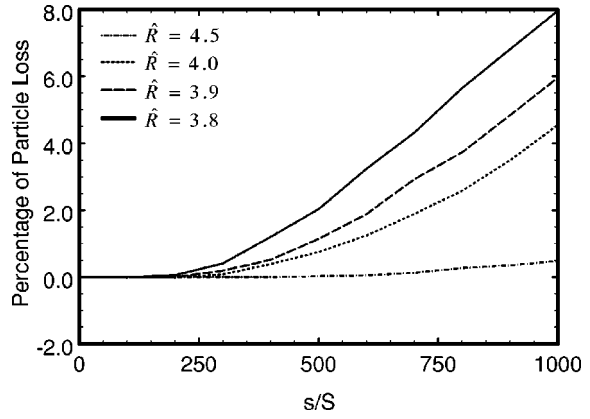

FIG. 4. Plots of the percentage of particles striking the conductor wall as a function of propagation distance for $\eta=0.5$, $KS/\epsilon_x=10.0$, $\epsilon_x=\epsilon_y=\epsilon$, $\sigma_v=80°$ and several choices of $\hat{R}\equiv R/\sqrt{\epsilon S}$. Here, 10 000 test particles with the KV distribution initially are used in the simulations.

ods) focusing system. They also suggest that in short (2 to 30 periods) systems such as the existing Neutralized Transport Experiment (NTX) and High-Current Experiment (HCX),[9] imperfections such as charge-density fluctuations, mismatch, and focusing field nonlinearity and error may play a more important role than image charge effects on beam halo production.

To summarize, we have shown using a test-particle model that in a small-aperture alternating-gradient focusing channel, image-charge effects induce a new mechanism for chaotic particle motion and halo formation in intense charge-particle beams. This mechanism occurs for well-matched beams with the ideal Kapchinskij–Vladimirskij (KV) distribution. The percentage of beam loss has been calculated as a function of distance and aperture size.

ACKNOWLEDGMENTS

This work was supported by US Department of Energy, High-Energy Physics Division Grant No. DE-FG02-95ER40919, Office of Fusion Energy Science, Grant No. DE-FG02-01ER54662, and in part by Air Force Office of Scientific Research, Grant No. F49620-00-1-0007.

[1] R. L. Gluckstern, Phys. Rev. Lett. **73**, 1247 (1994).
[2] J. M. Lagniel, Nucl. Instrum. Methods Phys. Res. A **345**, 405 (1994).
[3] Q. Qian, R. C. Davidson, and C. Chen, Phys. Plasmas **2**, 2674 (1995); Phys. Rev. E **51**, R5216 (1995).
[4] C. M. Celata, I. Haber, and D. P. Grote, *Proceedings of the 2001 Particle Accelerator Conference, Chicago, IL* (IEEE, Piscataway, NJ, 2001), pp. 2926–2928.
[5] C. M. Celata, F. M. Bieniosek, L. Prost *et al.*, *Proceedings of the 2003 Particle Accelerator Conference, Portland, OR* (IEEE, Piscataway, NJ, 2003).
[6] R. W. Garnett, J. H. Billen, K. C. D. Chan *et al.*, in *Space Charge Dominated Beams and Applications of High Brightness Beams*, edited by S. Y. Lee, AIP Conf. Proc. No. **377** (AIP, New York, 1996), p. 60.
[7] C. K. Allen, K. C. D. Chan, P. L. Colestock *et al.*, Phys. Rev. Lett. **89**, 214802 (2002).
[8] F. M. Bieniosek, J. W. Kwan, E. Henestroza, and C. Kim, Nucl. Instrum. Methods Phys. Res. A **464**, 592 (2001).
[9] P. A. Seidl, F. M. Bieniosek, C. M. Celata *et al.*, Nucl. Instrum. Methods Phys. Res. A **464**, 369 (2001).
[10] I. Kapchinskij and V. Vladimirskij, *Proceedings of the International Conference on High Energy Accelerators and Instrumentation* (CERN Scientific Information Service, Geneva, 1959), p. 274.
[11] B. L. Qian, J. Zhou, and C. Chen, Phys. Rev. ST Accel. Beams **6**, 014201 (2003).
[12] R. C. Davidson, *Physics of Nonneutral Plasmas* (Addison-Wesley, Reading, MA, 1990), Chap. 10, and references therein.
[13] R. Pakter and C. Chen, *Proceedings of the 1997 Particle Accelerator Conference* (IEEE, Vancouver, Canada, 1997), p. 1938.

Available online at www.sciencedirect.com
SCIENCE DIRECT®
Nuclear Instruments and Methods in Physics Research A 544 (2005) 492–496
NUCLEAR INSTRUMENTS & METHODS IN PHYSICS RESEARCH Section A
www.elsevier.com/locate/nima

Parametric studies of image-charge effects on an intense beam in a small-aperture alternating-gradient focusing system

Jing Zhou*, Chiping Chen

Plasma Science and Fusion Center, Massachusetts Institute of Technology, Cambridge, MA 02139, USA

Available online 17 March 2005

Abstract

The image-charge effects on an intense charged-particle beam propagating through an alternating-gradient focusing channel with a small aperture, circular, perfectly conducting pipe are studied using a test-particle model. For a well-matched elliptical beam with the Kapchinskij–Vladimirskij (KV) distribution, it is found that halo formation and beam loss are induced by nonlinear fields due to image charges on the wall. The halo formation and chaotic particle motion is found to depend sensitively on the system parameters: the occupancy of the quadrupole focusing field, the vacuum phase advance, the beam perveance, and the ratio of the beam size to the aperture. Furthermore, the percentage of beam loss to the conductor wall is calculated as a function of propagating distance and aperture.

PACS: 41.85.Ja; 41.75.–i

Keywords: Intense charged-particle beam; Alternating-gradient focusing

1. Introduction

Alternating-gradient accelerators required to handle high average power and high brightness beams are being constructed or proposed for basic scientific research such as heavy ion fusion, high-energy physics, high-energy density physics, and spallation neutron sources. An important aspect in the design of periodically focused beams in such accelerators and RF drivers for the next linear collider (NLC) is to prevent the beams from developing halos and chaos which may cause beam losses to the conducting walls of the accelerating structures [1–7]. The problem of halo formation and beam losses is of a serious concern in the design of small-aperture focusing transport systems [8,9] that are often required in order to keep accelerator costs manageable.

Two key mechanisms for halo formation, namely, mismatch in a constant focusing channel [1] and non-uniform density in an alternating-gradient focusing channel [3], have been studied using analytical models [1–3] and self-consistent

*Corresponding author. Tel.: +1 617 253 1669.
E-mail address: jea_zhou@mit.edu (J. Zhou).

0168-9002/$ - see front matter © 2005 Elsevier B.V. All rights reserved.
doi:10.1016/j.nima.2005.03.010

simulations with particle-in-cell (PIC) [4–7] and Green's function techniques. A new mechanism for chaotic particle motion and halo formation due to the image-charge effects in intense charged-particle beams has been reported recently [10]. In particular, use is made of a test-particle model to investigate the dynamics of RMS matched intense charged particle beams propagating through an alternating-gradient quadrupole magnetic field and a small aperture.

We consider an RMS-matched continuous intense charged-particle beam propagating in the longitudinal direction through an alternating-gradient quadrupole magnetic field with axial periodicity length S in a perfectly conducting round pipe with radius R. The beam density is assumed to be $n = n(x^2/a^2 + y^2/b^2)$. An analytical expression for the scalar potential can be obtained for the assumed density profile,

$$\phi = -\pi abq \int_0^\infty \frac{\mathrm{d}s}{\sqrt{(a^2+s)(b^2+s)}} \int_0^T n(T)\,\mathrm{d}T + \pi abq \left[\int_0^\infty \frac{\mathrm{d}s}{\sqrt{(a^2+s)(b^2+s)}} \int_0^{T_1} n(T_1)\,\mathrm{d}T_1 - 2\ln\left(\frac{R}{r}\right) \int_0^\infty n(T_1)\,\mathrm{d}T_1 \right] \quad (1)$$

where $T = x^2/(a^2+s) + y^2/(b^2+s)$, $T_1 = x_1^2/(a^2+s) + y_1^2/(b^2+s)$, $r = (x^2+y^2)^{1/2}$, $x_1 = R^2 x/(x^2+y^2)$, and $y_1 = R^2 y/(x^2+y^2)$. The periodic beam envelope functions $a(s) = a(s+S)$ and $b(s) = b(s+S)$ can be calculated from the envelope equations [11].

In the paraxial approximation, the transverse equations of motion for an individual test particle can be obtained [10] with the potential given in Eq. (1). While initial results of test-particle studies have been reported [10], the purpose of this paper is to discuss the results of parametric studies based on the test-particle model.

2. Image-charge effects

For the Kapchinskij–Vladimirskij (KV) beam distribution [12], as the pipe radius goes to infinity, the image charge fields vanish. Therefore, in the free-space case, the self-fields have a linear dependence on x and y within the beam boundary $x^2/a^2 + y^2/b^2 = 1$. The equations of motion reduce to uncoupled Hill's equations, and the particle orbits are confined within the beam envelope, provided the latter is stable.

As the pipe radius gets close to the beam envelope, the fields become nonlinear due to the image charge on the pipe. The particle orbits are non-integrable, and can become chaotic. As shown in Fig. 1, the Poincaré surface-of section maps of the trajectories of 100 test particles as the test particles pass each lattice period is plotted for an initial KV beam with pipe radius $\hat{R} = R/\sqrt{\varepsilon S} = 4.0$. In the simulations, we use a periodic step-function lattice with occupancy η (see Eq. (26) in Ref. [11]). The system parameters are $\eta = 0.5$, $KS/\varepsilon_x = 10.0$, $\varepsilon_x = \varepsilon_y = \varepsilon = 4\varepsilon_{\mathrm{rms}}$, and vacuum phase advance $\sigma_v = 80^\circ$ which correspond to those in the High-Current Experiment (HCX) at Lawrence Berkeley National Laboratory (LBNL) [9]. A halo develops around the dense beam core.

It is important to specify initial conditions for the test-particle motion that are consistent with the

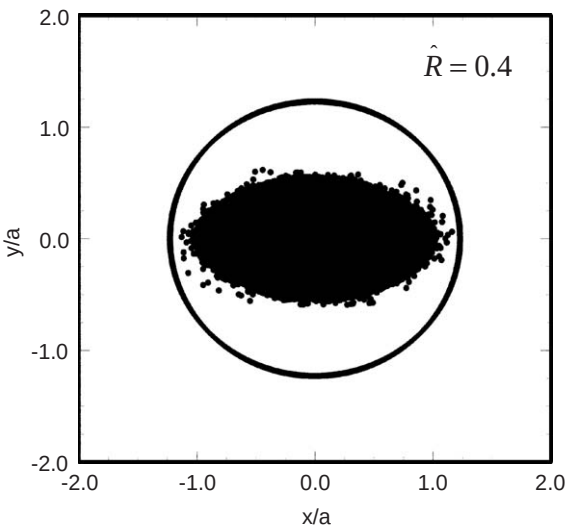

Fig. 1. Poincaré surface-of-section plot for the trajectories of 100 test particles for propagation over 400 lattice periods in the phase plane (x,y) with pipe radius $\hat{R} = 4.0$. The system parameters are chosen to be $\eta = 0.5$, $KS/\varepsilon_x = 10.0$, $\varepsilon_x = \varepsilon_y = \varepsilon$, and $\sigma_v = 80^\circ$.

assumed beam density, which is accomplished in the simulation shown in Fig. 1 by the particular choice of an initial distribution function at $s = s_0 = 0$, i.e., $f_b(x, y, x', y', s_0) = N_b\delta(W - 1)/\pi^2\varepsilon_x\varepsilon_y$, where $x' = \mathrm{d}x/\mathrm{d}s$, and W is the variable defined by $W = x^2/a^2 + (ax' - xa')^2/\varepsilon_x^2 + y^2/b^2 + (by' - yb')^2/\varepsilon_y^2$. Here, a, a', b, and b' denote the "initial" values at $s = s_0 = 0$.

The best way to illustrate the image charge effects on inducing chaotic particle motion and halo formation is by plotting the range of W for various initial conditions, instead of using the usual Poincaré surface-of-section plot [3]. In Fig. 2, the range of transverse energy $W_x = x^2/a^2 + (ax' - xa')^2/\varepsilon^2$ is plotted for test particles propagating over 2000 lattice periods with $\hat{R} = 3.8$, $\eta = 0.5$, $KS/\varepsilon_x = 10.0$, $\varepsilon_x = \varepsilon_y = \varepsilon$, and $\sigma_v = 80^\circ$. For these parameters, the maximum value of the normalized envelope is $a(0)/\sqrt{\varepsilon S} \cong 3.25$. The 115 test particles are loaded uniformly at $s = 0$ between the interval $0 \leqslant W_x \leqslant 1.15$ along the x'-axis. Because all of the test particles have $(y(0), y'(0)) = 0$ initially, their trajectories remain in the (x, x') plane of the phase space. For free-space

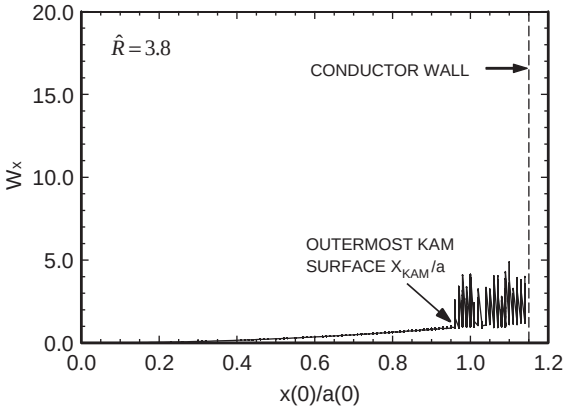

Fig. 2. Plot of the range of W_x for test particles propagating over 2000 lattice periods for $\hat{R} = 3.8$, $\eta = 0.5$, $KS/\varepsilon_x = 10.0$, $\varepsilon_x = \varepsilon_y = \varepsilon$, and $\sigma_v = 80^\circ$. The 115 test particles are loaded uniformly at $s = 0$ between the interval $0 \leqslant W_x \leqslant 1.15$ along the x'-axis in phase space.

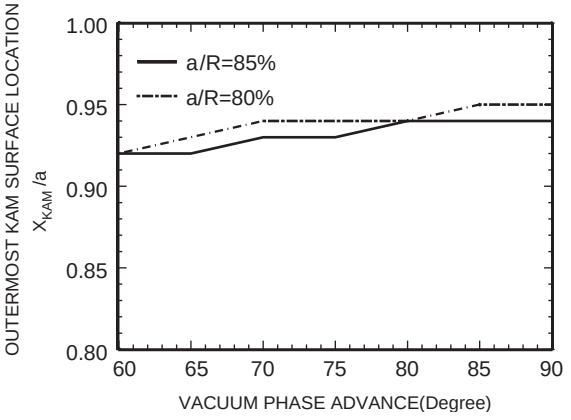

Fig. 3. Plots of the outermost KAM surface location X_{KAM}/a as a function of the vacuum phase advance σ_v for $\eta = 0.5$, $KS/\varepsilon_x = 10.0$, $\varepsilon_x = \varepsilon_y = \varepsilon$, and two cases: (a) $a/R = 80\%$, and (b) $a/R = 85\%$.

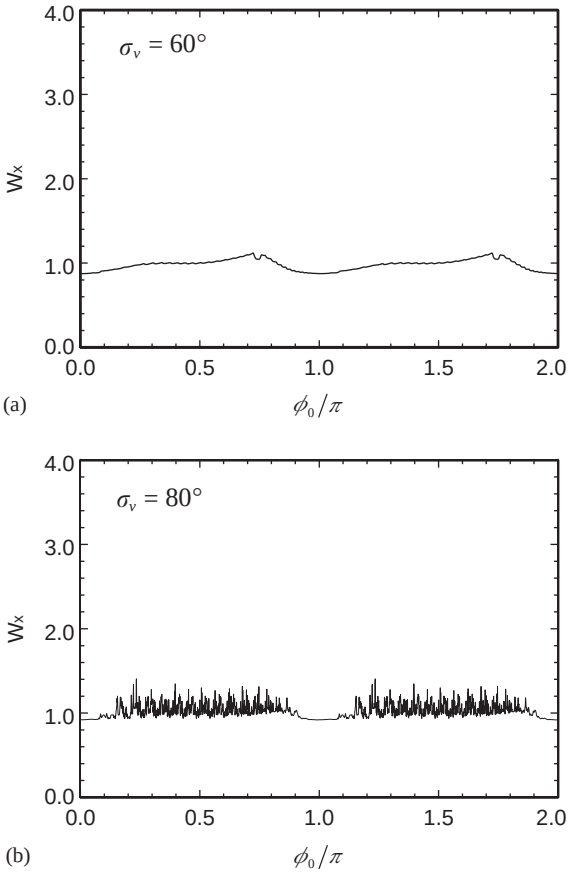

Fig. 4. Plots of W_x vs ϕ_0 for 2000 test particles at axial distance $s/S = 50$ for $\eta = 0.5$, $KS/\varepsilon_x = 10.0$, $\varepsilon_x = \varepsilon_y = \varepsilon$, and two cases: (a) $\sigma_v = 60^\circ$, and (b) $\sigma_v = 80^\circ$. The test particles are initially loaded uniformly with phase ϕ_0 ranging from 0 to 2π on the beam boundary $W_x(0) = 1$ in the phase space.

cases, the particles inside the beam core have regular motion and cannot escape to form a halo, so the outermost Kolmogorov–Arnold–Moser (KAM) surface for the beam core is located outside the beam boundary and there is a continuum of KAM surfaces where W_x is conserved. As the pipe radius R decreases, the conductor wall intersects the chaotic sea. Furthermore, the image force induced by the conductor wall becomes important and the outermost KAM surface for the beam core moves into the beam interior, reaching $x/a = 0.96$, as shown in Fig. 2 for $\hat{R} = 3.8$. In this case some particles inside the beam core will escape to form a halo and eventually strike the wall.

3. Dependence of the image-charge effects on system parameters

The halo formation and chaotic particle motion dependent sensitively on the system parameters: the occupancy of the quadrupole focusing field, vacuum phase advance, the beam intensity, and the ratio of the beam size to the aperture.

As the vacuum phase advance decreases, the regular region of particle motion decreases, which means that for smaller vacuum phase advance more particles are in the chaotic sea and can form halo. As shown in Fig. 3 the outermost KAM surface location relative to the beam boundary decreases as the vacuum phase advance for two cases: (a) $a/R = 80\%$ and (b) $a/R = 85\%$ with $\eta = 0.5$, $KS/\varepsilon_x = 10.0$, and $\varepsilon_x = \varepsilon_y = \varepsilon$. However, the rate of the halo production decreases as the vacuum phase advance decreases. The locations and evolution of the chaotic particles are illustrated in Fig. 4, where the transverse energy $W_x(s/S = 50)$ is plotted for 2000 test particles loaded at $s = 0$ on the beam boundary $W_x(0) = 1$ in the phase space with the initial phases $\phi_0 = \tan^{-1}\left[(S/\varepsilon)^{1/2}a(0)x'(0)/x(0)\right]$ uniformly distributed from 0 to 2π for two cases: (a) $\sigma_v = 60^\circ$ and (b) $\sigma_v = 80^\circ$. Those regular particles remain inside the beam with $W_x \cong 1$, while the other test particles

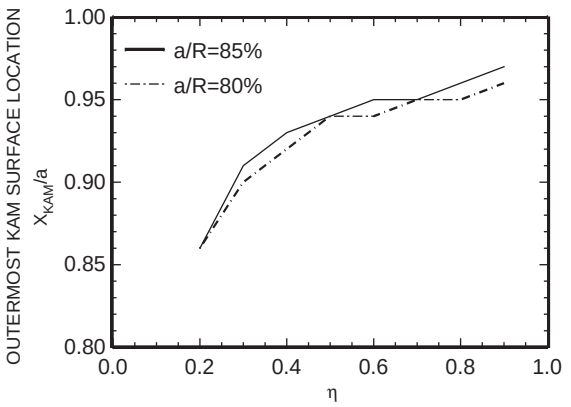

Fig. 5. Plots of the outermost KAM surface location X_{KAM}/a as a function of the occupancy of the quadrupole focusing field η, for, $KS/\varepsilon_x = 10.0$, $\varepsilon_x = \varepsilon_y = \varepsilon$, $\sigma_v = 80^\circ$ and two cases: (a) $a/R = 80\%$ and (b) $a/R = 85\%$.

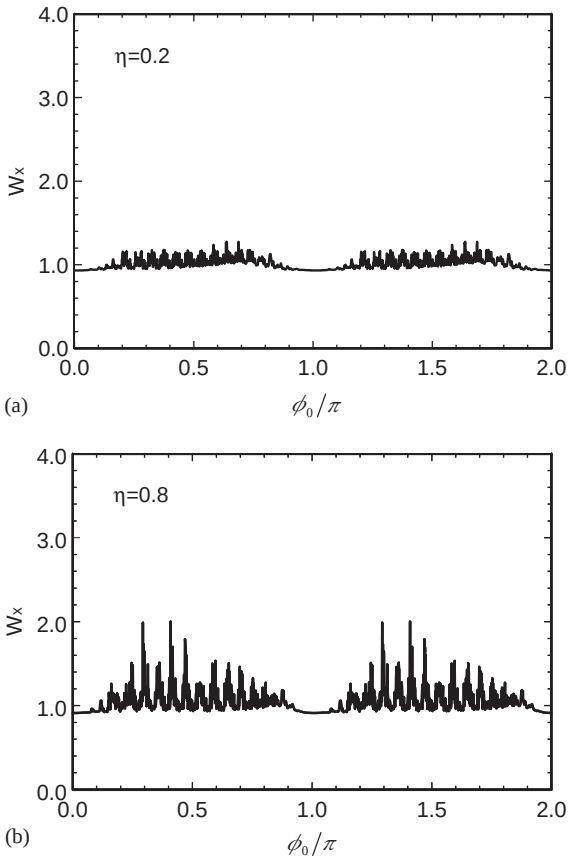

Fig. 6. Plots of W_x vs ϕ_0 for 2000 test particles at axial distance $s/S = 50$ for $KS/\varepsilon_x = 10.0$, $\varepsilon_x = \varepsilon_y = \varepsilon$, $\sigma_v = 80^\circ$, and two cases: (a) $\eta = 0.2$ and (b) $\eta = 0.8$. The test particles are initially loaded uniformly with phase ϕ_0 ranging from 0 to 2π on the beam boundary $W_x(0) = 1$ in the phase space.

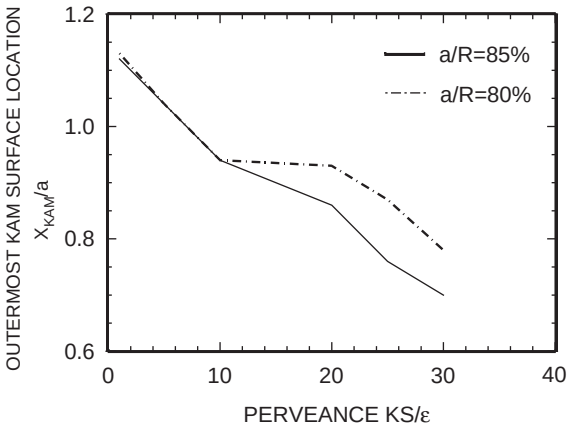

Fig. 7. Plots of the outermost KAM surface location X_{KAM}/a as a function of the scaled perveance $\hat{K} = KS/\varepsilon$ for $\eta = 0.5$, $\varepsilon_x = \varepsilon_y = \varepsilon$, $\sigma_v = 80^\circ$ and two cases: (a) $a/R = 80\%$ and (b) $a/R = 85\%$.

are chaotic and gain energy with $W_x > 1$. It is shown in Fig. 4 that for $\sigma_v = 80^\circ$ much more halo is form with $W_x > 1$ than $\sigma_v = 60^\circ$ at $s/S = 50$.

Figs. 5 and 6 show the dependence of the halo formation and chaotic particle motion on the occupancy of the quadrupole focusing field. As the occupancy of the quadrupole focusing field decreases, the regular region of particle motion decreases, which means that for smaller occupancy of the quadrupole focusing field more particles are in the chaotic sea. However, the rate of the halo production decreases as the occupancy of the quadrupole focusing field decreases. It is shown in Fig. 6 that the halo for $\eta = 0.2$ is more pronounced than that for $\eta = 0.8$ at $s/S = 50$.

Finally, Fig. 7 shows the dependence of the halo formation and chaotic particle motion on the beam intensity. As the beam intensity increases, more halo occurs.

4. Summary

We reviewed a mechanism for chaotic particle motion and halo formation due to image-charge effects in intense charged-particle beams in a small-aperture alternating-gradient focusing channel. This mechanism occurs for well-matched beams with the ideal Kapchinskij–Vladimirskij (KV) distribution. We also discussed the dependence of the chaotic particle motion and halo formation on the occupancy of the quadrupole focusing field, the vacuum phase advance, the beam intensity, and the ratio of the beam size to the aperture.

Acknowledgments

This work was supported by US Department of Energy, High-Energy Physics Division Grant No. DE-FG02-95ER40919, Office of Fusion Energy Science, Grant No. DE-FG02-01ER54662, and in part by Air Force Office of Scientific Research, Grant No. F49620-00-1-0007.

References

[1] R.L. Gluckstern, Phys. Rev. Lett. 73 (1994) 1247.
[2] J.M. Lagniel, Nucl. Instr. and Meth. A 345 (1994) 405.
[3] Q. Qian, R.C. Davidson, C. Chen, Phys. Plasmas 2 (1995) 2674;
Q. Qian, R.C. Davidson, C. Chen, Phys. Rev. E 51 (1995) R5216.
[4] C.M. Celata, I. Haber, D.P. Grote, Proceedings of the 2001 Particle Accelerator Conference, Chicago, IL, 2001, IEEE, Piscataway, NJ, 2001, pp. 2926–2928.
[5] C.M. Celata, F.M. Bieniosek, L. Prost, et al., Proceedings of the 2003 Particle Accelerator Conference, Portland, OR, May 2003, IEEE, Piscataway, NJ, 2003.
[6] R.W. Garnett, J.H. Billen, K.C.D. Chan, et al., in: S.Y. Lee (Ed.), Space Charge Dominated Beams and Applications of High Brightness Beams, AIP Conference Proceedings No. 377, AIP, New York, 1996, p. 60.
[7] C.K. Allen, K.C.D. Chan, P.L. Colestock, et al., Phys. Rev. Lett. 89 (2002) 214802.
[8] F.M. Bieniosek, J.W. Kwan, E. Henestroza, C. Kim, Nucl. Instr. and Meth. A 464 (2001) 592.
[9] P.A. Seidl, F.M. Bieniosek, C.M. Celata, et al., Nucl. Instr. and Meth. A 464 (2001) 369.
[10] J. Zhou, B.L. Qian, Chiping Chen, Phys. Plasma 10 (2003) P4203.
[11] B.L. Qian, J. Zhou, C. Chen, Phys. Rev. ST Accel. Beams 6 (2003) 014201.
[12] I. Kapchinskij, V. Vladimirskij, Proceedings of the International Conference on High Energy Accelerators and Instrumentation, CERN Scientific Information Service, Geneva, 1959, p. 274.

Theory and simulation of nonrelativistic elliptic-beam formation with one-dimensional Child-Langmuir flow characteristics

Ronak Bhatt and Chiping Chen

Plasma Science and Fusion Center, Massachusetts Institute of Technology, Cambridge, Massachusetts 02139, USA

(Received 2 July 2004; published 3 January 2005)

A theory of nonrelativistic, laminar, elliptic-beam formation is presented. The beam is shown to have the one-dimensional Child-Langmuir flow form. An analytic expression for the electrostatic potential outside the beam is derived. Equipotentials corresponding to electrode surfaces are computed numerically. The effectiveness of the electric field formed by the electrodes in focusing and preserving the elliptic, 1D Child-Langmuir flow beam is verified via 3D ray-tracing simulations.

DOI: 10.1103/PhysRevSTAB.8.014201 PACS numbers: 41.75.–i, 41.85.Ar, 52.59.Sa

I. INTRODUCTION

Electron beams of elongated elliptic cross sections have generated great interest in vacuum electronics [1] because of their low space-charge energy and efficient coupling to rf structures when compared to circular beams. It is well known that high space charge reduces conversion efficiency in conventional microwave tubes employing circular beams. Presently, there are vigorous activities in the development of sheet-beam traveling wave amplifiers [2,3], klystrons [4], and focusing systems [5,6].

In high-intensity ion and electron accelerators, beams often exhibit nonlaminar flows such as large-amplitude density fluctuations [7], mismatched envelope oscillations [8], emittance growth, chaotic particle orbits, beam interception, and difficulty in beam focusing and compression. Many of these effects are due to beam mismatch or nonequilibrium behavior. Elliptic beams may allow simplified and more natural matching [9] between beam injectors and commonly used magnetic focusing lattices, reducing the emittance growth associated with beam mismatch.

Although elliptic beams present numerous advantages, their inherent three-dimensional nature has made diode design a challenging process, both analytically and numerically. For the applications discussed above, desirable beam characteristics include uniform current density, parallel flow, and zero magnetic flux threading the emitter—properties consistent with one-dimensional Child-Langmuir (C-L) [10] flow, in which the electrostatic potential varies as $\Phi \propto z^{4/3}$, where z is the beam propagation distance. In general, however, such flows are difficult to produce [11]. Recent studies of 2D and 3D [12–16] extensions of the Child-Langmuir law in an infinite applied magnetic field have shown that the beam exhibits significant current density enhancements near the beam-vacuum boundary. In the absence of an infinite confining magnetic field, the beam will tend to spread in phase space, resulting in a degradation of beam quality. As we will show in this paper, it is possible to induce the space-charge flow in a 3D system to take the 1D Child-Langmuir flow form by constructing a 3D external electrode geometry that is consistent with the 1D Child-Langmuir electric field within the beam.

In order to enforce 1D Child-Langmuir [10] flow in a beam interior, the diode design problem requires solving Laplace's equation for the exterior electric potential with Cauchy boundary conditions on the beam-vacuum boundary. General solutions of such elliptic-equation Cauchy problems are difficult or impossible to obtain [11,17], and standard numerical methods fail due to the exponential growth of errors, which is characteristic of such problems. Nonetheless, Pierce [18], in a classic result, analytically solved the exterior problem for an infinite 2D sheet-beam geometry (i.e., neglecting end effects). By employing the Cauchy-Riemann conditions, Pierce could write the potential outside the beam as the real part of a complex analytic function. He found that the function $\Phi \propto \mathrm{Re}[(z + ix)^{4/3}]$, where x is the transverse distance from the beam edge, satisfies the Child-Langmuir condition, $\Phi \propto z^{4/3}$, on the beam edge ($x = 0$). This solution possesses an equipotential surface that corresponds to an external focusing electrode—the "Pierce electrode"—which is inclined at a 67.5° angle ($3\pi/8$ rad) to the beam.

Later, Radley [19] employed a Laplace transform technique to determine the exterior potential for a beam of circular cross section. Nakai [20] attempted to generalize Radley's technique to the 3D elliptic-beam problem, but neglected the full functional dependence of the angular Mathieu functions, and as a result, arrived at a simple, but incorrect expression for the exterior potential.

In this paper we present a new analytic technique, based on a 3D generalization of [19], to determine elliptic-beam shaping electrodes which may be used independently or in conjunction with 3D modeling codes. A sample set of electrodes is computed explicitly for a one microperveance, large aspect ratio (10:1) elliptic-beam diode. The geometry is tested via 3D OMNITRAK [21] simulations to show nearly ideal 1D Child-Langmuir space-charge-limited flow with high laminarity and a constant elliptic cross section.

For the design of physical beam diodes, designers, guided by analytic results, make use of ray-tracing codes such as the 2D EGUN [22] and 3D OMNITRAK [21], or particle-in-cell codes such as MICHELLE [23] and WARP [24]. These codes can be used as part of an iterative optimization process in order to arrive at an approximate set of external electrodes which support the desired beam cross section. The analytic elliptic-beam results of this paper facilitate the numerical design of nonaxisymmetric diodes, which are complicated by the presence of an extra dimension in the electrode geometry optimization. In addition, the present analytic results provide a useful protocol for benchmarking new 3D simulation tools.

II. THEORY

We consider a nonrelativistic charged-particle beam of length d and elliptic cross section with semimajor axis a and semiminor axis b, as shown in Fig. 1. The charged particles are emitted from a flat elliptic plate, held at potential $\Phi = 0$, in the $z = 0$ plane, and collected by another flat elliptic plate, held at potential $\Phi = \Phi_d$, in the $z = d$ plane. The cold fluid equations describing the beam interior are

$$\partial n/\partial t + \nabla \cdot (n\mathbf{V}) = 0, \tag{1}$$

$$\partial \mathbf{V}/\partial t + (\mathbf{V} \cdot \nabla)\mathbf{V} = -(q/m)\nabla\Phi, \tag{2}$$

$$\nabla^2\Phi = -4\pi qn, \tag{3}$$

for the region $x^2/a^2 + y^2/b^2 \le 1$ and $0 \le z \le d$. In Eqs. (1)–(3), $\mathbf{V}$ is the flow velocity, and n is the density of particles, each of mass m and charge q. Note that,

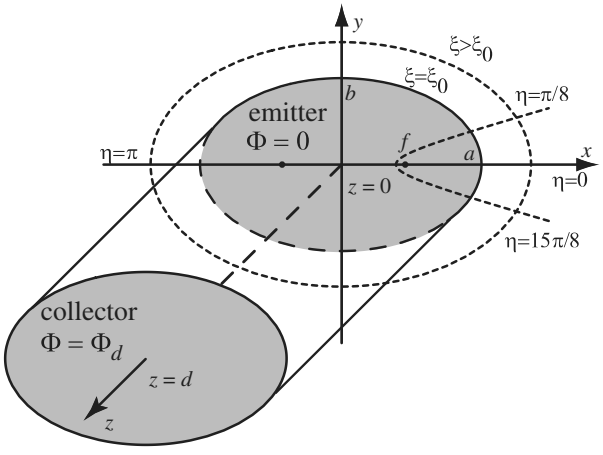

FIG. 1. A beam of elliptic cross section (semimajor axis a, semiminor axis b) is shown in Cartesian and elliptic-cylindrical coordinates. The beam is emitted from an elliptic plate at $\Phi = 0$ in the $z = 0$ plane and collected by an elliptic plate at $\Phi = \Phi_d$ in the $z = d$ plane. The beam fills the area enclosed by the surface $\xi = \xi_0$. In any z plane, lines of constant ξ are ellipses, and lines of constant η are semihyperbolas.

consistent with the nonrelativistic approximation, we neglect any self-magnetic field. In the beam exterior, the potential satisfies Laplace's equation

$$\nabla^2\Phi = 0. \tag{4}$$

The 1D steady-state solution to the interior problem defined by Eqs. (1)–(3) can be obtained by using the plate potentials as boundary conditions for Poisson's equation and imposing the constraint that particles emerge from the $\Phi = 0$ emitter with zero velocity, i.e., the space-charge-limited boundary condition. This results in the well-known 1D Child-Langmuir [10] solution for laminar, space-charge-limited flow with $\mathbf{V}(z) = \hat{\mathbf{e}}_z(2q\Phi_d/m)^{1/2}(z/d)^{2/3}$, $n(z) = (\Phi_d/9\pi qd^2)(z/d)^{-2/3}$, and $\Phi(z) = \Phi_d(z/d)^{4/3}$. For example, an electron diode of length $d = 5.2$ mm and diode voltage $\Phi_d = 5$ kV produces a current density of 3 A/cm^2, while a Cs^+ ion diode of the same length and voltage generates a current density of 6 mA/cm^2.

To determine the potential distribution in the beam exterior, we solve Laplace's equation (4) while matching the interior and exterior electric fields on the elliptic-beam boundary. From the C-L solution, the matching conditions on the elliptic-beam boundary imply, for $0 \le z \le d$,

$$\Phi|_{\text{beam bound}} = \Phi_d(z/d)^{4/3}, \tag{5}$$

$$(\hat{\mathbf{n}} \cdot \nabla)\Phi|_{\text{beam bound}} = 0, \tag{6}$$

where $\hat{\mathbf{n}}$ is a unit vector normal to the elliptic-beam boundary $x^2/a^2 + y^2/b^2 = 1$. We aim to find exterior equipotential surfaces corresponding to the emitter and collector potentials $\Phi = 0$ and $\Phi = \Phi_d$, respectively. If electrodes at the given potentials are made to lie along these surfaces, they will enforce the conditions in Eqs. (5) and (6) on the interval $0 \le z \le d$.

It is useful to introduce the elliptic-cylindrical coordinate system (ξ, η, z), i.e.,

$$x = f\cosh(\xi)\cos(\eta), \qquad y = f\sinh(\xi)\sin(\eta), \qquad z = z, \tag{7}$$

where $0 \le \xi < \infty$ is a radial coordinate, $0 \le \eta < 2\pi$ is an angular coordinate, and $f = \sqrt{a^2 - b^2}$ is the distance from the center of the ellipse to either of its foci, as illustrated in Fig. 1. The elliptic-beam boundary is specified by the surface $\xi = \xi_0 = \coth^{-1}(a/b)$. In these coordinates, Laplace's equation may be expressed

$$\frac{2}{f^2(\cosh 2\xi - \cos 2\eta)}\left(\frac{\partial^2\Phi}{\partial\eta^2} + \frac{\partial^2\Phi}{\partial\xi^2}\right) + \frac{\partial^2\Phi}{\partial z^2} = 0, \tag{8}$$

and the boundary conditions in Eqs. (5) and (6) are

$$(\partial\Phi/\partial\xi)|_{\xi=\xi_0} = 0, \tag{9}$$

$$(\partial\Phi/\partial\eta)|_{\xi=\xi_0} = 0, \tag{10}$$

$$\Phi|_{\xi=\xi_0} = \Phi_d(z/d)^{4/3}. \tag{11}$$

Expressing a product solution as $\Phi(\xi, \eta, z) = \Xi(\xi)\Theta(\eta)\mathrm{Z}(z)$ and applying separation of variables to Eq. (8), we find

$$d^2\mathrm{Z}/dz^2 - k^2\mathrm{Z} = 0, \tag{12}$$

$$d^2\Theta/d\eta^2 + (\lambda - \tfrac{1}{2}k^2f^2\cos 2\eta)\Theta = 0, \tag{13}$$

$$d^2\Xi/d\xi^2 - (\lambda - \tfrac{1}{2}k^2f^2\cosh 2\xi)\Xi = 0, \tag{14}$$

where k and λ are separation constants. Equation (12) leads simply to exponential solutions $\mathrm{Z} = e^{kz}$. Equation (13) is the angular Mathieu equation, but we are only interested in those angular Mathieu functions which have a periodicity of 2π and are even about $\eta = 0$ and $\eta = \pi/2$, since the boundary conditions of Eqs. (10) and (11) possess these same symmetries. Such solutions exist only for discrete eigenvalues of the separation constant λ, and we adopt the convention of Morse and Feshbach [25] to denote these angular Mathieu functions by $\Theta = Se_{2n}(kf, \eta)$ and the associated normalization constants $M^e_{2n} \equiv \int_0^{2\pi}[Se_{2n}(kf, u)]^2du$, where n is a non-negative integer indexing the eigenvalues λ, as detailed in Ref. [25]. The corresponding radial solutions, $\Xi = Je_{2n}(kf, \xi)$ and $\Xi = Ne_{2n}(kf, \xi)$, are radial Mathieu functions of the first and second kind, respectively.

Any superposition of product solutions of the separated equations must satisfy Laplace's equation (8), and hence we write

$$\Phi(\xi, \eta, z) = \int_C dkA(k)e^{kz}G(kf, \xi, \eta), \tag{15}$$

where

$$G(h, \xi, \eta) \equiv \sum_{n=0}^{\infty} \alpha_{2n}(h)Se_{2n}(h, \eta)[Je_{2n}(h, \xi)Ne'_{2n}(h, \xi_0) - Ne_{2n}(h, \xi)Je'_{2n}(h, \xi_0)]. \tag{16}$$

We have chosen $\alpha_{2n}(h) \equiv [M^e_{2n}]^{-1}\int_0^{2\pi} Se_{2n}(h, u)du$, and the primes denote differentiation with respect to ξ. The corresponding expression in Nakai [20] does not have $Se_{2n}(h, \eta)$ and omits the normalization factor α_{2n}.

The expansion in Eq. (15) assures that Φ satisfies Laplace's equation (8), and it is readily seen that the particular linear combination of radial Mathieu functions in Eq. (16) satisfies the boundary condition in Eq. (9). Moreover, using the Wronskian for the radial Mathieu functions and the orthogonality of the angular Mathieu functions, it can be shown that our definition of α_{2n} assures $G(h, \eta, \xi_0) = 1$, and thereby the boundary condition in Eq. (10). Equations (11) and (15) now imply

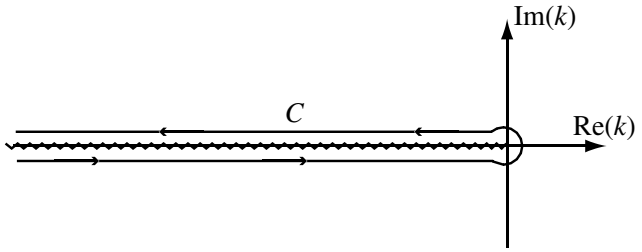

FIG. 2. The Hankel contour in the complex k plane is taken around the $-\infty < k < 0$ branch cut.

$$\Phi(\xi_0, \eta, z) = \int_C A(k)e^{kz}dk = \Phi_d(z/d)^{4/3}. \tag{17}$$

We follow the analysis by Radley [19] and make use of the integral representation of the gamma function $\Gamma(u)$ [26] to obtain

$$z^{4/3} = \frac{1}{\Gamma(-\frac{4}{3})}\frac{i}{2\sin(\frac{4\pi}{3})}\int_C e^{kz}k^{-7/3}dk, \tag{18}$$

where the Hankel contour C is taken around the branch cut defined by the line $-\infty < k < 0$, as shown in Fig. 2. Substituting Eq. (18) into Eq. (17), we find that

$$A(k) = \frac{\Phi_d d^{-4/3}}{\Gamma(-\frac{4}{3})}\frac{i}{2\sin(\frac{4\pi}{3})}k^{-7/3}, \tag{19}$$

provided the same Hankel contour is used for the integration. Having determined $A(k)$, the expression for the exterior potential in Eq. (15) is fully specified.

III. SIMULATION

The prescription of Sec. II can be used to compute the potential outside a 1D Child-Langmuir flow beam of arbitrary elliptic-cylindrical geometry. However, for definiteness, we use the above technique to compute the potential outside a 10:1:8.7 space-charge-limited elliptical diode of semimajor axis $a = 10b$, semiminor axis b, and length $d = 8.7b$. Equipotentials corresponding to $\Phi = 0$ and $\Phi = \Phi_d$ are shown in Figs. 3(a) and 3(b), respectively, for several values of z. The level contours are roughly elliptical in shape, and the $\Phi = \Phi_d$ surface is more steeply inclined to the beam than the $\Phi = 0$ surface, as expected from the 2D theory [18]. The equipotentials in Fig. 3 were computed by applying a numeric root-finding scheme to the potential defined in Eq. (15). The Hankel contour integral is numerically evaluated employing standard techniques for the evaluation of the Mathieu functions [17,27]. It should be noted that these results differ significantly from those obtained using the method of Nakai [20]. For example, the $z/b = 3.3$ equipotential of Fig. 3(a) intersects the x axis at $x/b = 33.2$ and the y axis at $y/b = 9.2$. The same $z/b = 3.3$ equipotential, computed using Nakai's expression, incorrectly gives an ellipse which intersects the axes at $x/b = 15.7$ and $y/b = 12.1$, respectively.

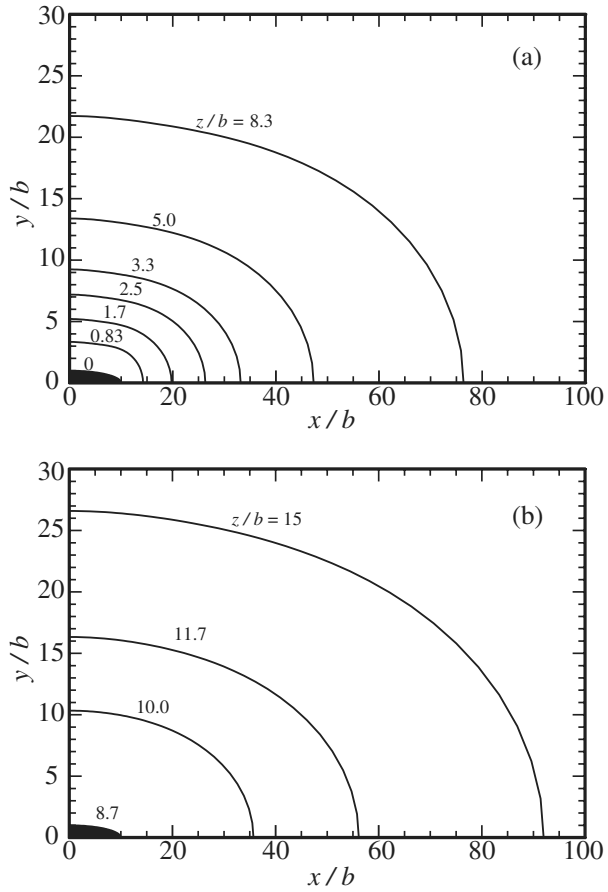

FIG. 3. Level curves of (a) $\Phi = 0$ and (b) $\Phi = \Phi_d$ surfaces for a 10:1:8.7 space-charge-limited elliptical diode of semimajor radius $10b$, semiminor radius b, and length $8.7b$. The beam fills the shaded area, which is intersected by the $\Phi = 0$ surface at $z = 0$ and the $\Phi = \Phi_d$ surface at $z = 8.7b$.

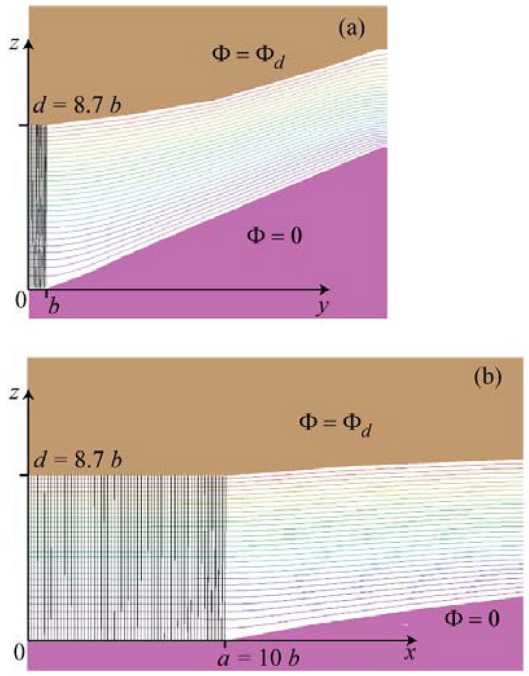

FIG. 4. (Color) A 3D OMNITRAK simulation of space-charge-limited Child-Langmuir flow using the 10:1:8.7 elliptical diode geometry shown in Fig. 3. Particle trajectories and equipotentials are shown in (a) the $x = 0$ plane and (b) the $y = 0$ plane.

We verify our theory by a cold-beam 3D space-charge-limited emission simulation using OMNITRAK [21], a commercially available ray-tracing code. Simulation results are shown in Fig. 4 for the same geometry as in Fig. 3, using a variable-resolution computational mesh with x spacing of 0.1 mm for $0 \le x \le 8$ mm and 0.5 mm for $8 \le x \le 15$ mm, y spacing of 0.05 mm for $0 \le y \le 1$ mm, 0.1 mm for $1 \le y \le 5$ mm, and 0.4 mm for $5 \le y \le 12$ mm, and z spacing of 0.05 mm for $0 \le z \le 0.8$ mm, 0.02 mm for $0.8 \le z \le 1.2$ mm, 0.05 mm for $1.2 \le z \le 2$ mm, 0.1 mm for $2 \le z \le 5.7$ mm, 0.05 mm for $5.7 \le z \le 7$ mm, and 0.1 mm for $7 \le z \le 10$ mm. The mesh resolution is higher in x and y across the cross section of the beam, and in z where the beam intersects the emitter and collector. The 3D electrode structure was linearly interpolated between the equipotentials in Fig. 3, each sampled at 46 points evenly distributed in η, for $0 \le \eta \le \pi/2$. Nearby computational nodes are shifted to conform to the electrode surfaces using the OMNITRAK *surface* flag. Neumann boundaries were used for the symmetry planes of the beam as well as for the outer boundaries of the simulation region, which is shown in Fig. 4 along with computed equipotentials and particle trajectories projected to the $x = 0$ and $y = 0$ planes. The entire simulation runs in approximately 30 min on a 3 GHz personal computer.

The beam produced by the simulation is essentially parallel, laminar, uniform density Child-Langmuir flow. Beam laminarity is often characterized by the rms beam emittances $\varepsilon_x \equiv (\langle x^2\rangle\langle x'^2\rangle - \langle xx'\rangle^2)^{1/2}$ and $\varepsilon_y \equiv (\langle y^2\rangle \times \langle y'^2\rangle - \langle yy'\rangle^2)^{1/2}$, where the averages of transverse particle position (x, y) and divergence $(x', y') \equiv (dx/dz, dy/dz)$ are taken over a slice of the beam at $z = d$. For a uniform density elliptic beam, these emittances can be related to effective beam temperatures [28] by the relations $\varepsilon_x = a(kT_{\mathrm{eff},x}/8q\Phi_d)^{1/2}$ and $\varepsilon_y = b(kT_{\mathrm{eff},y}/8q\Phi_d)^{1/2}$. If we use the parameters of our earlier examples, a 10:1:8.7 elliptical electron or ion diode with $\Phi_d = 5.0$ kV, $d = 5.2$ mm, $a = 6.0$ mm, and $b = 0.6$ mm, the cold-beam OMNITRAK simulation shown in Fig. 4 predicts the effective beam temperatures $T_{\mathrm{eff},x} = 6.7 \times 10^{-4}$ eV and $T_{\mathrm{eff},y} = 8.1 \times 10^{-3}$ eV. For a realistic beam, of course, the lower limit of the effective beam temperature (and emittance) will be given by the physical temperature of the emitter, approximately 0.1 eV for a typical thermionic electron or ion diode. Since the simulated temperatures are negligibly small compared to this value, we can infer that the emittance of an elliptical diode constructed using the above prescription will approach the theoretical limits imposed by finite emitter temperature.

For most cases of interest with highly elliptic beams, the focusing electrode slopes are nearly straight lines, except for a small region near the beam edge. Thus, in practice, very usable electrodes for the 10:1:8.7 beam can be designed even when omitting several intermediate equipotentials in the interpolation. For example, for the 10:1:8.7 beam discussed above, we may interpolate directly between the $z/b = 0$, $z/b = 0.83$, and $z/b = 8.3$ equipotentials of Fig. 3(a) without measurably affecting the simulated emittance. For a somewhat rounder 6:1:6.6 aspect ratio example, we find the emittance increases by approximately 15% when we omit intermediate equipotentials, which is similar to the results for cylindrical beams.

Our ongoing studies include extending the theory to the relativistic regime. In addition, engineering considerations generally require a thermally insulating gap between the emitter edge and the $\Phi = 0$ electrode, which will introduce a perturbation to the beam. Nonetheless, for small gaps, we do not expect a significant modification of the bulk flow. Preliminary simulation studies of the effect of collector hole lensing are encouraging. Although the introduction of a hole through which the beam is extracted alters the nearby field lines, the field perturbation is nearly linear. As a result, the beam divergence is well correlated with position such that emittance growth is modest (factor of 2 or less), which is still negligible.

IV. CONCLUSION

To summarize, a theory of nonrelativistic, laminar, elliptic-beam formation was presented. The beam was shown to have the one-dimensional Child-Langmuir flow form. An analytic expression for the electrostatic potential outside the beam was derived. Equipotentials corresponding to electrode surfaces were computed numerically. The effectiveness of the electric field formed by the electrodes in focusing and preserving the elliptic, 1D Child-Langmuir flow beam was verified via 3D ray-tracing simulations.

ACKNOWLEDGMENTS

This work was performed under the auspices of U.S. Department of Energy, Office of High-Energy Physics, Grant No. DE-FG02-95ER40919, Office of Fusion Energy Science, Grant No. DE-FG 02-01-ER54662, Air Force Office of Scientific Research Grant No. F49620-03-1-0230, and the Deshpande Center for Technological Innovation.

[1] P. A. Sturrock, J. Electron. Control **7**, 162 (1959).
[2] S. Humphries, S. Russell, B. Carlsten, and L. Earley, Phys. Rev. ST Accel. Beams **7**, 060401 (2004).
[3] B. E. Carlsten, Phys. Plasmas **9**, 5088 (2002).
[4] G. Caryotakis *et al.*, in *6th Workshop on High Energy Density and High Power RF*, edited by S. H. Gold and G. S. Nusinovich, AIP Conf. Proc. No. 691 (AIP, New York, 2003), p. 22.
[5] M. A. Basten and J. H. Booske, J. Appl. Phys. **85**, 6313 (1999).
[6] R. Pakter and C. Chen, Phys. Rev. E **62**, 2789 (2000).
[7] S. Bernal *et al.*, Phys. Plasmas **11**, 2907 (2004).
[8] T. P. Wangler *et al.*, Nucl. Instrum. Methods Phys. Res., Sect. A **519**, 425 (2004).
[9] C. Chen, R. Pakter, and R. C. Davidson, Nucl. Instrum. Methods Phys. Res., Sect. A **464**, 518 (2001).
[10] C. D. Child, Phys. Rev. **32**, 492 (1911); I. Langmuir, *ibid.* **21**, 419 (1923).
[11] P. Kirstein, G. Kino, and W. Waters, *Space Charge Flow* (McGraw-Hill, New York, 1967), p. 331.
[12] J. W. Luginsland, Y. Y. Lau, R. J. Umstattd, and J. J. Watrous, Phys. Plasmas **9**, 2371 (2002).
[13] J. J. Watrous, J. W. Luginsland, and M. Frese, Phys. Plasmas **8**, 4202 (2001).
[14] J. W. Luginsland, Y. Y. Lau, and R. M. Gilgenbach, Phys. Rev. Lett. **77**, 4668 (1996).
[15] R. J. Umstattd and J. W. Luginsland, Phys. Rev. Lett. **87**, 145002 (2001).
[16] Y. Y. Lau, Phys. Rev. Lett. **87**, 278301 (2001).
[17] P. Morse and H. Feshbach, *Methods of Theoretical Physics* (McGraw-Hill, New York, 1953), Vol. 1, Chap. 6, p. 702.
[18] J. R. Pierce, *Theory and Design of Electron Beams* (Van Nostrand, Princeton, 1954), 2nd ed.
[19] D. E. Radley, J. Electron. Control **4**, 125 (1957).
[20] A. Nakai, Nucl. Instrum. Methods **54**, 57 (1967).
[21] OMNITRAK software, copyright Field Precision, Albuquerque, NM.
[22] W. B. Hermannsfeldt, SLAC Report No. SLAC 226, 1979.
[23] J. Petillo *et al.*, IEEE Trans. Plasma Sci. **30**, 1238 (2002).
[24] D. P. Grote, A. Friedman, I. Haber, W. Fawley, and J. L. Vay, Nucl. Instrum. Methods Phys. Res., Sect. A **415**, 428 (1998).
[25] See Ref. [17], Vol. 2, Chap. 11, p. 1568.
[26] See Ref. [17], Vol. 1, Chap. 4, p. 421.
[27] J. C. Gutierrez-Vega *et al.* (unpublished).
[28] J. D. Lawson, *Physics of Charged Particle Beams* (Clarendon, Oxford, 1988), p. 210.

Final focus system for high intensity beams

Enrique Henestroza, Shmuel Eylon, Prabir K. Roy, Simon S. Yu, Frank M. Bieniosek,
Derek B. Shuman, and William L. Waldron

Lawrence Berkeley National Laboratory, University of California, Berkeley, California 94720, USA

(Received 30 June 2004; published 20 May 2005)

The neutralized transport experiment (NTX) at the Heavy Ion Fusion Virtual National Laboratory is exploring the performance of neutralized final-focus systems for high perveance heavy ion beams. The final-focus scenario in a heavy ion fusion driver consists of several large aperture quadrupole magnets followed by a drift section in which the beam space charge is neutralized by a plasma. This beam is required to hit a millimeter-sized target spot at the end of the drift section. The objective of the NTX experiments and associated theory and simulations is to study the various physical mechanisms that determine the final spot size (radius r_s) at a given distance (f) from the end of the last quadrupole. In a fusion driver, f is the standoff distance required to keep the chamber wall and superconducting magnets properly protected. The NTX final quadrupole focusing system produces a converging beam at the entrance to the neutralized drift section where it focuses to a small spot. The final spot is determined by the conditions of the beam entering the quadrupole section, the beam dynamics in the magnetic lattice, and the plasma neutralization dynamics in the drift section. The main issues are the control of emittance growth due to high order fields from magnetic multipoles and image fields. In this paper, we will describe the theoretical and experimental aspects of the beam dynamics in the quadrupole lattice, and how these physical effects influence the final beam size. In particular, we present theoretical and experimental results on the dependence of final spot size on geometric aberrations and perveance.

DOI: 10.1103/PhysRevSTAB.8.052801 PACS numbers: 52.58.Hm

I. INTRODUCTION

The topic of final-focus systems for high intensity beams has been an important subject of analytical [1–4], and experimental [5] efforts since the beginning of the Heavy Ion Fusion project in 1976. The first designs were derived from systems already in use in particle accelerators for high energy physics where space charge is negligible, and which incorporated sextupoles and octupoles elements for the correction of chromatic and geometric aberrations. Chromatic aberrations affect the focal spot radius due to deviations from the nominal ion momentum causing a variation in the focal length produced by the magnet system. These aberrations may result from initial transients in the injector, from residual momentum tilt due to beam compression, or from the momentum spread, or longitudinal emittance produced along the beam line. Geometric aberrations are due to nonlinear external fields and also from deviations from paraxial ray optics.

In a possible scenario of a final-focus system for a heavy ion fusion (HIF) driver, the beam is transported in the final-focus section through several strong large aperture magnetic quadrupoles, and is then allowed to drift ballistically through neutralizing plasma in a low-density (millitorr) gas onto the target. There are nonlinear processes both in the magnetic section as well as in the neutralized transport section. To investigate these phenomena, the neutralized transport experiment (NTX) has begun at LBNL [6]. The NTX beam line (Fig. 1) consists of 4 large bore quadrupoles followed by a neutralized drift section. A low emittance K^+ beam is made to traverse this 4-quad lattice, at the exit of which, the beam enters a 1-meter-long drift section with injected plasma. The beam is diagnosed at the exit of the 4-quad section as well as the end of the drift section.

The relevance of NTX to the fusion driver is derived from the observation that the key scaling parameter is perveance, defined as

$$Q = \frac{1}{4\pi\varepsilon_0}\frac{2ZeI_b}{m_i v_i^3}, \tag{1}$$

where I_b is the beam current, and Z , m_i, and v_i are, respectively, the charge state, mass, and velocity of the beam ions. The beam dynamics of a low current, low energy beam, as in NTX, is identical to a high current, high energy beam in a fusion driver, as long as the perveance is the same, and the focusing fields are scaled appropriately (Sec. II).

In the NTX experiment the injector is designed to generate a very high-brightness, space-charge-dominated potassium beam where the perveance is varied by means of a beam aperturing system immediately downstream of the ion source and upstream of the first quadrupole. By changing the aperture size, we vary the beam current at a fixed energy.

A simple theoretical model for neutralized drift provides us the framework in which to analyze the more detailed experiments and simulations. For a beam, which is nearly ballistic, the focal length f is given by

$$f = \frac{r_0}{\theta}, \tag{2}$$

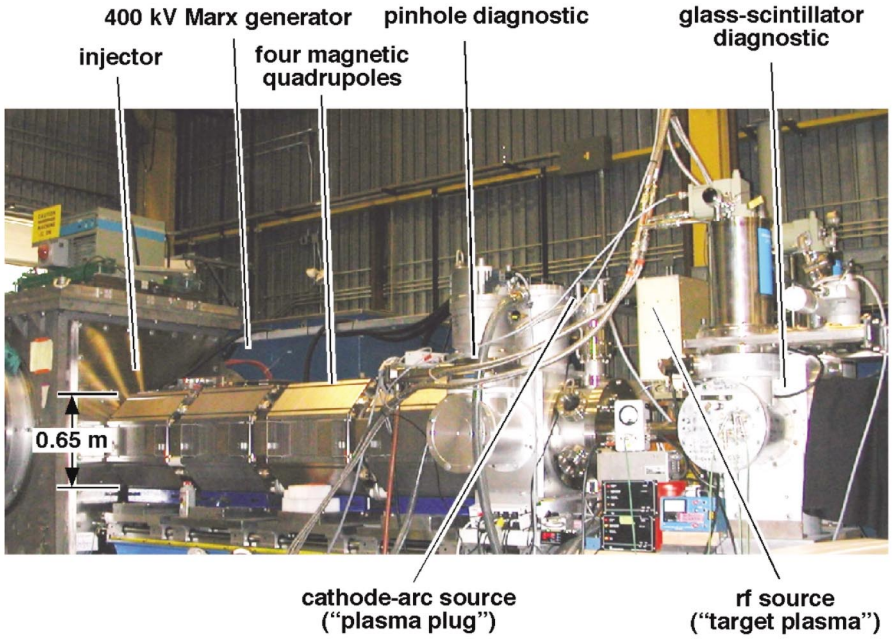

FIG. 1. (Color) neutralized transport experiment (NTX).

where r_0 is the beam radius and θ is the angle of convergence at the entrance of the drift section (i.e., exit of the quadrupole lattice). The final spot size r_s at the focal point is given by

$$r_s = \frac{\varepsilon}{\theta}, \tag{3}$$

where ε is the unnormalized emittance of the beam at target.

The first question, addressed with a combination of simulations and experiment, is whether we can place the focal spot at target, more specifically, whether we can control the beam in the quadrupole lattice to produce any desired beam size r_0 and convergence angle θ at the entrance to the drift section. Beam control is obtained by changing the magnetic strength of the 4 quadrupoles. We have varied the quadrupoles to obtain various values of θ (5, 10, 15, and 20 mr) for a given beam energy and current. The agreement between theory and experiment is excellent. We have also varied individual quadrupole strengths, and demonstrated that the beam shape changes in a predictable manner. In addition, the beam energy (and current) was varied, and again, the beam shape varied in a predictable manner. Finally, the perveance was varied, and the same code/experiment agreement was demonstrated.

The ultimate objective for the fusion application is to deliver the entire pulse onto the target with the same small spot. This is a nontrivial task because the beam energy and current from head to tail is not uniform. The different slices of the beam may have somewhat different beam envelopes through the magnetic lattice, leading to different beam size and convergence angle, and therefore variable focal length from head to tail. We need to know the sensitivity of the beam optics to small changes in beam energy. To evaluate this effect, we measured the beam size as the energy varied. We observed that energy variations of 1% led to reduction of current density by 50%. This experimental result is consistent with theory. We also measured directly the spot size variation from head to tail and significant changes were observed. The voltage waveform shows a variation of $\sim$1%, and this energy variation is enough to account for the head-to-tail variation in spot size. For future work, we need to study the energy sensitivity for other lattices (e.g., 6-quad lattice) to see if the energy sensitivity could be reduced. Also, time-dependent focusing may be used to correct for the head-to-tail variations.

This paper describes the experiments and associated theory and simulations to study the various physical mechanisms in the magnetic lattice that affect the final spot size (radius r_s) at a given distance (f) from the end of the last quadrupole of the neutralized transport experiment. The physics of final-focus magnetic lattice, in the context of neutralized drift, is reviewed in Sec. II, including the effects of geometric and chromatic aberration on the final spot size. In Sec. 3, we describe the NTX beam-line layout and diagnostic suite as well as the numerical particle-in-cell simulation code WARP3D [7]. The improved measurement techniques are essential for quantitative validation of code predictions. Section IV presents the measurements of beam transport through the magnetic lattice and comparison with simulations made using the WARP3D code, and includes the control of convergence angle, energy sensitivity and shift of focus, geometric aberrations and emittance growth, and perveance scaling. Section V describes several factors that influence the interpretation of the experimental results, including secondary electron effects,

energy calibration, measurement of quadrupole field strength, and efficiency of the diagnostic devices. Conclusions are presented in Sec. VI.

II. FINAL-FOCUS MAGNETIC LATTICE

The NTX transport section is designed to correspond closely to a prototypical HIF driver final-focus channel. It consists of four pulsed quadrupole magnets with short drift regions, including the drift from the source into the channel and the drift from the channel to the plasma neutralization chamber. For a beam with a uniform transverse current density, the description of the beam transverse size along the channel is given to first order by the envelope equations of Kapchinskij and Vladimirskij [8]

$$\frac{d^2a}{dz^2} = Ka + \frac{2Q}{a+b} + \frac{\varepsilon_x^2}{a^3}, \tag{4}$$

$$\frac{d^2b}{dz^2} = -Kb + \frac{2Q}{a+b} + \frac{\varepsilon_y^2}{b^3}, \tag{5}$$

where a and b are the transverse edge dimensions, z is the dimension along the quadrupole lattice centerline, K is the quadrupole force given by $B'/[B\rho]$, B' is the magnetic field gradient, and $[B\rho]$ is the beam rigidity. The space-charge force is proportional to the perveance Q and the phase-space pressure is given by the unnormalized emittance ε_x and ε_y. For a given perveance and unnormalized emittance, the beam envelopes do not change when the magnetic field is transformed proportional to the rigidity; and for a given perveance and rigidity, the beam envelopes are self-similar when the emittance is proportional, and the magnetic field is inversely proportional to the beam size. For NTX, $Q \sim 0.0006$, corresponding to a 25 mA potassium beam at 300 keV. An equal perveance driver beam will correspond to a 10 kA Xenon beam at 2.5 GeV. It is worth noticing that during the final-focus transport the beam dynamics is space-charge dominated, and becomes emittance dominated when the beam approaches the focal plane.

Figure 2 shows the horizontal and vertical beam envelopes through the NTX system, with and without beam neutralization after the final-focus lattice. The quadrupole fields are chosen to obtain a beam of one-meter focal length (20 mm radius, and 20 mr convergence) at the entrance to the neutralization region.

The heavy ion beam is space-charge dominated in the final-focus system, where it has a large cross section and is highly nonparaxial. The beam expands in the two center magnets, which determines the amount of nonlinear magnetic fields that the beam samples as well as the degree of nonparaxial motion. These geometrical aberrations will change the focusing properties calculated by the envelope equations. Therefore, particle tracking simulations require the knowledge of the multipole field content of the magnetic field. It can be shown [1] that to third order the main

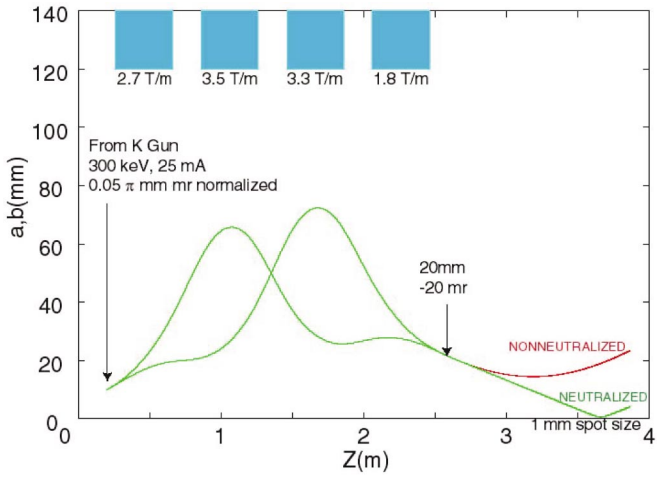

FIG. 2. (Color) Final-focus lattice for ballistically neutralized drift.

contribution to the beam dynamics come from the normal quadrupole, the normal sextupole and the pseudooctupole components of the magnetic field. These three components are included in all the numerical simulations performed for the design of the lattice.

Neuffer [1] has shown that the geometric aberrations depend only on the nonperturbed (first order) particle trajectories; therefore the scaling properties of the geometric aberrations for a final-focus system depend only on the perveance Q, if the scaled field reproduces the multipole components of the original field. He also found a formula to estimate the correction (increase) of the spot size [Eq. (3)] due to geometric aberrations:

$$\Delta r_s \approx 1350 l_{\text{quad}} \theta^3, \tag{6}$$

where l_{quad} is the length of the last quadrupole magnet and θ is the convergence angle in radians. For NTX the unnormalized emittance $\varepsilon \sim 20\ \pi$-mm-mr, the convergence angle $\theta \sim 20$ mr, and $l_{\text{quad}} \sim 0.4$ m, from which we get $r_s \sim 1$ mm, and $\Delta r_s \sim 4$ mm. In Sec. 3 we will show that experimentally and numerically we get $\Delta r_s \sim 0.5$ mm, about a factor of 10 less increase in spot size due to geometric aberrations. The discrepancy comes from the fact that the estimate [Eq. (6)] was obtained by analyzing a specific lattice configuration (a quadrupole doublet) which is very different from the NTX lattice.

For fusion applications we require that the final-focus system will deliver the entire beam pulse onto the target with the same small spot size. Chromatic aberrations affect the focal spot radius due to deviations from the nominal ion momentum causing a variation in the focal length produced by the magnet system, and can be separated into two types. The first kind of chromatic aberrations depends on the velocity and current change from beam head to tail and it results from initial transients in the injector, from voltage errors in the accelerating gaps, and from residual momen-

tum tilt due to beam compression. In this case the different slices of the beam may have somewhat different beam envelopes through the magnetic lattice, leading to different beam size and convergence angle, and therefore variable focal length from head to tail. The second kind of chromatic effects depends on the momentum spread at a given beam slice (longitudinal emittance) and is produced along the beam line by thermalization of velocity errors. For a driver there is a requirement to keep the relative momentum spread $\delta p/p \sim 0.1\%$, and remove the velocity tilt by the time the beam reaches the focal plane.

An estimate of the correction (increase) of the spot size [Eq. (3)] due to chromatic aberrations from momentum spread was obtained by Lee [9]:

$$\delta r_s \approx 6 f \theta \left(\frac{\delta p}{p}\right), \tag{7}$$

where f is the focal length of the last quadrupole magnet, θ is the convergence angle in radians, and $\delta p/p$ is the beam momentum spread. For NTX the focal length $f = 1$ m, the convergence angle $\theta \sim 20$ mr, and $\delta p/p \sim 0.1\%$, from which we get $\Delta r_s \sim 0.1$ mm. Hence, spot size increase due to chromatic aberrations from momentum spread is negligible on NTX. Equation (7) includes the partial cancellation of chromatic effects by the space charge of a uniform density beam. The effects of beam space charge on the beam dynamics also include nonlinear forces arising from nonuniform charge density distribution as well as image forces from the beam pipe. These effects depend on the length of the lattice and the clearance between the edge of the beam and the walls of the chamber, and are negligible for a short system as NTX.

It is possible to infer the effects of momentum spread by studying the sensitivity of the beam parameters to small changes in energy for a given beam slice. This can be evaluated by measuring the beam size as the energy is varied for a given beam slice.

III. EXPERIMENTAL AND NUMERICAL METHODS

Figure 3 shows a sketch of the NTX beam line, consisting of an ion beam injector, 4 quadrupoles and a meter-long neutralized drift section with a cathode arc plasma plug, an rf plasma source, and diagnostics. Optical scintillators imaged by CCD cameras and mechanical slit scanners [6] were used to measure the beam profiles and phase-space distributions of the beam at the end of the final-focus lattice.

The K^+ beam is produced within the source chamber by a standard hot plate [10] of a 2.54 cm diameter aluminosilicate source across a diode with a 12 cm gap. The pulsed power is provided by a Marx generator and crowbar switch that were used in the multiple beam test experiment (MBE-4) [11]. This Marx generator produces a pulse with 0.5–1 μs rise time and is crowbared to produce a 6-μs "flat top." A smooth uniform bright beam profile is generated by increasing the source temperature, smoothing the source surface and aperturing the beam [6]. The use of an aperture to vary the perveance also generates a high-brightness beam by removing the edge of the beam after it exits the diode. Beam scraping, however, produces secondary electrons that are controlled by an electron trap. Figure 4(a) shows a sketch of the beam scraper system, as designed using the EGUN code, and 4(b) a photograph of the aperture and electron trap located at the exit of the NTX diode. The trap consists of two metal tubes, each of 5 cm length, and 6.2 cm inner diameter with an aperture plate in between. The upstream and downstream tubes are located 0.8 cm from the aperture plate. A nominal negative 3 kV

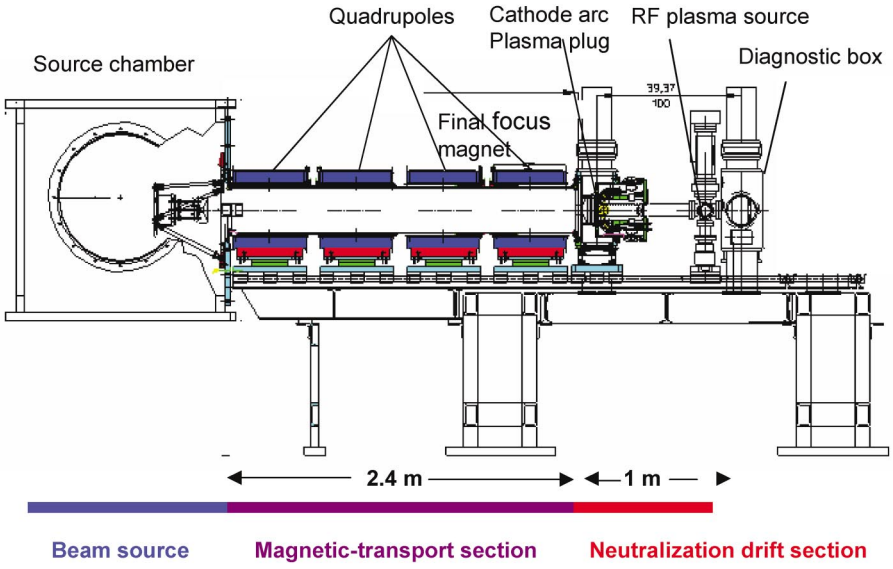

FIG. 3. (Color) Schematic of the NTX beam line.

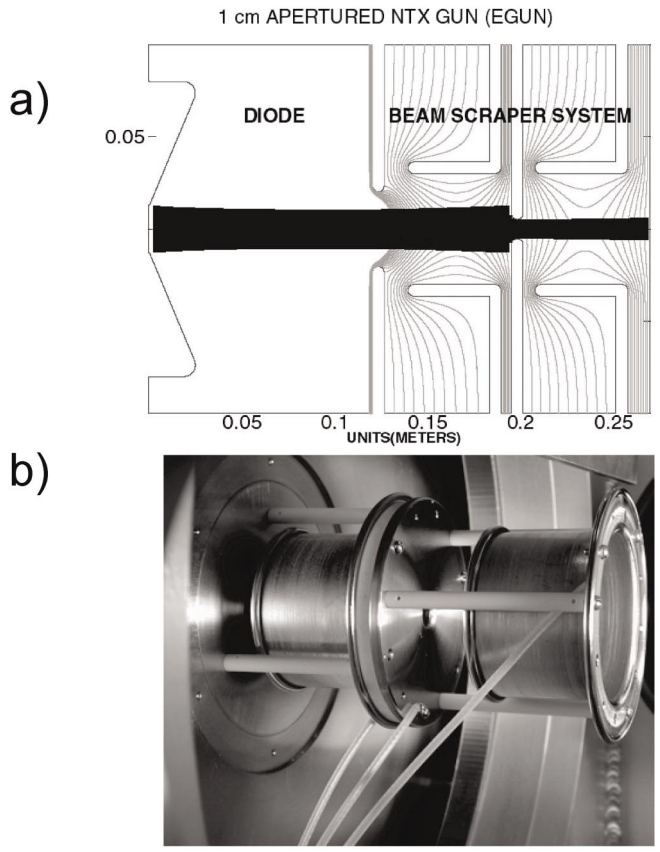

FIG. 4. (a) Equipotential plot of the beam scraper system, and (b) aperture and electron trap system located at the exit of the NTX diode.

potential is provided on each of the metal tubes, providing adequate electron trapping in the presence of the ion beam. Another electron trap, 7.5 cm in radius, is located at the downstream end of the beam line, 10.16 cm downstream from the last quadrupole magnet. A nominal negative 7 KV voltage is used across this second trap to make it effective for collection of stray electrons.

The transport section consists of a double FODO channel with very short drift regions, including the drift from the source into the channel, and the drift into the plasma neutralization chamber. Figure 2 shows the calculated beam envelope (X and Y) through the system. The beam is quite large in the two center magnets, which determines the required bore size and winding radius. The magnet has a relatively short center section and a substantial portion of the magnetic field is contained in the end fringe fields, with significant axial components. The beam is transported through a 2.4 m long path magnetic section, as shown in Fig. 3, using four pulsed quadrupole magnets, as mentioned earlier. The distance from the beam aperture radius to the center of the first magnet, the quadrupole length, and the quadrupole to quadrupole spacing are 26, 46.50, and 60 cm, respectively. Field gradient and maximum field of a magnet are calculated to be 2–5 T/m and 0.6 T, respectively, with a current range of 3.3 to 8.2 kA. The pulser for each NTX quadrupole magnet consists of a bipolar-charged 2 mF capacitor which is discharged through thyristors to produce a current half-sine wave with a pulse width of 2.3 ms. Bipolar charging and a large capacitance were chosen to minimize the voltage from the magnet leads to the grounded magnet housing for the maximum design current. The pulser output voltage is monitored with a resistive voltage divider and the magnet current is monitored with a current transformer. Inside the magnetic lattice, a thin wall (3.3 mm) stainless steel tube of 13 cm inner radius is installed. Eddy currents were calculated by transient 2D finite element analysis, and it was found to result in a 7.4% loss of peak field, and a 275 ms peak field time lag from the source current peak. It was observed that the measured axial field falloff profile agreed well with the computational model [12]. Our measurements with and without stainless steel tube also agree well with the calculations.

The final section of the beam line is known as the neutralized drift section, consisting of a cathode arc plasma plug and an rf plasma source. This section is 1-m long, and beam diagnostics are installed at the end of the drift section to measure nonneutralized and neutralized beams.

Several diagnostics have been used to characterize the ion beam. The primary diagnostics for this experiment consist of (1) a Faraday cup, (2) a slit /slit-cup system, and (3) a scintillator with a gated CCD camera system. The Faraday cup and the slit cup each consists of a collector and a guard ring (grid) with bias voltages that are controlled to collect beam ions only. In addition, we can also monitor currents flowing through the aperture plate and each of the two electron traps. The removable Faraday cup is inserted into the NTX beam line at the exit of the injector and at the end of the magnetic lattice to measure total beam current. The slit/ slit-cup arrangement is used to measure the line-integrated beam profile (with slit cup only) and emittance (with slit and slit cup) at the same locations. The beam profile is measured optically using a glass or ceramic (96% alumina) scintillator with associated camera. Charge neutralization of this scintillator is provided by a high-transparency (80%–90% transmission) metallic mesh placed on or near the surface of the scintillator. By applying a negative bias to the mesh, stray external electrons are decelerated and deflected away from the scintillator, limiting their contribution to the optical image to negligible levels. Time-resolved beam-induced images on the scintillator screen are captured with a Roper Scientific gated intensified CCD camera viewing the scintillator through a vacuum window, and images were processed using the public domain program IMAGEJ.

We are developing a new technique to measure the 4-dimensional phase-space distribution of the beam using the beam imaging diagnostics [6]. The phase-space distribution $f(x, y, x', y')$ can be measured by scanning the beam

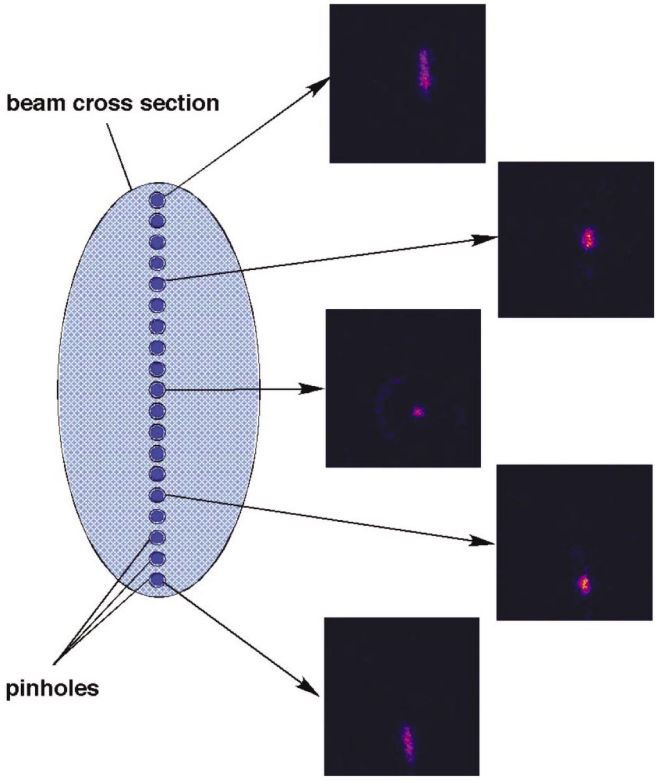

FIG. 5. (Color) Beam imaging technique to measure the phase-space distribution $f(x, y, x', y')$.

with a small pinhole (20 mils in diameter) and letting the transmitted beamlet travel a long distance ($\sim$1 m) before striking the scintillator where an image is taken. The position of the pinhole defines the coordinates x and y, and from the image we can extract the density distribution of x' and y'. Because of the fact that the beam at the exit of the final-focus system is prepared to focus to small spot in the absence of space charge, a standard pepperpot technique does not work since all the individual beamlets would fall on a single spot. Figure 5 shows schematically this technique along with some images of the individual beamlets that show a very detailed structure of the phase-space distribution. The knowledge of the 4-dimensional phase space is essential in order to run more realistic simulations of the beam focusing to a small spot when drifting through neutralizing plasma.

The primary simulation tool is WARP3D [7]. The code is used to simulate the ion beam from source through the 4-quadrupoles and the neutralized drift section to the target. Details of the experimental setup are incorporated into the code including all electric (electrodes) and magnetic fields (third order nonlinear magnetic fields as calculated by ANSYS). Figure 6 shows the dominant quadrupole and pseudooctupole magnetic fields used in WARP3D for the numerical simulations. In the neutralized drift section, a simple approximation is applied in which the space-charge forces are uniformly reduced by a neutralization factor, of the order of 95% to 97%, which is a result obtained from a more detailed neutralized beam transport calculation using LSP code [6]. LSP models the plasma-beam interaction in detail, while WARP3D is the code of choice for magnetic lattice beam dynamics. The simplifying approximation allows us to extrapolate the beam dynamics effects in the quadrupole section to the final beam spot.

IV. TRANSPORT IN FINAL-FOCUS SYSTEM

A high-brightness, low emittance ion beam is an essential component of the neutralized transport experiment (NTX) to obtain the minimal spot size at the focal plane [Eq. (3)]. An ion beam extracted from a Pierce-type diode suffers from spherical aberrations as evidenced from phase-space distortions (high emittance) and from nonuniform charge density profiles. Since the source of these aberrations are the high order field components, the particles at the edge of the beam are the most affected. One way to generate high-brightness beams is to remove the edge of the beam after it is generated in the diode [6]. To study

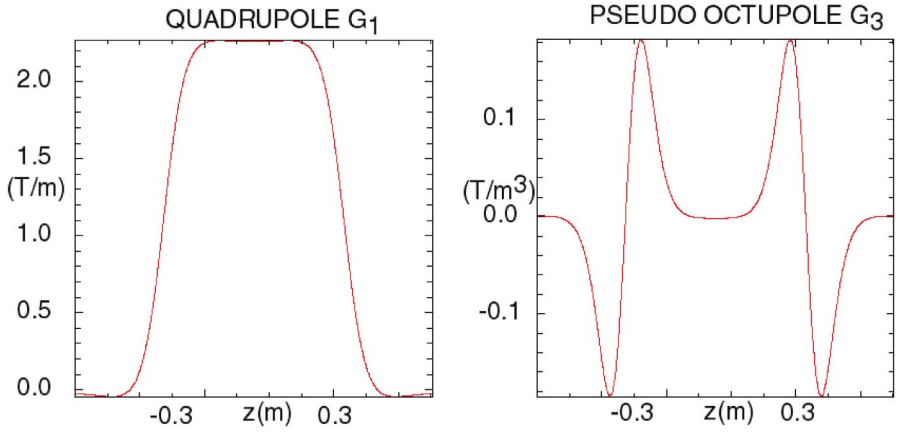

FIG. 6. (Color) Dominant (a) quadrupole and (b) pseudooctupole coefficients for the multipole decomposition $B_\perp(r, \theta, z) = G_1(z) r \cos(2\theta) + G_3(z) r^3 \cos(2\theta) + \ldots$.

beam transport through the final-focus system a 300 keV, 50 mA beam extracted from the diode, has been apertured to a 1 cm, 25 mA beam with a normalized emittance of 0.05 π–mm-mr and a uniform density profile. Figure 7 shows the good agreement between the measured (left) and calculated (right) beam profiles and phase space.

A. Envelope control

A series of measurements were performed to demonstrate the control that WARP3D has in predicting the quadrupole fields to obtain prescribed beam parameters.

The first case was to produce a round beam with the nominal parameters of 20 mm radius and 20 mr convergence (one-meter focal length). Figure 8 shows the good agreement between the measured (top) and calculated (bottom) beam profiles and phase-space distributions at the entrance to the neutralization region. The slight distortion of the beam profile can be traced back to a small rotation (5 mr) of one of the quadrupoles. The beam is uniform with a narrow rim due to field aberrations, and the measured final unnormalized emittance of the beam is $\sim$25 π–mm-mr, small enough to focus the beam to a spot radius of $r_s \sim 1$ mm.

We also compared the beam profiles for several quadrupole strength configurations as calculated by WARP3D and as measured. In Fig. 9, for each quadrupole, the corresponding row shows the profiles for a change of -5%, 0%, and $+5\%$ from the nominal quadrupole strength. This comparison shows the good agreement that we have obtained so far, between measurements and simulations.

In order to study the spot size dependence on convergence angle, we have varied the quadrupoles to obtain various values of the convergence angle θ (5, 10, and 20 mr) for a given beam energy and current. The agreement between theory and experiment is excellent. Finally, the perveance was varied, and the same code-experiment agreement was demonstrated.

As a preliminary test of the NTX system, the beam at the end of the magnetic lattice was injected into a vacuum pipe without any neutralization. Figure 10 shows the measured beam profiles at 1 m downstream from the exit of the final-focus system. The energy varies from 260 to 300 keV, and the beam profiles are in good agreement with WARP3D simulations.

B. Energy scan

We have also performed a complete characterization of the quadrupole lattice by comparing experimental results with particle simulations when the beam energy (and current) was varied. Again, the beam shape varied as predicted by WARP3D, when a 3% energy shift correction is applied. Figure 11 shows the good agreement between the calculated and measured beam size at the exit of the final-focus system when the beam energy is varied. The numerical

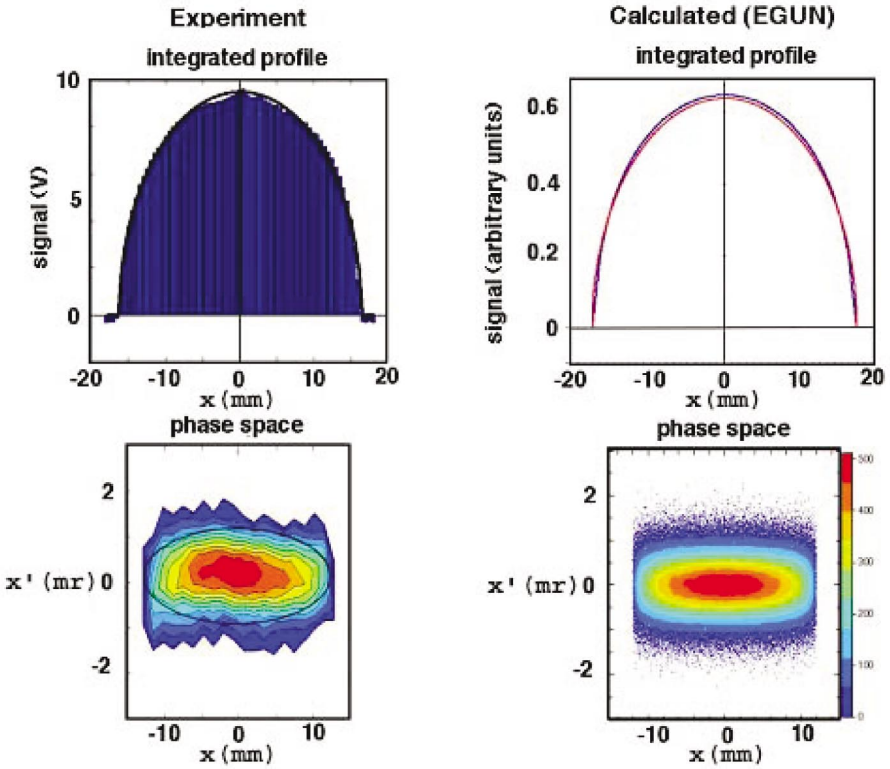

FIG. 7. (Color) Slit-integrated density profile and (x, x') phase space of a high-brightness apertured beam (300 kV, 25 mA, 2-cm aperture diameter). The corresponding EGUN calculations are shown to the right.

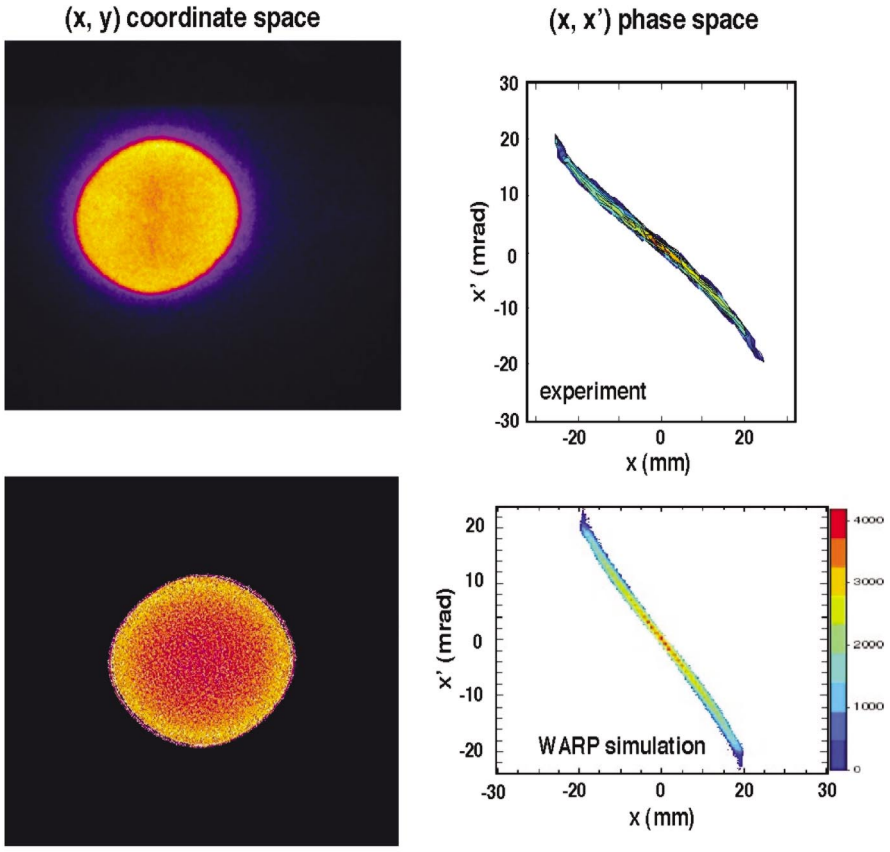

FIG. 8. (Color) Experimental results and simulations of beam profile and phase-space distribution at exit of channel.

simulations track the beam behavior as the beam expands by a large factor when the energy changes from -9% to $+9\%$ around the nominal energy.

The sensitivity of the beam optics to small changes in beam energy was evaluated by measuring the beam size as the energy varied for a given beam slice. We observed that energy variations of 1% led to reduction of current density by 50%. This experimental result is consistent with numerical simulations. Since on NTX there is an uncompensated beam head-to-tail energy and current variation from

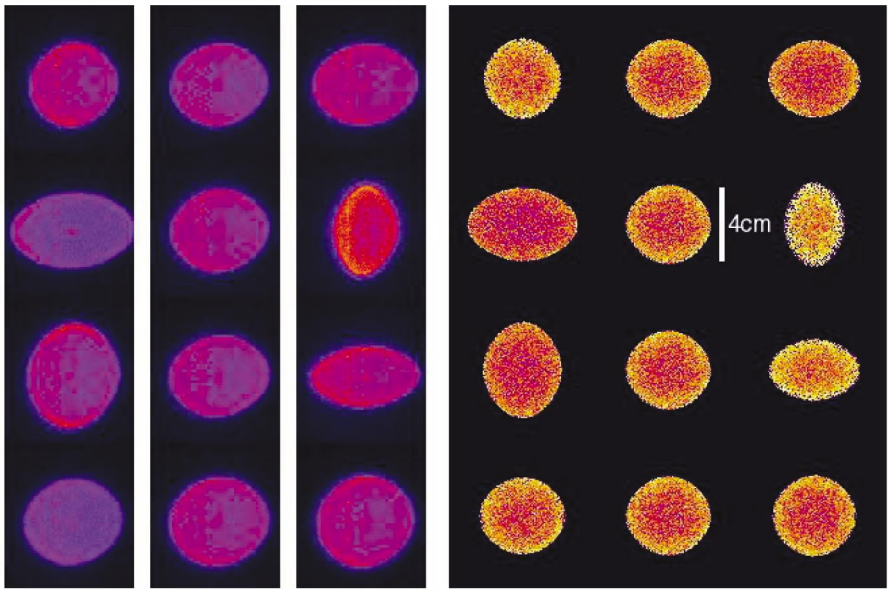

FIG. 9. (Color) Numerical results and camera images of beam profiles as a function of quadrupole field configuration.

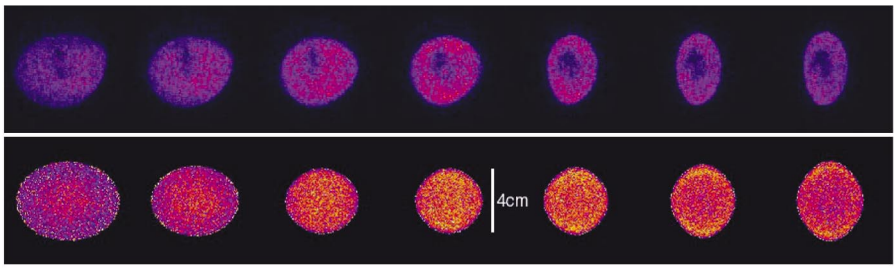

FIG. 10. (Color) Experimental (top) and theoretical (bottom) NTX beam profiles for a nonneutralized beam 1 m downstream from the exit of the final-focus system.

initial transients in the injector, we also measured directly the spot size variation from head to tail (Fig. 12), where significant changes were observed. The voltage (energy) waveform shows a variation of ~1%, and this energy variation is enough to account for the head-to-tail variation in spot size. For future work, we need to study the energy sensitivity for other lattices (e.g., 6-quad lattice) to see if the energy sensitivity could be reduced. Also, time-dependent focusing may be used to correct for the head-to-tail variations.

C. Geometric aberrations

The goal of a final-focus experiment is to obtain the minimal spot radius. Equation (2) suggests that one could reduce the spot size by increasing the convergence angle, provided that the emittance is not significantly increased. In general, as the angle is increased, the beam envelope goes through larger excursions in the magnetic lattice, which in turn leads to increase in emittance through higher order (particularly third order) aberrations. The distortion of phase space due to geometric aberrations has been studied numerically. In this experiment, we see the same phase-space distortions, leading to increased spot size with large angles. Both code and experiment predict minimum spot radius at ~15 mrad (Fig. 13). Equation (6) predicts a monotonically increasing spot size as the convergence angle is varied, but in the experiments, however, the results are complicated by nonoptimal entrance conditions from the apertured source which is the same for the different magnet tunes. In fact for the NTX lattice and for fixed entrance conditions, the emittance growth along the lattice may be larger for smaller convergence angles.

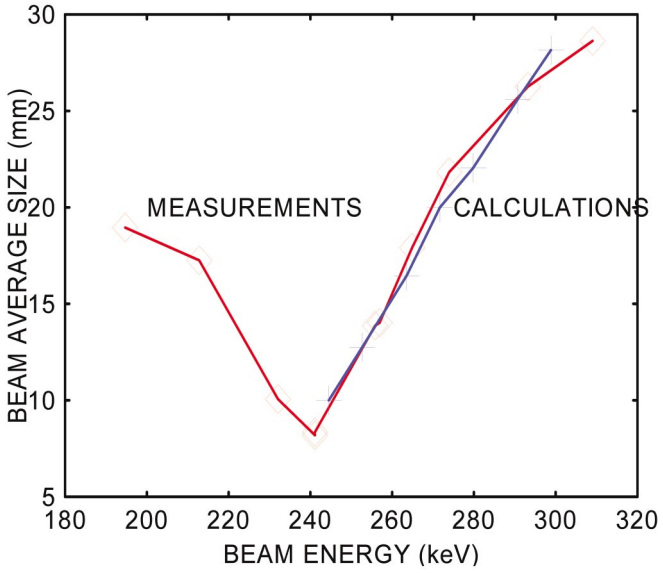

FIG. 11. (Color) Calculated (blue plus sign) and measured (red diamond) beam size at the exit of the final-focus system as the beam energy is varied. A factor of 3% was subtracted from the energy used in the calculation.

D. Spot size dependence on perveance

Finally, we consider variations of perveance. In general, we expect the geometric aberrations to be less significant for lower perveance beams. This is true if the final-focus lattice is ''matched'' to the beam perveance; it is always possible to design a final-focus system for a lower perveance beam that will be less affected by geometric aberrations. The NTX lattice was designed for the 25 mA potassium beam at 300 keV, with perveance $Q \sim 0.0006$.

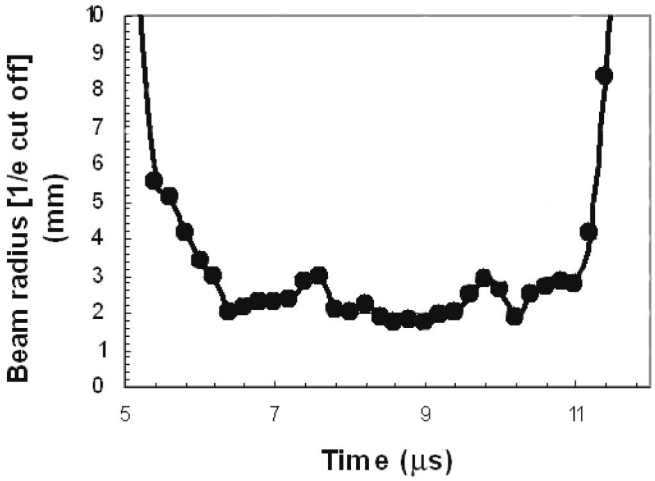

FIG. 12. Spot size variation from head to tail measured at the focal plane, showing blow up of the beam head and tail.

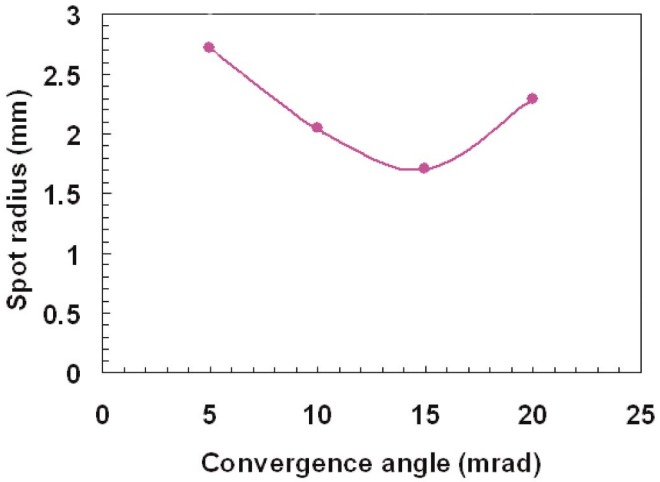

FIG. 13. (Color) Spot size as function of convergence angle.

Figure 14 shows the spot size dependence on perveance by comparing the beam images at the focal plane for a 264 keV beam that has been apertured to 25 and 6 mA, respectively, and that are transported through the final-focus system using the same quadrupole fields. There is a large reduction in spot size for the lower perveance beam.

It is important to point out that the low emittance ($\sim$25 π–mm-mr unnormalized) of the beam at the entrance to the neutralized region allows for the beam to be focused to a small spot size (1–2 mm radius) at the focal plane for neutralized ballistic transport. Furthermore, Faraday cup measurements of the beam current at entrance and exit of the final-focus system have shown negligible beam loss along the transport channel.

The pinhole diagnostics system described in Sec. 3 can be used to simulate the effect of full neutralization on a beam, since each beamlet going through a pinhole only carries the information about the phase-space distribution at a given location without being perturbed by the space charge of the full beam. The superposition of all the pinhole images at a given location can be compared with a beam transport calculation where the space charge is turned off from the pinhole-scan plane to the focal plane. Figure 15 shows a comparison between this "analog experiment" and WARP3D simulations; the agreement is excellent and shows that the emittance is low enough to get a small spot (~1 mm radius).

While we have very good agreement between theory and experiment in many aspects, there are several observations, which are not yet well understood. We have mentioned the need for an arbitrary energy calibration factor in order to obtain agreement between theory and code. To refine the energy calibration in the experiment, we performed a series of time-of-flight (TOF) experiments, as well as careful calibration of resistive and capacitive monitors. While the 3 different ways of energy calibration agree within the experimental uncertainties, the discrepancy with theory persists.

In pursuit of the explanation of this discrepancy, we suspect that stray electrons might play a role. To ascertain this effect, we incorporated a mesh liner along the pipe. However, while currents were clearly collected on the mesh, its net effect on the beam profile was relatively minor.

Finally, we have observed clear evidence of halo formation, in both configuration space (Fig. 16) and velocity space (Fig. 17) as evidenced by the rings surrounding the central image. However, we have not been able to account, from numerical simulations, for the origin of these halo particles thus far.

V. ERROR ANALYSIS

In this section, we discuss several factors that may influence our interpretation of the ion beam data. To quantify these effects, a series of experiments were performed. These include: (a) stray electron effects on the beam inside the quadrupole lattice, (b) calibration of beam energy, (c) measurements of quadrupoles field strength, and (d) efficiency of the diagnostic devices.

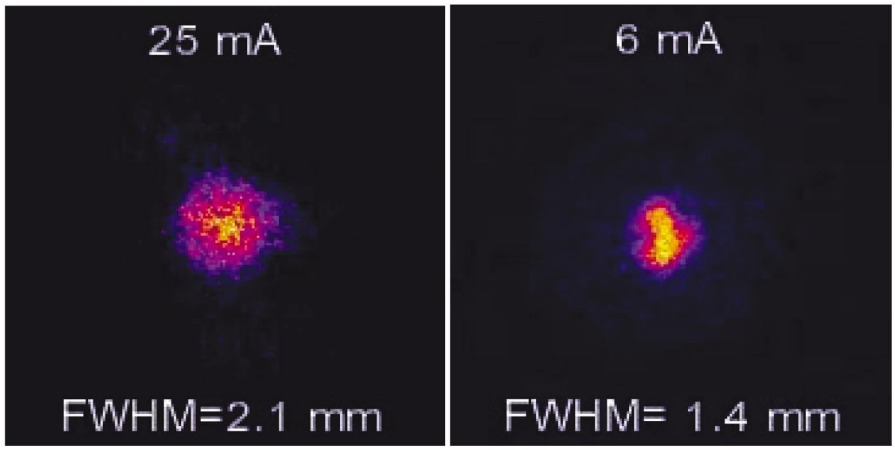

FIG. 14. (Color) Spot size dependence on perveance.

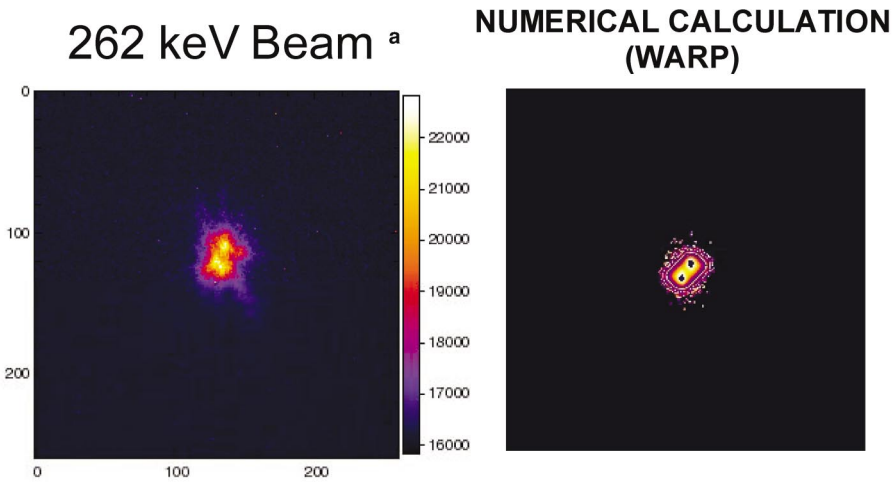

FIG. 15. (Color) Analog (pinhole) simulation and WARP3D calculation of fully neutralized beam focused to a small spot. Image box size is 4 cm $b \times 4$ cm squares.

A. Stray electron effects inside the quadrupole lattice section

As we mentioned in Sec. 3 the NTX magnetic transport section contains an aperturing system for variable perveance, brightness, and beam size. This aperturing technique is provided with a sandwich-type electron trap to collect electrons. Ions from the poorly matched beam head and halo ions in the main pulse of the beam can strike the outer wall of the beam tube. A single ion impact can produce thousands of secondary electrons depending on the energy and angle of incidence, with ions of grazing-angle incidence producing the largest secondary electron yields. Only a small fraction of the beam ions striking the wall are needed to provide a space-charge-limited supply of electrons from the wall. If the secondary electrons are not stopped, they are attracted by the beam potential and can provide some degree of beam neutralization. The presence of wall electrons was measured using a long radial metal mesh, which was installed inside the magnetic drift section. Mesh radial diameter, space of wire and mesh length were 23.5 cm, 1.27 cm, and 2.28 m, respectively.

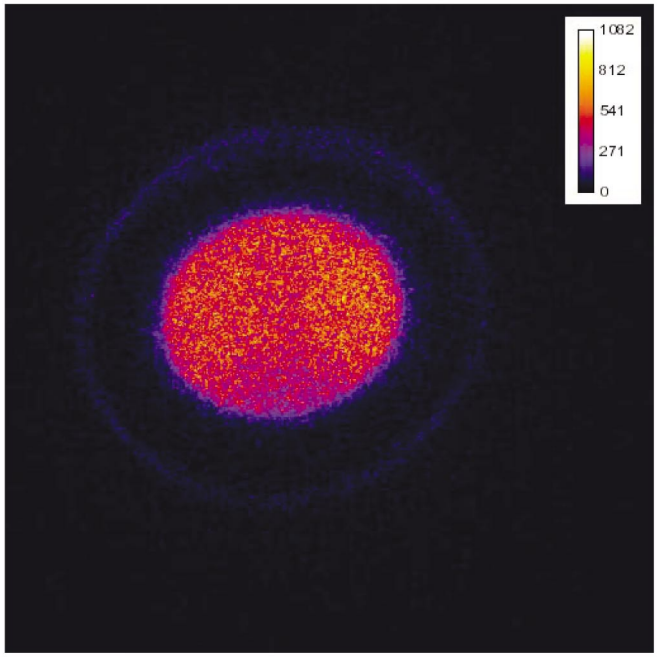

FIG. 16. (Color) Evidence of beam halo formation in configuration space. Image for a 6% off-energy beam, measured at end of the final-focus system (beam size ~2 cm).

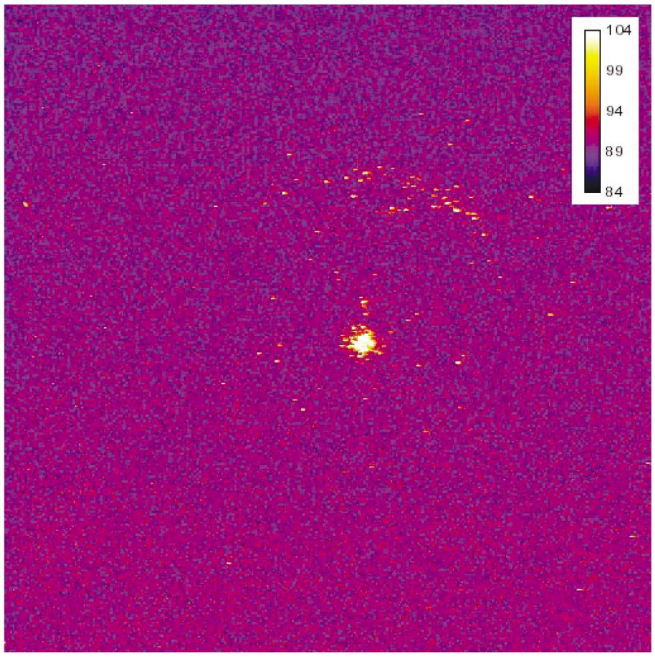

FIG. 17. (Color) Evidence of beam halo formation in velocity space. Image from a pinhole positioned at end of the final-focus system and at the center of the beam, and measured at the focal plane.

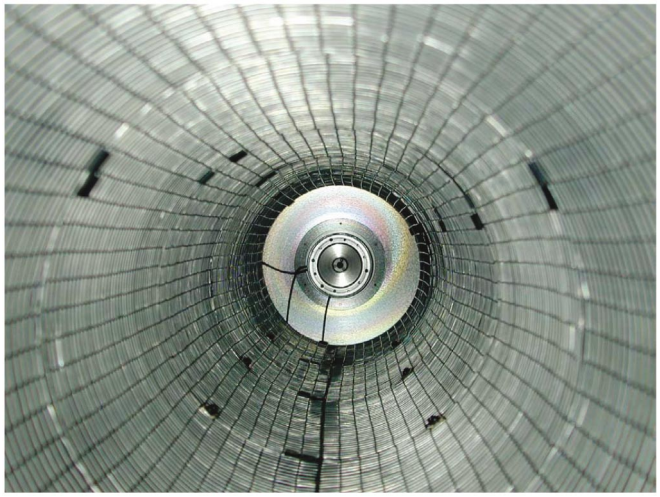

FIG. 18. (Color) A cylindrical metal mesh inside the beam pipe in the magnetic final-focus section.

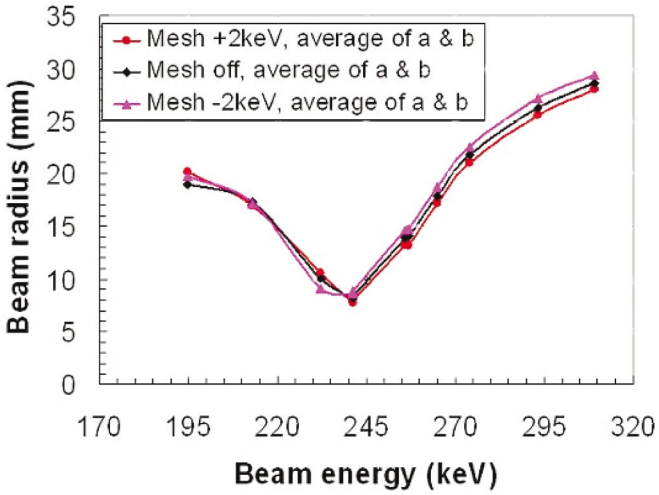

FIG. 20. (Color) Beam radius as a function of beam energy as mesh bias is turned on ($\pm$ 2 kV) and off.

Figure 18 shows the 23.5 cm diameter metal mesh inside the magnetic transport section, which was biased with a ± 2 kV potential. Beam profile at the scintillator, located at the end of the final-focus magnets, and current in the mesh as a function of the mesh voltage were measured. Figure 19 shows the measured current in the mesh by varying its bias voltage.

As a negative voltage was applied across the mesh, there was no significant current measured in the mesh. It shows that there was no significant number of ions from the beam halo near the beam pipe wall. When the voltage was switched to positive, significant current in the mesh was measured. It shows that wall electrons were collected in the positive biased mesh. These electrons were generated in the drift tube wall. But the beam was not significantly affected by electrons. Figure 20 shows beam radii corresponding to several beam energies in condition of mesh bias powered to ± 2 kV and without any mesh voltage. By comparing these 3 cases, we see that the beam radius changes were not significant. It is inferred that for a large pipe, the wall electrons spend only a small fraction of their time within the beam. The electrons were moving at their greatest velocity while passing through the beam, reducing their net effect of beam neutralization.

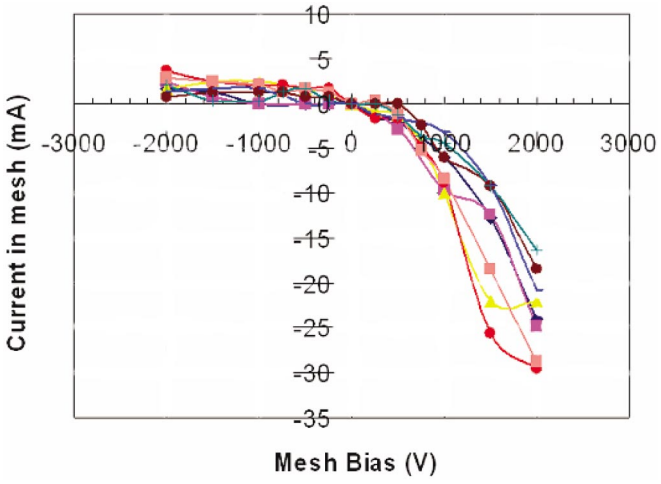

FIG. 19. (Color) Mesh current when applying voltage across the mesh. Different lines correspond to different energies, ranging from 244 to 320 keV.

Though a mesh inside the final-focus magnetic section was not necessarily effective due to the large diameter of the beam pipe, it provided good evidence that a positively biased metal mesh can reduce beam neutralization due to stray electrons. This effect can be very significant in a small size drift tube, as we have found in the neutralized drift section with its 3 in. diameter pipe [6].

B. Calibration of energy

The NTX source is powered from a Marx generator as mentioned in the experimental Sec. 3. This voltage is measured with a capacitive voltage divider. Calibration of beam energy is important because of the sensitivity of beam transport to the beam energy in a quadrupole transport channel as we have shown in Sec. IV. To provide a cross check of the beam energy measurement, the capacitive system, was compared to time-of-flight measurements and a resistive voltage divider system.

Charged particle beams are capable of supporting and transmitting a variety of waves. Longitudinal space-charge waves are longitudinal oscillations of the beam within the conducting boundary of a vacuum wall. These waves have been studied and applied to continuous electron beams in microwave devices, bunched charged particle beams in particle accelerators, and space-charge dominated charged particle beams. The theoretical equilibrium and stability of these waves have been explored extensively. Here we discuss a diagnostic technique that utilizes longitudinal space-

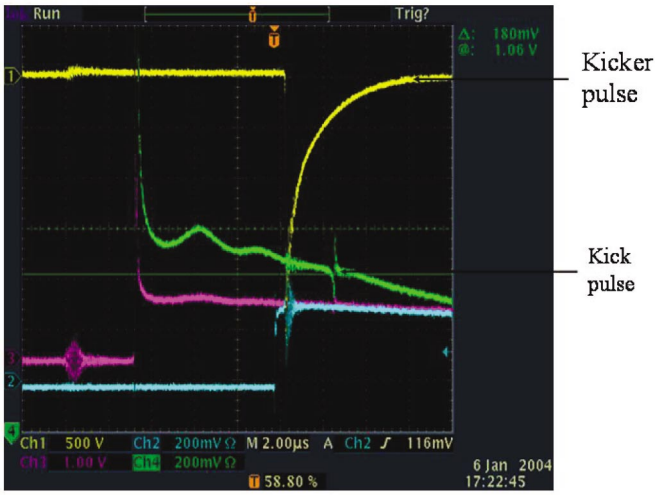

FIG. 21. (Color) Typical waveforms of kicker (yellow trace) and kick (green trace) pulses for time-of-flight measurements. The oscilloscope vertical scale is arbitrary, the horizontal scale is 2 μs per division. The magenta and blue traces are auxiliary traces captured in this image.

charge waves in heavy-ion beams to determine beam energy by TOF.

The TOF method described here is to longitudinally perturb a slice of the beam with a fast voltage pulse applied to a ''kicker'' near the path of the beam. The kicker may be any cylindrically symmetric mechanical structure near the beam that can rapidly generate a localized longitudinal electric field on the beam. A typical kicker and kick pulses are shown in Fig. 21. The voltage pulse applied to the kicker locally perturbs the energy of the beam particles passing near the structure. The perturbation propagates in the form of a wave that travels with the beam. In the long wavelength limit, there is a fast wave traveling toward the front of the beam pulse and a slow wave traveling toward the rear. Measuring the arrival time of the resulting space-charge wave at a detector placed a suitable distance downstream provides a measure of the beam energy.

The structure utilized as a kicker is a thin aperture which also limits the beam transversely for the final-focus experiments. The NTX TOF pulse has a rise time of about 4 ns, a fall time of about 1 μs, and the peak output voltage is -2.5 kV. The path length between the kicker and registering beam current at a Faraday cup is 2.48 m.

The initial pulse resembles the longitudinal electric field (spatial derivative of the potential perturbation) at the kicker. Beam ions are spread apart at the front of the wave and compressed at the rear. The result is a double pulse which is very well defined in time. The time reference for TOF measurements is the point in which the wave passes through zero. This corresponds to those particles which were at the location of the aperture at the time that the pulser voltage is turned on.

The comparison between data and the 1D model is shown in Fig. 22 for a small current (1 mA). The agreement between model and data is good. However, for a large current (25 mA) the discrepancy varies. Figure 23 shows the relative difference between TOF beam energy (open squares), resistive divider voltage (diamonds), and capacitive divider voltage readings as a function of NTX Marx voltage. Both TOF and resistive divider measurements are shown as a function of capacitive divider voltage. 2% error bars are assumed for both sets of measurements. A linear fit to the data points is also shown for each set of measurements. The voltage indicated by the resistive divider lies between the capacitive divider and the TOF measurements.

C. Field of the 4 quadrupole magnets

The strength of the 4 quadrupole magnets is provided by 4 separate power supplies using a pulser. Waveforms of each power supply are monitored on an oscilloscope screen. There is a $\pm 0.5\%$ magnetic field error bar when measured on wave forms displayed on the oscilloscope.

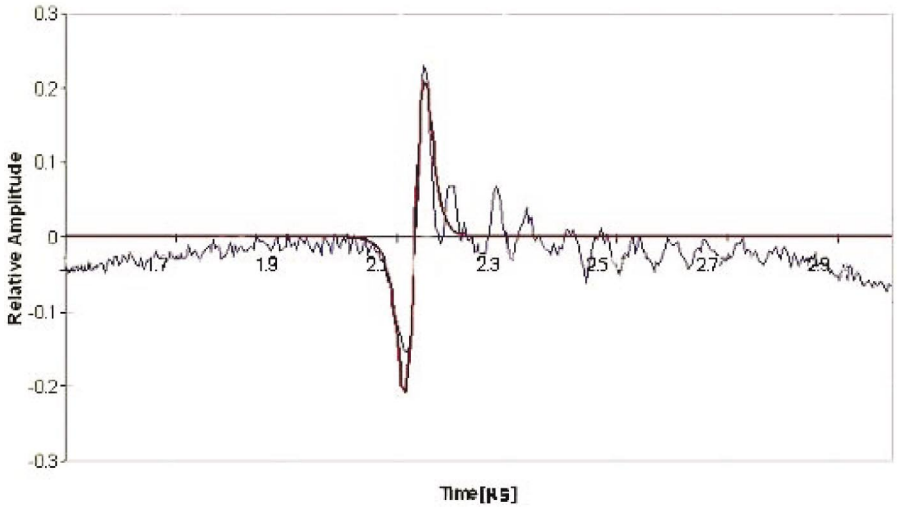

FIG. 22. (Color) Space-charge wave in NTX for a low-current beam.

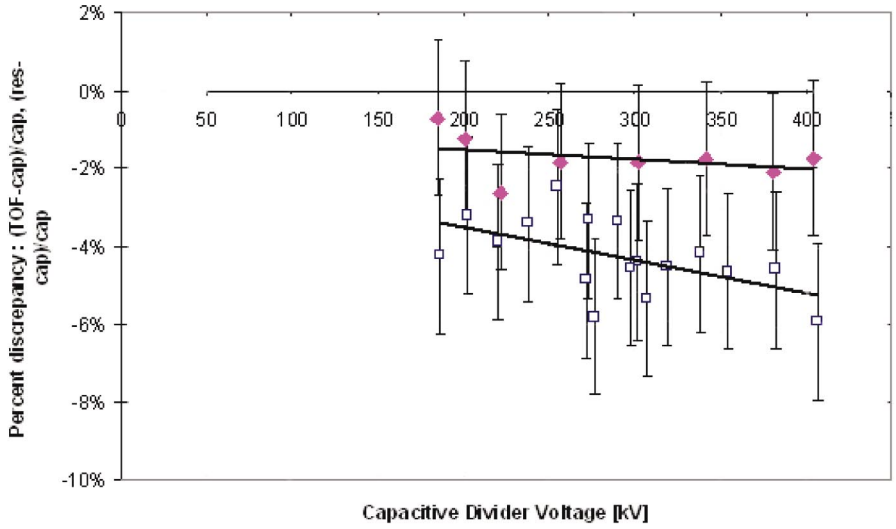

FIG. 23. (Color) The relative difference between TOF beam energy (open squares), resistive divider voltage (diamonds), and capacitive divider voltage readings (0% line) as a function of NTX Marx voltage. Both TOF and resistive divider measurements are shown as a function of capacitive divider voltage. 2% error bars are assumed for both sets of measurements. A linear fit to the data points is also shown for each set of measurements. The voltage indicated by the resistive divider lies between the capacitive divider and the TOF measurements.

Moreover, the magnet current monitor is a current transformer with an accuracy specification of $+1\%$ and -0%. The existing timing setup assumes that the peak quadrupole field occurs at the peak of the monitored magnet current. In reality, there is attenuation and a time shift because of the diffusion of the magnetic field through the 3.3 mm pipe wall. This phase shift is approximately 275 μs based on ANSYS 2D transient EM finite element modeling. Because of this time shift, the timing of the beam may not be during the peak quadrupole field. By the same modeling, the peak field is attenuated by approximately 7% and has been considered in setting the magnet currents.

D. Efficiency of diagnostic devices

As was mentioned in Sec. 3, the diagnostics that have been used in this experiment are Faraday cups, slit cups, and scintillators associated with electronics and a CCD gated camera. Though slit cups have available an electron guard ring, there exists the possibility of the generation of secondary electrons noise by energetic particles, whose presence can mislead the interpretation of halo particles studies. Moreover, once energetic particles strike on a scintillator, its efficiency degrades as a function of incoming beam particle energy.

VI. CONCLUSIONS

The key question of a final-focus experiment is what determines the spot size. In this paper, the emphasis is on the role of the final magnetic system. The effects of plasma neutralization dynamics are discussed elsewhere.

We have shown from both theory and experiment on how to prepare the beam envelope for final neutralized drift. We have also studied the effects of beam energy variations and demonstrated the importance of head-to-tail energy uniformity. We have studied the higher order aberrations, and, in particular, the geometric aberrations and its effect on the spot size. Finally, we have considered the dependence of spot size on perveance.

Overall, the comparisons between theory and experiment are quite good. We have discussed some possible factors in the experiment which are not included in the theory, and an attempt to resolve these issues experimentally.

In terms of future experimental work, the most important task is an *in situ* measurement of the magnetic field, including all the eddy current effects of the pipe and flanges.

One additional unexplained observation has to do with haloes in both configuration and velocity space. We presented two examples in Figs. 16 and 17, respectively. Numerical simulations have not been able to account for these haloes thus far, and will be the subject of future studies.

While we still have a couple of puzzles to resolve, we believe that much has been learned about the final-focus magnetic system relevant for a HIF driver. The questions of how to control energy sweep, design constraints on aberrations, and perveance, are now much better understood as a result of this work.

ACKNOWLEDGMENTS

This work was performed under the auspices of the U.S. Department of Energy by University of California Lawrence Berkeley National Laboratory under Contract No. DE-AC03-76SF00098; E. Henestroza was also sup-

ported by Department of Energy, Office of Fusion Energy Science, Grant No. DE-FG02-01-ER54662.

[1] D. Neuffer, in *Proceedings of the Heavy Ion Fusion Workshop, Argonne National Laboratory, 1978* (Argonne National Laboratory Report No. ANL-79-41, 1978), p. 333.

[2] E. Colton, in *Proceedings of the Heavy Ion Fusion Workshop, Argonne National Laboratory, 1978* (Argonne National Laboratory Report No. ANL-79-41, 1979), pp. 365–378.

[3] A. A. Garren, in *Proceedings of the ERDA Summer Study for Heavy Ions for Inertial Fusion, 1976*, edited by R. O. Bangerter, W. B. Herrmannsfeldt, D. L. Judd, and L. Smith (Lawrence Berkeley National Laboratory Report No. LBL-5543, 1976), pp. 102–109.

[4] D. D.-M. Ho, I. Haber, K. R. Crandall, and T. S. Brandon, Particle Accelerators **36**, 141 (1991).

[5] S. MacLaren, A. Faltens, and P. A. Seidel, Phys. Plasmas **9**, 1712 (2002).

[6] E. Henestroza *et al.*, Phys. Rev. ST Accel. Beams **7**, 083501 (2004).

[7] D. P. Grote, A. Friedman, G. D. Craig, W. M. Sharp, and I. Haber, Nucl. Instrum. Methods Phys. Res., Sect. A **464**, 563 (2001).

[8] I. M. Kapchinskij and V. V. Vladimirskij, in Proceedings of the 1959 International Conference on High Energy Accelerators. Geneva, Switzerland: CERN, 1959.

[9] E. P. Lee, Lawrence Berkeley National Laboratory Report No. LBL-28463, 1991.

[10] D. Baca, J. W. Kwan, and J. K. Wu, in *Proceedings of the 2003 Particle Accelerator Conference*, edited by J. Chew, P. Lucas, and S. Webber (IEEE, Piscataway, NJ, 2003), p. 3294.

[11] W. M. Fawley, T. Garvey, S. Eylon, E. Henestroza, A. Faltens, T. J. Fessenden, K. Hahn, L. Smith, and D. P. Grote, Phys. Plasmas **4**, 880 (1997).

[12] D. Shuman, S. Eylon, E. Henestroza, P. K. Roy, W. Waldron, S. S. Yu, and T. Houck, in *Proceedings of the 2003 Particle Accelerator Conference*, edited by J. Chew, P. Lucas, and S. Webber (IEEE, Piscataway, NJ, 2003), p. 2628.

THREE DIMENSIONAL THEORY AND SIMULATION OF AN ELLIPSE-SHAPED CHARGED-PARTICLE BEAM GUN*

R. Bhatt, T. Bemis, and C. Chen
Plasma Science and Fusion Center, MIT, Cambridge, MA 02139

Abstract

A three-dimensional (3D) theory of non-relativistic, laminar, space-charge-limited, ellipse-shaped, charged-particle beam formation has been developed recently [1] whereby charged particles (electrons or ions) are accelerated across a diode by a static voltage differential and focused transversely by Pierce-type external electrodes placed along analytically specified surfaces. The treatment is extended to consider whether the diode geometry solutions thus obtained are robust to perturbations and limitations of the sort likely to be encountered in a realistic device: finite extent, part misalignment, tolerances for mechanical and thermal stresses, etc. Analytic and semi-analytic estimates are presented along with simulations utilizing the 3D trajectory code, OMNITRAK [2]. It is found that the elliptic-beam solution is quite stable and robust, and its desirable properties can be maintained in a realistic diode.

INTRODUCTION

Electron beams of elongated elliptic cross-sections have generated great interest in vacuum electronics, because of their low space-charge energy and efficient coupling to rf structures when compared to circular beams. It is well-known that high space-charge reduces conversion efficiency in conventional microwave tubes employing circular beams. Presently, there are vigorous activities in the development of sheet-beam traveling wave amplifiers [3,4], klystrons [5], and focusing systems [6,7].

In high-intensity ion and electron accelerators, beams often exhibit non-laminar flows such as large-amplitude density fluctuations, mismatched envelope oscillations, emittance growth, chaotic particle orbits, beam interception, and difficulty in beam focusing and compression. Many of these effects are due to beam mismatch or non-equilibrium behavior. Elliptic beams may allow simplified and more natural matching [8] between beam injectors and commonly used magnetic focusing lattices, reducing the emittance growth associated with beam mismatch.

Although elliptic beams present numerous advantages, their inherent three-dimensional nature has made diode design a challenging process, both analytically and numerically. For the applications discussed above, desirable beam characteristics include uniform current density, parallel flow, and zero magnetic flux threading the emitter – properties consistent with one-dimensional Child-Langmuir [9] flow, in which the electrostatic potential varies as $\Phi \propto z^{4/3}$, where z is the beam propagation distance. In general, however, such flows are difficult to produce. Recent studies of 2D and 3D extensions of the Child-Langmuir law in an infinite applied magnetic field have shown that the beam exhibits significant current density enhancements near the beam-vacuum boundary. In the absence of an infinite confining magnetic field, the beam will tend to spread in phase-space, resulting in a degradation of beam quality. As shown in Ref. [1], it is possible to induce the space-charge flow in a 3D system to take the 1D Child-Langmuir flow form by calculating a 3D equipotential geometry that is consistent with the 1D Child-Langmuir electric field within the beam and constructing external electrodes lying along the equipotentials as prescribed that focus the beam. Such a beam can, in theory, exhibit extremely low emittance, laminar flow.

The equipotential surfaces calculated using the methods of Ref. [1], however, are idealizations, and it is an important question whether the solutions thus obtained are robust to perturbations and limitations of the sort likely to be encountered in a realistic device: finite extent, part misalignment, tolerances for mechanical and thermal stresses, etc. Analytic and semi-analytic estimates are presented along with 3D simulations utilizing the 3D trajectory code, OMNITRAK [2], and it is found that the elliptic-beam solution is quite stable and robust, and its desirable properties can be maintained in a realistic diode.

ELLIPTIC GUN GEOMETRY

We consider a non-relativistic charged-particle beam of length d and elliptic cross-section with semi-major axis a and semi-minor axis b, as shown in Fig. 1. The charged particles are emitted from a flat elliptic plate, held at potential $\Phi = 0$, in the $z = 0$ plane and collected by another flat elliptic plate, held at potential $\Phi = \Phi_d$, in the $z = d$ plane. The cold fluid equations describing the beam interior are $\nabla^2\Phi = -4\pi qn$, $\partial n/\partial t + \nabla \cdot (n\mathbf{V}) = 0$, and $\partial \mathbf{V}/\partial t + (\mathbf{V} \cdot \nabla)\mathbf{V} = -(q/m)\nabla\Phi$, for the region $x^2/a^2 + y^2/b^2 \le 1$ and $0 \le z \le d$. In these equations, $\mathbf{V}$ is the flow velocity, and n is the density of particles, each of mass m and charge q. Note that, consistent with the non-relativistic approximation, we neglect any self-magnetic field. In the beam exterior, the potential satisfies Laplace's equation, $\nabla^2\Phi = 0$.

* Work supported by the U.S. Department of Energy, High-Energy Physics Division, Grant No. DE-FG02-95ER40919, Office of Fusion Energy Science, Grant No. DE-FG02-01ER54662, Air Force Office of Scientific Research, Grant No. F49620-03-1-0230, and the MIT Deshpande Center for Technological Innovation.

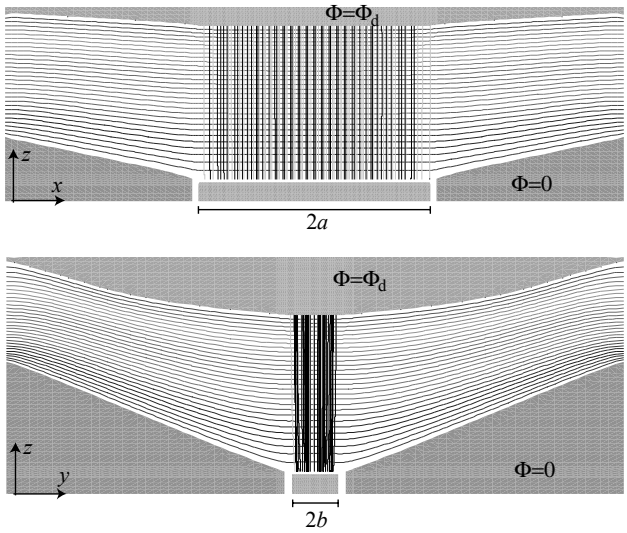

Figure 1: Elliptic charged-particle beam diode shown in the *x*-*z* and *y*-*z* planes. The beam has semi-major axis *a* and semi-minor axis *b*, emitted at potential $\Phi = 0$ and collected at potential $\Phi = \Phi_d$ after propagating a distance *d* along $\hat{\mathbf{e}}_z$.

The 1D steady-state solution to the interior problem defined by the cold fluid equations can be obtained by using the plate potentials as boundary conditions for Poisson's equation and imposing the constraint that particles emerge from the $\Phi = 0$ emitter with zero velocity, i.e. the space-charge-limited boundary condition. This results in the well-known 1D Child-Langmuir (C-L) [12] solution for laminar, space-charge-limited flow with $\mathbf{V}(z) = \hat{\mathbf{e}}_z (2q\Phi_d/m)^{1/2}(z/d)^{2/3}$, $n(z) = (\Phi_d/9\pi q d^2)(z/d)^{-2/3}$, and $\Phi(z) = \Phi_d (z/d)^{4/3}$. For example, an electron diode of length $d = 4.11\,\text{mm}$ and diode voltage $\Phi_d = 2.29\,\text{kV}$ produces a current density of $1.51\,\text{A/cm}^2$.

A 3D cold-beam space-charge-limited emission simulation using the commercially-available ray-tracing code OMNITRAK is shown in Fig. 1 for a 6:1 elliptic beam using the example parameters $a = 3.73\,\text{mm}$ and $b = 0.62$ mm. A variable-resolution computational mesh is employed with x-spacing of 0.05 mm for $0 \le x \le 4$ mm and 0.05 mm for $4 \le x \le 10$ mm, y-spacing of 0.05 mm for $0 \le y \le 1$ mm and 0.2 mm for $1 \le y \le 8$ mm, and z-spacing of 0.05 mm for $0 \le z \le 0.4$ mm and 0.1 mm for $0.4 \le z \le 10$ mm. The mesh resolution is higher in x and y across the cross-section of the beam, and in z where the beam leaves the emitter as shown in Fig. 1. Nearby computational nodes are shifted to conform to the electrode surfaces using the OMNITRAK *surface* flag. Neumann boundaries were used for the symmetry planes of the beam as well as for the outer boundaries of the mesh, which is shown in Fig. 1 along with computed equipotentials and particle trajectories projected to the $x = 0$ and $y = 0$ planes. The entire simulation runs in approximately 30 minutes on a 3 GHz personal computer.

The beam produced by the simulation is essentially parallel, laminar, uniform density Child-Langmuir flow. Beam laminarity is often characterized by the rms beam emittances $\varepsilon_x \equiv \left(\langle x^2\rangle\langle x'^2\rangle - \langle xx'\rangle^2\right)^{1/2}$ and $\varepsilon_y \equiv \left(\langle y^2\rangle\langle y'^2\rangle - \langle yy'\rangle^2\right)^{1/2}$, where the averages of transverse particle position (x, y) and divergence $(x', y') \equiv (dx/dz, dy/dz)$ are taken over a slice of the beam at $z = d$. For a uniform density elliptic beam, these emittances can be related to effective beam temperatures [10] by the relations $\varepsilon_x = a\left(kT_{eff,x}/8q\Phi_d\right)^{1/2}$ and $\varepsilon_y = b\left(kT_{eff,y}/8q\Phi_d\right)^{1/2}$. Using the example parameters of Fig. 1, the OMNITRAK simulation shown predicts the effective beam temperatures $T_{eff,x} = 280\,\text{K}$ and $T_{eff,y} = 1700\,\text{K}$.

PARAMETRIC ROBUSTNESS

The effective beam temperatures of the previous section are not meaningful in practice beyond their use as a measure of the minimum beam temperature growth associated with the gun optics.

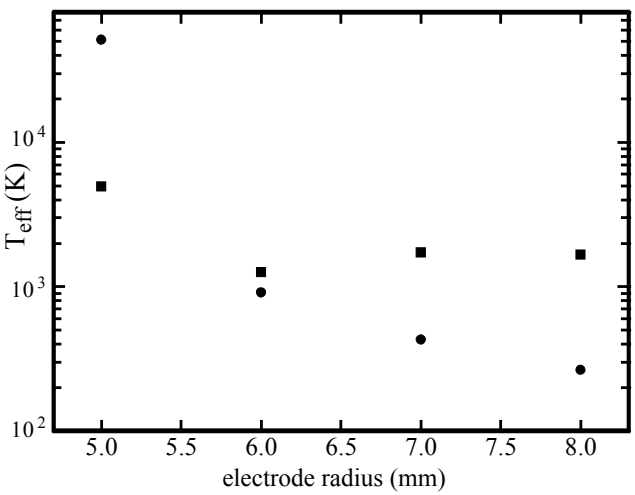

Figure 2: The effective beam temperature T_{eff} is plotted as the termination radius of the beam-focusing electrodes is varied. The circles indicate $T_{eff,x}$, while the squares indicate $T_{eff,y}$.

The theory of Ref. [1] computes equipotentials extending infinitely far from the beam. In practice, electrodes lying along these equipotentials will have a finite length, and it is important to assess the impact of the edge effects thus admitted on the beam. Since the potential satisfies Laplace's equation in the free-space region outside the beam, we expect that electrostatic potential variations caused by localized perturbations of the electrode geometry will be exponentially decaying with distance from the perturbation point. We test this hypothesis by performing several cold-beam OMNITRAK simulations where the radial extent of the electrodes is

varied, while the Neumann boundaries at the edge of the simulation region are kept constant. The effective beam temperatures at the anode are shown as a function of electrode radius in Fig. 2. We see that the influence of electrode structure beyond 6mm in radius is minimal.

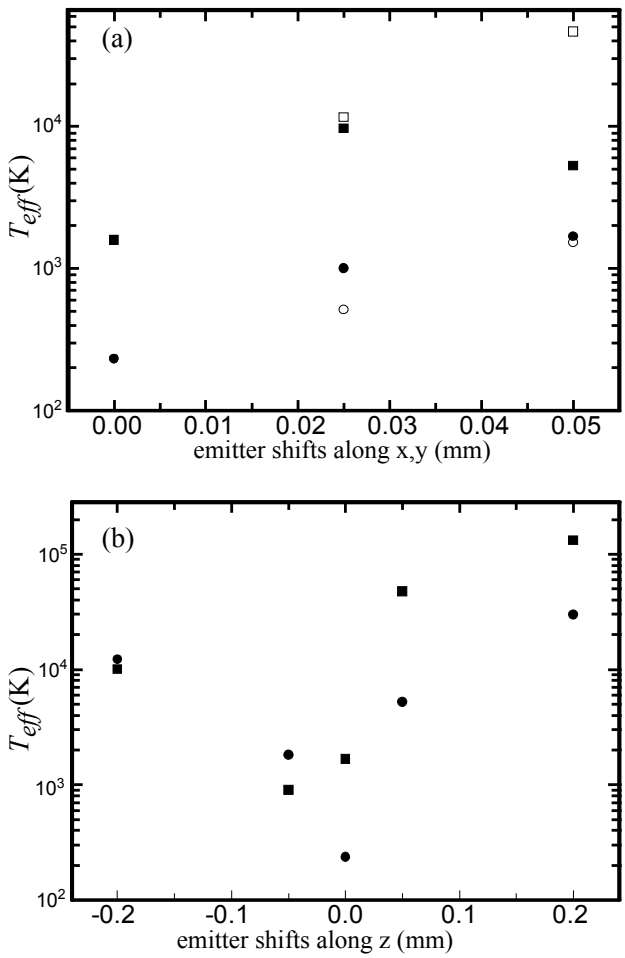

Figure 3: The effective beam temperature, T_{eff} is plotted as the emitter is shifted (a) in the transverse *x*-*y* plane and (b) in *z*. The circles indicate $T_{eff,x}$, while the squares indicate $T_{eff,y}$. In (a), the solid circles and squares represent shifts along *x*, while the open circles and squares represent shifts along *y*.

While the electrode length study establishes the insensitivity of the beam quality to geometry perturbations far from the beam, we must allow for machining tolerances in the cutting and alignment of parts close to the beam as well. Several cold-beam OMNITRAK simulations were performed with small shifts in the emitter stalk position, and results are shown in Fig. 3. The greatest sensitivity is observed with respect to transverse misalignments – precise emitter positioning within 0.02 mm is desirable to minimize beam temperature growth.

A hot thermionic emitter is often thermally isolated from the focus electrode by a vacuum gap. We vary the elliptical gap width by a single parameter, δ_g, which represents the difference between the semi-major/minor radii of the inner edge of the focus electrode and the semi-major/minor radii of the emitter, and show the results in Fig. 4.

As expected, for large values of the gap, the electrodes no longer impose the proper boundary conditions on the beam edge, and thus emittance growth is seen. We find that, a gap thickness greater than 0.05 – 0.1 mm would not be desirable.

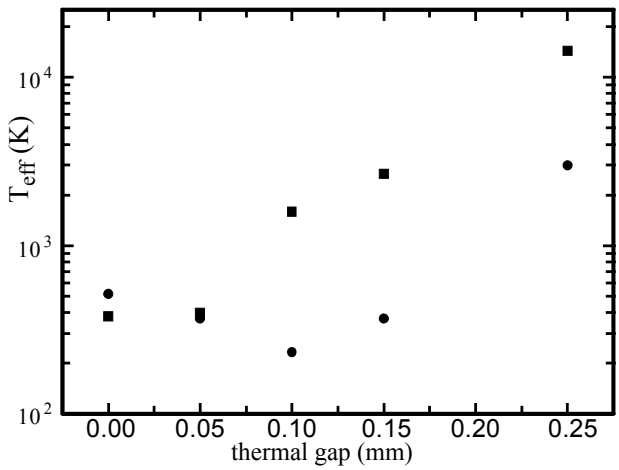

Figure 4: The effective beam temperature, T_{eff} is plotted as the vacuum gap thickness δ_g around the emitter is varied. The circles indicate $T_{eff,x}$, while the squares indicate $T_{eff,y}$.

CONCLUSION

The sensitivity of the electrode specification theory of Ref [1] to physical geometry and machining limitations such as finite extent, part misalignment, and tolerances for mechanical and thermal stresses is established. The greatest sensitivity is seen to transverse misalignments of the emitter stalk.

REFERENCES

[1] R. Bhatt and C. Chen, Phys. Rev. ST Accel. Beams 8, 104201 (2005).
[2] OMNITRAK software, copyright Field Precision, Albuquerque, NM.
[3] S. Humphries, S. Russell, B. Carlsten, and L. Earley, Phys. Rev. ST AB 7, 060401 (2004).
[4] B.E. Carlsten, Phys. Plasmas 9, 5088 (2002).
[5] G. Caryotakis, et al., AIP Conference Proceedings 691, 22 (2003).
[6] M.A. Basten and J.H. Booske, J. Appl. Phys. 85, 6313 (1999).
[7] R. Pakter and C. Chen, Phys. Rev. E 62, 2789 (2000).
[8] C. Chen. R. Pakter, and R.C. Davidson, Nucl. Inst. And Methods A 464, 518 (2001).
[9] C.D. Child, Phys. Rev. 32, 492 (1911); I. Langmuir, ibid. 21, 419 (1923).
[10] F. Zhou, et al., Phys. Rev. ST Accel Beams 5, 094203 (2003).

Three-Dimensional Theory and Simulation of Nonrelativistic Elliptic Electron and Ion Beam Generation

Ronak Bhatt, *Member, IEEE*, Thomas Bemis, *Member, IEEE*, and Chiping Chen

Invited Paper

***Abstract*—A three-dimensional theory of nonrelativistic, laminar, space-charge-limited, ellipse-shaped, charged-particle beam formation has been developed recently. Charged particles (electrons or ions) are accelerated across a diode by a static voltage differential and focused transversely by Pierce-type external electrodes placed along analytically specified surfaces. The theory is presented here along with design examples for a 6:1 elliptic electron beam diode and a 3:2 heavy ion beam diode. OMNITRAK simulations are performed to verify the theory and to explore beam tolerances with respect to perturbations of the diode geometry of the sort likely to be encountered in a realistic device: finite electrode extent, part misalignment, and allowances for thermal isolation.**

***Index Terms*—Beam injection, elliptic beams, particle beams, sheet beams.**

I. Introduction

CHARGED-PARTICLE beams of elongated elliptic cross sections have long generated great interest in vacuum electronics [1] because of their low space-charge energy and efficient coupling to radio frequency (RF) structures as compared to circular beams. It is well known that high space-charge reduces conversion efficiency in conventional microwave tubes employing circular beams. Presently, there are vigorous activities in the development of sheet-beam sources [2], [3], traveling wave amplifiers, klystrons [4], and focusing systems [5]–[7].

In high-intensity ion and electron accelerators, beams often exhibit nonlaminar flows, such as large-amplitude density fluctuations [8], mismatched envelope oscillations [9], emittance growth, and chaotic particle orbits. Many of these effects, which are caused by a beam mismatch or nonequilibrium behavior, lead to beam interception and make beam focusing and compression more difficult. Elliptic beams may allow simplified and more natural matching [10] between beam injectors and commonly used magnetic focusing lattices, reducing the emittance growth associated with beam mismatch.

Although elliptic beams present numerous advantages, their inherent three-dimensional (3-D) nature has made diode design a challenging process, both analytically and numerically. For the applications discussed above, desirable beam characteristics include uniform current density, parallel flow, and zero magnetic flux threading the emitter—properties consistent with one-dimensional (1-D) Child–Langmuir (C–L) [11], [29] flow, in which the electrostatic potential varies as $\Phi \propto z^{4/3}$, where z is the beam propagation distance. In general, however, such flows are difficult to produce [12]. Recent studies of two-dimensional (2-D) and 3-D [13]–[17] extensions of the C–L law in an infinite applied magnetic field have shown that the beam exhibits significant current density enhancements near the beam-vacuum boundary. In the absence of an infinite confining magnetic field, the beam will tend to spread in phase-space, resulting in a degradation of beam quality. As shown in [18], it is possible to induce the space-charge flow in a 3-D system to take the 1-D C–L flow form by calculating a 3-D equipotential geometry that is consistent with the 1-D C–L electric field within the beam and constructing external electrodes lying along the prescribed equipotentials that focus the beam. Such a beam can, in theory, exhibit extremely low emittance, laminar flow.

In order to clarify the treatment of the elliptic beam problem, we briefly discuss some important space-charge flow results in Section II. We then present the elliptic diode design methodology in Section III, followed by OMNITRAK [19] simulation results and tolerance studies in Section IV.

Manuscript received November 10, 2005; revised January 13, 2006. This work was supported in part by the U.S. Department of Energy, Office of High-Energy Physics under Grant DE-FG02-95ER40919, in part by the Office of Fusion Energy Science under Grant DE-FG02-01ER54662, in part by the Air Force Office of Scientific Research under Grant F49620-03-1-0230, and in part by the Massachusetts Institute of Technology Deshpande Center for Technological Innovation.

R. Bhatt and C. Chen are with the Plasma Science and Fusion Center, Massachusetts Institute of Technology, Cambridge, MA 02139 USA (e-mail: ronak@mit.edu; chenc@psfc.mit.edu).

T. Bemis is with Beam Power Technology, Inc., Boston, MA 02111 USA (e-mail: tombemis@beampower.com).

Digital Object Identifier 10.1109/TPS.2006.872162

II. Review of Space-Charge Flow Results

A. C–L Flow

Consider two infinite, parallel plates located at $z = 0$ and $z = d$ and held at fixed potentials $\Phi = 0$ and $\Phi = \Phi_d$, respectively. If the $z = 0$ plate is a charge emitter and the $z = d$ plate

a charge absorber, a 1-D, laminar, space-charge-limited flow solution of the nonrelativistic C–L [11], [29] form is established by applying the nonrelativistic cold fluid equations

$$\frac{\partial n}{\partial t} + \nabla \cdot (n\mathbf{V}) = 0 \tag{1}$$

$$\frac{\partial \mathbf{V}}{\partial t} + (\mathbf{V} \cdot \nabla)\mathbf{V} = -\left(\frac{q}{m}\right)\nabla\Phi \tag{2}$$

$$\nabla^2\Phi = -4\pi q n \tag{3}$$

where m represents the particle mass, q the particle charge, n the number density, and $\mathbf{V}$ the fluid velocity. By requiring a 1-D, steady-state solution, all quantities become functions of z alone. The continuity (1) implies constant current density J, while the equation of motion (2) yields conservation of energy. Combining these with Poisson's (3) yields a differential equation for the electric potential Φ

$$\frac{\partial^2\Phi}{\partial z^2} = -4\pi J\left(-\frac{2q\Phi}{m}\right)^{-\frac{1}{2}}. \tag{4}$$

Equation (4) is integrable, yielding potential $\Phi(z) = \Phi_d(z/d)^{4/3}$, fluid velocity $\mathbf{V}(z) = \hat{\mathbf{e}}_z(2q\Phi_d/m)^{1/2}(z/d)^{2/3}$, current density $J(z) = \sqrt{2}mc^3/(9\pi q d^2)(q\Phi_d/mc^2)^{3/2}$, and number density $n(z) = (\Phi_d/9\pi q d^2)(z/d)^{-2/3}$. While this is a powerful and simple solution for laminar flow, its infinite transverse extent makes it unphysical.

B. Pierce Sheet Beam Diode

Pierce [20] noted that, while such an infinitely wide flow is not realizable, a portion of such a flow is, provided one used "electrodes outside of the beam shaped so that they would fool the electrons in the beam into thinking that they were part of a larger ... flow." Mathematically, this is achieved by postulating a beam boundary and specifying boundary conditions there which are consistent with the C–L [11], [29] solution. Since the particles in the beam interior are influenced only by local fields, C–L boundary conditions on the beam edge are sufficient to enforce C–L flow in the beam interior.

For example, the infinite beam solution becomes a semi-infinite one if a beam boundary exists along the $x = 0$ plane. Along this boundary, according to the C–L solution, the electric potential and its derivative are both specified, giving a set of Cauchy boundary conditions

$$\Phi(x = 0) = \Phi_d\left(\frac{z}{d}\right)^{\frac{4}{3}} \tag{5}$$

$$\left(\frac{\partial\Phi}{\partial x}\right)\bigg|_{x=0} = 0. \tag{6}$$

In the vacuum region outside the beam, the potential satisfies Laplace's equation, $\nabla^2\Phi = 0$. While the *interior* beam problem is solved by C–L, Pierce's *exterior* problem requires solving Laplace's equation in the region outside the beam, subject to the boundary conditions (5) and (6) on the beam edge. Solutions to elliptic-equation Cauchy problems are usually difficult or impossible to obtain [21], and standard numerical methods fail due to the exponential growth of errors which is characteristic of such problems. Pierce [22], however, saw a solution by inspection, writing

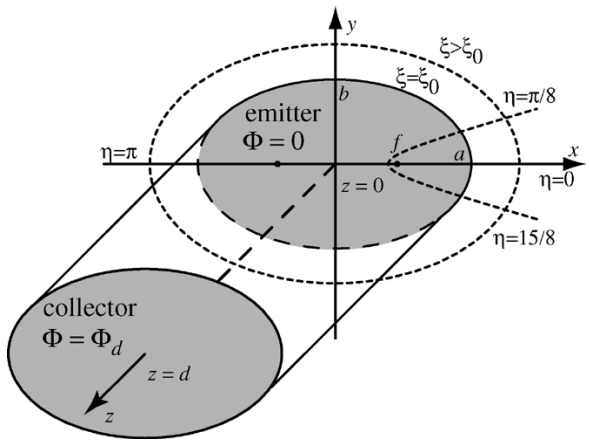

Fig. 1. Beam of elliptic cross section (semimajor axis a, semiminor axis b) is shown in Cartesian and elliptic cylindrical coordinates. Beam is emitted from an elliptic plate at $\Phi = 0$ in the $z = 0$ plane and collected by an elliptic plate at $\Phi = \Phi_d$ in the $z = d$ plane. Beam fills the area enclosed by the surface $\xi = \xi_0$. In any z plane, lines of constant ξ are ellipses, and lines of constant η are semihyperbolas.

$$\Phi(z, x) = \mathrm{Re}\left[(z + ix)^{\frac{4}{3}}\right] = r^{\frac{4}{3}}\cos\left(\frac{4\theta}{3}\right) \tag{7}$$

where $z = r\cos\theta$ and $x = r\sin\theta$. Equation (7) for the potential is valid in the region $x \geq 0$ outside the beam, and electrodes placed along equipotentials of (7) will enforce C–L flow on a semiinfinite charged particle stream. In particular, by examining the polar form, we can see that the $\Phi = 0$ "Pierce" electrode is a plane inclined at an angle $\theta_P = 3\pi/8$, with respect to the beam edge.

A similar operation can be performed to create another beam boundary (and corresponding set of electrodes) at some $x = x_b < 0$, which results in an infinitely wide sheet beam confined in the space $x_b < x < 0$. This 2-D sheet beam, however, is unbounded in y.

C. Radley Cylindrical Beam Diode

Radley [23] resolved the unboundedness problem by finding a solution for a circular beam of radius a. In cylindrical coordinates (ρ, θ), one can express the C–L boundary conditions for the circular beam as

$$\Phi|_{\rho=\mathrm{a}} = \Phi_d\left(\frac{z}{d}\right)^{\frac{4}{3}} \tag{8}$$

$$\frac{\partial\Phi}{\partial\rho}\bigg|_{\rho=\mathrm{a}} = 0 \tag{9}$$

for $r > a$. Note that $\partial\Phi/\partial\theta|_{\rho=\mathrm{a}} = 0$ is also a boundary condition, but it is implied by (8).

A simple solution of the Pierce planar form does not hold in the cylindrical geometry, since the analog between Laplace's equation and the Cauchy–Riemann conditions for analytic functions only exists in 2-D Cartesian coordinates. Radley's method [23] employs separation of variables and expression of the potential as a complex contour integral of a sum of Bessel func-

tions chosen to satisfy the boundary conditions at the beam edge. Rather than review this method in detail, we present the 3-D generalization to the elliptic geometry in the following section and note where reductions to Radley's form can be made.

III. Elliptic Diode Geometry

We consider a nonrelativistic charged-particle beam of length d and elliptic cross section with semimajor axis a and semiminor axis b, as shown in Fig. 1. The charged particles are emitted from a flat elliptic plate, held at potential $\Phi = 0$, in the $z = 0$ plane, and collected by another flat elliptic plate, held at potential $\Phi = \Phi_d$, in the $z = d$ plane.

It is useful to introduce the elliptic cylindrical coordinate system (ξ, η, z), i.e., $x = f\cosh(\xi)\cos(\eta)$, $y = f\sinh(\xi)\sin(\eta)$, where $0 \le \xi < \infty$ is a radial coordinate, $0 \le \eta < 2\pi$ is an angular coordinate, and $f = \sqrt{a^2 - b^2}$ is the distance from the center of the ellipse to either of its foci, as illustrated in Fig. 1. The elliptic beam boundary is specified by the surface $\xi = \xi_0 = \coth^{-1}(a/b)$.

The potential in the beam interior follows the C–L form [11], [29]. To determine the potential distribution in the beam exterior, we solve Laplace's equation while matching the interior and exterior electric fields on the elliptic beam boundary. From the C–L solution, the matching conditions on the elliptic beam boundary imply [18], for $0 \le z \le d$

$$\Phi|_{\xi=\xi_0} = \Phi_d \left(\frac{z}{d}\right)^{\frac{4}{3}} \tag{10}$$

$$\left.\frac{\partial \Phi}{\partial \xi}\right|_{\xi=\xi_0} = 0 \tag{11}$$

where the condition $\partial\Phi/\partial\eta|_{\xi=\xi_0} = 0$ is implied by (10).

We aim to find exterior equipotential surfaces corresponding to the emitter and collector potentials $\Phi = 0$ and $\Phi = \Phi_d$, respectively. If electrodes at the given potentials are made to lie along these surfaces, they will enforce the conditions in (10) and (11) on the interval $0 \le z \le d$.

In these coordinates, Laplace's equation may be expressed as

$$\frac{2}{f^2(\cosh 2\xi - \cos 2\eta)}\left(\frac{\partial^2\Phi}{\partial\eta^2} + \frac{\partial^2\Phi}{\partial\xi^2}\right) + \frac{\partial^2\Phi}{\partial z^2} = 0. \tag{12}$$

We can write a product solution of the form $\Phi(\xi, \eta, z) = \Xi(\xi)\Theta(\eta)\mathrm{Z}(z)$ and apply separation of variables to (12) to yield [18]

$$\frac{d^2\mathrm{Z}}{dz^2} - k^2\mathrm{Z} = 0 \tag{13}$$

$$\frac{d^2\Theta}{d\eta^2} + \left(\lambda - \frac{1}{2}k^2f^2\cos 2\eta\right)\Theta = 0 \tag{14}$$

$$\frac{d^2\Xi}{d\xi^2} - \left(\lambda - \frac{1}{2}k^2f^2\cosh 2\xi\right)\Xi = 0 \tag{15}$$

where k and λ are separation constants. Equation (13) leads simply to exponential solutions $Z = e^{kz}$. Equation (14) is the angular Mathieu equation, but we are only interested in those angular Mathieu functions which have a periodicity of 2π and are even about $\eta = 0$ and $\eta = \pi/2$, since the boundary conditions of (10) and (11) possess these same symmetries. Such solutions exist only for discrete eigenvalues of the separation constant λ, and we adopt the convention of Morse and Feshbach [24] to denote these angular Mathieu functions by $\Theta = Se_{2n}(kf, \eta)$ and the associated normalization constants $M^e_{2n} \equiv \int_0^{2\pi}[Se_{2n}(kf, u)]^2 du$, where n is a nonnegative integer indexing the eigenvalues λ, as detailed in [24]. The corresponding radial solutions, $\Xi = Je_{2n}(kf, \xi)$ and $\Xi = Ne_{2n}(kf, \xi)$ are radial Mathieu functions of the first and second kind, respectively. We note here that, in the Radley circular beam solution [23], the eigenfunctions are the exponentials and Bessel functions, since there is no angular dependence.

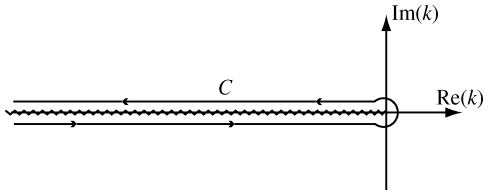

Fig. 2. Hankel contour in the complex k plane is taken around the $-\infty < k < 0$ branch cut.

Any superposition of product solutions of the separated equations must satisfy Laplace's (12), and hence we write [18]

$$\Phi(\xi, \eta, z) = \int_C dk A(k) e^{kz} G(kf, \xi, \eta) \tag{16}$$

where the transverse dependence is carried in

$$G(h, \xi, \eta) \equiv \sum_{n=0}^{\infty} \alpha_{2n}(h) Se_{2n}(h, \eta) \times [Je_{2n}(h, \xi) Ne'_{2n}(h, \xi_0) - Ne_{2n}(h, \xi) Je'_{2n}(h, \xi_0)] \tag{17}$$

we have chosen $\alpha_{2n}(h) \equiv [M^e_{2n}]^{-1} \int_0^{2\pi} Se_{2n}(h, u) du$, and the primes denote differentiation with respect to ξ. The integration contour C appearing in (16) is yet to be defined (see Fig. 2).

The expansion in (16) assures that Φ satisfies Laplace's (12), and it is readily seen that the particular linear combination of radial Mathieu functions in (17) satisfies the boundary condition in (11). Moreover, using the Wronskian for the radial Mathieu functions and the orthogonality of the angular Mathieu functions, it can be shown that our definition of α_{2n} assures $G(h, \eta, \xi_0) = 1$, which assures that $\partial\Phi/\partial\eta|_{\xi=\xi_0} = 0$. Note that in the Radley circular beam solution [23], a superposition of the form of (16) is still used, but G takes the simple form

$$G(k, \rho) = \frac{ka\pi}{2}[J_1(ka)N_0(kr) - N_1(ka)J_0(kr)]. \tag{18}$$

Boundary condition (10) now implies

$$\Phi_d \left(\frac{z}{d}\right)^{\frac{4}{3}} = \int_C A(k) e^{kz} dk. \tag{19}$$

To invert this, we make use of the integral representation of the Gamma function Γ [25] to obtain

$$z^{\frac{4}{3}} = \frac{1}{\Gamma\left(-\frac{4}{3}\right)} \frac{i}{2\sin\left(\frac{4\pi}{3}\right)} \int_C e^{kz} k^{-\frac{7}{3}} dk \tag{20}$$

where the Hankel contour C is taken around the branch cut defined by the line $-\infty < k < 0$, as shown in Fig. 2.

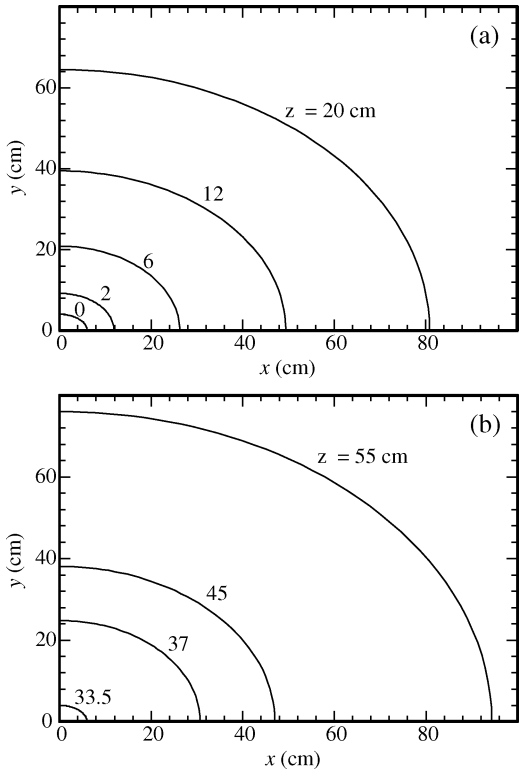

Fig. 3. Level curves (at various values of z) shown for equipotential surfaces (a) $\Phi = 0$ and (b) $\Phi = \Phi_d$ of a 3:2 space-charge-limited elliptical Na^+ diode with semimajor axis $a = 6$ cm, semiminor axis $b = 4$ cm, and diode gap $d = 33.5$ cm.

Equations (19) and (20) may be combined to yield

$$A(k) = \frac{\Phi_d d^{-\frac{4}{3}}}{\Gamma\left(-\frac{4}{3}\right)} \frac{i}{2\sin\left(\frac{4\pi}{3}\right)} k^{-\frac{7}{3}} \tag{21}$$

which completes the specification of the potential Φ in (16) with the Hankel contour of Fig. 2 used for integration.

Having derived an expression for the electric potential external to the beam (the *exterior* problem), we can proceed to compute equipotentials corresponding to $\Phi = 0$ and $\Phi = \Phi_d$ electrodes. The equipotentials were computed by applying a numeric root-finding scheme to the potential defined in (16). The Hankel contour integral is numerically evaluated employing standard techniques for the evaluation of the Mathieu functions [21], [26]. In Fig. 3, we depict the level curves of electrodes (a) $\Phi = 0$ and (b) $\Phi = \Phi_d$ for a 3:2 space-charge-limited elliptical Na^+ diode with semimajor axis $a = 6$ cm, semiminor axis $b = 4$ cm, diode gap $d = 33.5$ cm, diode voltage $\Phi_d = 1.0$ MV, and current density $J = 10$ mA/cm^2. Such a beam could find application in ion beam accelerators for high-energy density physics research.

In Fig. 4, we depict the level curves of electrodes (a) $\Phi = 0$ and (b) $\Phi = \Phi_d$ for a 6:1 space-charge-limited elliptical electron diode with semimajor axis $a = 3.73$ mm, semiminor axis $b = 0.62$ mm, diode gap $d = 4.11$ mm, diode voltage $\Phi_d = 2290$ V, and current density $J = 1.5$ A/cm^2. Such a beam may have applications in high-efficiency microwave tubes, however for high-power or high-frequency applications where greater current density is desired, further beam compression will be required.

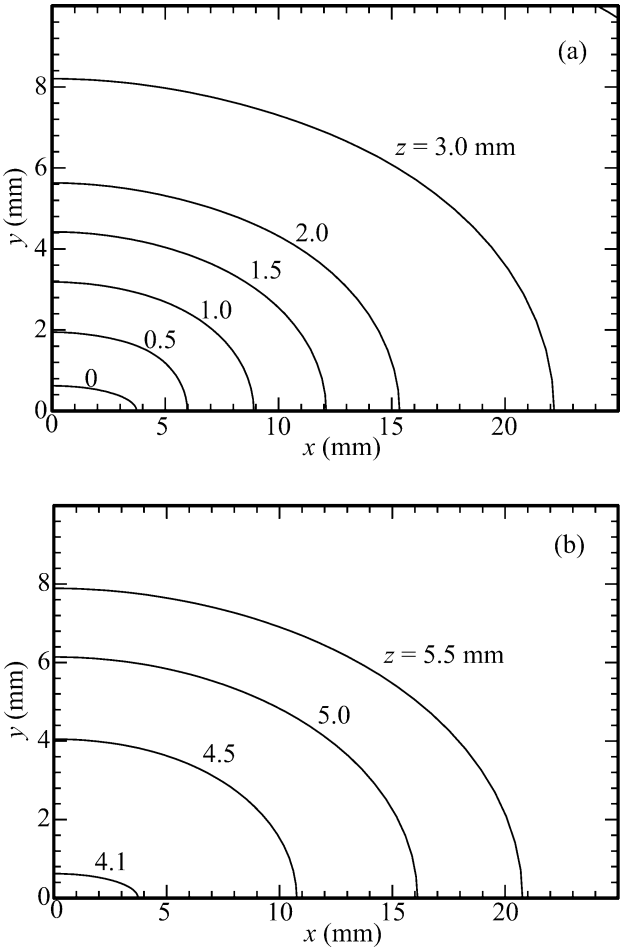

Fig. 4. Level curves (at various values of z) shown for equipotential surfaces (a) $\Phi = 0$ and (b) $\Phi = \Phi_d$ of a 6:1 space-charge-limited elliptical electron diode with semimajor axis $a = 3.73$ mm, semiminor axis $b = 0.62$ mm, and diode gap $d = 4.11$ mm.

IV. Simulation Results and Tolerance Studies

In order to verify the theory, the surfaces computed in Fig. 4 are used as electrode boundaries in a 3-D cold-beam space-charge-limited emission simulation using the commercially-available ray-tracing code OMNITRAK [19]. As shown in Fig. 5, the beam produced by the simulation is essentially a parallel, laminar, uniform density C–L flow.

Beam laminarity is often characterized by the root mean square (rms) beam emittances $\varepsilon_x \equiv \left(\langle x^2\rangle\langle x'^2\rangle - \langle xx'\rangle^2\right)^{1/2}$ and $\varepsilon_y \equiv \left(\langle y^2\rangle\langle y'^2\rangle - \langle yy'\rangle^2\right)^{1/2}$, where the averages of transverse particle position (x, y) and divergence $(x', y') \equiv (dx/dz, dy/dz)$ are taken over a slice of the beam at $z = d$. For a uniform density elliptic beam, these emittances can be related to effective beam temperatures [27] by the relations $\varepsilon_x = a(kT_{\mathrm{eff},x}/8q\Phi_d)^{1/2}$ and $\varepsilon_y = b(kT_{\mathrm{eff},y}/8q\Phi_d)^{1/2}$.

While thermal effects are not included in the simulations, we point out that in a physical system, the effective beam temperature cannot be reduced below the intrinsic temperature of the beam emitter—roughly 1500 K. The cold-beam effective temperature is an approximate measure of the beam temperature growth (beyond intrinsic) associated with nonideal diode optics. In simulations, however, the effective temperature will also

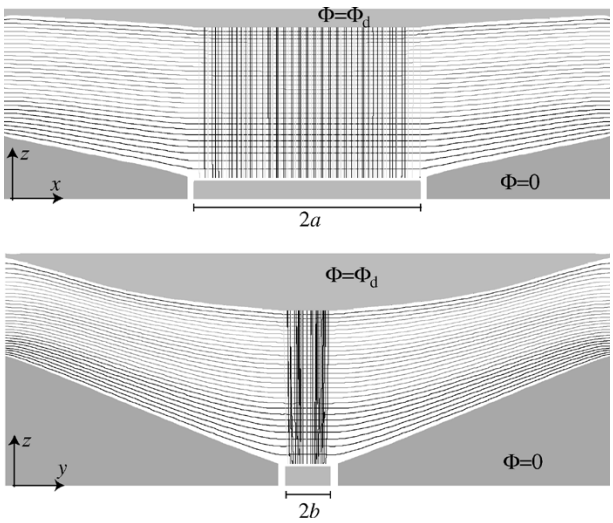

Fig. 5. Results of an OMNITRAK simulation for a 6:1 elliptic electron beam diode. Particle trajectories are projected to the $x-z$ and $y-z$ center planes of the beam. Beam has semimajor axis $a = 3.73$ mm, semiminor axis $b = 0.062$ mm, diode gap $d = 4.11$ mm, and diode voltage $\Phi_d = 2290$ V.

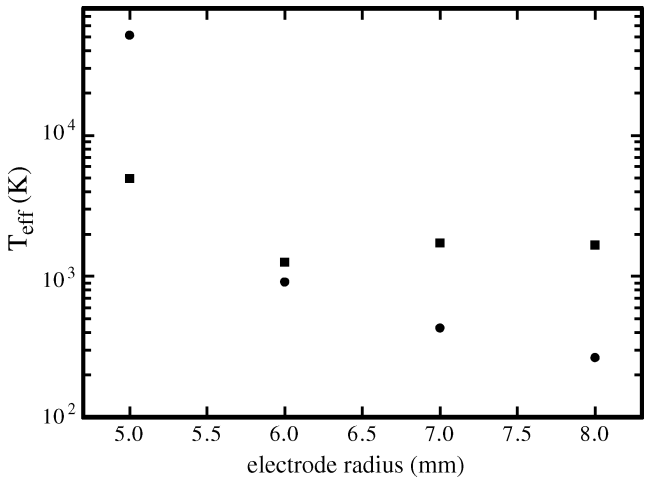

Fig. 6. Cold-beam effective temperature $T_{\rm eff}$ is plotted as the termination radius of the beam-focusing electrodes is varied. Circles indicate $T_{{\rm eff},x}$, while the squares indicate $T_{{\rm eff},y}$.

have a significant component generated by numerical noise. Indeed, computational memory limitations are a significant obstacle in using 3-D simulations to assess beam quality. Using the example parameters of Fig. 3, the cold-beam OMNITRAK simulation in Fig. 5 has several million computational nodes and several thousand particles, however resolution is still insufficient, particularly along the beam edge in the shorter (y) direction. Therefore, the resulting cold-beam effective beam temperatures, $T_{{\rm eff},x} = 280$ K and $T_{{\rm eff},y} = 1700$ K, should be regarded as an upper bound on the achievable cold-beam effective temperatures for the given diode geometry. As higher resolution simulations are performed with more particles, we expect the particle noise and field interpolation errors to be reduced, and the cold-beam effective temperatures should reduce accordingly. Once these cold-beam effective temperatures are reduced much below the intrinsic thermal limit (1500 K), further reduction is not physically significant.

Note that we choose to use the effective beam temperature (rather than emittance) as a measure of beam quality in our discussion because it allows for a uniform comparison with the intrinsic limit imposed by the hot emitter across a wide range of beam parameters. The intrinsic (emitter-temperature-limited) emittance, on the other hand, is a function both of emitter size and diode voltage, and thus not as useful for comparisons between simulations of different beams.

Whether a diode can approach the intrinsic limit depends on its geometric design, as well as its tolerance to perturbations and limitations of the sort likely to be encountered in a realistic device: finite extent, part misalignment, and allowances for thermal isolation. For example, the theory of [18] computes equipotentials extending infinitely far from the beam. In practice, electrodes lying along these equipotentials will have a finite length, and it is important to assess the impact of the edge effects thus admitted on the beam. Since the potential satisfies Laplace's equation in the free-space region outside the beam, we expect that electrostatic potential variations caused by localized perturbations of the electrode geometry will be exponentially decaying with distance from the perturbation point. We test this hypothesis by performing several cold-beam OMNITRAK simulations for the 6:1 electron diode example where the radial extent of the electrodes is varied and the Neumann boundaries at the edge of the simulation region are kept fixed. The cold-beam effective temperatures at the anode are shown as a function of electrode radius in Fig. 6. While the simulation noise in the y direction obscures the result somewhat, we can regard the measured cold-beam effective temperatures as upper bounds and see from the general trend that the beam temperatures do not significantly exceed intrinsic thermal levels unless the focusing electrodes are curtailed below a 6-mm radius.

While the electrode length study establishes the insensitivity of the beam quality to geometry perturbations far from the beam, we must allow for machining tolerances in the cutting and alignment of parts close to the beam as well. Several cold-beam OMNITRAK simulations were performed with small shifts in the emitter stalk position, and results are shown in Fig. 7. Particular sensitivity is observed with respect to transverse misalignments in Fig. 7(a), however we believe that this effect is largely a numerical artifact resulting from the broken symmetry between the computation grid and model geometry when subject to transverse perturbations. Higher resolution simulations are required here to reduce the noise component of the effective temperature. Nonetheless, for many space-charge-dominated beam applications (such as the present example of a microwave tube beam), an effective beam temperature even several times the intrinsic limit (corresponding to transverse emitter shifts of 0.02 mm) can still be assured to yield a high-quality beam.

The effective temperature is much less sensitive to symmetry-preserving longitudinal emitter shifts in the negative z direction, as seen in Fig. 7(b). The positive z shifts lead to a greater effective temperature, largely because of enhanced edge emission. A slight depression of the emitter to a position near $z \cong -0.025 \pm 0.025$ mm ensures effective temperatures near the intrinsic limit.

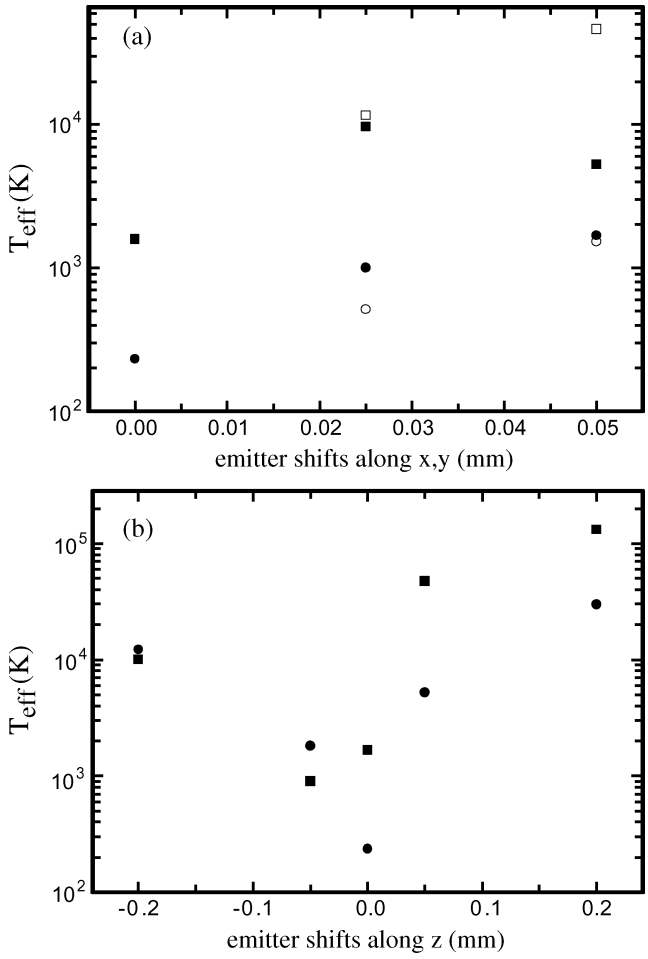

Fig. 7. Cold-beam effective temperature, $T_{\rm eff}$ is plotted as the emitter is shifted (a) in the transverse $x-y$ plane and (b) in z. Circles indicate $T_{{\rm eff},x}$, while the squares indicate $T_{{\rm eff},y}$. In (a), the solid circles and squares represent shifts along x, while the open circles and squares represent shifts along y.

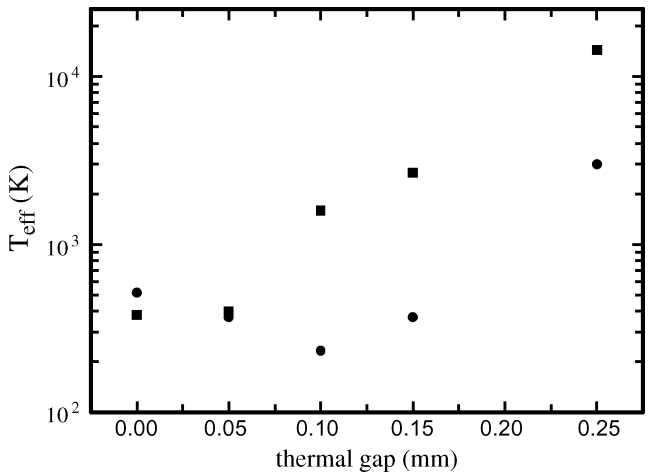

Fig. 8. Cold-beam effective temperature, $T_{\rm eff}$ is plotted as the vacuum gap thickness δ_g around the emitter is varied. Circles indicate $T_{{\rm eff},x}$, while the squares indicate $T_{{\rm eff},y}$.

A hot thermionic emitter is often thermally isolated from the focus electrode by a vacuum gap. We vary the elliptical gap width by a single parameter δ_g which represents the difference between the semimajor/minor radii of the inner edge of the focus electrode and the semimajor/minor radii of the emitter, and show the results in Fig. 8. As expected, for large values of the gap, the electrodes no longer impose the proper boundary conditions on the beam edge, and thus temperature growth is seen. We find that, a gap thickness greater than 0.05–0.1 mm would not be desirable.

V. Conclusion

A theory of nonrelativistic, laminar, elliptic beam formation has been developed. The theory provides an analytic prescription for electrode geometries which support high-quality elliptic beam formation for use in vacuum electron devices and particle accelerators. 3-D simulations have been performed which support the theory, however higher-resolution simulations are needed in order to assess its ultra low-emittance predictions.

The sensitivity of the electrode specification theory to physical geometry and machining limitations such as finite extent, part misalignment, and allowances for mechanical and thermal stresses is studied, and a tolerance range is established for low-emittance, low effective-temperature beam generation.

References

[1] P. A. Sturrock, "Magnetic deflection focusing," *J. Electron. Control*, vol. 7, pp. 162–168, Aug. 1959.

[2] S. J. Russell *et al.*, "First observation of elliptical sheet beam formation with an asymmetric solenoid lens," *Phys. Rev. ST Accel. Beams*, vol. 8, p. 080401, Aug. 2005.

[3] S. Humphries *et al.*, "Circular-to-planar transformations of high-perveance electron beams by asymmetric solenoid lenses," *Phys. Rev. ST Accel. Beams*, vol. 7, p. 060401, Jun. 2004.

[4] G. Caryotakis *et al.*, "Design of an 11.4 GHz, 150-MW, sheet beam, PPM-focused klystron," in *AIP Conf. Proc.*, vol. 691, Dec. 2003, pp. 22–33.

[5] B. E. Carlsten *et al.*, "Stable two-plane focusing for emittance-dominated sheet-beam transport," *Phys. Rev. ST Accel. Beams*, vol. 8, p. 062002, Jun. 2005.

[6] M. A. Basten and J. H. Booske, "Two-plane focusing of high-space-charge sheet electron beams using periodically cusped magnetic fields," *J. Appl. Phys.*, vol. 85, pp. 6313–6322, May 1999.

[7] R. Pakter and C. Chen, "Cold-fluid equilibrium for a corkscrewing elliptic beam in a variably focusing channel," *Phys. Rev. E, Stat. Phys. Plasmas Fluids Relat. Interdiscip. Top.*, vol. 62, pp. 2789–2796, August 2000.

[8] S. Bernal *et al.*, "Beam experiments in the extreme space-charge limit on the University of Maryland electron ring," *Phys. Plasmas*, vol. 11, pp. 2907–2915, May 2004.

[9] T. P. Wangler *et al.*, "Beam-halo in mismatched proton beams," *Nucl. Instrum. Methods A*, vol. 519, pp. 425–431, Feb. 2004.

[10] C. Chen, R. Pakter, and R. C. Davidson, "Ideal matching of heavy ion beams," *Nucl. Instrum. Methods A*, vol. 464, pp. 518–523, May 2001.

[11] C. D. Child, "Discharge from hot cao," *Phys. Rev.*, vol. 32, pp. 492–511, May 1911.

[12] P. Kirstein, G. Kino, and W. Waters, *Space Charge Flow*. New York: McGraw-Hill, 1967, p. 331.

[13] J. W. Luginsland, Y. Y. Lau, R. J. Umstattd, and J. J. Watrous, "Beyond the Child-Langmuir law: a review of recent results on multidimensional space-charge-limited flow," *Phys. Plasmas*, vol. 9, pp. 2371–2376, May 2002.

[14] J. J. Watrous, J. W. Luginsland, and M. Frese, "Current and current density of a finite-width, space-charge-limited electron beam in two-dimensional, parallel-plate geometry," *Phys. Plasmas*, vol. 8, pp. 4202–4210, Sep. 2001.

[15] J. W. Luginsland, Y. Y. Lau, and R. M. Gilgenbach, "Two-dimensional Child-Langmuir law," *Phys. Rev. Lett.*, vol. 77, pp. 4668–4670, Nov. 1996.

[16] R. J. Umstattd and J. W. Luginsland, "Two-dimensional space-charge-limited emission: Beam-edge characteristics and applications," *Phys. Rev. Lett.*, vol. 87, p. 145002, Oct. 2001.

[17] Y. Y. Lau, "Simple theory for the two-dimensional Child-Langmuir law," *Phys. Rev. Lett.*, vol. 87, p. 278301, Dec. 2001.
[18] R. Bhatt and C. Chen, "Theory and simulation of nonrelativistic elliptic-beam formation with one-dimensional Child-Langmuir flow characteristics," *Phys. Rev. ST Accel. Beams 8*, p. 014201, Jan. 2005.
[19] OMNITRAK Software, Copyright Field Precision, Albuquerque, NM. [Online]. Available: http://www.fieldp.com
[20] (1991) SMEEC Vintage Electrics. [Online]. Available: http://www.smecc.org/john_r__pierce____electron_tubes.htm
[21] P. Morse and H. Feshbach, *Methods of Theoretical Physics*. New York: McGraw-Hill, 1953, vol. 1, ch. 6, p. 702.
[22] J. R. Pierce, *Theory and Design of Electron Beams*, 2nd ed. Princeton, NJ: D. Van Nostrand, 1954.
[23] D. E. Radley, "Theory of the Pierce type electron gun," *J. Electron. Control*, vol. 4, p. 125, 1957.
[24] P. Morse and H. Feshbach, *Methods of Theoretical Physics*, 1953, vol. 2, ch. 11, p. 1568.
[25] P. Morse and H. Feshbach, *Methods of Theoretical Physics*, 1953, vol. 1, ch. 4, p. 421.
[26] J. C. Gutierrez-Vega *et al.*. Theory and numerical analysis of the Mathieu functions. [Online]. Available: http://homepages.mty.itesm.mx/jgutierr/mathieu.htm
[27] J. D. Lawson, *Physics of Charged Particle Beams*. Oxford, U.K.: Clarendon, 1988, p. 210.
[28] F. Zhou *et al.*, "Experimental characterization of emittance growth induced by the nonuniform transverse laser distribution in a photoinjector," *Phys. Rev. ST Accel Beams*, vol. 5, p. 094203, Sep. 2002.
[29] I. Langmuir, "Effect of space charge and initial velocities on the potential distribution and thermionic current between parallel plane electrodes," *Phys. Rev.*, vol. 21, pp. 419–435, Apr. 1923.

Ronak Bhatt (M'05) received the B.S. degree (with honors) in physics from the California Institute of Technology, Pasadena, in 1998. He is currently working toward the Ph.D. degree in physics at the Massachusetts Institute of Technology, Cambridge.

He is a Graduate Research Assistant in Intense Beam Theoretical Research Group of Plasma Science and Fusion Center, Massachusetts Institute of Technology, where his work focuses on laminar space-charge flow solutions for intense beams in novel geometries.

Mr. Bhatt won the Outstanding Student Paper at the 2005 Particle Accelerator Conference, Knoxville, TN.

Thomas Bemis (M'95) received the B.S. degree in physics and the M.S. degree in electrical engineering from the University of Illinois, Urbana, in 1976 and 1977, respectively, and the M.S. degree in applied physics from the California Institute of Technology, Pasadena, in 1977.

He is the author or coauthor of 23 papers and is the co-holder of two patents. He has worked in the microwave tube industry for 15 years and in defense electronics for 11 years. He is proficient in seven different finite element analysis codes and is presently a Senior Engineer with Beam Power Technology, Inc., Boston, MA.

Chiping Chen received the B.S. degree in physics from Peking University, Beijing, China, in 1982 and the M.S. and Ph.D. degrees in physics from Stevens Institute of Technology, Hoboken, NJ, in 1985 and 1987, respectively.

He is a Principal Research Scientist and Leader of Intense Beam Theoretical Research Group of Plasma Science and Fusion Center, Massachusetts Institute of Technology, Cambridge. His research interests include charged-particle accelerators and beams, plasma physics, coherent radiation generation, nonlinear dynamics and chaos, and optics. He is the author or coauthor of over 120 papers and holds three patents.

Cold-fluid theory of equilibrium and stability of a high-intensity periodically twisted ellipse-shaped charged-particle beam

Jing Zhou, Ronak Bhatt, and Chiping Chen

Plasma Science and Fusion Center, Massachusetts Institute of Technology, Cambridge, Massachusetts 02139, USA

(Received 14 January 2005; published 3 March 2006)

It is shown that there exists an exact paraxial cold-fluid equilibrium of a high-intensity, space-charge-dominated charged-particle beam with a periodically twisted elliptic cross section in a nonaxisymmetric periodic magnetic field. Generalized envelope equations, which determine the beam envelopes, ellipse orientation, density, and internal flow velocity profiles, are derived. Nonrelativistic and relativistic examples of such beam equilibria are presented. The equilibrium and stability of such beams are demonstrated by self-consistent particle-in-cell (PIC) simulations.

DOI: 10.1103/PhysRevSTAB.9.034401 PACS numbers: 41.75.−i, 41.85.Ja, 41.85.Lc, 52.59.Sa

I. INTRODUCTION

High-intensity ribbon (thin sheet) beams are of great interest for applications in particle accelerators, such as storage rings and rf and induction linacs, as well as vacuum electron devices, such as klystrons and traveling-wave tubes with periodic permanent magnet (PPM) focusing. They have the following remarkable properties. First, they can transport large amounts of beam currents at reduced intrinsic space-charge forces and energies. Second, they couple efficiently to rectangular rf structures. The combination of the space-charge reduction and efficient coupling allows efficient rf generation in vacuum electronic devices, and efficient acceleration in particle accelerators. Third, elliptic beams provide an additional adjustable parameter (e.g., the aspect ratio) which may be useful for better matching a beam into a periodic focusing channel.

Although ribbon beams have been discussed in the literature for four decades, the equilibrium of a high-intensity, space-charge-dominated beam with a large-aspect-ratio elliptic cross section has not been discovered until this paper. Sturrock [1] first suggested the use of a periodic magnetic focusing consisting of an array of planar-wiggler magnets for rectilinear beams. Zhang *et al.* [2] had some modest success in the experimental demonstration of the transport of a low-intensity (10 A, 500 kV) sheet beam in a planar-wiggler magnetic field, and observed considerable beam loss. Researchers made use of the multiple-time-scale analysis and the paraxial approximations to obtain the smooth-beam approximation of high-intensity ribbon-beam equilibria [3–6]. In the smooth-beam approximation, the effects of the planar-wiggler field [1,2], or the periodic cusp magnetic (PCM) field [3,4], or the hybrid of PCM and periodic quadrupole magnet (PQM) fields [5,6], or the offset pole PCM field [6] are treated as some averaged focusing constants in the transverse directions. While the smooth-beam approximation yields simple results, the multiple-time-scale analysis requires time averaging, losing the detailed information about the beam dynamics. As a result, it does not provide adequate information about how to generate high-intensity ribbon beams in practice.

A widely used tool for the determination of evolution of the charged-particle beam systems is based on the rms beam description. The construction of self-consistent beam distributions with linear focusing forces is discussed in Refs. [7,8], such as Kapchinskij-Vladmirskij equilibrium [7–10] in an alternating-gradient quadrupole magnetic focusing field and the periodically focused rigid-rotor Vlasov equilibrium [11,12] in a periodic solenoid magnetic focusing field. For ultrahigh-brightness beams with negligibly small emittance, a cold-fluid theory can be used to examine the detailed information about the beam dynamics, especially the evolution of the density and flow velocity profiles [13–15], such as the cold-fluid corkscrewing equilibrium [13,14] in a linear focusing channel consisting of solenoidal and quadrupole magnetic focusing fields.

In this paper, we present the cold-fluid equilibrium theory of an ultrahigh-brightness, space-charge–dominated, large–aspect-ratio beam propagating through a nonaxisymmetric periodic magnetic focusing field. Our beam distribution satisfies the assumptions for the distribution functions described generally in Refs. [7,8]. A paraxial cold-fluid model is employed to derive generalized envelope equations which determine the equilibrium flow properties of ellipse-shaped beams with negligibly small emittance. A matched envelope solution is obtained numerically from the generalized envelope equations, and the results show that the beam edges in both transverse directions are well confined, and that the angle of the beam ellipse exhibits a periodic small-amplitude twist. Two-dimensional (2D) particle-in-cell (PIC) simulations with our Periodic Focused Beam 2D (PFB2D) code show good agreement with the predictions of equilibrium theory as well as beam stability.

The organization of the present paper is as follows. In Sec. II, the cold-fluid equilibrium theory of a periodically twisted ellipse-shaped charged-particle beam is presented

and the generalized envelope equations are derived. In Sec. III, the generalized envelope equations are solved numerically for several examples of periodically twisted ellipse-shaped charged-particle beams. In Sec. IV, PIC simulations are used to verify the theoretical results. Conclusions are presented in Sec. V.

II. COLD-FLUID EQUILIBRIUM THEORY

We consider a high-intensity, space-charge–dominated beam, in which kinetic (emittance) effects are negligibly small. The beam can be adequately described by cold-fluid equations. In the paraxial approximation, the steady-state cold-fluid equations for time-stationary flow ($\partial/\partial t = 0$) in cgs units are [13,14]

$$\beta_b c \frac{\partial}{\partial s} n_b + \nabla_\perp \cdot (n_b \mathbf{V}_\perp) = 0, \tag{1}$$

$$\nabla_\perp^2 \phi^s = \beta_b^{-1} \nabla_\perp^2 A_z^s = -4\pi q n_b, \tag{2}$$

$$n_b \left(\beta_b c \frac{\partial}{\partial s} + \mathbf{V}_\perp \cdot \nabla_\perp \right) \mathbf{V}_\perp = \frac{q n_b}{\gamma_b m} \left[-\frac{1}{\gamma_b^2} \nabla_\perp \phi^s + \beta_b \hat{\mathbf{e}}_z \times \mathbf{B}_\perp^{\text{ext}} + \frac{\mathbf{V}_\perp}{c} \times B_z^{\text{ext}}(s) \hat{\mathbf{e}}_z \right], \tag{3}$$

where $s = z$, $\mathbf{x}_\perp = x\hat{\mathbf{e}}_x + y\hat{\mathbf{e}}_y$, $\nabla_\perp = \partial/\partial \mathbf{x}_\perp$, q and m are the particle charge and rest mass, respectively, n_b is the particle density, $\mathbf{V}_\perp$ is the transverse flow velocity, $\gamma_b = (1 - \beta_b^2)^{-1/2}$ is the relativistic mass factor, use has been made of $\beta_z = V_z/c \cong \beta_b = \text{const}$, c is the speed of light in vacuum and the self-electric field $\mathbf{E}^s$ and self-magnetic field $\mathbf{B}^s$ are determined from the scalar potential ϕ^s and vector potential $A_z^s \hat{\mathbf{e}}_z$, i.e., $\mathbf{E}^s = -\nabla_\perp \phi^s$ and $\mathbf{B}^s = \nabla_\perp \times A_z^s \hat{\mathbf{e}}_z$.

For the beam dimensions small relative to the characteristic scale of magnetic variations, i.e., $(k_{0x}x)^2/6 \ll 1$ and $(k_{0y}y)^2/6 \ll 1$, a three-dimensional (3D) nonaxisymmetric periodic magnetic field can be described to the lowest order in the transverse dimension as

$$\mathbf{B}^{\text{ext}}(\mathbf{x}) \approx B_0 \left[\frac{k_{0x}^2}{k_0} \cos(k_0 s) x \hat{\mathbf{e}}_x + \frac{k_{0y}^2}{k_0} \cos(k_0 s) y \hat{\mathbf{e}}_y - \sin(k_0 s) \hat{\mathbf{e}}_z \right], \tag{4}$$

where $k_0 = 2\pi/S$, $k_{0x}^2 + k_{0y}^2 = k_0^2$, and S is the axial periodicity length. The 3D magnetic field in Eq. (4) is fully specified by the three parameters B_0, S, and k_{0x}/k_{0y}.

We seek solutions to Eqs. (1)–(3) of the form

$$n_b(\mathbf{x}_\perp, s) = \frac{N_b}{\pi a(s) b(s)} \Theta \left[1 - \frac{\tilde{x}^2}{a^2(s)} - \frac{\tilde{y}^2}{b^2(s)} \right], \tag{5}$$

$$\mathbf{V}_\perp(\mathbf{x}_\perp, s) = [\mu_x(s)\tilde{x} - \alpha_x(s)\tilde{y}] \beta_b c \hat{\mathbf{e}}_{\tilde{x}} + [\mu_y(s)\tilde{y} + \alpha_y(s)\tilde{x}] \beta_b c \hat{\mathbf{e}}_{\tilde{y}}. \tag{6}$$

In Eqs. (5) and (6), $\mathbf{x}_\perp = \tilde{x}\hat{\mathbf{e}}_{\tilde{x}} + \tilde{y}\hat{\mathbf{e}}_{\tilde{y}}$ is a transverse displacement in the twisted coordinate system illustrated in Fig. 1; $\theta(s)$ is the twist angle of the ellipse; $\Theta(x) = 1$ if $x > 0$ and $\Theta(x) = 0$ if $x < 0$; and the functions $a(s)$, $b(s)$, $\mu_x(s)$, $\mu_y(s)$, $\alpha_x(s)$, $\alpha_y(s)$, and $\theta(s)$ are to be determined self-consistently [see Eqs. (8)–(12)].

The self-electric and self-magnetic fields are well known for an elliptical beam with density distribution specified in Eq. (5), i.e.,

$$\phi^s = \beta_b^{-1} A_z^s = -\frac{2qN_b}{a+b} \left(\frac{\tilde{x}^2}{a} + \frac{\tilde{y}^2}{b} \right). \tag{7}$$

Using the expressions in Eqs. (4)–(7), it can be shown that both the equilibrium continuity equation (1) and force equation (3) are satisfied if the dynamical variables $a(s)$, $b(s)$, $\mu_x(s) \equiv a^{-1}da/ds$, $\mu_y(s) \equiv b^{-1}db/ds$, $\alpha_x(s)$, $\alpha_y(s)$ and $\theta(s)$ obey the generalized beam envelope equations (see appendix)

$$\frac{d^2 a}{ds^2} - \left[\frac{b^2(\alpha_x^2 - 2\alpha_x\alpha_y) + a^2\alpha_y^2}{a^2 - b^2} + \sqrt{\kappa_{z0}} \frac{k_{0x}^2 - k_{0y}^2}{k_0} \cos(k_0 s) \sin(2\theta) - 2\sqrt{\kappa_{z0}} \alpha_y \sin(k_0 s) \right] a - \frac{2K}{a+b} = 0, \tag{8}$$

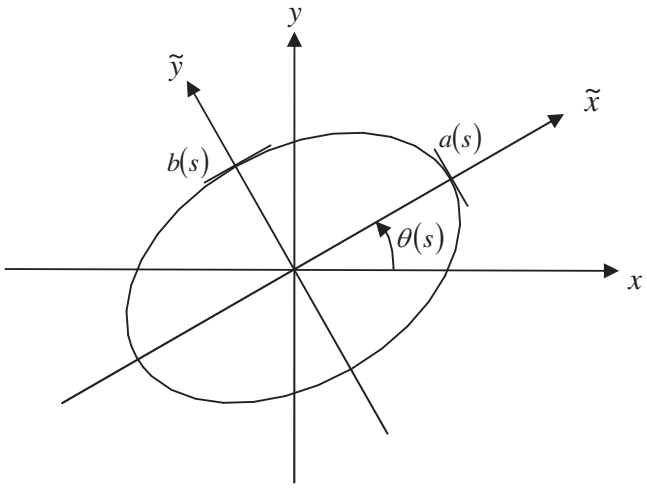

FIG. 1. Laboratory and twisted coordinate systems.

$$\frac{d^2b}{ds^2} + \left[\frac{a^2(\alpha_y^2 - 2\alpha_x\alpha_y) + b^2\alpha_x^2}{a^2 - b^2} + \sqrt{\kappa_{z0}}\frac{k_{0x}^2 - k_{0y}^2}{k_0}\cos(k_0 s)\sin(2\theta) + 2\sqrt{\kappa_{z0}}\alpha_x \sin(k_0 s)\right]b - \frac{2K}{a+b} = 0, \quad (9)$$

$$\frac{d}{ds}(a^2\alpha_y) - \frac{ab^3(\alpha_x - \alpha_y)}{a^2 - b^2}\frac{d}{ds}\left(\frac{a}{b}\right) - 2\sqrt{\kappa_{z0}}\cos(k_0 s)\frac{k_{0x}^2\cos^2\theta + k_{0y}^2\sin^2\theta}{k_0}a^2 - 2\sqrt{\kappa_{z0}}a\frac{da}{ds}\sin(k_0 s) = 0, \quad (10)$$

$$\frac{d}{ds}(b^2\alpha_x) - \frac{a^3b(\alpha_x - \alpha_y)}{a^2 - b^2}\frac{d}{ds}\left(\frac{b}{a}\right) - 2\sqrt{\kappa_{z0}}\cos(k_0 s)\frac{k_{0x}^2\sin^2\theta + k_{0y}^2\cos^2\theta}{k_0}b^2 - 2\sqrt{\kappa_{z0}}b\frac{db}{ds}\sin(k_0 s) = 0, \quad (11)$$

$$\frac{d\theta}{ds} = \frac{a^2\alpha_y - b^2\alpha_x}{a^2 - b^2}, \quad (12)$$

where

$$\sqrt{\kappa_{z0}} \equiv \frac{qB_0}{2\gamma_b\beta_b mc^2} \quad \text{and} \quad K \equiv \frac{2q^2N_b}{\gamma_b^3\beta_b^3 mc^2}.$$

Equations (8)–(12) have "time" reversal symmetry under the transformation $(s, a, b, a', b', \alpha_x, \alpha_y, \theta) \rightarrow (-s, a, b, -a', -b', -\alpha_x, -\alpha_y, \theta)$. This implies that the dynamical system described by Eqs. (8)–(12) has the hypersymmetry plane $(a', b', \alpha_x, \alpha_y)$.

III. EXAMPLES OF PERIODICALLY TWISTED ELLIPSE-SHAPED CHARGED-PARTICLE BEAMS

A numerical module in the PFB2D code has been developed to solve the generalized envelope equations (8)–(12). There are, in total, seven functions $a(s)$, $b(s)$, $a'(s)$, $b'(s)$, $\alpha_x(s)$, $\alpha_x(s)$, and $\theta(s)$ to be determined. The time reversal symmetry of the dynamical system requires the quantities $(a', b', \alpha_x, \alpha_y)$ vanish at $s = 0$ for matched solutions, therefore, only the three initial values $a(0)$, $b(0)$, and $\theta(0)$ corresponding to a matched solution need to be determined with Newton's method.

As an example, we consider a relativistic elliptic beam with $V_b = 198.5$ keV, current $I_b = 85.5$ A, aspect ratio $a/b = 5$, and nonaxisymmetric periodic permanent magnet focusing with $B_0 = 2.4$ kG, $S = 2.2$ cm, and $k_{0y}/k_{0x} = 1.52$ (see Table I, Col. 4). [We propose to use it in a 10 MW L-Band ribbon-beam klystron for the International Linear Collider.] For such a system the matched solution of the generalized envelope equations (8)–(12) is calculated numerically as shown in Figs. 2(a)–2(c) (solid curves) with the corresponding parameters: $k_{0x} = 1.57$ cm^{-1}, $k_{0y} = 2.39$ cm^{-1}, $\sqrt{\kappa_{z0}} = 0.732$ cm^{-1}, and $K = 1.13 \times 10^{-2}$. The solution to the generalized envelope equations (8)–(12), displayed as solid and dashed curves in Fig. 2, shows that the semiaxes of the elliptical beam remain roughly constant with small oscillations, that the orientation of the ellipse twists periodically with an amplitude of 8.8 degrees, and that the normalized rotation flow velocities α_x and α_y oscillate with the magnet periodicity. It is worthwhile pointing out that the normalized velocities μ_x, μ_y, α_x, and α_y vanish at $s = 0$ which makes it a natural matching point for a parallel-flow beam with negligibly small emittance [16].

These high-intensity twisted elliptic-beam equilibria exist over a wide region of parameters ranging from the nonrelativistic to relativistic regimes. In addition to the relativistic elliptic-beam equilibrium discussed above, we present a nonrelativistic elliptic-beam equilibrium and a mildly relativistic elliptic-beam equilibrium in Table I. The

TABLE I. System parameters for elliptic-beam examples.

Parameter Application	Nonrelativistic Wireless communication	Mildly relativistic Missile defense	Fully relativistic International Linear Collider
Frequency (GHz)	1.95	2.8	1.3
rf Power (kW)	0.2 (cw)	500 (pulsed)	10 000 (pulsed)
Current (A)	0.11	18.5	85.5
Voltage (kV)	2.29	45.0	198.5
S (cm)	1.912	2.626	2.2
k_{0x}/k_{0y}	1.60	1.44	1.52
B_0 (kG)	0.337	1.099	2.40
a/b	6.0	4.0	5.0
a (cm)	0.373	0.585	0.425
$\theta_{\max}$ (deg)	10.4	11.5	8.8

nonrelativistic elliptic beam corresponds to a beam design for a high-efficiency 200 W ribbon-beam amplifier (RBA) which is being developed at Massachusetts Institute of Technology (MIT) for communication, whereas the mildly relativistic elliptic beam is proposed for a high-power, high-efficiency RBA for radar applications.

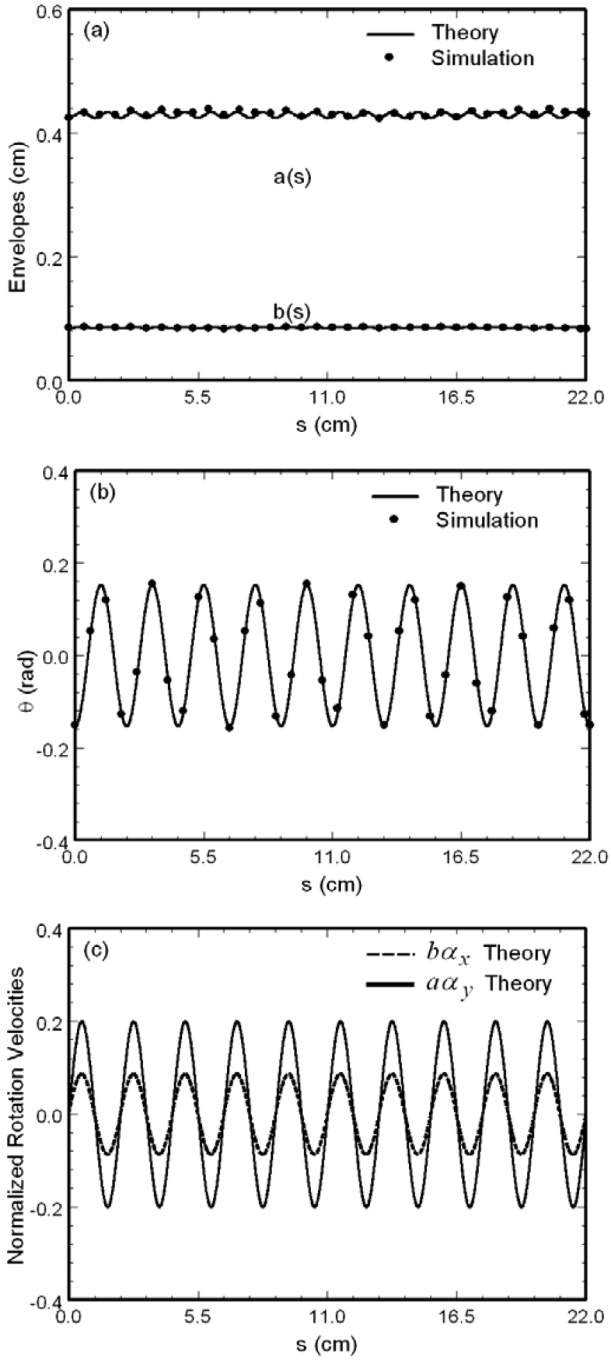

FIG. 2. Plots of (a) envelopes $a(s)$ and $b(s)$, (b) twist angle $\theta(s)$, and (c) normalized rotational velocities $b(s)\alpha_x(s)$ and $a(s)\alpha_y(s)$ versus the axial distance s for the fully relativistic twisted ellipse-shaped beam in Table I (column 4). The solid and dashed curves are the generalized envelope solution, whereas the dotted curves are from the PFB2D simulation.

IV. PIC SIMULATIONS

The beam equilibria predicted by the generalized envelope equations are verified by 2D PIC simulations using the PFB2D code. In the PFB2D simulations, we use the paraxial field in Eq. (4), typically 5×10^5 particles, a square grid with 400×400 cells, and a square conducting pipe with a full width which is 3 times the semimajor axis of the beam.

Shown in Figs. 2(a) and 2(b), the dotted curves are the envelopes and angle of the beam ellipse obtained from the PFB2D simulation for the example of a fully relativistic elliptic beam with $V_b = 198.5$ keV, current $I_b = 85.5$ A, aspect ratio $a/b = 5$, and nonaxisymmetric periodic permanent magnet focusing with $B_0 = 2.4$ kG, $S = 2.2$ cm, and $k_{0y}/k_{0x} = 1.52$. In the simulation, the emittance is set to be negligibly small in order to demonstrate the cold-fluid approximation. As shown in Fig. 2, there is excellent agreement between the theoretical envelope solution (solid curves) and the self-consistent PIC simulation results (dotted curves).

The PFB2D simulation also shows that the transverse beam distribution preserves the equilibrium profile as it propagates. In Fig. 3, 10 000 particles (a sample of the 5×10^5 particles in the PFB2D simulation) are plotted in the (x, y) plane and $(x, dy/ds)$ plane for five snapshots within one period: $s/S = 9.0, 9.25, 9.5, 9.75$, and 10.0 for the same beam shown in Fig. 2. The preservation of the beam distribution is further demonstrated in Fig. 4, which displays the evolution of the normalized fourth moments $\langle x^4\rangle/\langle x^2\rangle^2$ and $\langle y^4\rangle/\langle y^2\rangle^2$ for the same beam shown in Fig. 2. In Fig. 4, it is evident that the normalized fourth moments $\langle x^4\rangle/\langle x^2\rangle^2$ and $\langle y^4\rangle/\langle y^2\rangle^2$, which are both equal to 2 for a uniform-density distribution, remain to be 2 within $\pm 1\%$ as the beam propagates for ten periods. The PIC simulation results suggest that the beam equilibrium is stable.

V. CONCLUSION

In conclusion, a novel exact paraxial cold-fluid equilibrium was found for a high-intensity, space-charge–dominated charged-particle beam with a periodically twisted elliptic cross section in a nonaxisymmetric periodic magnetic field. Generalized envelope equations, which determine the beam envelopes, ellipse orientation, density, and internal flow velocity profiles, were derived, and solved numerically for nonrelativistic and relativistic examples of such beams. The equilibrium and stability of such beams were demonstrated by self-consistent particle-in-cell (PIC) simulations. We anticipate that the equilibrium theory will provide a valuable tool in the design of high-intensity elliptic beams in novel vacuum electronic devices, especially for ribbon-beam klystrons and traveling-wave tubes.

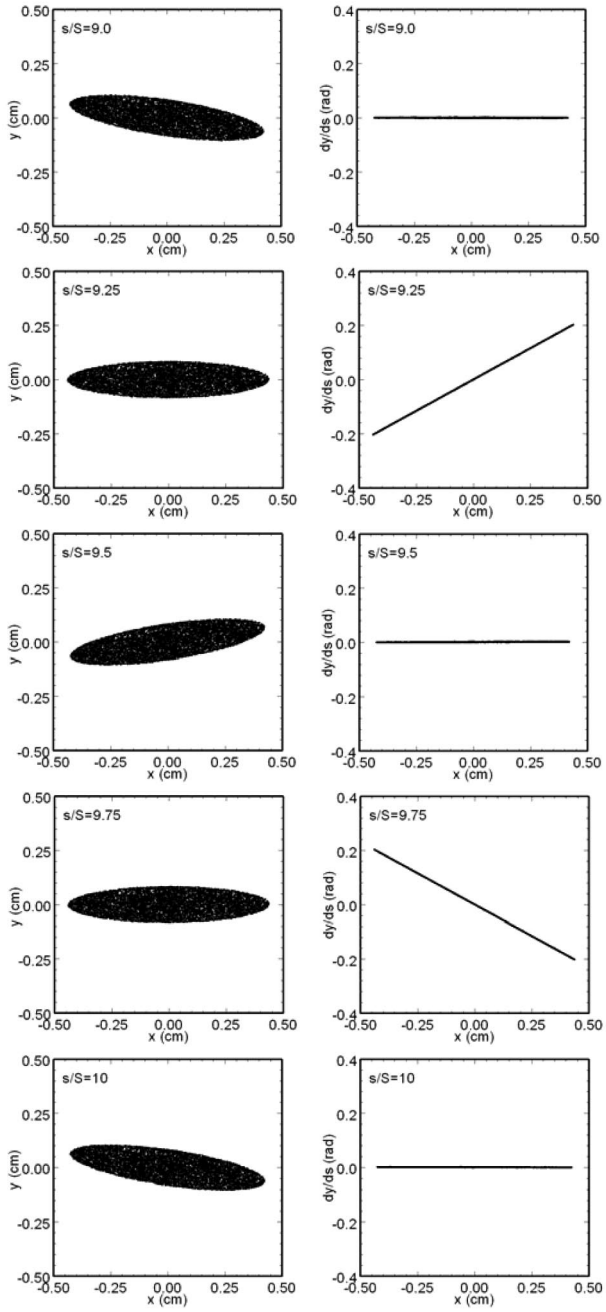

FIG. 3. Plots of 10 000 particles (a sample of the 5×10^5 particles in the PFB2D simulation) in the (x, y) plane and $(x, dy/ds)$ plane for five snapshots within one period: $s/S =$ 9.0, 9.25, 9.5, 9.75, and 10.0 for the same beam shown in Fig. 2.

The ellipse-shaped beam equilibrium may provide some flexibility in the design and operation of high-intensity accelerators.

ACKNOWLEDGMENTS

This work was supported by U.S. Department of Energy, Office of High-Energy Physics, Grant No. DE-FG02-95ER40919, Office of Fusion Energy Science, Grant No. DE-FG 02-01-ER54662, Air Force Office of Scientific Research, Grant No. F49620-03-1-0230, and the MIT Deshpande Center for Technological Innovation.

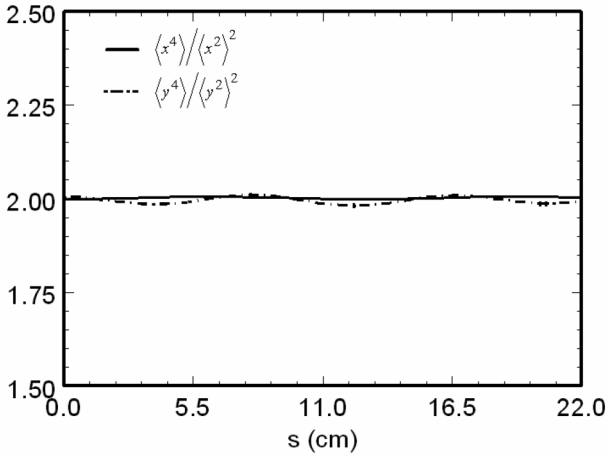

FIG. 4. Plots of the evolution of normalized fourth moments $\langle x^4 \rangle / \langle x^2 \rangle^2$ and $\langle y^4 \rangle / \langle y^2 \rangle^2$ for the same beam shown in Fig. 2.

APPENDIX

Substituting Eqs. (5) and (6) into Eq. (1) and expressing the result in terms of the tilde coordinates, we obtain

$$\left(\mu_x + \mu_y - \frac{a'}{a} - \frac{b'}{b}\right)\Theta\left(1 - \frac{\tilde{x}^2}{a^2} - \frac{\tilde{y}^2}{b^2}\right) + 2\left[\left(\frac{a'}{a} - \mu_x\right)\frac{\tilde{x}^2}{a^2} + \left(\frac{b'}{b} - \mu_y\right)\frac{\tilde{y}^2}{b^2} + \left(-\frac{b}{a}\theta' + \frac{a}{b}\theta' + \frac{b}{a}\alpha_x - \frac{a}{b}\alpha_y\right)\frac{\tilde{x}}{a}\frac{\tilde{y}}{b}\right] \times \delta\left(1 - \frac{\tilde{x}^2}{a^2} - \frac{\tilde{y}^2}{b^2}\right) = 0, \quad \text{(A1)}$$

where the prime denotes $\partial/\partial s$, and the relations $\tilde{x}' = \tilde{y}\theta'$, $\tilde{y}' = -\tilde{x}\theta'$, $\partial \mathbf{e}_{\tilde{x}}/\partial s = \mathbf{e}_{\tilde{y}}\theta'$ and $\partial \mathbf{e}_{\tilde{y}}/\partial s = -\mathbf{e}_{\tilde{x}}\theta'$ have been used. Since Eq. (A1) must be satisfied for all $\tilde{x}$ and $\tilde{y}$, the coefficients of the terms proportional to Θ, $\tilde{x}^2\delta$, $\tilde{y}^2\delta$ and $\tilde{x}\,\tilde{y}\,\delta$ must vanish independently. This leads to the following equations:

$$\mu_x = \frac{1}{a}\frac{da}{ds}, \quad \text{(A2)}$$

$$\mu_y = \frac{1}{b}\frac{db}{ds}, \quad \text{(A3)}$$

$$\frac{d\theta}{ds} = \frac{a^2\alpha_y - b^2\alpha_y}{a^2 - b^2}. \quad \text{(A4)}$$

The force balance equation (3) represents two equations, one in the direction $\mathbf{e}_{\tilde{x}}$ and the other in the $\mathbf{e}_{\tilde{y}}$ direction. Substituting Eqs. (4)–(7) into Eq. (3), the two equations can be expressed as

$$f_x\tilde{x} + g_y\tilde{y} = 0, \tag{A5}$$

$$g_x\tilde{x} + f_y\tilde{y} = 0, \tag{A6}$$

where

$$f_x = {\mu_x}^2 + \mu_x' - \alpha_x\alpha_y + (\alpha_x - \alpha_y)\theta' - \frac{2K}{(a+b)} - 2\sqrt{\kappa_{z0}}\sin(k_0 s)\alpha_y + \sqrt{\kappa_{z0}}\frac{k_{0x}^2 - k_{0y}^2}{k_0}\sin(2\theta)\cos(k_0 s), \tag{A7}$$

$$f_y = {\mu_y}^2 + \mu_y' - \alpha_x\alpha_y - (\alpha_x - \alpha_y)\theta' - \frac{2K}{(a+b)} + 2\sqrt{\kappa_{z0}}\sin(k_0 s)\alpha_x + \sqrt{\kappa_{z0}}\frac{k_{0x}^2 - k_{0y}^2}{k_0}\sin(2\theta)\cos(k_0 s), \tag{A8}$$

$$g_x = \alpha_y' + (\mu_x - \mu_y)\theta' + (\mu_x + \mu_y)\alpha_y - 2\sqrt{\kappa_{z0}}\left(\frac{k_{0x}^2}{k_0}\cos^2\theta + \frac{k_{0y}^2}{k_0}\sin^2\theta\right)\cos(k_0 s) - 2\sqrt{\kappa_{z0}}\mu_x\sin(k_0 s), \tag{A9}$$

$$g_y = -\alpha_x' + (\mu_x - \mu_y)\theta' - (\mu_x + \mu_y)\alpha_x + 2\sqrt{\kappa_{z0}}\left(\frac{k_{0x}^2}{k_0}\sin^2\theta + \frac{k_{0y}^2}{k_0}\cos^2\theta\right)\cos(k_0 s) + 2\sqrt{\kappa_{z0}}\mu_y\sin(k_0 s). \tag{A10}$$

Since Eqs. (A5) and (A6) must be satisfied for all $\tilde{x}$ and $\tilde{y}$, the coefficients of the terms proportional to $\tilde{x}$ and $\tilde{y}$ must vanish independently, which lead to

$$f_x = 0, \tag{A11}$$

$$f_y = 0, \tag{A12}$$

$$g_x = 0, \tag{A13}$$

$$g_y = 0. \tag{A14}$$

After substituting Eqs. (A2) and (A3) into Eqs. (A11)–(A14), we obtain the generalized envelope equations (A8)–(A12).

[1] P. A. Sturrock, J. Electron. Control **7**, 162 (1959).
[2] Z. X. Zhang, V. L. Granatstein, W. W. Destler *et al.*, IEEE Trans. Plasma Sci. **21**, 760 (1993).
[3] J. H. Booske, B. D. McVey, and T. M. Antonsen, Jr., J. Appl. Phys. **73**, 4140 (1993).
[4] J. H. Booske, A. H. Kumbasar, and M. A. Basten, Phys. Rev. Lett. **71**, 3979 (1993).
[5] J. H. Booske and M. A. Basten, IEEE Trans. Plasma Sci. **27**, 134 (1999).
[6] M. A. Basten and J. H. Booske, J. Appl. Phys. **85**, 6313 (1999).
[7] F. J. Sacherer, Ph.D. thesis, Lawrence Radiation Laboratory, University of California, Berkeley, 1968, pp. 15–19.
[8] V. Danilov, S. Cousineau, S. Henderson, and J. Holmes, Phys. Rev. ST Accel. Beams **6**, 094202 (2003).
[9] I. M. Kapchinskij, and V. V. Vladimirskij, in *Proceedings of the International Conference on High Energy Accelerators* (CERN, Geneva, 1959), p. 274.
[10] R. C. Davidson, *Physics of Nonneutral Plasma* (Addison-Wesley, Reading, MA, 1990), p. 694.
[11] C. Chen, R. Pakter, and R. C. Davidson, Phys. Rev. Lett. **79**, 225 (1997).
[12] R. C. Davidson and H. Qin, *Physics of Intense Charged Particle Beams in High Energy Accelerators* (World Scientific, Singapore, 2001), p. 242.
[13] R. Pakter and C. Chen, Phys. Rev. E **62**, 2789 (2000).
[14] C. Chen and R. Pakter, Phys. Plasmas **7**, 2203 (2000).
[15] R. C. Davidson, P. Stoltz, and C. Chen, Phys. Plasmas **4**, 3710 (1997).
[16] R. Bhatt and C. Chen, Phys. Rev. ST Accel. Beams **8**, 014201 (2005).

Cold-fluid theory of equilibrium and stability of a high-intensity periodically twisted ellipse-shaped charged-particle beam

Jing Zhou, Ronak Bhatt, and Chiping Chen

Plasma Science and Fusion Center, Massachusetts Institute of Technology, Cambridge, Massachusetts 02139, USA

(Received 14 January 2005; published 3 March 2006)

It is shown that there exists an exact paraxial cold-fluid equilibrium of a high-intensity, space-charge-dominated charged-particle beam with a periodically twisted elliptic cross section in a nonaxisymmetric periodic magnetic field. Generalized envelope equations, which determine the beam envelopes, ellipse orientation, density, and internal flow velocity profiles, are derived. Nonrelativistic and relativistic examples of such beam equilibria are presented. The equilibrium and stability of such beams are demonstrated by self-consistent particle-in-cell (PIC) simulations.

DOI: 10.1103/PhysRevSTAB.9.034401 PACS numbers: 41.75.−i, 41.85.Ja, 41.85.Lc, 52.59.Sa

I. INTRODUCTION

High-intensity ribbon (thin sheet) beams are of great interest for applications in particle accelerators, such as storage rings and rf and induction linacs, as well as vacuum electron devices, such as klystrons and traveling-wave tubes with periodic permanent magnet (PPM) focusing. They have the following remarkable properties. First, they can transport large amounts of beam currents at reduced intrinsic space-charge forces and energies. Second, they couple efficiently to rectangular rf structures. The combination of the space-charge reduction and efficient coupling allows efficient rf generation in vacuum electronic devices, and efficient acceleration in particle accelerators. Third, elliptic beams provide an additional adjustable parameter (e.g., the aspect ratio) which may be useful for better matching a beam into a periodic focusing channel.

Although ribbon beams have been discussed in the literature for four decades, the equilibrium of a high-intensity, space-charge-dominated beam with a large-aspect-ratio elliptic cross section has not been discovered until this paper. Sturrock [1] first suggested the use of a periodic magnetic focusing consisting of an array of planar-wiggler magnets for rectilinear beams. Zhang *et al.* [2] had some modest success in the experimental demonstration of the transport of a low-intensity (10 A, 500 kV) sheet beam in a planar-wiggler magnetic field, and observed considerable beam loss. Researchers made use of the multiple-time-scale analysis and the paraxial approximations to obtain the smooth-beam approximation of high-intensity ribbon-beam equilibria [3–6]. In the smooth-beam approximation, the effects of the planar-wiggler field [1,2], or the periodic cusp magnetic (PCM) field [3,4], or the hybrid of PCM and periodic quadrupole magnet (PQM) fields [5,6], or the offset pole PCM field [6] are treated as some averaged focusing constants in the transverse directions. While the smooth-beam approximation yields simple results, the multiple-time-scale analysis requires time averaging, losing the detailed information about the beam dynamics. As a result, it does not provide adequate information about how to generate high-intensity ribbon beams in practice.

A widely used tool for the determination of evolution of the charged-particle beam systems is based on the rms beam description. The construction of self-consistent beam distributions with linear focusing forces is discussed in Refs. [7,8], such as Kapchinskij-Vladmirskij equilibrium [7–10] in an alternating-gradient quadrupole magnetic focusing field and the periodically focused rigid-rotor Vlasov equilibrium [11,12] in a periodic solenoid magnetic focusing field. For ultrahigh-brightness beams with negligibly small emittance, a cold-fluid theory can be used to examine the detailed information about the beam dynamics, especially the evolution of the density and flow velocity profiles [13–15], such as the cold-fluid corkscrewing equilibrium [13,14] in a linear focusing channel consisting of solenoidal and quadrupole magnetic focusing fields.

In this paper, we present the cold-fluid equilibrium theory of an ultrahigh-brightness, space-charge–dominated, large–aspect-ratio beam propagating through a nonaxisymmetric periodic magnetic focusing field. Our beam distribution satisfies the assumptions for the distribution functions described generally in Refs. [7,8]. A paraxial cold-fluid model is employed to derive generalized envelope equations which determine the equilibrium flow properties of ellipse-shaped beams with negligibly small emittance. A matched envelope solution is obtained numerically from the generalized envelope equations, and the results show that the beam edges in both transverse directions are well confined, and that the angle of the beam ellipse exhibits a periodic small-amplitude twist. Two-dimensional (2D) particle-in-cell (PIC) simulations with our Periodic Focused Beam 2D (PFB2D) code show good agreement with the predictions of equilibrium theory as well as beam stability.

The organization of the present paper is as follows. In Sec. II, the cold-fluid equilibrium theory of a periodically twisted ellipse-shaped charged-particle beam is presented

and the generalized envelope equations are derived. In Sec. III, the generalized envelope equations are solved numerically for several examples of periodically twisted ellipse-shaped charged-particle beams. In Sec. IV, PIC simulations are used to verify the theoretical results. Conclusions are presented in Sec. V.

II. COLD-FLUID EQUILIBRIUM THEORY

We consider a high-intensity, space-charge–dominated beam, in which kinetic (emittance) effects are negligibly small. The beam can be adequately described by cold-fluid equations. In the paraxial approximation, the steady-state cold-fluid equations for time-stationary flow ($\partial/\partial t = 0$) in cgs units are [13,14]

$$\beta_b c \frac{\partial}{\partial s} n_b + \nabla_\perp \cdot (n_b \mathbf{V}_\perp) = 0, \tag{1}$$

$$\nabla_\perp^2 \phi^s = \beta_b^{-1} \nabla_\perp^2 A_z^s = -4\pi q n_b, \tag{2}$$

$$n_b \left(\beta_b c \frac{\partial}{\partial s} + \mathbf{V}_\perp \cdot \nabla_\perp \right) \mathbf{V}_\perp = \frac{q n_b}{\gamma_b m} \left[-\frac{1}{\gamma_b^2} \nabla_\perp \phi^s + \beta_b \hat{\mathbf{e}}_z \times \mathbf{B}_\perp^{\text{ext}} + \frac{\mathbf{V}_\perp}{c} \times B_z^{\text{ext}}(s) \hat{\mathbf{e}}_z \right], \tag{3}$$

where $s = z$, $\mathbf{x}_\perp = x\hat{\mathbf{e}}_x + y\hat{\mathbf{e}}_y$, $\nabla_\perp = \partial/\partial \mathbf{x}_\perp$, q and m are the particle charge and rest mass, respectively, n_b is the particle density, $\mathbf{V}_\perp$ is the transverse flow velocity, $\gamma_b = (1 - \beta_b^2)^{-1/2}$ is the relativistic mass factor, use has been made of $\beta_z = V_z/c \cong \beta_b = \text{const}$, c is the speed of light in vacuum and the self-electric field $\mathbf{E}^s$ and self-magnetic field $\mathbf{B}^s$ are determined from the scalar potential ϕ^s and vector potential $A_z^s \hat{\mathbf{e}}_z$, i.e., $\mathbf{E}^s = -\nabla_\perp \phi^s$ and $\mathbf{B}^s = \nabla_\perp \times A_z^s \hat{\mathbf{e}}_z$.

For the beam dimensions small relative to the characteristic scale of magnetic variations, i.e., $(k_{0x}x)^2/6 \ll 1$ and $(k_{0y}y)^2/6 \ll 1$, a three-dimensional (3D) nonaxisymmetric periodic magnetic field can be described to the lowest order in the transverse dimension as

$$\mathbf{B}^{\text{ext}}(\mathbf{x}) \approx B_0 \left[\frac{k_{0x}^2}{k_0} \cos(k_0 s) x \hat{\mathbf{e}}_x + \frac{k_{0y}^2}{k_0} \cos(k_0 s) y \hat{\mathbf{e}}_y - \sin(k_0 s) \hat{\mathbf{e}}_z \right], \tag{4}$$

where $k_0 = 2\pi/S$, $k_{0x}^2 + k_{0y}^2 = k_0^2$, and S is the axial periodicity length. The 3D magnetic field in Eq. (4) is fully specified by the three parameters B_0, S, and k_{0x}/k_{0y}.

We seek solutions to Eqs. (1)–(3) of the form

$$n_b(\mathbf{x}_\perp, s) = \frac{N_b}{\pi a(s) b(s)} \Theta \left[1 - \frac{\tilde{x}^2}{a^2(s)} - \frac{\tilde{y}^2}{b^2(s)} \right], \tag{5}$$

$$\mathbf{V}_\perp(\mathbf{x}_\perp, s) = [\mu_x(s)\tilde{x} - \alpha_x(s)\tilde{y}] \beta_b c \hat{\mathbf{e}}_{\tilde{x}} + [\mu_y(s)\tilde{y} + \alpha_y(s)\tilde{x}] \beta_b c \hat{\mathbf{e}}_{\tilde{y}}. \tag{6}$$

In Eqs. (5) and (6), $\mathbf{x}_\perp = \tilde{x}\hat{\mathbf{e}}_{\tilde{x}} + \tilde{y}\hat{\mathbf{e}}_{\tilde{y}}$ is a transverse displacement in the twisted coordinate system illustrated in Fig. 1; $\theta(s)$ is the twist angle of the ellipse; $\Theta(x) = 1$ if $x > 0$ and $\Theta(x) = 0$ if $x < 0$; and the functions $a(s)$, $b(s)$, $\mu_x(s)$, $\mu_y(s)$, $\alpha_x(s)$, $\alpha_y(s)$, and $\theta(s)$ are to be determined self-consistently [see Eqs. (8)–(12)].

The self-electric and self-magnetic fields are well known for an elliptical beam with density distribution specified in Eq. (5), i.e.,

$$\phi^s = \beta_b^{-1} A_z^s = -\frac{2qN_b}{a+b} \left(\frac{\tilde{x}^2}{a} + \frac{\tilde{y}^2}{b} \right). \tag{7}$$

Using the expressions in Eqs. (4)–(7), it can be shown that both the equilibrium continuity equation (1) and force equation (3) are satisfied if the dynamical variables $a(s)$, $b(s)$, $\mu_x(s) \equiv a^{-1}da/ds$, $\mu_y(s) \equiv b^{-1}db/ds$, $\alpha_x(s)$, $\alpha_y(s)$ and $\theta(s)$ obey the generalized beam envelope equations (see appendix)

$$\frac{d^2 a}{ds^2} - \left[\frac{b^2(\alpha_x^2 - 2\alpha_x\alpha_y) + a^2\alpha_y^2}{a^2 - b^2} + \sqrt{\kappa_{z0}} \frac{k_{0x}^2 - k_{0y}^2}{k_0} \cos(k_0 s) \sin(2\theta) - 2\sqrt{\kappa_{z0}} \alpha_y \sin(k_0 s) \right] a - \frac{2K}{a+b} = 0, \tag{8}$$

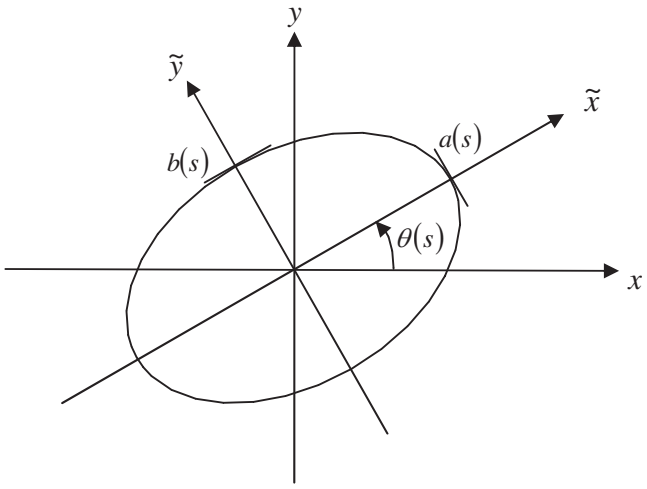

FIG. 1. Laboratory and twisted coordinate systems.

$$\frac{d^2b}{ds^2} + \left[\frac{a^2(\alpha_y^2 - 2\alpha_x\alpha_y) + b^2\alpha_x^2}{a^2 - b^2} + \sqrt{\kappa_{z0}}\frac{k_{0x}^2 - k_{0y}^2}{k_0}\cos(k_0 s)\sin(2\theta) + 2\sqrt{\kappa_{z0}}\alpha_x \sin(k_0 s)\right]b - \frac{2K}{a+b} = 0, \quad (9)$$

$$\frac{d}{ds}(a^2\alpha_y) - \frac{ab^3(\alpha_x - \alpha_y)}{a^2 - b^2}\frac{d}{ds}\left(\frac{a}{b}\right) - 2\sqrt{\kappa_{z0}}\cos(k_0 s)\frac{k_{0x}^2\cos^2\theta + k_{0y}^2\sin^2\theta}{k_0}a^2 - 2\sqrt{\kappa_{z0}}a\frac{da}{ds}\sin(k_0 s) = 0, \quad (10)$$

$$\frac{d}{ds}(b^2\alpha_x) - \frac{a^3b(\alpha_x - \alpha_y)}{a^2 - b^2}\frac{d}{ds}\left(\frac{b}{a}\right) - 2\sqrt{\kappa_{z0}}\cos(k_0 s)\frac{k_{0x}^2\sin^2\theta + k_{0y}^2\cos^2\theta}{k_0}b^2 - 2\sqrt{\kappa_{z0}}b\frac{db}{ds}\sin(k_0 s) = 0, \quad (11)$$

$$\frac{d\theta}{ds} = \frac{a^2\alpha_y - b^2\alpha_x}{a^2 - b^2}, \quad (12)$$

where

$$\sqrt{\kappa_{z0}} \equiv \frac{qB_0}{2\gamma_b\beta_b mc^2} \quad \text{and} \quad K \equiv \frac{2q^2N_b}{\gamma_b^3\beta_b^3 mc^2}.$$

Equations (8)–(12) have "time" reversal symmetry under the transformation $(s, a, b, a', b', \alpha_x, \alpha_y, \theta) \rightarrow (-s, a, b, -a', -b', -\alpha_x, -\alpha_y, \theta)$. This implies that the dynamical system described by Eqs. (8)–(12) has the hypersymmetry plane $(a', b', \alpha_x, \alpha_y)$.

III. EXAMPLES OF PERIODICALLY TWISTED ELLIPSE-SHAPED CHARGED-PARTICLE BEAMS

A numerical module in the PFB2D code has been developed to solve the generalized envelope equations (8)–(12). There are, in total, seven functions $a(s)$, $b(s)$, $a'(s)$, $b'(s)$, $\alpha_x(s)$, $\alpha_x(s)$, and $\theta(s)$ to be determined. The time reversal symmetry of the dynamical system requires the quantities $(a', b', \alpha_x, \alpha_y)$ vanish at $s = 0$ for matched solutions, therefore, only the three initial values $a(0)$, $b(0)$, and $\theta(0)$ corresponding to a matched solution need to be determined with Newton's method.

As an example, we consider a relativistic elliptic beam with $V_b = 198.5$ keV, current $I_b = 85.5$ A, aspect ratio $a/b = 5$, and nonaxisymmetric periodic permanent magnet focusing with $B_0 = 2.4$ kG, $S = 2.2$ cm, and $k_{0y}/k_{0x} = 1.52$ (see Table I, Col. 4). [We propose to use it in a 10 MW L-Band ribbon-beam klystron for the International Linear Collider.] For such a system the matched solution of the generalized envelope equations (8)–(12) is calculated numerically as shown in Figs. 2(a)–2(c) (solid curves) with the corresponding parameters: $k_{0x} = 1.57$ cm^{-1}, $k_{0y} = 2.39$ cm^{-1}, $\sqrt{\kappa_{z0}} = 0.732$ cm^{-1}, and $K = 1.13 \times 10^{-2}$. The solution to the generalized envelope equations (8)–(12), displayed as solid and dashed curves in Fig. 2, shows that the semiaxes of the elliptical beam remain roughly constant with small oscillations, that the orientation of the ellipse twists periodically with an amplitude of 8.8 degrees, and that the normalized rotation flow velocities α_x and α_y oscillate with the magnet periodicity. It is worthwhile pointing out that the normalized velocities μ_x, μ_y, α_x, and α_y vanish at $s = 0$ which makes it a natural matching point for a parallel-flow beam with negligibly small emittance [16].

These high-intensity twisted elliptic-beam equilibria exist over a wide region of parameters ranging from the nonrelativistic to relativistic regimes. In addition to the relativistic elliptic-beam equilibrium discussed above, we present a nonrelativistic elliptic-beam equilibrium and a mildly relativistic elliptic-beam equilibrium in Table I. The

TABLE I. System parameters for elliptic-beam examples.

Parameter Application	Nonrelativistic Wireless communication	Mildly relativistic Missile defense	Fully relativistic International Linear Collider
Frequency (GHz)	1.95	2.8	1.3
rf Power (kW)	0.2 (cw)	500 (pulsed)	10 000 (pulsed)
Current (A)	0.11	18.5	85.5
Voltage (kV)	2.29	45.0	198.5
S (cm)	1.912	2.626	2.2
k_{0x}/k_{0y}	1.60	1.44	1.52
B_0 (kG)	0.337	1.099	2.40
a/b	6.0	4.0	5.0
a (cm)	0.373	0.585	0.425
$\theta_{\max}$ (deg)	10.4	11.5	8.8

nonrelativistic elliptic beam corresponds to a beam design for a high-efficiency 200 W ribbon-beam amplifier (RBA) which is being developed at Massachusetts Institute of Technology (MIT) for communication, whereas the mildly relativistic elliptic beam is proposed for a high-power, high-efficiency RBA for radar applications.

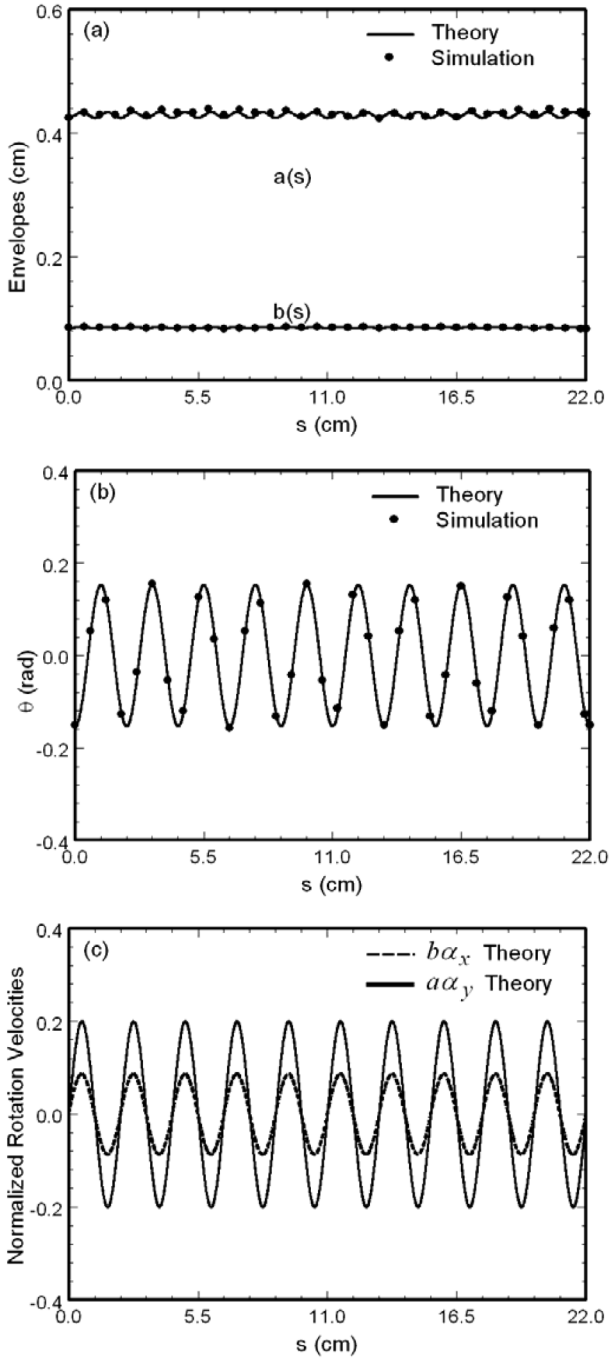

FIG. 2. Plots of (a) envelopes $a(s)$ and $b(s)$, (b) twist angle $\theta(s)$, and (c) normalized rotational velocities $b(s)\alpha_x(s)$ and $a(s)\alpha_y(s)$ versus the axial distance s for the fully relativistic twisted ellipse-shaped beam in Table I (column 4). The solid and dashed curves are the generalized envelope solution, whereas the dotted curves are from the PFB2D simulation.

IV. PIC SIMULATIONS

The beam equilibria predicted by the generalized envelope equations are verified by 2D PIC simulations using the PFB2D code. In the PFB2D simulations, we use the paraxial field in Eq. (4), typically 5×10^5 particles, a square grid with 400×400 cells, and a square conducting pipe with a full width which is 3 times the semimajor axis of the beam.

Shown in Figs. 2(a) and 2(b), the dotted curves are the envelopes and angle of the beam ellipse obtained from the PFB2D simulation for the example of a fully relativistic elliptic beam with $V_b = 198.5$ keV, current $I_b = 85.5$ A, aspect ratio $a/b = 5$, and nonaxisymmetric periodic permanent magnet focusing with $B_0 = 2.4$ kG, $S = 2.2$ cm, and $k_{0y}/k_{0x} = 1.52$. In the simulation, the emittance is set to be negligibly small in order to demonstrate the cold-fluid approximation. As shown in Fig. 2, there is excellent agreement between the theoretical envelope solution (solid curves) and the self-consistent PIC simulation results (dotted curves).

The PFB2D simulation also shows that the transverse beam distribution preserves the equilibrium profile as it propagates. In Fig. 3, 10 000 particles (a sample of the 5×10^5 particles in the PFB2D simulation) are plotted in the (x, y) plane and $(x, dy/ds)$ plane for five snapshots within one period: $s/S = 9.0, 9.25, 9.5, 9.75$, and 10.0 for the same beam shown in Fig. 2. The preservation of the beam distribution is further demonstrated in Fig. 4, which displays the evolution of the normalized fourth moments $\langle x^4\rangle/\langle x^2\rangle^2$ and $\langle y^4\rangle/\langle y^2\rangle^2$ for the same beam shown in Fig. 2. In Fig. 4, it is evident that the normalized fourth moments $\langle x^4\rangle/\langle x^2\rangle^2$ and $\langle y^4\rangle/\langle y^2\rangle^2$, which are both equal to 2 for a uniform-density distribution, remain to be 2 within $\pm 1\%$ as the beam propagates for ten periods. The PIC simulation results suggest that the beam equilibrium is stable.

V. CONCLUSION

In conclusion, a novel exact paraxial cold-fluid equilibrium was found for a high-intensity, space-charge–dominated charged-particle beam with a periodically twisted elliptic cross section in a nonaxisymmetric periodic magnetic field. Generalized envelope equations, which determine the beam envelopes, ellipse orientation, density, and internal flow velocity profiles, were derived, and solved numerically for nonrelativistic and relativistic examples of such beams. The equilibrium and stability of such beams were demonstrated by self-consistent particle-in-cell (PIC) simulations. We anticipate that the equilibrium theory will provide a valuable tool in the design of high-intensity elliptic beams in novel vacuum electronic devices, especially for ribbon-beam klystrons and traveling-wave tubes.

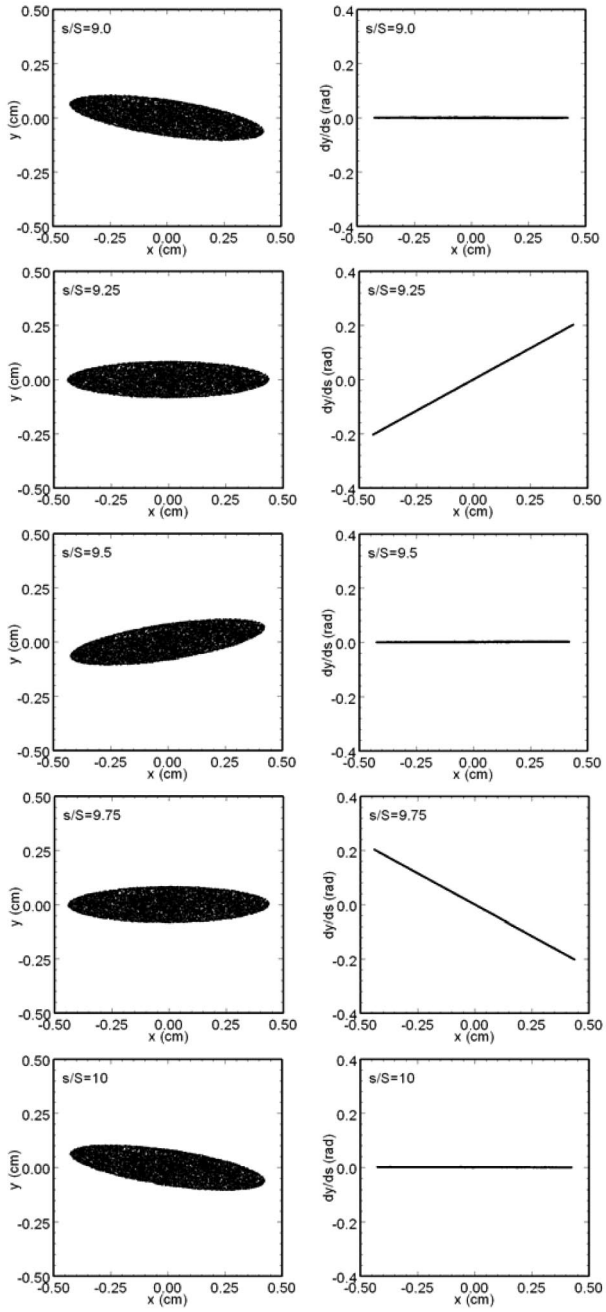

FIG. 3. Plots of 10 000 particles (a sample of the 5×10^5 particles in the PFB2D simulation) in the (x, y) plane and $(x, dy/ds)$ plane for five snapshots within one period: $s/S =$ 9.0, 9.25, 9.5, 9.75, and 10.0 for the same beam shown in Fig. 2.

The ellipse-shaped beam equilibrium may provide some flexibility in the design and operation of high-intensity accelerators.

ACKNOWLEDGMENTS

This work was supported by U.S. Department of Energy, Office of High-Energy Physics, Grant No. DE-FG02-95ER40919, Office of Fusion Energy Science, Grant No. DE-FG 02-01-ER54662, Air Force Office of Scientific Research, Grant No. F49620-03-1-0230, and the MIT Deshpande Center for Technological Innovation.

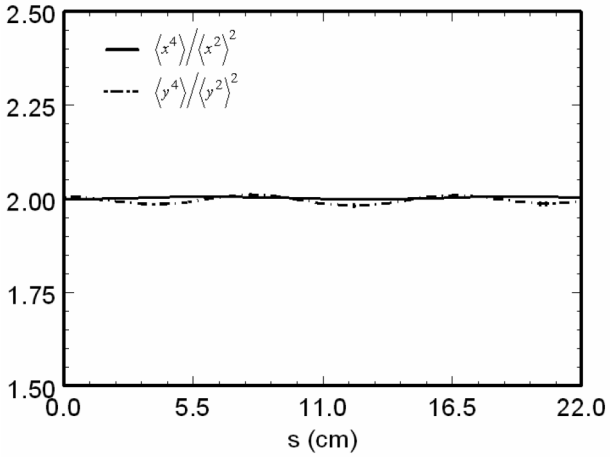

FIG. 4. Plots of the evolution of normalized fourth moments $\langle x^4 \rangle / \langle x^2 \rangle^2$ and $\langle y^4 \rangle / \langle y^2 \rangle^2$ for the same beam shown in Fig. 2.

APPENDIX

Substituting Eqs. (5) and (6) into Eq. (1) and expressing the result in terms of the tilde coordinates, we obtain

$$\left(\mu_x + \mu_y - \frac{a'}{a} - \frac{b'}{b}\right)\Theta\left(1 - \frac{\tilde{x}^2}{a^2} - \frac{\tilde{y}^2}{b^2}\right) + 2\left[\left(\frac{a'}{a} - \mu_x\right)\frac{\tilde{x}^2}{a^2} + \left(\frac{b'}{b} - \mu_y\right)\frac{\tilde{y}^2}{b^2} + \left(-\frac{b}{a}\theta' + \frac{a}{b}\theta' + \frac{b}{a}\alpha_x - \frac{a}{b}\alpha_y\right)\frac{\tilde{x}}{a}\frac{\tilde{y}}{b}\right] \times \delta\left(1 - \frac{\tilde{x}^2}{a^2} - \frac{\tilde{y}^2}{b^2}\right) = 0, \quad \text{(A1)}$$

where the prime denotes $\partial/\partial s$, and the relations $\tilde{x}' = \tilde{y}\theta'$, $\tilde{y}' = -\tilde{x}\theta'$, $\partial \mathbf{e}_{\tilde{x}}/\partial s = \mathbf{e}_{\tilde{y}}\theta'$ and $\partial \mathbf{e}_{\tilde{y}}/\partial s = -\mathbf{e}_{\tilde{x}}\theta'$ have been used. Since Eq. (A1) must be satisfied for all $\tilde{x}$ and $\tilde{y}$, the coefficients of the terms proportional to Θ, $\tilde{x}^2\delta$, $\tilde{y}^2\delta$ and $\tilde{x}\,\tilde{y}\,\delta$ must vanish independently. This leads to the following equations:

$$\mu_x = \frac{1}{a}\frac{da}{ds}, \quad \text{(A2)}$$

$$\mu_y = \frac{1}{b}\frac{db}{ds}, \quad \text{(A3)}$$

$$\frac{d\theta}{ds} = \frac{a^2\alpha_y - b^2\alpha_y}{a^2 - b^2}. \quad \text{(A4)}$$

The force balance equation (3) represents two equations, one in the direction $\mathbf{e}_{\tilde{x}}$ and the other in the $\mathbf{e}_{\tilde{y}}$ direction. Substituting Eqs. (4)–(7) into Eq. (3), the two equations can be expressed as

$$f_x\tilde{x} + g_y\tilde{y} = 0, \tag{A5}$$

$$g_x\tilde{x} + f_y\tilde{y} = 0, \tag{A6}$$

where

$$f_x = {\mu_x}^2 + \mu_x' - \alpha_x\alpha_y + (\alpha_x - \alpha_y)\theta' - \frac{2K}{(a+b)} - 2\sqrt{\kappa_{z0}}\sin(k_0 s)\alpha_y + \sqrt{\kappa_{z0}}\frac{k_{0x}^2 - k_{0y}^2}{k_0}\sin(2\theta)\cos(k_0 s), \tag{A7}$$

$$f_y = {\mu_y}^2 + \mu_y' - \alpha_x\alpha_y - (\alpha_x - \alpha_y)\theta' - \frac{2K}{(a+b)} + 2\sqrt{\kappa_{z0}}\sin(k_0 s)\alpha_x + \sqrt{\kappa_{z0}}\frac{k_{0x}^2 - k_{0y}^2}{k_0}\sin(2\theta)\cos(k_0 s), \tag{A8}$$

$$g_x = \alpha_y' + (\mu_x - \mu_y)\theta' + (\mu_x + \mu_y)\alpha_y - 2\sqrt{\kappa_{z0}}\left(\frac{k_{0x}^2}{k_0}\cos^2\theta + \frac{k_{0y}^2}{k_0}\sin^2\theta\right)\cos(k_0 s) - 2\sqrt{\kappa_{z0}}\mu_x\sin(k_0 s), \tag{A9}$$

$$g_y = -\alpha_x' + (\mu_x - \mu_y)\theta' - (\mu_x + \mu_y)\alpha_x + 2\sqrt{\kappa_{z0}}\left(\frac{k_{0x}^2}{k_0}\sin^2\theta + \frac{k_{0y}^2}{k_0}\cos^2\theta\right)\cos(k_0 s) + 2\sqrt{\kappa_{z0}}\mu_y\sin(k_0 s). \tag{A10}$$

Since Eqs. (A5) and (A6) must be satisfied for all $\tilde{x}$ and $\tilde{y}$, the coefficients of the terms proportional to $\tilde{x}$ and $\tilde{y}$ must vanish independently, which lead to

$$f_x = 0, \tag{A11}$$

$$f_y = 0, \tag{A12}$$

$$g_x = 0, \tag{A13}$$

$$g_y = 0. \tag{A14}$$

After substituting Eqs. (A2) and (A3) into Eqs. (A11)–(A14), we obtain the generalized envelope equations (A8)–(A12).

[1] P. A. Sturrock, J. Electron. Control **7**, 162 (1959).
[2] Z. X. Zhang, V. L. Granatstein, W. W. Destler *et al.*, IEEE Trans. Plasma Sci. **21**, 760 (1993).
[3] J. H. Booske, B. D. McVey, and T. M. Antonsen, Jr., J. Appl. Phys. **73**, 4140 (1993).
[4] J. H. Booske, A. H. Kumbasar, and M. A. Basten, Phys. Rev. Lett. **71**, 3979 (1993).
[5] J. H. Booske and M. A. Basten, IEEE Trans. Plasma Sci. **27**, 134 (1999).
[6] M. A. Basten and J. H. Booske, J. Appl. Phys. **85**, 6313 (1999).
[7] F. J. Sacherer, Ph.D. thesis, Lawrence Radiation Laboratory, University of California, Berkeley, 1968, pp. 15–19.
[8] V. Danilov, S. Cousineau, S. Henderson, and J. Holmes, Phys. Rev. ST Accel. Beams **6**, 094202 (2003).
[9] I. M. Kapchinskij, and V. V. Vladimirskij, in *Proceedings of the International Conference on High Energy Accelerators* (CERN, Geneva, 1959), p. 274.
[10] R. C. Davidson, *Physics of Nonneutral Plasma* (Addison-Wesley, Reading, MA, 1990), p. 694.
[11] C. Chen, R. Pakter, and R. C. Davidson, Phys. Rev. Lett. **79**, 225 (1997).
[12] R. C. Davidson and H. Qin, *Physics of Intense Charged Particle Beams in High Energy Accelerators* (World Scientific, Singapore, 2001), p. 242.
[13] R. Pakter and C. Chen, Phys. Rev. E **62**, 2789 (2000).
[14] C. Chen and R. Pakter, Phys. Plasmas **7**, 2203 (2000).
[15] R. C. Davidson, P. Stoltz, and C. Chen, Phys. Plasmas **4**, 3710 (1997).
[16] R. Bhatt and C. Chen, Phys. Rev. ST Accel. Beams **8**, 014201 (2005).

Generation, Transport and Focusing of High-Brightness Heavy Ion Beams

by

Enrique Henestroza

Submitted to the Department of Physics
in partial fulfillment of the requirements for the degree of

Doctor of Philosophy in Physics

at the

MASSACHUSETTS INSTITUTE OF TECHNOLOGY

June 2006

Author .....
Department of Physics
May 24, 2006

Certified by .....
Richard J. Temkin
Senior Scientist
Thesis Supervisor

Certified by .....
Chiping Chen
Principal Research Scientist
Thesis Supervisor

Accepted by .....
Thomas J. Greytak
Professor & Associate Department Head for Education

Generation, Transport and Focusing of High-Brightness Heavy Ion Beams

by

Enrique Henestroza

Submitted to the Department of Physics
on May 24, 2006, in partial fulfillment of the
requirements for the degree of
Doctor of Philosophy in Physics

Abstract

The Neutralized Transport Experiment (NTX) has been built at the Heavy Ion Fusion Virtual National Laboratory. NTX is the first successful integrated beam system experiment that explores various physical phenomena, and determines the final spot size of a high intensity ion beam on a scaled version of a Heavy Ion Fusion driver. The final spot size is determined by the conditions of the beam produced in the injector, the beam dynamics in the focusing lattice, and the plasma neutralization dynamics in the final transport. A high brightness ion source using an aperturing technique delivers 25 mA of single charged potassium ion beam at 300 keV and a normalized edge emittance of 0.05 π-mm-mr. The ion beam is injected into a large bore magnetic quadrupole lattice, which produces a 20 mm radius beam converging at 20 mr. The converging ion beam is further injected into a plasma neutralization drift section where it is compressed ballistically down to a 1 mm spot size. NTX provides the first experimental proof of plasma neutralized ballistic transport of a space-charge dominated ion beam, the information about higher order aberration effects on the spot size, the validation of numerical tools based on excellent agreement between measurements and numerical simulations over a broad parameter regime, and the development of new diagnostics to study the ion beam dynamics. The theoretical and experimental results are presented on the beam dynamics in the ion diode, downstream quadrupole lattice, and final neutralized transport.

Thesis Supervisor: Richard J. Temkin
Title: Senior Scientist

Thesis Supervisor: Chiping Chen
Title: Principal Research Scientist

Acknowledgments

I would like to thank Dr. Chiping Chen, Dr. Richard Temkin, Prof. Miklos Porkolab and Prof. Bruno Coppi for serving on my thesis committee; a second round of thanks to Dr. Chiping Chen and Dr. Richard Temkin for being my thesis supervisors, and to Prof. Miklos Porkolab for being my academic advisor during my graduate studies; a third round goes to Dr. Chiping Chen for the extraordinary amount of time that he has spent so that I could reach my goal. My not being a typical graduate student made every step of this effort more involved for all of you, and I thank you very much for your help and understanding. I also would like to acknowledge the hospitality of the Plasma Science and Fusion Center and the great conversations that I have always had with Mark Hess, Jing Zhou and Ronak Bhatt.

I would like to acknowledge the financial support from the Department of Energy during my graduate studies.

Thanks to all my colleagues at the HIFS-VNL at LBNL where I have spent most of my professional career. A special thanks to Dr.Grant Logan for his continuous support during this period. Being that the NTX is a rather complex machine, it required the collaboration of a large number of people. Therefore I want to thank Will Waldron who was in charge of the electrical engineering for this project, Derek Shuman for the mechanical design and fabrication of the quadrupoles, Matthaeus Leitner for the mechanical engineering support at the end of the project, Dave Baca for fabricating the ion source, Andre Anders for making available the MEVVA plasma source, Ron Davidson, Erik Gilson and Phil Efthimion at PPPL for supplying the RF plasma source, Frank Bieniosek who introduced us to the wonderful world of optical diagnostics, and all the technical staff in Bldg. 58 at LBNL, especially Wayne Greenway and Dave Vanecek for their outstanding job in putting together the NTX experiment in record time.

Thanks to my long time lab partner Shmuel Eylon and to Prabir Roy who were in charge of the experimental effort, to Alex Friedman, Dave Grote, Jean-Luc Vay and Bill Sharp for all the hours that we have spent discussing the numerical simulations of the experiment, and to Dale Welch and Carsten Thoma for running the LSP simulations of the final transport. A special thanks goes to my colleagues Peter Seidl, Steve Lund, Irving Haber, Christine Celata, John Barnard, Joe Kwan, and Art Molvik, for all your suggestions and advice during the design and the experimental phase of the project; and to Andy Faltens and Ed Lee who have always had time to discuss beam dynamics issues with me. And finally, I would like to say thank you to the administrative support team: Lynn Heimbucher, Wes Tabler, Sharon Buckley at LBNL and Carol Arlington at MIT.

This thesis is dedicated to the following people who had made it possible for me to reach my goal.

To Dr. Simon S. Yu for being a friend, a mentor and an example of what a creative scientist and a perfect gentleman should be; I hope to live up to your expectations.

To my extended family, my late father, my mother, brothers and sisters.

To my kids Monica and Enrique, you are my pride and joy.

And last but certainly not least to my lovely wife Dolores who has been my companion during this long journey. You have always being there for me. “Hasta que se nos hizo.”

Contents

1 Introduction **23**

1.1 Highly Compressed Ion Beams and their Applications 23

1.1.1 Heavy ion fusion (HIF) 25

1.1.2 High energy density physics (HEDP) 30

1.2 Integrated Beam Systems for Highly Compressed Ion Beams 33

1.2.1 HIF driver and small scale experiments 33

1.2.2 The integrated research experiment (IRE) and the integrated beam experiment (IBX) 36

1.2.3 The neutralized transport experiment (NTX) as a first integrated beam experiment 40

1.3 Key findings and thesis organization 43

2 Overview of the Neutralized Transport Experiment NTX **47**

2.1 NTX, a Prototype Integrated Beam Experiment for the Final Focus System for Heavy Ion Fusion 50

2.2 NTX Objectives 52

2.3 NTX Beamline and Parameters 58

2.4 Diagnostics 61

2.4.1 Single and double slit mechanical diagnostics 61

2.4.2 Optical diagnostics 63

2.4.3 Non-interception charge-density diagnostic 64
2.5 Numerical Tools 73
2.5.1 EGUN 76
2.5.2 WARP 76
2.5.3 LSP 78
2.5.4 ImageJ 78

3 Ion Source **81**

3.1 Calculation of the Pierce Electrode Shape for Aberration-free Sheet Particle Guns 81
3.1.1 Cold fluid description of non-relativistic beams 82
3.1.2 Prescription to Find Aberration-Free Gun Geometries 85
3.1.3 Sheet beams and Pierce diode solution for 2-D flow 89
3.1.3.1 Electrostatic potential solution inside the beam. . . . 89
3.1.3.2 Electrostatic potential solution outside the beam. . . 90
3.2 Current transient elimination in one-dimensional diodes 92
3.2.1 Current transient elimination in a one-dimensional planar diode 93
3.2.1.1 Correction of beam head oscillations 96
3.2.1.2 Correction of beam tail oscillations 97
3.2.2 Current transient elimination between concentric spheres . . . 99
3.2.3 Current transient elimination in general geometries 101
3.3 The NTX Variable-perveance Heavy Ion Source 104
3.3.1 Design and performance of a high brightness ion source 104
3.3.2 Current-voltage relation 108
3.3.3 Current transient in the NTX gun 108
3.3.4 Control of secondary electrons 109

4 Matching and Transport in a Magnetic Quadrupole Focusing System 113

4.1 Final Focus Physics and Scaling Relations . . . 113

4.2 The NTX Final Focus Lattice . . . 119

4.2.1 Lattice design . . . 119

4.2.2 Magnetic field modeling . . . 121

4.2.3 Magnet design and fabrication . . . 122

4.2.4 Magnetic field characterization . . . 125

4.3 Beam Matching and Transport . . . 129

4.3.1 Envelope control . . . 133

4.3.2 Energy scan . . . 136

4.4 Sources of Errors . . . 137

4.4.1 Stray electron effects inside the quadrupole lattice section . . 138

4.4.2 Calibration of energy . . . 141

4.4.3 Effectiveness of diagnostic devices . . . 145

4.4.4 Beam halo formation . . . 145

5 Final Neutralized Drift to Target 149

5.1 Ballistic Neutralized Transport . . . 149

5.2 Plasma Source . . . 151

5.2.1 Cathode-arc plasma source . . . 151

5.2.2 Radio-frequency plasma source . . . 157

5.3 Neutralized-drift experiments . . . 164

5.3.1 Beam transport in vacuum . . . 166

5.3.1.1 Uncontrolled neutralization . . . 166

5.3.1.2 Control technique of unwanted neutralization . . . 167

5.3.2 Neutralized transport . . . 172

5.3.2.1 Beam current . . . 178

5.3.2.2 Beam focal plane 178
5.3.2.3 Energy dependence and head-to-tail variation 180
5.3.2.4 Spot size dependence on plasma parameters 181
5.3.2.5 Geometric aberrations 185
5.3.2.6 Spot size dependence on perveance. 186
5.3.3 "Analog simulation" of fully neutralized beam transport 187

6 Conclusions **191**

6.1 Summary 191
6.2 Follow-on Experiments and Future research directions 193

7 References **195**

List of Figures

1-1 IFE power plant. 24

1-2 HEDP facility. 25

1-3 Fusion. 26

1-4 ICF. 27

1-5 IFE targets. 28

1-6 HIF Driver. 29

1-7 Beam quality preservation. 30

1-8 Bragg peak heating. 31

1-9 HIF-Driver-requirements. 34

1-10 High brightness injector for Warm Dense Matter applications. 37

1-11 IRE-schematics. 40

1-12 IBX-schematics. 41

2-1 Geometric and Chromatic aberrations. 48

2-2 Neutralized Final Focus System. 49

2-3 Side view of NTX. 49

2-4 Photograph of the Neutralized Transport Experiment (NTX). 53

2-5 Plan view of NTX 58

2-6 Plan view of the NTX Neutralization Section. 60

2-7 Generic layout of a plasma-neutralization system. 61

2-8 Slit scanner diagnostics. 62

2-9 Optical slit scanner diagnostics. 65

2-10 Typical image from optical diagnostics. 65

2-11 Phase space optical scanner. 66

2-12 Electron beam deflection by ion beam space charge. (a) A transverse cross-sectional view of an arbitrary charge distribution in the x and y directions. Probe electrons of velocity v_x are directed horizontally from left to right ($-x$ to $+x$) at various heights, y, and acquire a velocity v_y orthogonal to v_x, (b) an axisymmetric nonrelativistic charged particle beam which is long relative to its transverse dimensions, and where the charge density is a function of radius only, the electric field E_r at any given radial distance, r, from the beam center will be proportional to the charge enclosed within a concentric cylindrical Gaussian surface of radius r, as shown by the dashed circle. 67

2-13 Sketch of the NTX non-intercepting beam diagnostics. 71

2-14 Photograph of the NTX non-intercepting beam diagnostics. 72

2-15 Transverse displacement of perturbed e-beam trajectory by an ion beam as a function of unperturbed e- beam trajectory. Experimental (solid diamonds) and calculated (hollow circles). 73

2-16 A comparison of the integrated ion beam density profile measurements. The lines with hollow and solid circles show, respectively, the ion beam profiles measured destructively by directly placing a ceramic scintillator in front of the ion beam, and nondestructively using the e-beam diagnostic system. 74

2-17 Codes for beam dynamics simulations. 75

2-18 WARP simulation of the ESQ Injector. 78

3-1 Schematic of a typical ion diode. 81

3-2 Photograph of the emitter and Pierce (focusing) electrode assembly. . 82

3-3 Generic Gun System for Constant Current Density Flow. 87
3-4 Boundary conditions for Generic Gun System for Constant Current Density Flow. 87
3-5 Boundary conditions for exterior solution of Generic Gun System for Constant Current Density Flow 88
3-6 Equipotentials of ψ. 91
3-7 Pierce solution for uniform rectilinear space-charge flow in slab geometry. 92
3-8 Current and energy transient oscillations for the case of a sudden turn-on of the extracting voltage. 94
3-9 Schematic diagram of a planar diode. 95
3-10 Beam head uniform current flow. 97
3-11 Beam tail uniform current flow. 98
3-12 Schematic diagram of a concentric-spheres diode. 99
3-13 Beam head uniform current flow. 101
3-14 Current profile for the 2 MeV injector using the numerically calculated voltage wave form. 102
3-15 Voltage waveform as calculated and used in WARP3D and the corresponding ideal waveforms for the planar, and spherical-equivalent diodes.103
3-16 EGUN simulation of the NTX diode and beam aperture system. . . . 105
3-17 Photograph of the NTX beam scraper system. 105
3-18 Slit integrated NTX ion beam profile. Profile a) is obtained by increasing source temperature, smoothing source surface and biasing aperture. 107
3-19 Measured slit integrated density profile and (x, x') phase space of a high-brightness apertured beam (300 kV, 25mA, 2-cm aperture). The corresponding EGUN calculations are shown to the right. 107
3-20 Measured voltage and current waveforms and verification of the Child-Langmuir law 109

3-21 Electron effect on density 111

3-22 EGUN simulation of ions and electrons in the NTX diode and the scraper system. 112

4-1 Final focus lattice for ballistically neutralized drift. 116

4-2 NTX final focus transport layout. 120

4-3 Symmetrical magnet model with one-half octant shown. 122

4-4 Dominant (a) quadrupole and (b) pseudo-octupole coefficients for the multipole decomposition $B_\perp(r,\theta,z) = G_1(z)r\cos(2\theta)+G_3(z)r^3\cos(2\theta)+$ 123

4-5 Concept for correcting coil winding errors. (a) Single-layer coil normally introduces error currents due to incomplete current loops. (b) Adding a diagonal lead-out can correct this problem and produce nearly perfect fields. 124

4-6 NTX beam-pipe eddy currents and magnetic fields from 2-D finite-element analysis. The linear dimensions indicate the beam-pipe thickness. 125

4-7 Photograph of an NTX magnet during fabrication. 126

4-8 Illustration of the orientation of the windings on the magnetic-field probe. All windings have circular cross sections and consist of two layers. 127

4-9 Oscilloscope traces of the probe output when the supporting cylinder is rotated to place probes at center of the quadrupole windings. The left traces are from loops oriented to sense the radial flux, and the right traces are from loops sensing the azimuthal flux. 128

4-10 Magnet current along with the integrated and calibrated radial field (left), and the corresponding azimuthal field (right). 129

4-11 Calculated and measured NTX quadrupole gradients. 130

4-12 Experimental (top) and WARP-3D simulation (bottom) results of the NTX beam profile and phase-space distribution at exit of channel. . . 134

4-13 Numerical results (right) and camera images (left) of the NTX beam profiles as a function of the quadrupole field configuration. 135

4-14 Numerical results (above) and camera images (below) of NTX beam profiles as a function of the beam energy. 136

4-15 Calculated (blue plus sign) and measured (red diamond) beam sizes at the exit of the final focus system as the beam energy is varied. A factor of 3% is subtracted from the energy used in the calculation. . . 137

4-16 A cylindrical metal mesh inside the beam pipe in the magnetic final focus section. 139

4-17 Mesh current when applying voltage across the mesh. Different lines correspond to different energies, ranging from 244 keV to 320 keV. . . 140

4-18 Beam radius as a function of beam energy as the mesh bias is turned on at ± 2 kV and is turned off. 140

4-19 Typical waveforms of kicker (yellow trace) and kick (green trace) pulses for time-of-flight measurements. The oscilloscope vertical scale is arbitrary, the horizontal scale is 2 μs per division. The magenta and blue traces are auxiliary traces captured in this image. 142

4-20 Space charge wave in NTX for a low-current beam. 143

4-21 The relative difference between TOF beam energy (open squares), resistive divider voltage (diamonds), and capacitive divider voltage readings (0% line) as a function of NTX Marx voltage. Both TOF and resistive divider measurements are shown as a function of capacitive divider voltage. 2% error bars are assumed for both sets of measurements. A linear fit to the data points is also shown for each set of measurements. The voltage indicated by the resistive divider lies between the capacitive divider and the TOF measurements. 144

4-22 Evidence of beam halo formation in the configuration space. Image for a 6% off-energy beam, measured at the end of the final focus system (beam size ∼2 cm) 146

4-23 Evidence of beam halo formation in the velocity space. Image from a pinhole positioned at the end of the final focus system and at the center of the beam, as measured at the focal plane. 146

4-24 Translaminar components originated from non-ideal emitter position with respect to Pierce electrode. 147

5-1 NTX neutralization section layout. 150

5-2 NTX cathode-arc plasma sources mounted on beam pipe. Plasma is injected in the path of the ion beam through openings in the aluminum metal shield. The shield is designed to reduce the magnetic field at the location of the ion beam, to limit plasma entering the quadrupole region, and to prevent macroparticles from the source from entering the beam region. 152

5-3 Ion current signal from the two cathode-arc plasma sources, each operating with 450 A arc current and fed by the same pulse-forming network.154

5-4 Aluminum ion current of ten successive arc pulses collected by an ion collector at the location of the NTX ion beam. 154

5-5 Each point on the I–V characteristic is taken from a single shot of the cathode-arc plasma source. The shot-to-shot variability produces a spread in the data. The ion saturation current can be used to determine the plasma density. 156

5-6 Ion saturation current as a function of NTX cathode-arc dischage voltage. The plasma density varies proportionally with this current. . . . 157

5-7 Axial profile of the plasma density as a function of longitudinal position near the plasma entry ports. 158

5-8 PPPL rf Argon plasma source before installation. Plasma is created in the six-way cross along the ion-beam path. 159

5-9 Time evolution of neutral gas pressure and plasma electron density (solid circles) in the pulsed plasma source. One upgrade under consideration is replacing the gas valve with a faster one to reduce the length of the gas puff and the total amount of gas into the system. Another upgrade would use a pulsed rf supply to increase the rf power level. . 161

5-10 Plasma density profile transverse to the plasma source in the six-way cross. 162

5-11 Plasma density in the transverse direction, towards the rf power source, showing a steep gradient. 163

5-12 Electron density in the center of the cross as a function of rf power. . 163

5-13 LSP simulation schematic. 165

5-14 Beam images for a 255 keV beam measured 1m downstream, transported through a tube of diameter a) 15 cm and b) 7.6 cm. 166

5-15 Cylindrical metal mesh of outer diameter 6.3 cm is installed inside a 7.6 cm diameter beam drift tube. 168

5-16 Beam diameters corresponding to beam energies as measured in the (a) x-axis and (b) y-axis by varying mesh bias, and (c) a comparison of beam size for a 255-keV beam transported through a 15-cm tube (dotted lines for the x-y axis) and a mesh included 7.6 cm diameter tube (solid lines for the x-y axis) with bias 250 V. 170

5-17 Current in the mesh as the mesh bias is varied during a 255-keV beam pulse. 172

5-18 Beam profiles for vacuum transport as function of increasing energy (240 keV to 310 keV) from (a) WARP calculations (b) experimental measurements for transport through a 15 cm diameter tube, and (c) experimental measurements for transport through a 7.6 cm diameter tube using mesh bias of +1 keV. 173

5-19 NTX spot-size dependence on the neutralization mechanisms. Beam images (top row) and density distribution (bottom row) at the focal plane for three cases of space-charge neutralization for a high perveance (6×10^{-4}) 24 mA, 254 keV K^+ ion beam: a) non-neutralized, b) plasma plug neutralized, and c) plasma plug and RF volume plasma neutralized. 175

5-20 Calculated (a) radius and (b) emittance of NTX beam from the WARP-LSP simulations of neutralization by a plasma plug alone and combined with a volume plasma near the focal point. The rms focal-spot radius is 1.3 mm with the plug only and 0.9 mm with both plasmas. 176

5-21 Comparison of experimental (top) and numerical (bottom) results of the NTX spot-size dependence on the neutralization mechanisms. . . 177

5-22 Comparison of a radial density profile from an unneutralized NTX shot with a theoretical profile (magenta) from an LSP simulation. 178

5-23 Measured beam current. The solid circles represent the currents measured at the entrance of the 1m final transport section; the solid diamonds represent the currents measured at the end of the 1m drift section; and the hollow circles represent the currents measured when beam is neutralized using the MEVVA plasma plug. 179
5-24 Axial beam envelope variations in (a) 7.6cm drift tube (mesh with +250 V bias), and (b) theoretical calculation (without mesh). 180
5-25 Spot size as a function of energy as measured in NTX. 181
5-26 Beam images from head-to-tail taken at the focal plane, showing blow up of the beam head and tail. 182
5-27 Spot size variation from head-to-tail measured at the focal plane, showing blow up of the beam head and tail. 183
5-28 Comparison of radial density profiles from two plasma-neutralized NTX shots with a theoretical profile (magenta) from an LSP simulation. . . 184
5-29 (a) Neutralized beam radius vs. plasma discharge voltage, and (b) comparison between experimental and theoretical radial distribution profiles. 185
5-30 Spot size as function of convergence angle as measured in NTX. . . . 186
5-31 Spot size dependence on perveance as measured in NTX. 187
5-32 Ballistic propagation of the fully neutralized NTX beam by propagating the 4-D phase space down to the focal plane. Images from top left to bottom right correspond to beam profile at 5 cm steps starting from the pinhole plane and ending at the focal plane. 188
5-33 Analog (pinhole) simulation (left) and WARP calculation (right) of fully neutralized NTX beam focused to a small spot. Each image box is a 4-cm by 4-cm square. 189

THIS PAGE INTENTIONALLY LEFT BLANK

List of Tables

4.1 NTX quadrupole magnet parameters 123

THIS PAGE INTENTIONALLY LEFT BLANK

Chapter 1

Introduction

1.1 Highly Compressed Ion Beams and their Applications

High brightness heavy ion beams are required in several applications in which a large amount of power is delivered in a small volume. The two applications which motivate the present work are Heavy Ion Fusion (HIF) and High Energy Density Physics (HEDP). The Heavy Ion Fusion Program has been working for three decades (starting in 1976) to design a HIF driver that will accelerate heavy ion beams and focus them to a small spot to implode a DT target by inertial confinement. A possible scenario would be to accelerate 120 ion beams to an energy of 4 GeV and a total current of 10 kA, compress them to short pulses of 8 ns, and focus each beam to a spot size of 2 mm, achieving a peak deposition of $10^{12} J/m^3$ (Figure 1-1). The Heavy Ion Fusion Virtual National Laboratory (HIF-VNL) is also developing the intense ion beams needed to drive matter to the regimes required for High Energy Density Physics. A possible scenario for accessing the Warm Density Matter regime (temperatures of 1–10 eV) would be to accelerate one beam of single charged Neon ions to an energy of 30 MeV and a current of 1–2 kA, compress it to a short pulse of

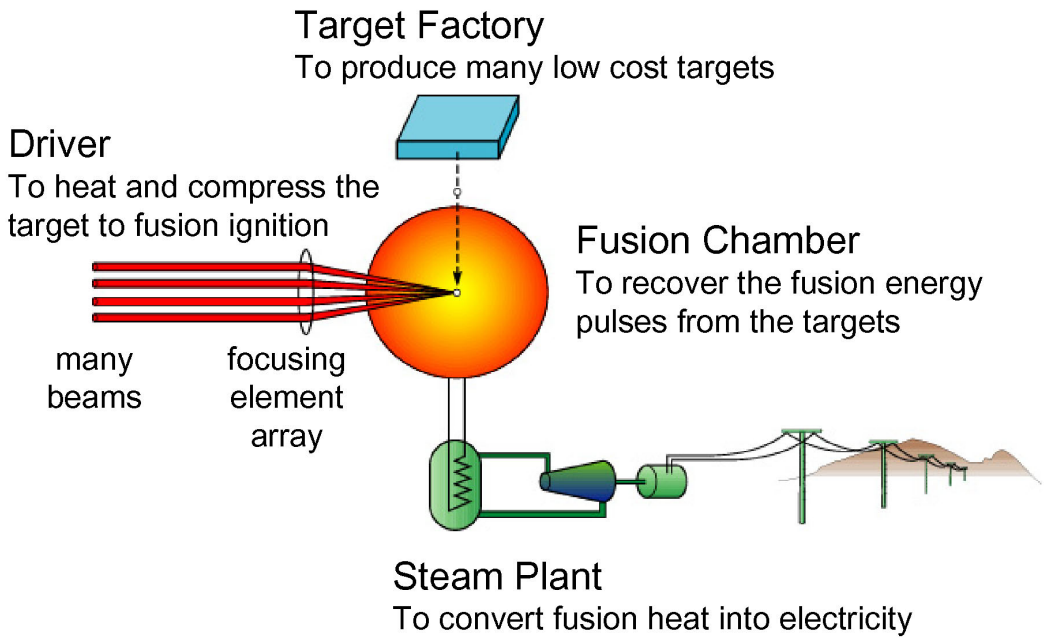

Figure 1-1: IFE power plant.

0.5–1.0 ns, and focus the beam to a spot size of 1 mm, achieving a peak deposition of $10^{11} J/m^3$ (Figure 1-2).

The common beam physics required to obtain such densities involves high brightness beam injection and acceleration, neutralized drift compression, and final focus optics that can generate the necessarily small focal spots in space and time. Accelerators producing appropriately tailored energy profiles of intense heavy ion beams can provide a useful tool for creating uniform high energy density matter to study the strongly coupled plasma physics of warm dense matter in the near term, and for inertial fusion in the longer term. Both fusion and high energy density physics applications of heavy ion beams require understanding the fundamental physics limits to the compression of ion beams in both space and time before they reach the target, as well as a basic understanding of collective beam-plasma interaction processes and beam energy deposition profiles within the dense plasma targets.

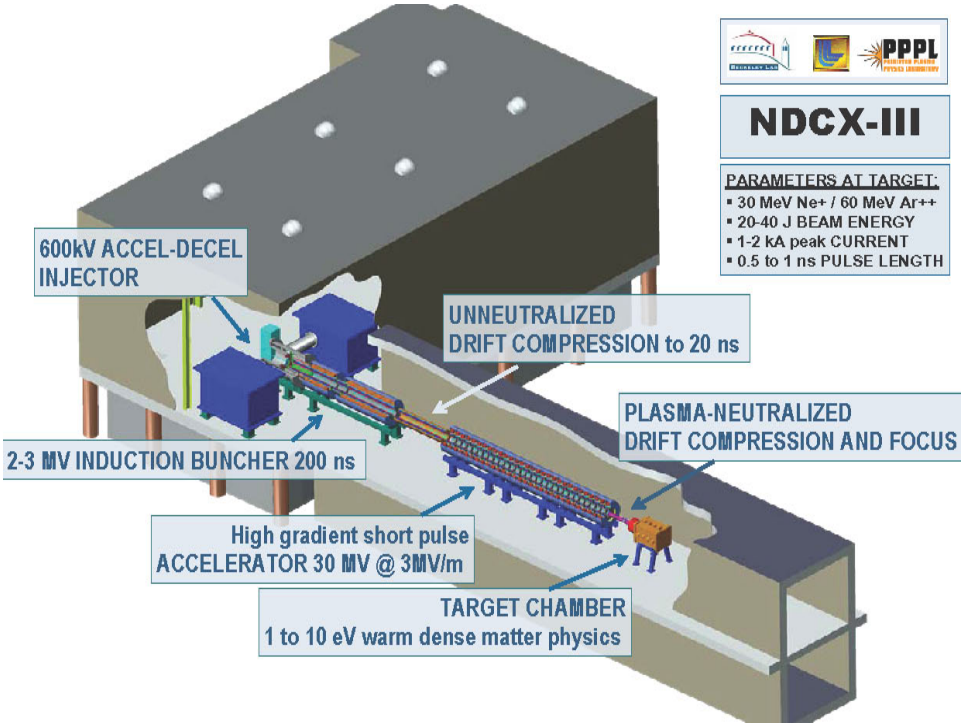

Figure 1-2: HEDP facility.

1.1.1 Heavy ion fusion (HIF)

Fusion is the reaction in which two light atoms, such as atoms of hydrogen, combine or fuse to form a heavier atom, such as an atom of helium (Figure 1-3). In the process, some of the mass of the hydrogen is converted into energy. Hydrogen atoms repel each other due to the electrical charge of their core or nucleus. For fusion to occur, the atoms of hydrogen must be heated to extremely high temperatures (millions of °C) so they have enough thermal energy to overcome this repulsion, and then they must be held together or confined long enough for fusion to occur.

The US Department of Energy (DOE) supports two major fusion-research programs, one based on the magnetic confinement of large volumes of low-density fusion fuel, the other on the inertial-confinement of small, high-density targets of the same fuel. With the magnetic confinement fusion, strong magnetic fields hold the electrically charged or ionized atoms together as they are heated. With the inertial con-

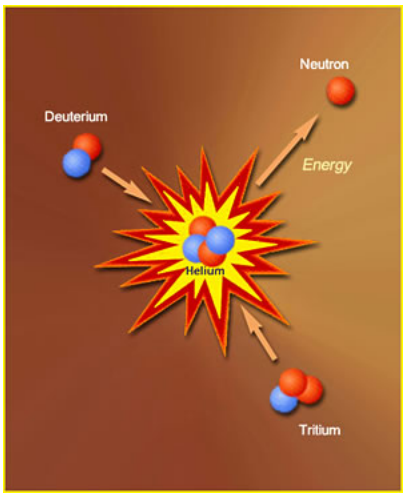

Figure 1-3: Fusion.

finement fusion (ICF), a tiny pellet of frozen hydrogen is compressed and heated so quickly that fusion occurs before the atoms can fly apart, so the reaction is confined, in effect, by the inertia of the fuel. With ICF (Figure 1-4), the fuel capsule consists of a hollow shell of frozen deuterium, and tritium which is set inside a chamber a few millimeters in size. This frozen shell of thermonuclear fuel is surrounded by an outer "ablation" layer that is rapidly heated by energetic laser or charged-particle beams until it turns to plasma. The plasma flying out from the ablation layer implodes the fuel, compressing its density about a thousand times and causing it to burn. If the fuel burns rapidly enough, it is confined by its own inertia and requires no external confinement system. This confinement lasts long enough for the reaction to produce energy.

In July of 1976, a meeting was held in Berkeley, California, to discuss an idea for using accelerator technology to produce fusion energy that was first proposed by Alfred Maschke and Denis Keefe [1]. The issue discussed was whether intense, short bursts of high powered heavy ion beams could ignite thermonuclear fuel confined by its own inertia so as to produce a net gain of energy. The implosion that ignites the fuel is set off or driven by high-powered beams of heavy ions such as xenon, mercury,

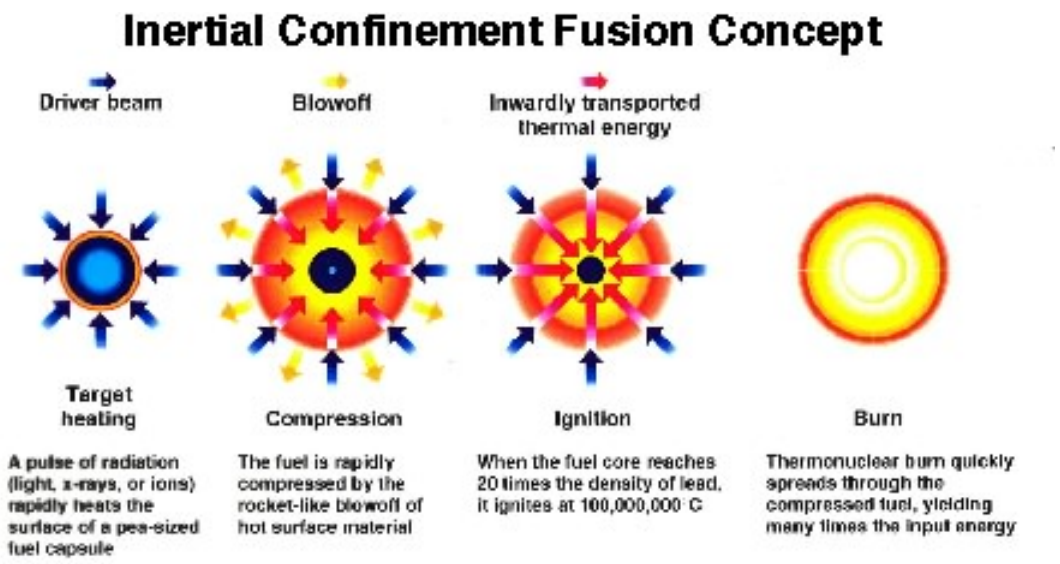

Figure 1-4: ICF.

or cesium, which are focused on the capsule. At such a high current, space-charge forces–the mutual repulsion among so many positively charged ions–become a serious impediment. The accepted solution is to simultaneously bombard a fuel capsule with a large number of independently focused, lower current beams. Since that date, scientists and engineers in the USA, Europe and Japan began working on techniques of accelerating, transporting, and focusing heavy ion beams at higher currents than ever before.

The fusion target most compatible with HIF is the so-called "indirect drive target" which consists of a metal shell or Hohlraum containing a spherical shell of frozen thermonuclear fuel (Figure 1-5). The heated Hohlraum emits intense X-rays that compress the fuel capsule to thousands of times its initial density and heat it, near the center, to thermonuclear temperatures. The key requirement for the beams used to heat an inertial-fusion target is power density. During the brief time the target is being heated, energy must be deposited at a rate of about $4 \times 10^{14}\ W$.

In principle, both lasers and beams of charged particles are able to meet this requirement. To date, most research has focused on developing high-power lasers to

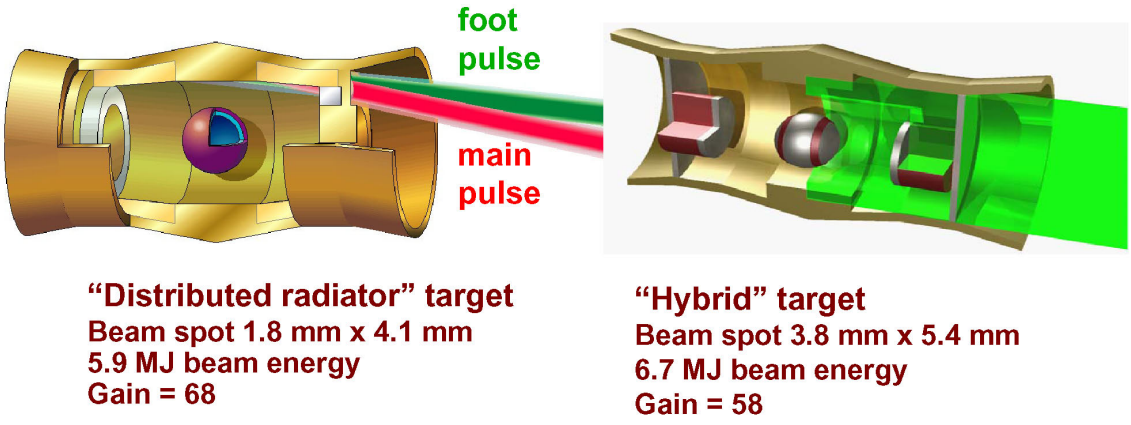

Figure 1-5: IFE targets.

study target ignition, like in the National Ignition Facility (NIF), which is currently the most important physics issue for inertial fusion. Proof-of-principle experiments like these, however, are designed to operate at few shots per day, so repetition rate and efficiency are unimportant. Commercial energy production imposes additional requirements on an inertial-fusion driver. Besides producing the required power density, a commercial driver must also have an adequate repetition rate and be efficient and reliable. These added requirements are best satisfied by ion accelerators. Accelerators have been shown to work reliably at high repetition rates for ten years or more, giving them a better demonstrated reliability than large laser systems. For these reasons, committees chartered by the US Department of Energy and by Congress have identified ion accelerators as the most promising drivers for inertial-fusion power plants. Ion drivers for fusion are expected to share the same basic technology of existing accelerators; however, the unusual demands for very large instantaneous beam power and a small ($\sim$3 mm) focal spot require a substantial revision of conventional designs. A low transverse beam temperature or emittance is essential for a small focal spot, so low-temperature injectors with a high current density are being developed. To manage the large space charge of the ions, conceptual designs accelerate many beams

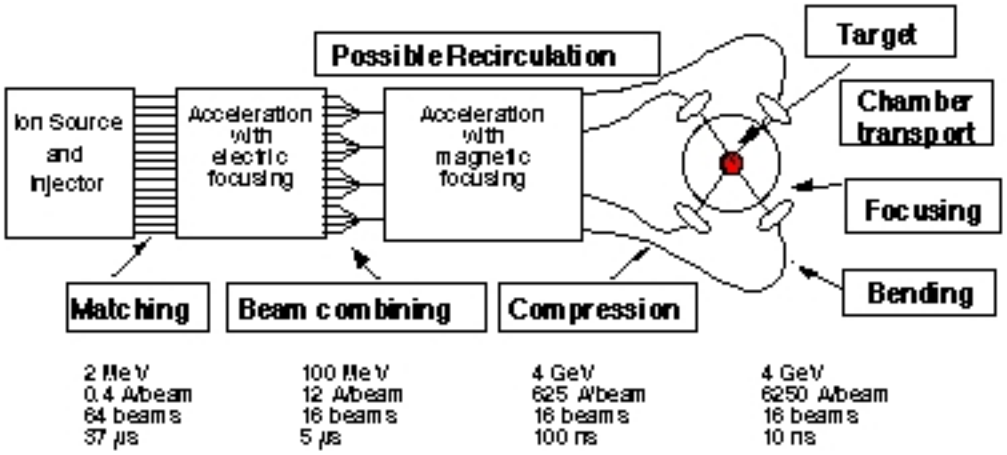

Figure 1-6: HIF Driver.

in parallel, which also require the beam duration to be reduced from its initial value, by about three orders of magnitude. Much of the present research is directed toward meeting these stringent requirements.

A schematic diagram of a generic induction accelerator designed to produce 100 kA of cesium ions at 4 GeV is shown in Figure 1-6. To achieve 100 kA, it uses several methods: multiple beams, beam combining, acceleration, and longitudinal bunching. The accelerator systems and beam manipulations found in typical heavy-ion driver designs are represented by boxes. Typical ion kinetic energy, beam current, and pulse length at various points in the accelerator are also shown in Figure 1-6.

Typical parameters at the target are: Total Beam Energy of 5 MJ, Focal Spot Radius of 3 mm, Ion Range of 0.1 g/cm^2 (1 mm in typical materials), Pulse Duration of 10 ns, Peak Power of 400 TW, Ion Energy of 3–10 GeV, Current on Target of 40 kA (total), Ion Mass of 200 amu. The target chamber and final focus requirements add more constraints: Target yield requires the repetition rate to be about 5 Hz for an attractive power plant of $\sim$1 GW. Thermal and mechanical stresses require the standoff from the target to the wall to be about 5 m. Chromatic aberration of optical system requires the energy variation to be less than 0.3%. Standoff and spot size

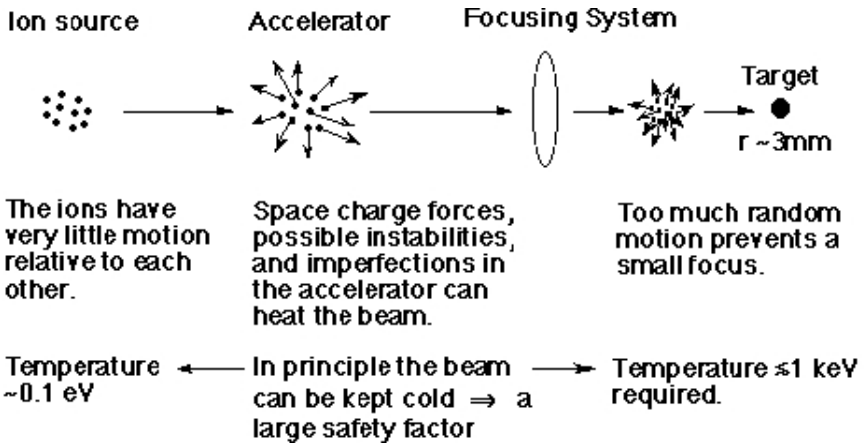

Figure 1-7: Beam quality preservation.

require the transverse beam temperature to be less than 1 keV.

There are many scientific and technical challenges that remain before a practical HIF power plant can be realized. The main scientific challenge (Figure 1-7) is to accelerate, compress and focus short bunches of heavy ion beams at high beam currents and high peak-power levels required to drive targets, while preserving high beam brightness (i.e., highly parallel motion of ions co-moving within the ion bunch) sufficient to focus onto targets of a few millimeters in size. Another scientific challenge is to understand how the intense ion-beam pulses interact with a low-density gas and plasma in the fusion chamber while they travel to the target.

1.1.2 High energy density physics (HEDP)

High Energy Density Physics is a new frontier of physics with multiple applications. The physics and applications of this new discipline are described in detail in two recent reports [2,3]. Of particular interest to the ion beam community is the Warm Dense Matter regime (1–10 eV) where the plasma is strongly coupled.

Heavy ion beams have a number of advantages as drivers of targets to create matter with extremely high energy density. First, heavy ions have a range exceeding the mean-free-path of thermal x-rays, so that they can penetrate and deposit most of

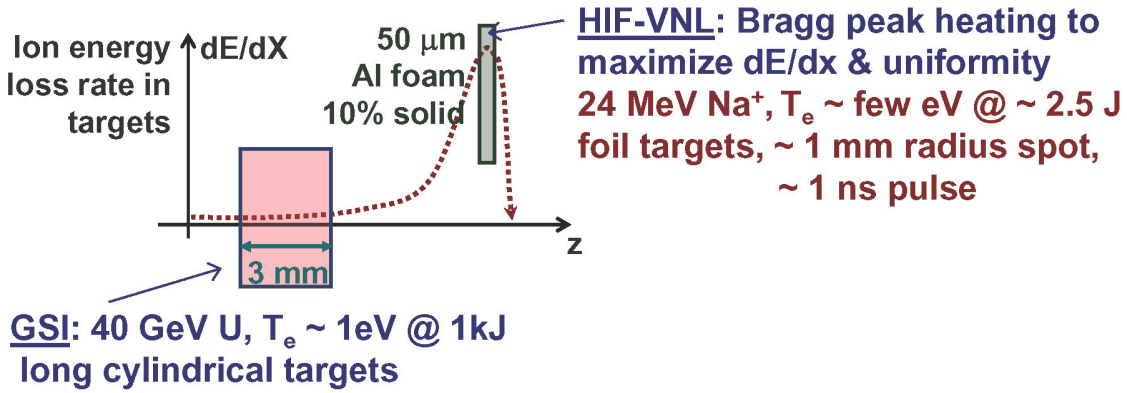

Figure 1-8: Bragg peak heating.

their energy deep inside the targets. Second, the range of heavy ion beams in dense plasma targets is determined primarily by Coulomb collisions with the target electrons; the ions slow down with minimal side-scattering, and their energy deposition has a pronounced peak in the rate of energy loss dE/dx that increases with the beam ion charge state Z. Also isochoric heating of substantial volumes to uniform, elevated temperatures are expected to be achievable using heavy ion beams. These properties make heavy ions an excellent candidate for high energy density physics studies, where thin target plasmas would be uniformly heated by locating the deposition peak near the target center (Bragg peak heating). Figure 1-8 shows the technique used in experiments at the Gesellschaft fuer Schwerionenforschung (GSI) in Germany, and the technique proposed for the experiments at HIF-VNL.

The primary scientific challenge in exploiting these desirable properties in the creation of high energy density matter conditions in the laboratory is to compress the beam in time (by 1000 times overall, requiring 10–100 times more longitudinal bunch compression than the present state-of-the-art) to a pulse length that is short compared to the target disassembly time, while simultaneously compressing the beam in the transverse direction (by 10 times) to a small focal spot size for high local deposition energy density. Proposed new experiments, like the Neutralized Drift

Compression Experiments (NDCX series) [4], compressing intense ion beams within a neutralizing plasma would significantly extend the beam current into high-intensity regimes where the beam would not otherwise propagate in the absence of background plasma, and where beam-plasma collective effects with longitudinal and azimuthal magnetic focusing fields have not been previously explored. For low energy ions (in the few to tens of MeV range), requirements to study strongly-coupled plasma properties in the warm dense matter regime are: target foils of thickness a few to tens of microns, 1 to 20 Joules (in a single beam), 0.5 to 10 eV temperature, 0.2 to 2 nanosecond final pulse duration, and 0.5 to 2 mm diameter focal spot size.

A basic understanding of the collective processes and nonlinear dynamics of intense, high-brightness, heavy ion beams, and a determination of how best to create, accelerate, transport, compress and focus these beams to a small spot size are critical to achieving the scientific objectives of heavy ion fusion and ion-beam-driven studies of warm dense matter. Most of the kinetic energy of heavy-ion beams is in the directed motion of the beam particles, but a small fraction is in random kinetic energy, characterized by the effective temperature of the beam particles. Plasma electrons can be used to neutralize much of the repulsive space charge that resists the beam compression in time and space, but the beam temperature ultimately limits the smallest achievable spot size and pulse duration after the space charge forces are removed from the beam inside plasmas. To minimize the beam temperature, and thereby maximize the energy deposition in the target, the beam dynamics must be controlled with high precision throughout the entire dynamical trajectory, using accurately positioned and tuned confining magnets, carefully tailored accelerating fields, and final charge neutralization techniques that do not degrade the beam quality.

Accelerators for both high energy density physics and fusion must initially inject sufficiently bright (low temperature) beams, accelerate the heavy ions to the desired energy range, and then longitudinally compress and radially focus the beams onto the

target with minimal growth in the longitudinal beam temperature (much less than a factor of 10 to allow overall axial bunch compression by a factor of 100 or more), and with minimum transverse temperature growth (much less than a factor of 10 to allow radial focusing by more than a factor of 10).

1.2 Integrated Beam Systems for Highly Compressed Ion Beams

The concept of integrated beam systems, which follow an ion beam from the source to the target, is a key aspect for achieving the HIF and HEDP goals. The ability to produce a highly compressed ion beam at the target depends ultimately on our understanding of the ion beam history from the source, through the accelerator and the final focus systems, to the target. The development path towards an ultimate HIF or HEDP driver has to involve several intermediate proof-of-principle experiments. The Integrated Research Experiment (IRE) [5] and the Integrated Beam Experiment (IBX) [6] described in Section 1.2.2 are two projects that have been proposed. The Neutralized Transport Experiment (NTX), the subject of the present thesis, may be considered the first of such integrated beam experiments (see Section 1.2.3). Before we consider these integrated beam experiments, we review in Section 1.2.1 the driver issues addressed in the past with small scale experiments.

1.2.1 HIF driver and small scale experiments

In order to accelerate enough ions to deposit the $\sim$5 MJ of energy needed to implode and ignite the target, while minimizing the diameter (and therefore the cost) of the accelerator, the accelerated beams must be very intense. Thus one major task of the heavy ion fusion research program is to determine the stability and behavior of these intense beams. Since the charge can not be transported economically in a single

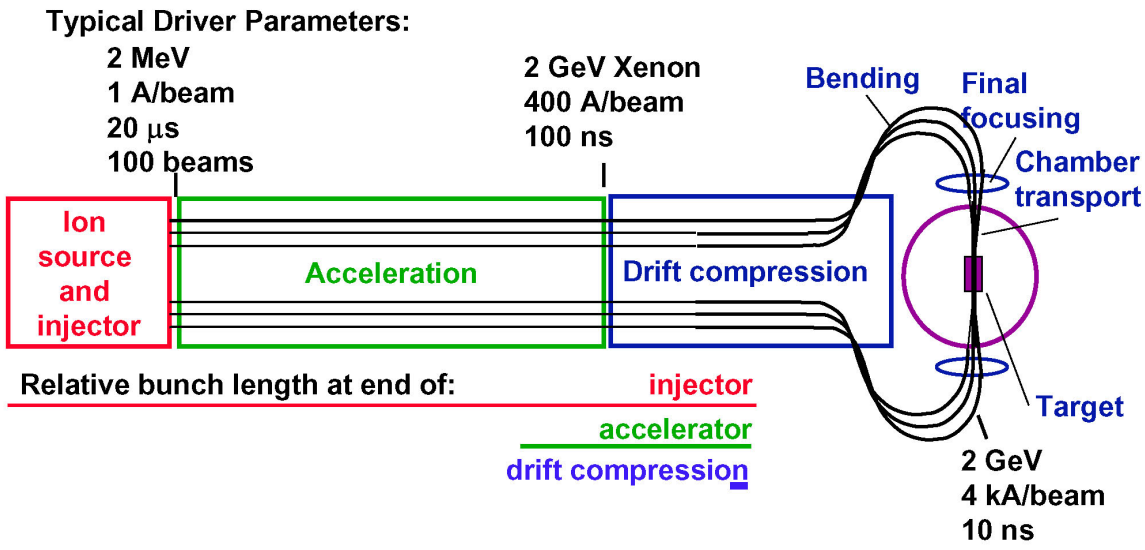

Figure 1-9: HIF-Driver-requirements.

beam, the accelerator must transport in parallel a large array of beams ($\sim$ 30–100, depending on design). Cost optimization gives a time duration for the beams of tens of microseconds at the beginning of the accelerator. The beams must arrive at the final focusing system with low enough transverse temperature (emittance) that they can be focused to the small spots required, and low enough longitudinal temperature that aberrations in the final lens system do not enlarge the spot. The basic issues fundamental to feasibility of heavy ion fusion drivers therefore are those of producing low-emittance intense beams, maintaining good beam quality while accelerating to a few GeV and performing all necessary beam manipulations including a) bending the beam trajectory, b) compressing the beam longitudinally, and c) transporting the focused beam through the target chamber environment without degrading the focal spot (Figure 1-9).

The HIF-VNL has addressed many of these fundamental issues in small, relatively inexpensive experiments where relevant physics parameters, as the beam perveance,

important to particle dynamics are in the same range as in the driver, but the beam is at low energy. Using this approach of small experiments at low kinetic energy, the Heavy Ion Fusion program has investigated the stability of intense beams, including the emittance growth inherent in beam shape and profile changes; the interaction of the intense beam with the walls through image charge effects, and the effect on the beam of certain beam manipulations such as longitudinal compression, transverse combining of beams, and focusing to a spot.

These were experiments with ion density in the driver parameter range, and with sufficient length to allow evolution of beam emittance over several cycles of the frequencies of interest; but they were far from the parameter range of the driver in other key features, and therefore could not explore certain issues.

There is a class of important phenomena which can also be explored at low energy, in short length experiments, but which requires high current beams. With driver-scale beam radius comes a high space-charge potential, so that the beam can interact strongly with any electrons produced. Three experiments are investigating the interaction of intense beams with electrons. The High Current Experiment (HCX) [7] is measuring the quantity and orbits of electrons produced if the beam is allowed to scrape the vacuum wall (electron cloud effects). The Neutralized Transport Experiment (NTX) [8] has been conducted to study neutralization-assisted focus of an intense ion beam to a small spot. And the Neutralized Drift Compression Experiment (NDCX1) [9] which studies the longitudinal compression of intense ion beams by factors of over an order of magnitude. When these high-current low-energy experiments conclude, the program will have demonstrated the production, stable transport, acceleration, compression, beam neutralization using plasmas, electron production and control, and the final focus of intense space-charge-dominated beams. For each of these processes, phase space changes have been measured and matched with extensive particle-in-cell computer simulations.

The HIF-VNL has made advances over the past several years that include: (i) high current ion sources and injectors (0.1 to 1 A of potassium) that have been shown to have adequate initial beam brightness (sufficiently low transverse and parallel temperatures) to meet the requirements at injection [10]; (ii) negligible beam brightness degradation has been observed in the transport of 200 mA potassium ion beams through electric and magnetic quadrupole focusing lattices including control of electron cloud effects [7]; (iii) more than 95% of potassium beam space charge has been neutralized with a preformed plasma over ∼1 meter lengths without deleterious beam-plasma instabilities [8], and (iv) longitudinal compression of intense ion beams [9].

A high brightness heavy ion accelerator for creating powerful beams to study warm dense matter is also being designed at LBNL [11]. The components are an injector that delivers $\sim 0.1\mu C$ of lithium beam, and an accelerator that boosts the energy to about 3 MeV. Further beam manipulations will compress the beam to a final spot radius of 1 mm and a pulse length of 1 ns. In order to reach those final parameters, it is required to extract a high brightness beam and minimize the transverse and longitudinal emittance growth along the accelerator. The injector is based on the Accel-Decel concept [11] which enables the extraction of a high line charge density beam from the ion source, and the accelerator is based on the Pulse Line Ion Accelerator concept [12], which uses a slow-wave structure based on a helical winding, on which a voltage pulse is launched and propagated to generate the accelerating fields (Figure 1-10).

1.2.2 The integrated research experiment (IRE) and the integrated beam experiment (IBX)

The U.S. Heavy Ion Fusion program has considered building a set of proof-of-principle experiments which will demonstrate the feasibility of all driver beam manipulations

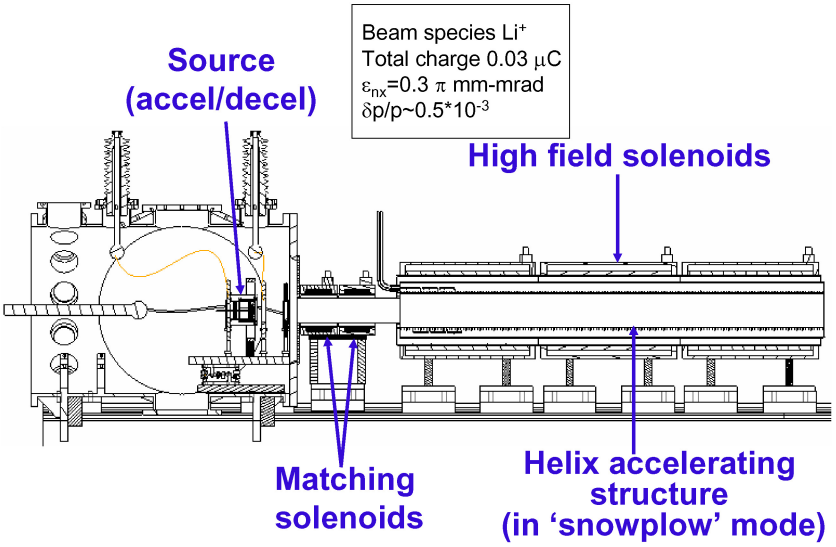

Figure 1-10: High brightness injector for Warm Dense Matter applications.

which can be investigated at small scales. An intermediate-scale experiment, the Integrated Beam Experiment (IBX) [6], is an experiment which would access important areas of physics, and constitute an integrated test of much of the physics of the driver. It would produce a base of data and experience which would lay the groundwork for a larger, proof-of-performance experiment, the Integrated Research Experiment (IRE) [5], a proof-of-performance experiment which would demonstrate all the physics and technology necessary for a driver (Figure 1-11).The IRE must address a wide variety of scientific issues. Some of these issues are associated with high intensity beam physics in the accelerator itself. In particular, the IRE must determine and, if possible, expand the limits on long-term transverse and longitudinal beam dynamics. It must measure transverse and longitudinal emittance growth. It must determine under what conditions there are longitudinal instabilities. If these instabilities are deleterious, it must provide a vehicle to develop countermeasures, e.g., feedback stabilization. The IRE must allow us to study halo formation and its effect on required beam clearance. It must allow us to study effects associated with high intensity beams such as the presence of unwanted electrons (electron cloud effects). There are also important

issues in the target chamber. Most heavy ion fusion concepts have, in the past, been designed to operate at sufficiently high kinetic energy that beam neutralization in the chamber is not required. Operation at lower kinetic energy (actually lower voltage) leads to lower cost for induction linacs but requires beam neutralization. The IRE must be capable of validating the unneutralized propagation mode and it must be capable of definitive research on the neutralized propagation modes such as neutralized ballistic focusing and the various channel transport modes. The IRE must be capable of addressing remaining target physics issues such as validating our understanding of the beam-plasma interaction. Additionally, it would be desirable to be able to study target physics issues such as fluid instabilities in direct drive and other topics in high energy density physics.

Though each fundamental beam manipulation has been individually explored in separate small scale experiments, in the driver they will be sequential, and the errors and changes in the beam distribution function which result from previous manipulations will be fed in as initial perturbations to the next area of transport. The integration of all beam manipulations in a single small scale experiment will be one of the chief scientific missions of the Integrated Beam Experiment (Figure 1-12). As a result, the experiment will also benchmark computer codes which will be used to design future experiments with end-to-end computer simulation. The science issues which could not been investigated in previous small scale experiments are those which require high energy, multiple beams, and long length scales. Simply extending the length of the accelerator offers entry into significant new physics without the higher cost of accelerating to near driver scale energy or adding a large number of beams. This is the choice that the Integrated Beam Experiment would represent. With one, or a few, beams accelerated to tens of MeV ($\sim$1/300 of the energy of a driver beam), which means propagation over $\sim$70 meters, it would be possible to include all driver beam manipulation sections (Figure 1-12) and test the integrated source to target

physics. New phenomena that can be studied in such machine include longitudinal wave production and propagation during acceleration and longitudinal pulse compression, and the beam emittance growth caused by these waves; longitudinal-transverse coupling; effects of electrons on the ion beam; production of beam halo; evolution of the shape of the beam head and tail, and production of longitudinal waves by this process; long-length-scale emittance growth; investigation of limits to acceleration rate; upstream correction of beam aiming at the final focus.

The main differences between the IBX and the IRE are consistent with this difference in scale, capability, and mission. They are: (1) the final kinetic energy of the IRE would be a few 100 MeV, while for the IBX we envision 5–20 MeV, (2) the IBX pulse length would be much shorter than that in the IRE in order to save induction acceleration core cost, and (3) the IRE would be a significant multibeam experiment ($\sim$30–100 beams), where the IBX is expected to have 1–to–a–few beams. The difference in number of beams and final kinetic energy imply a vast difference in total current in the two experiments. The scientific mission of the IRE covers the beam physics which can only be done at high energy or with the high total current implied by high energy and large numbers of beams. Most of the multiple beam physics of the driver would be studied first on the IRE, especially inductive effects that occur only at high velocity, and the interaction of multiple beams and the electrons neutralizing them in the target chamber. The effect on the longitudinal stability of the interaction of the beams with the induction cores is another important topic. This "beam loading" will be negligible in the IBX because of low beam velocity and the small number of beams. The study of electron accumulation in the beam requires a long pulse length, and therefore though much electron physics could be explored on the IBX, a significant part of the problem remains for the IRE. The IRE would also give the first transport for lengths of the order of the driver length, providing a definitive test of the effect of long transport on beam quality. For this reason much

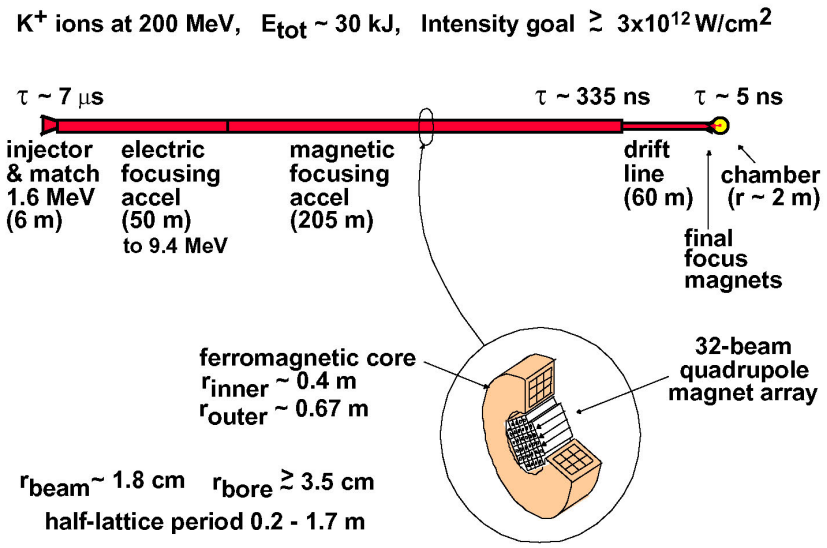

Figure 1-11: IRE-schematics.

of the physics first explored on the IBX would be tested again over long length scales in the IRE. Finally, the IRE is expected to be capable of exploring some heavy-ion target-interaction physics, while the IBX will not have the kinetic energy for this mission. The IRE would be capable of upgrade to an Engineering Test Facility (ETF) which could test target chamber design.This is a key step for heavy ion fusion, which would integrate the physics of previous experiments and introduce new capability for exploration of physics of high importance to the program.

1.2.3 The neutralized transport experiment (NTX) as a first integrated beam experiment

In preparation for the design and construction of the IBX and IRE, the Neutralized Transport Experiment (NTX) has been designed to be the first integrated beam experiment for the production of high energy density beams. NTX provides the first experimental validation of neutralized ballistic transport of a space-charge-dominated beam. It is an integrated beam experiment in the sense that the final focal spot

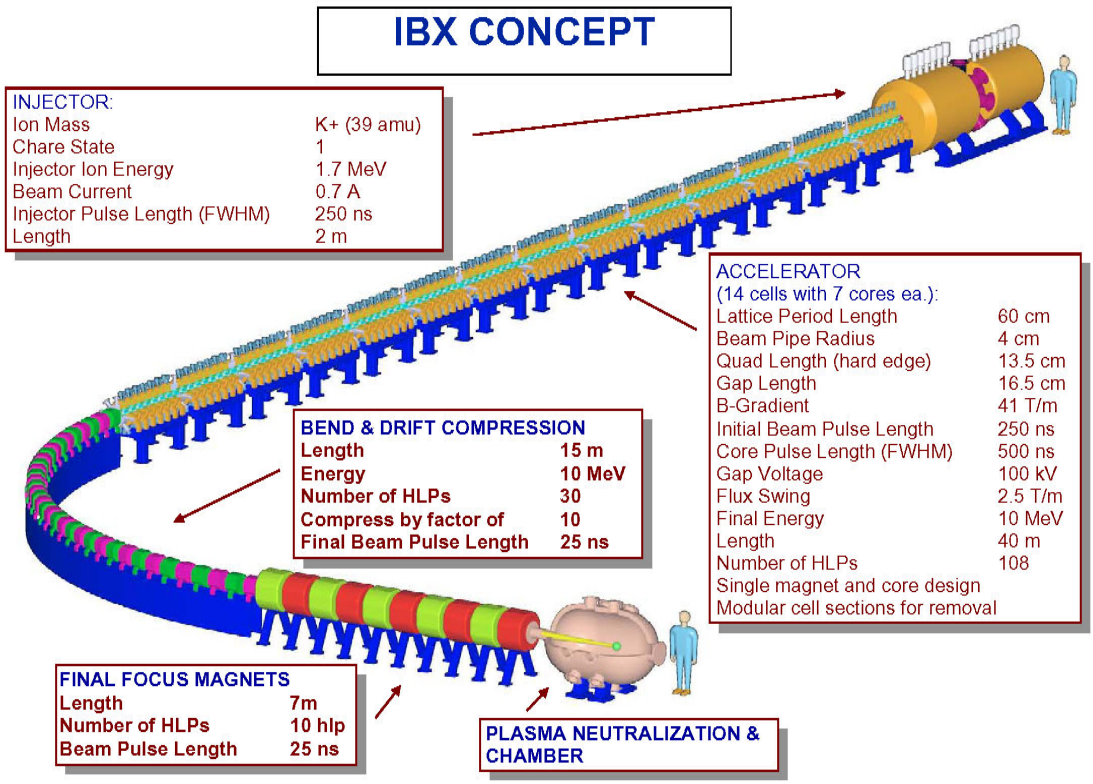

Figure 1-12: IBX-schematics.

size depends not only on the physics of neutralized ballistic transport but also on the production of a high brightness source, and an understanding of the quadrupole focusing system immediately upstream of the neutralized drift section. In support of the NTX experiment, we have also developed and calibrated end–to–end simulations that will be essential for future integrated experiments.

Although the NTX experiment uses a beam that is orders of magnitude lower in current than a driver for heavy-ion fusion, a careful choice of parameters guarantees that the transport physics closely matches that of a full-scale system. This beam is required to hit a millimeter-sized target spot at the end of the drift section. The objective of the NTX experiment and associated theory and simulations is to study the various physical mechanisms that determine the final spot size (radius r) at a given distance (f) from the end of the last quadrupole. In a fusion driver, f is the standoff distance required to keep the chamber wall and superconducting magnets properly protected. The NTX final quadrupole focusing system produces a converging beam at the entrance to the neutralized drift section where it focuses to a small spot. The final spot is determined by the conditions of the beam produced at the source before entering the quadrupole section, the beam dynamics in the magnetic lattice, and the plasma neutralization dynamics in the drift section. The main issues are how to control the emittance growth due to high order fields from magnetic multipoles and image fields. This system serves as a prototype from which larger integrated systems can evolve.

To date, beam-transport experiments through the NTX final-focus system have produced high-perveance beams with the emittance and convergence angle needed for chamber-transport experiments. These first experiments have demonstrated dramatically improved focusing by passing the beam through a low-density plasma produced by a metal-arc source and have studied the effects of a second plasma near the beam waist, mimicking the effects of a photo ionized plasma near the fusion target. We have

also compared the experimental findings with the results of numerical simulations. In parallel to the transport experiments, two new diagnostic tools were developed. The first, a refinement of the conventional "pepper-pot" imaging technique, gives a detailed time-resolved view of the 4-D transverse phase space for beams that have good pulse-to-pulse reproducibility. Using this technique to map the 4-D phase-space distribution at the exit of the NTX final-focus system provides initial conditions for more realistic simulations of the neutralized-transport experiments. The other tool is a non-intercepting diagnostic that uses a low-energy electron beam directed across the NTX beam line to map out the transverse charge distribution of the ion beam. Both diagnostic techniques provide information about the structure of the NTX beam and facilitate our understanding of neutralization physics.

1.3 Key findings and thesis organization

This thesis describes the physics design, numerical simulations, construction and experimental results of the Neutralized Transport Experiment (NTX) built at the Heavy Ion Fusion Virtual National Laboratory. NTX is the first successful integrated beam system experiment that explores various physical phenomena, and determines the final spot size of a high intensity ion beam on a scaled version of a Heavy Ion Fusion driver. The final spot size is determined by the conditions of the beam produced in the injector, the beam dynamics in the focusing lattice, and the plasma neutralization dynamics in the final transport. A high brightness ion source using an aperturing technique delivers 25 mA of single charged potassium ion beam at 300 keV and a normalized edge emittance of 0.05 π mm-mr. The ion beam is injected into a large bore magnetic quadrupole lattice, which produces a 20 mm radius beam converging at 20 mr. The converging ion beam is further injected into a plasma neutralization drift section where it is compressed ballistically down to a 1 mm spot size.

NTX provides the first experimental proof of plasma neutralized ballistic transport of a space-charge dominated ion beam, the information about higher order aberration effects on the spot size, the validation of numerical tools based on excellent agreement between measurements and numerical simulations over a broad parameter regime, and the development of new diagnostics to study the ion beam dynamics. The theoretical and experimental results are presented on the beam dynamics in the ion diode, downstream quadrupole lattice, and final neutralized transport.

The main contribution of this thesis is the conclusion that a challenging problem as is the concentration of a large amount of particles in a small space can be accomplished by following a careful integration of theory, design, computer simulations and experimental measurements to produce the required result. The main challenges in the production of a high concentration of beam power in a small volume are a reliable and accurate end–to–end simulation of the beam dynamics taking into account as much information as possible about the external fields and beam initial conditions, control of secondary electrons, and accurate beam diagnostics to measure the phase space distribution at various locations to compare with expected results as well as to reinitialize the simulation program. This paradigm is used in the design, construction and operation of the Neutralized Transport Experiment (NTX).

This thesis is organized as follows:

Chapter 2 gives an overview of the Neutralized Transport Experiment (NTX). The physics of neutralized transport for driver-scale beams is reviewed in Section 2.1 and used to explain the scale and experimental goals of NTX in Section 2.2. In Section 2.3, we describe the NTX beam-line layout. Section 2.4 describes the diagnostic suite, including a detailed description of two new diagnostics developed for NTX: an improved optical technique for mapping the 4-D transverse phase-space of the beam, and a non-intercepting diagnostic to measure the beam charge density. These improved measurement techniques are essential for quantitative validation of

code predictions. Section 2.5 describes the numerical tools used for the design and numerical simulations of the NTX experiment.

The beam line has three principal components: the injector, the magnetic-focus lattice, and the neutralized-transport section. Each of these components presents design challenges, and we discuss the design and characterization of each.

Chapter 3 describes the design of the diode that generates the ions from a source, the aperturing system that removes the unwanted ions to produce a high brightness ion beam, and a secondary-electron control system. It also describes the experimental results of the final source design used in NTX.

Chapter 4 gives a detailed account of the theoretical, computational and experimental effort to design a Final Focus System that produces a high quality beam with the appropriate initial condition to be injected into the neutralized drift section.

In Chapter 5, the components of the neutralized transport system and experimental results from NTX are presented. Measurements of beam transport through the magnetic lattice are presented first and compared with particle-in-cell (PIC) simulations made using the computer code WARP [13]. We then present the corresponding data in the neutralized drift section, along with theoretical results from WARP and the electromagnetic PIC code LSP [14, 15].

Chapter 6 summarizes NTX accomplishments to date, presents the conclusions, and discusses the directions of future work.

THIS PAGE INTENTIONALLY LEFT BLANK

Chapter 2

Overview of the Neutralized Transport Experiment NTX

The topic of final focus systems for high intensity beams has been an important subject of theoretical [16-19], and experimental [20] efforts since the beginning of the Heavy Ion Fusion project in 1976. The first designs were derived from systems already in use in particle accelerators for high energy physics where space-charge is negligible, and which incorporated sextupoles and octupoles elements for the correction of chromatic and geometric aberrations (Figure 2-1).

Chromatic aberrations affect the focal spot radius due to deviations from the nominal ion momentum causing a variation in the focal length produced by the magnet system. These aberrations may result from initial transients in the injector, from residual momentum tilt due to beam compression, or from the momentum spread, or longitudinal emittance produced along the beam line. Geometric aberrations are due to nonlinear external fields and deviations from paraxial ray optics.

In HIF the space charge effects are dominant, and the well-known chromatic and geometric effects are modified by space charge. In addition, during the final drift of the ion beam through the chamber, uncompensated space charge forces would lead

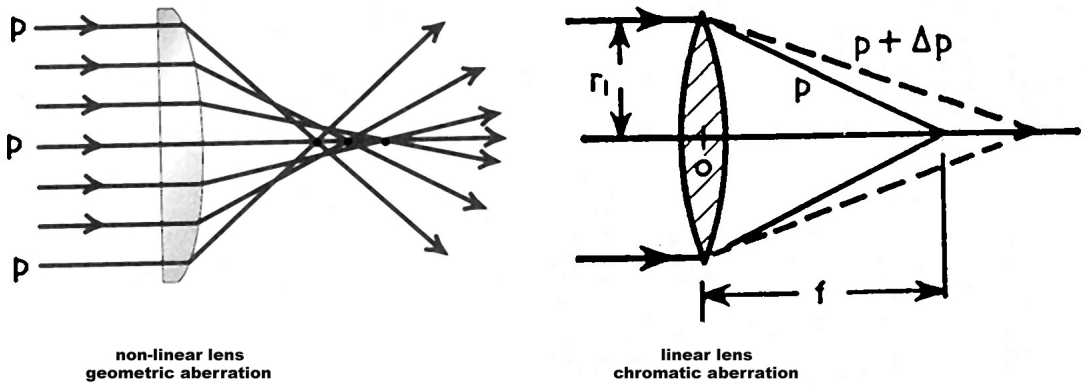

Figure 2-1: Geometric and Chromatic aberrations.

to blow-up of the final focal spot.

In the more recent mainline scenario of a final focus system for an HIF driver [12], the beam is transported in the final focus section through several strong large aperture magnetic quadrupoles, and is then allowed to drift ballistically through neutralizing plasma in a low-density (millitorr) gas onto the target (Figure 2-2).

There are nonlinear processes both in the magnetic section as well as in the neutralized transport section. To investigate these phenomena, the Neutralized Transport Experiment (NTX) was built at LBNL [8]. The NTX beamline (Figure 2-3) consists of 4 large bore quadrupoles followed by a neutralized drift section. A low emittance K^+ beam is made to traverse this 4-quad lattice, at the exit of which, the beam enters a 1-meter long drift section with an injected plasma. The beam is diagnosed at the exit of the 4-quad section as well as the end of the drift section.

This chapter provides an overview of the NTX experiment. NTX is designed to study the physics of a final focus system for an HIF driver. The key driver issues and the scaling laws that justify a small scale experiment are described in Section 2.1. The specific objectives and overall layout of NTX are discussed in Section 2.2 and 2.3. The diagnostic and simulation tools used througout the entire experimental campaign are presented in Sections 2.4 and 2.5 respectively.

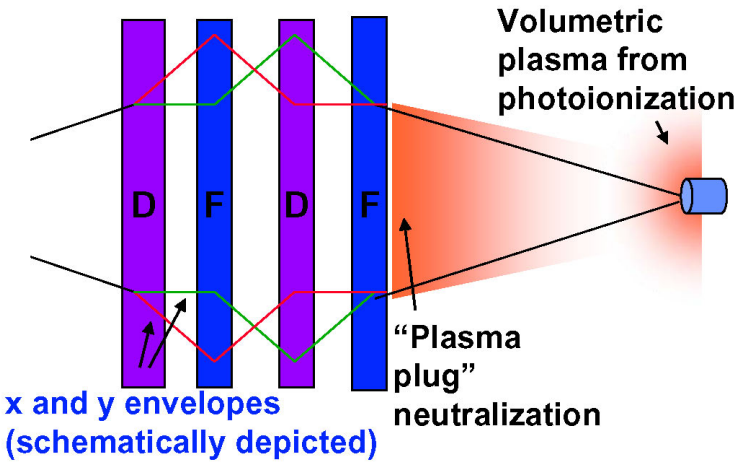

Figure 2-2: Neutralized Final Focus System.

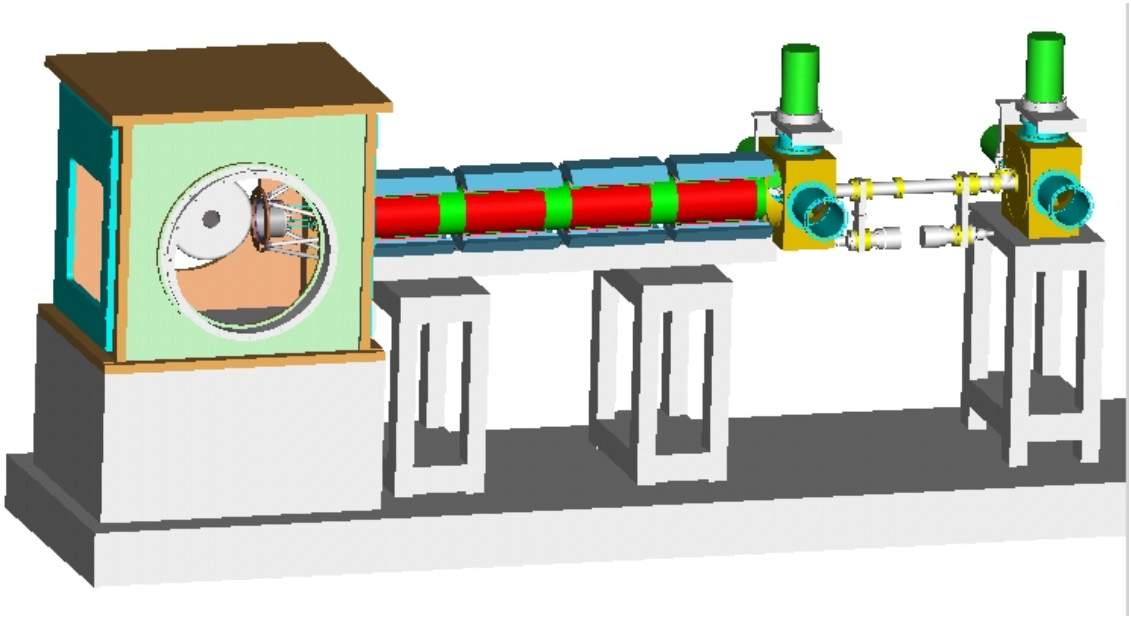

Figure 2-3: Side view of NTX.

2.1 NTX, a Prototype Integrated Beam Experiment for the Final Focus System for Heavy Ion Fusion

The NTX is intended as an integrated experiment to test simultaneously various aspects of a scaled version of a heavy ion fusion driver or HEDP facility, including the injector, the transport through a magnetic quadrupole lattice, the final focusing, and the transport through a plasma-neutralization region.

The final transport section in a heavy-ion inertial-confinement fusion system poses major challenges. After exiting the final-focus magnet system, intense beams of ions with a current totaling tens of kiloamperes must drift without further external focusing to the center of a target chamber, a distance of about 6 m in recent conceptual designs [21]. To obtain adequate target gain, these beams must all hit spots a few millimeters in diameter on the ends of the cylindrical fusion target.

From the very early days of heavy-ion fusion (HIF), final focusing has been a subject of intense study [22-24], with perhaps the most comprehensive study being that of HIBALL-II [25]. These studies assumed that the chamber could have a sufficiently high vacuum that beam ions would experience no forces other than their collective space charge during the final transport to the target. In this final drift section, the beam space charge acts to enlarge the focal spot, so the beam species, current, and energy in early studies were chosen to make the space-charge blowup manageable. For example, Olson [24] proposed a baseline case using 30 kA of 10 GeV U^{+1} ions in a moderate vacuum of 10^{-4}–10^{-3} Torr. Numerical and experimental studies indicate that such so-called "ballistic" transport could, in fact, be feasible. A 1998 scaled experiment [20] based on the HIBALL-II final-focus design was performed at Lawrence Berkeley National Laboratory (LBNL), obtaining excellent agreement between theory and experiment. Also, detailed numerical simulations of driver-scale systems showed good spot sizes for the Olson parameters [26].

Since the HIBALL-II study [25], however, several significant shifts in conceptual designs for HIF drivers have made ballistic chamber transport unattractive. One change has been the development of indirect-drive targets [27], which give a more symmetrical energy deposition on the deuterium-tritium capsule than the direct-drive HIBALL-II target [25], but require more energy to heat the cylindrical metal "hohlraum" enclosing the capsule. At the same time, driver economics favors beams with lower kinetic energy, at the cost of requiring higher total beam current. This higher current can be partly offset by using more beams, but even with an ion mass of 200 *amu*, more than 450 beams would be required to reduce space-charge effects sufficiently to allow ballistic transport. Another development has been the adoption of "thick-liquid" walls as the mainline US approach to protecting the fusion chamber. In HYLIFE-II [28] and more recent designs [21], jets of molten salt fill much of the volume between the target and the chamber interior wall and absorb much of the blast wave and the radiation. The vapor from these jets has a pressure about 0.6 *mTorr* and consists mainly of Be_2F and LiF. Due to collisional stripping by this gas, a singly charged ion beam develops a wide spread of charge states by the time it reaches the target, with the average charge state being about two. The effective perveance of the beam is not increased by a similar factor because the liberated electrons propagate along with the beam, but the beam itself becomes much more sensitive to the net space-charge field. Finally, the distributed-radiator targets [29,30] developed in recent years exacerbate the problem of beam focusing by requiring that beam energy be deposited in a narrow annulus on the hohlraum ends, rather than over the entire end surfaces. The gain for these targets degrades if the focal radii of the beams exceed two millimeters, thus requiring beams with a low transverse temperature and net charge.

A recent HIF driver study [21] reconciles these stringent final-focus requirements. A pivotal feature of this design is the use of low-density plasma in the beam line between the final-focus magnets and the chamber to neutralize much of the beam

space charge [14, 15, 31]. If there are enough electrons in the volume swept out by a beam, they can be trapped by the space-charge potential well of the beam and provide charge neutralization during the final transport to the target, thus allowing substantial beam currents while still maintaining the low net charge needed for good focus. In addition, after the target has been pre-heated by lower-current "foot" pulses, thermal radiation from the target will photoionize the nearby background gas, providing additional neutralization as the beam approaches the target.

2.2 NTX Objectives

The Neutralized Transport Experiment (NTX) has been designed to study, on a reduced scale, the physics of the final focus and neutralized transport of beams with high space charge. The experiment was designed as part of the research program developed by the Virtual National Laboratory for Heavy-Ion Fusion, a formal collaboration of Lawrence Berkeley National Laboratory (LBNL), Lawrence Livermore National Laboratory (LLNL), and Princeton Plasma Physics Laboratory (PPPL). Construction of the experiment at LBNL began in FY01, and the first transport experiments were carried out in the Fall of 2002. As the photograph in Figure 2-4 shows, the experiment is quite small in scale. Both the current and the energy are orders of magnitude smaller than driver parameters, but we have chosen the beam and lattice parameters so that the transverse dynamics and neutralization physics of NTX closely model a full-scale system. The experiment is designed to survey a wide parameter space, and there are two independent plasma sources to simulate the upstream neutralizing plasma and the photoionized plasma around the target. While the experiment is specifically designed to study the physics of neutralized chamber transport for heavy-ion fusion, the technique of plasma neutralization may also be applicable to other situations requiring the focusing of space-charge-dominated beams.

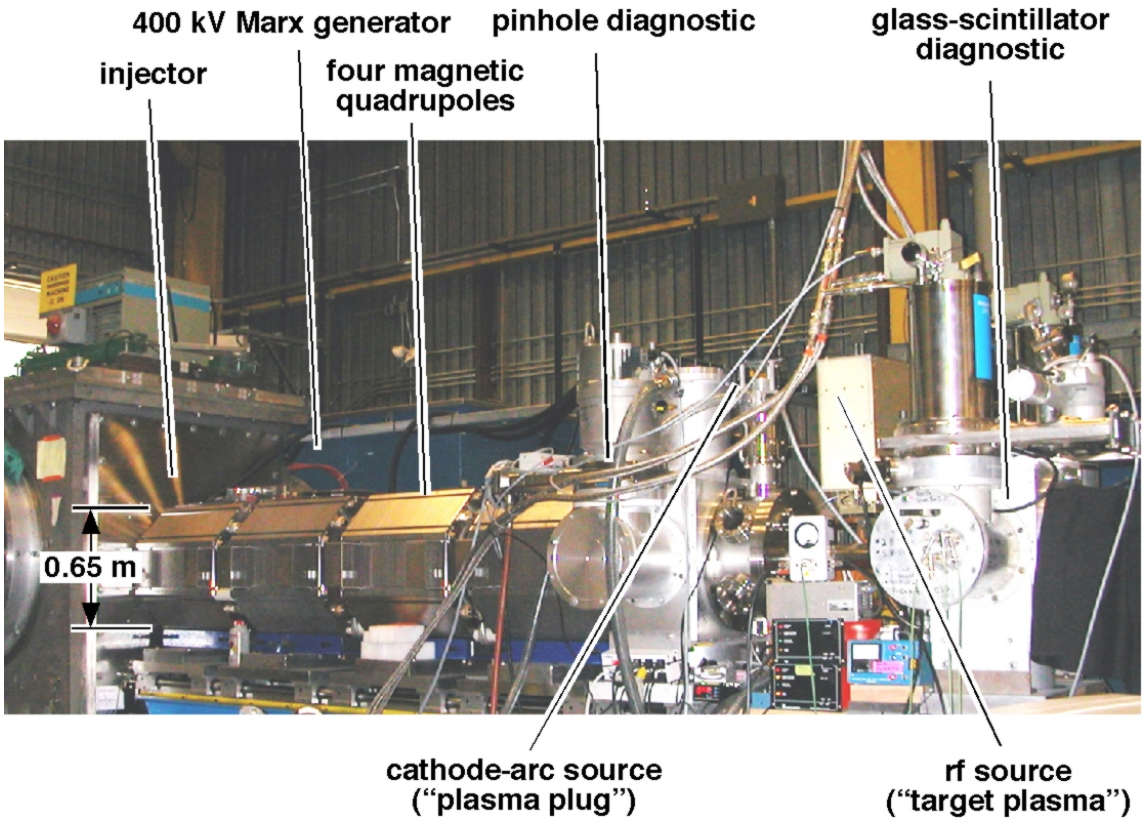

Figure 2-4: Photograph of the Neutralized Transport Experiment (NTX).

Two such situations are the focusing of collider beams near the interaction point and the study of high-energy physics using intense particle beams.

Two quantities are important for choosing the scaled parameters of NTX. The generalized perveance Q, loosely defined as the ratio of the edge potential of a beam to its directed kinetic energy [32], characterizes the importance of space charge in the transverse dynamics of a beam. The unnormalized emittance ε is a measure of the transverse phase-space area of the beam [33]. During the final transport, the perveance and emittance are constant in the absence of collisions and nonlinear space-charge fields, and for any particular choice of the initial beam radius and convergence angle, they determine the transverse beam dynamics during final transport.

Perveance is dimensionless and, for a nonrelativistic beam, is given in SI units by

$$Q = \frac{1}{4\pi\varepsilon_0}\frac{2ZeI_b}{m_i v_i^3}, \tag{2.1}$$

where I_b is the beam current, and Z, m_i, and v_i are respectively the charge state, mass, and velocity of the beam ions. Early analytical work by Olson [24] estimated that the upper perveance limit for ballistic transport is $Q \cong 1.6 \times 10^{-5}$. The earlier HIF designs, which had $Q \leq 10^{-6}$, satisfy this criterion comfortably, whereas recent designs typically require Q to be a few times 10^{-4}. The NTX injector can generate beams with Q values up to about 10^{-3}. This higher perveance has important ramifications for the focusing and final transport of an intense beam. Since the beam radius increases with perveance when the transverse dynamics is dominated by space charge, beams in a modern driver will sample more field aberrations in the final-focus magnets than in older designs, assuming a similar magnet design. These aberrations introduce radial and azimuthal variations in the focal distance, which degrades the focal spot. Due to their high perveance, beams for modern driver designs require some form of external neutralization after final focus in order to achieve an acceptable focal-spot radius.

The use of low-density plasmas to neutralize space-charge-dominated ion beams during the final transport has been studied analytically and numerically in recent years [34-41]. Due to the thick liquid wall in a modern fusion chamber, it is difficult to fill the inside of the chamber with a plasma at the repetition rate of several shots per second needed for a driver. However, it is straightforward to inject a low-density plasma, referred to as a "plasma plug," along the beam path between the last final-focus magnet and the chamber entrance. An ion beam passing through this plasma drags along electrons as it exits, and these co-moving electrons then provide substantial neutralization for the beam along the remaining path to the target. Two other

processes inescapably generate plasma in the chamber. First, collisions between the beam and the background gas ionize the gas molecules in addition to stripping electrons from the beam ions. Second, once the target becomes hot, photons are emitted which photoionize the background vapor in the region around the target. This photoionized plasma provides additional neutralization during the critical final part of the beam trajectory. None of these three plasma sources alone provides sufficient neutralization [34, 35, 39, 40], but detailed numerical simulations indicate that together they can give a usable beam focal-spot radius. One of the significant theoretical successes in recent years is use of the electromagnetic PIC code LSP to demonstrate the technical feasibility of a driver point design that meets all of the constraints imposed by the target, focusing, neutronics, and chamber-engineering considerations [21].

In addition to adequate neutralization, achieving a usable focal spot also requires that the transverse emittance of each beam remain sufficiently small during the final transport. In this thesis, we define emittance in terms of distribution averages over the transverse phase-space coordinates $x, y, x' \equiv dx/dz$ and $y' \equiv dy/dz$ by

$$\varepsilon \equiv \sqrt{\varepsilon_x \varepsilon_y}, \tag{2.2}$$

where ε_x and ε_y are the unnormalized "edge" emittances [33] in the two transverse directions, defined as

$$\varepsilon_x = 4\sqrt{\langle x^2 \rangle \langle x'^2 \rangle - \langle xx' \rangle^2} \tag{2.3}$$

and

$$\varepsilon_y = 4\sqrt{\langle y^2 \rangle \langle y'^2 \rangle - \langle yy' \rangle^2}. \tag{2.4}$$

The unnormalized "edge" emittances, which are four times the root-mean-square (rms) emittances, can be increased by nonlinearities both in the beam space-charge field and in the external focusing fields. The emittances of the beam entering the final-focus lattice are determined by the values at injection plus what are predicted to be

small growth during acceleration and compression. The final-focus magnetic lattice, however, is a potentially significant source of emittance growth. The primary function of this magnetic system is to prepare a converging beam for the final transport. To develop the needed convergence angle, a strongly space-charged-dominated ion beam must experience large envelope oscillations, during which phase-space distortions due to geometric aberrations in the magnetic fields can lead to emittance growth. While these higher-order effects are well known in final-focus systems with negligible space-charge effects, aberrations in space-charge-dominated beams remain an issue to be addressed in this thesis.

The major objectives of NTX are to study the final focusing and neutralized transport of space-charge-dominated heavy-ion beams, and to validate the physics models in the numerical simulations. To expedite the experiment and minimize the cost, we choose to use a beam with lower-mass ions than in a driver and a particle energy that is four orders of magnitude smaller. Also, the physical size of the beam line is about one sixth of the corresponding driver section. The remaining beam parameters are chosen to ensure that results from this low-energy experiment are relevant to the design of a HIF driver. By scaling the equations for transverse dynamics in the same manner as an earlier scaled final-focus experiment [20], we find that driver-like dynamics is obtained by using the same perveance as a driver, by reducing both the emittance and initial beam radius by the ratio of lattice lengths, and by scaling the final-focus magnetic fields appropriately with the ion mass and speed.

This scaling is easily shown to preserve the beam response both to the final-focus quadrupole fields and to any higher-order magnet aberrations. A low-energy beam will therefore have the same envelope trajectory and emittance-growth characteristics as a high-energy beam with the same perveance, provided that image forces and interaction with any background gas are negligible. This makes the NTX final-focus lattice a good model of a driver-scale lattice.

A small-scale experiment can also address key aspects of driver-scale neutralization physics. Theoretical work by Olson [24], as well as the results of recent simulations [39], indicates that the degree of neutralization from a plasma plug depends principally on the perveance, provided that the plasma has sufficiently high charge density and is in contact with a metal wall that can emit electrons. Space-charge-limited emission at this boundary is crucial because emitted electrons replace those captured by a passing ion beam and thereby maintain the quasineutrality of the plasma. The physics of beam neutralization by the photoionized plasma around the target is likewise determined mainly by the beam perveance and is modeled on NTX by generating a plasma with an appropriate density near the beam focal point.

The final objective of NTX is to make detailed, quantitative comparisons of experimental data with the results of numerical simulations. These comparisons will both help refine the numerical models in the simulation codes and guide improvements in the experimental design and operation. A clear demonstration of the predictive capability of these codes will justify our reliance on them for designing later experiments.

Of course, several driver issues cannot be addressed on NTX. Due to the low current in the experiment, no self-focusing by the beam net current will occur, and indeed, the effect is expected to be minor even at driver parameters. Image forces in the magnetic-transport section are likewise negligible on NTX. Cross-sections for collisional ionization of the beam and background gas have very different cross-sections for low-energy and high-energy ions, so the effects of collisions cannot be modeled in a scaled experiment. The effects of many beams overlapping as they converge on a target are obviously missing from a single-beam experiment like NTX. Finally, photoionization of an ion beam by X rays from the heated target cannot be studied due to the lack of suitable radiation source. Future experiments on a larger scale than NTX are needed to investigate these issues.

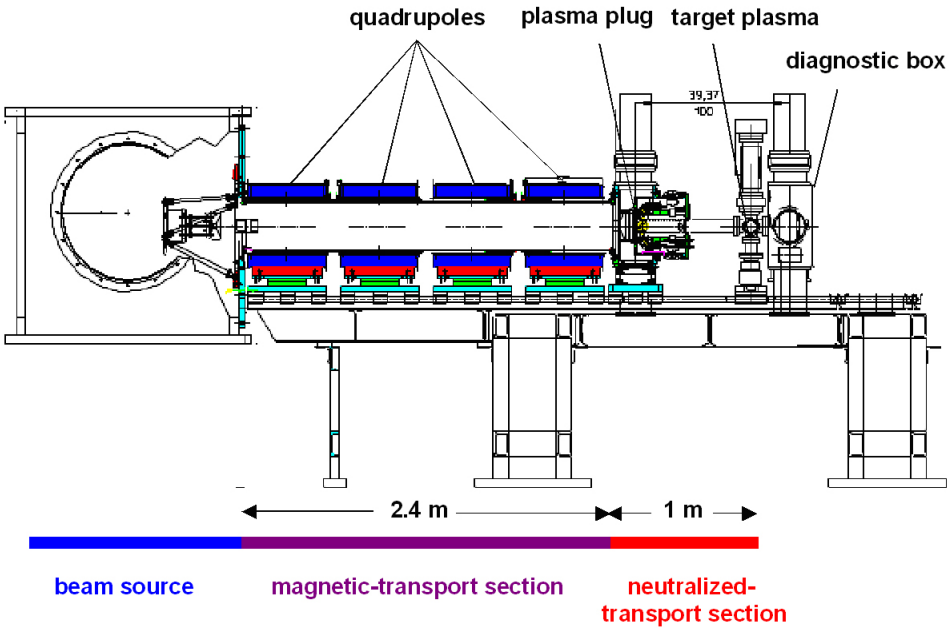

Figure 2-5: Plan view of NTX .

2.3 NTX Beamline and Parameters

NTX uses a 300–400 keV beam of singly charged potassium (K^+) ions to study the final focusing and plasma neutralization of a strongly space-charge-dominated ion beam. The energy, which is small compared with typical driver energies, is determined by the decision to use a pulsed-power source used from an earlier experiment. However, as discussed in Section 2.2, NTX replicates driver-like transverse dynamics by a careful choice of beam and lattice parameters. The beam source is designed to produce a current of 75 mA, corresponding to a perveance of about 10^{-3}, and we use beam aperturing to achieve the goals of variable perveance and low emittance. The apertures inserted after the source allow the current and perveance to be reduced by as much as an order of magnitude, and excluding the less intense portion of the beam near the edge simultaneously reduces the beam emittance and increases the brightness.

The drawing of the NTX beam line in Figure 2-5 shows the layout and scale of the experiment. Pulsed power is provided by the same Marx generator that was used in the Multiple Beam Experiment (MBE-4) [42]. This generator can deliver a pulse of up to 500 kV with a maximum duration of about 20 μs. A timed crowbar switch on NTX produces pulses with a rise time of 0.5–1 μs and a "flat-top" of about 10 μs. The remaining NTX components are designed specifically for the experiment and consist of three major sections: a low-emittance potassium gun [43], a magnetic transport section with four pulsed quadrupoles [44], and a one-meter-long drift section with plasma neutralization [45].

The K^+ beam is produced by a standard hot-plate source [46], and the perveance and emittance are controlled by passing the beam through a metal aperture after the diode. Negatively biased rings on either side are used to capture electrons liberated by ions striking the aperture plate. The change in transverse emittance that results from aperturing primarily affects the focal-spot size. For the space-charge-dominated NTX beam, WARP [13] simulations show that dynamics in the final-focus lattice is insensitive to the beam emittance.

Although the NTX beam typically has a 2-cm radius as it enters and exits the magnetic-transport section, the magnets nonetheless have a 15-cm radius bore. Any four-magnet focusing system gives the beam a large radial excursion before the last magnet, and in NTX, we want to handle perveances that are substantially higher than expected in a driver, so the large bore is used to accommodate large radius swings, while still keeping the beam away from the more nonlinear magnetic fields near the wall. The choice of a 60-cm half-lattice period and 2.4-m total length follows from practical considerations, such as the available power supplies for the magnets and limits on the overall length of NTX.

The layout of the 1-m NTX plasma neutralization section is shown in Figure 2-6, and the sketch in Figure 2-7 shows how it functions. The upstream plasma, modeling

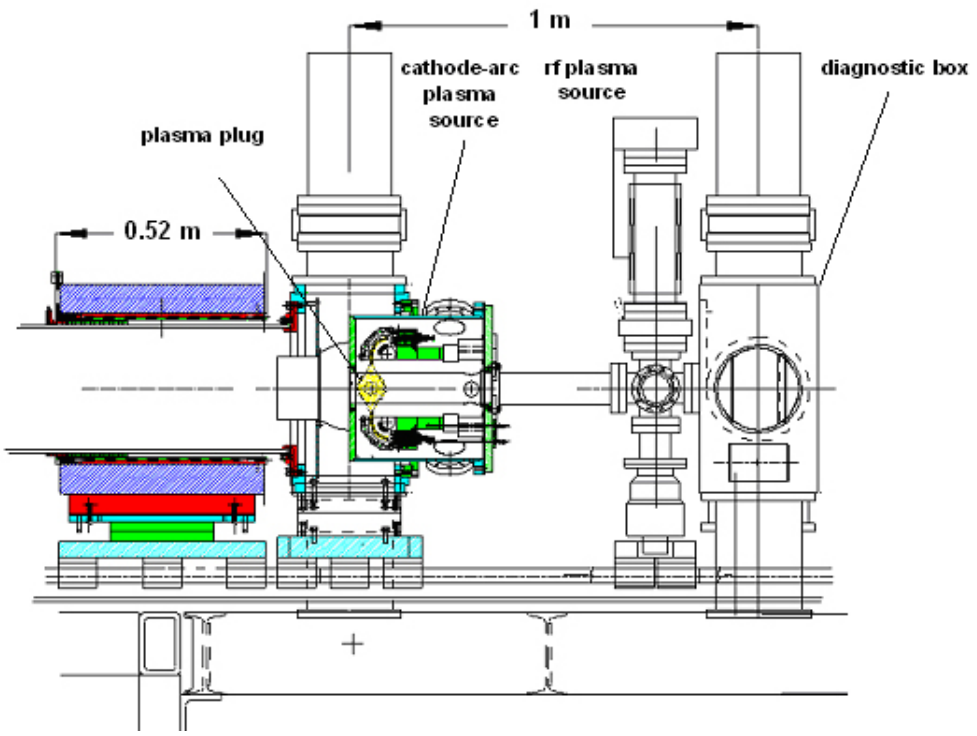

Figure 2-6: Plan view of the NTX Neutralization Section.

the plasma plug that neutralizes the beam after it exits the final-focus section, consists mainly of electrons and doubly charged aluminum ions from a pulsed cathode-arc source (sometimes called a metal-vapor vacuum arc or MEVVA source). The plasma itself is centered 0.25 m after the end of the last magnet so that it is well away from the fringe fields, and it extends about 0.05 m in both directions. After the beam exits this first plasma, it drifts 0.75 m through a 3.5-cm-radius beam pipe into a diagnostic area at the nominal focal point. A second plasma generated at the center of the cross simulates the photoionized gas that will surround a target hohlraum after it has been heated by early low-current "foot" beams. This "target" plasma is generated by a pulsed radio-frequency (rf) source and has a charge density approximating that expected in a fusion chamber. A diagnostic box is placed at the focal point.

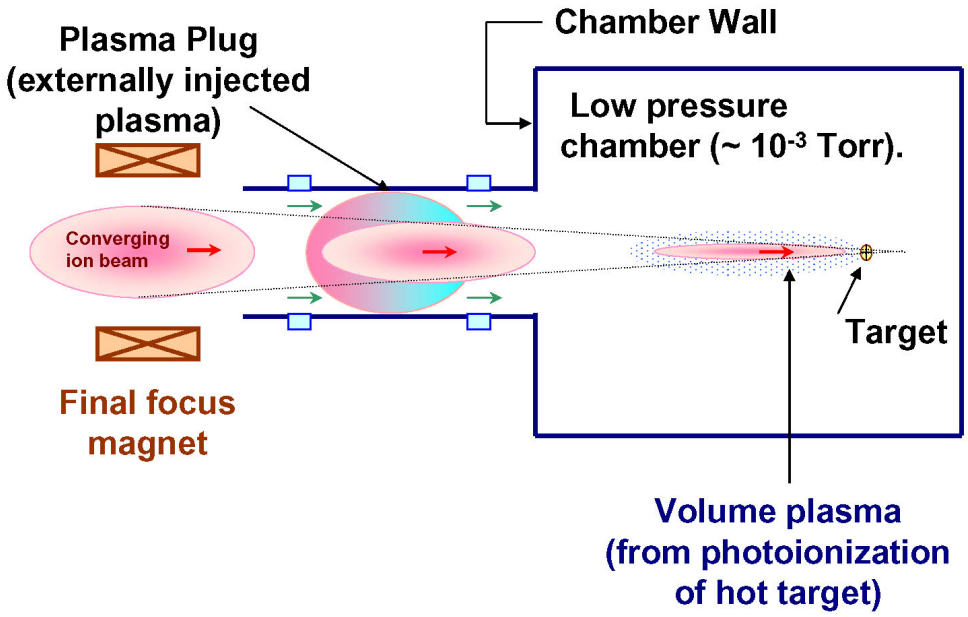

Figure 2-7: Generic layout of a plasma-neutralization system.

2.4 Diagnostics

2.4.1 Single and double slit mechanical diagnostics

The initial measurements of the NTX beam were made with the same diagnostic tools used on MBE-4 [42,47] and other early HIF experiments. A diagnostic box containing various combinations of slits and Faraday cups is moved to the end of each NTX section as the experiment is being assembled, and the beam is characterized at each of these points. A Faraday cup, with a 2-cm entrance radius and a guard ring biased to exclude electrons, is used to make time-dependent current measurements, and a "slit-cup," consisting of a movable slit with an attached Faraday cup to measure the transmitted current, is used to measure the line-integrated beam profile. A second movable slit is used along with the slit-cup to map out the transverse phase space of the beam by a standard double-slit technique [48]. The slit and the slit-cup, aligned in parallel to the first slit and located behind it, are moved so as to sample either the

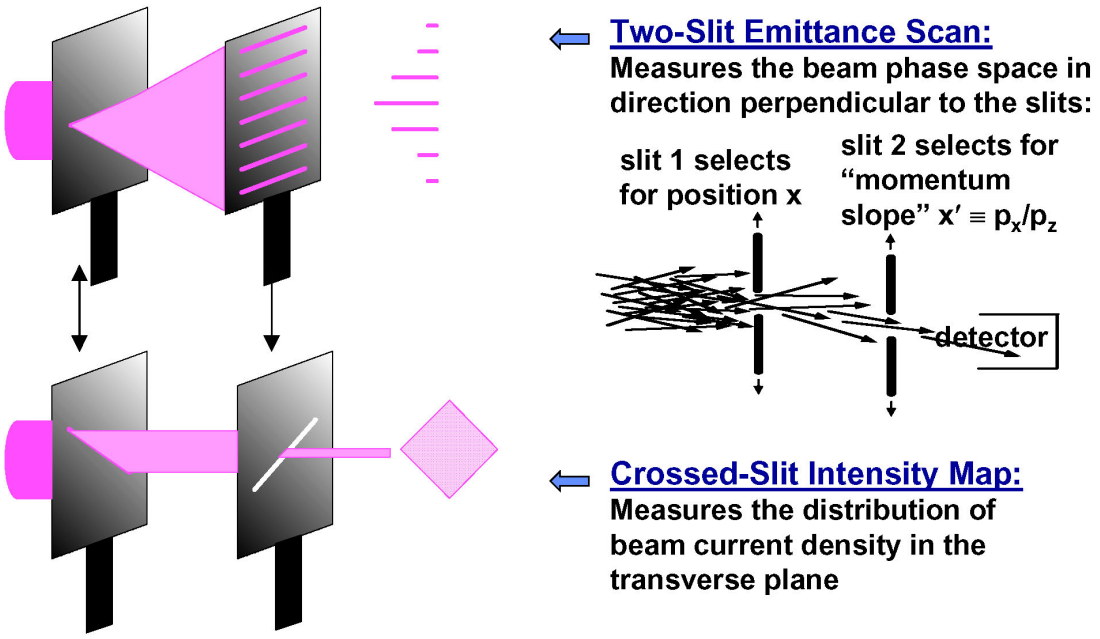

Figure 2-8: Slit scanner diagnostics.

(x, x') or (y, y') phase space, as illustrated in Figure 2-8, with the collected current being recorded for typically 400 or more shots. These data are then used to construct contour plots of phase-space density in the various two-dimensional (2-D) planes. The response time of the Faraday cup allows a time resolution of about 150 ns. In addition to transverse emittance, these data yield other time-resolved quantities, such as the beam size, centroid position, and density profile.

In addition to these conventional diagnostics, NTX now uses optical diagnostics to provide detailed, time-resolved information about the ion-beam transverse phase space. Work has also been performed to characterize a non-intercepting electron-probe technique that provides information about the transverse structure of the beam charge density. The design and implementation of these diagnostics are discussed in the following subsections.

2.4.2 Optical diagnostics

We have developed an optical diagnostic technique (Figure 2-9) for NTX as a faster and more flexible alternative to the double-slit technique. This optical technique, which is related to the gated beam imager (GBI) [49], uses scintillator plates imaged by an image-intensified charge-coupled-device (CCD) camera. The GBI uses a "pepper-pot" to create an array of beamlets that are imaged directly onto a gated microchannel plate (MCP). The new NTX technique differs in two ways. First, a thin sheet of scintillator material is substituted for the MCP imager, allowing the MCP to be placed away from the beam line with the camera. Second, a single movable pinhole replaces the pepper-pot because the convergence of the NTX beam would cause side-by-side beamlets to merge. The technique is simple, compact, and more flexible, because only the scintillator material is placed in the path of the beam. Hundreds of NTX shots are needed to map out the beam phase space than for the double-slit method, but this requirement is manageable due to the reproducibility of the NTX beam and the ease of each measurement.

For the images presented here, the scintillator material is a 98% aluminum oxide ceramic. Charge neutralization is provided by a 90% transmission metallic mesh (0.28-mm line spacing) placed on or near the surface of the scintillator. Beam ions striking the mesh generate secondary electrons. The secondary electron yield from beam ions striking the mesh is greater than ten electrons per ion, so sufficient free electrons are generated on the mesh to charge-neutralize the insulating surface of the scintillator. By applying a negative bias to the mesh, stray external electrons are decelerated and deflected away from the scintillator, limiting their contribution to the optical image to negligible levels. The measured rise time of the scintillator is less than 50 ns; while the fall time is about 1 μs. There is no evidence for saturation or thermal quenching in the scintillator response. We tested linearity over the range of measured intensities by imaging the same beam in horizontal and vertical slit scans.

The local intensities in the two scans differed by an order of magnitude, but the summed intensities of all images in each of the two scans agreed. The lifetime of the scintillator material under intense ion beam bombardment is limited, but the current and energy of NTX are sufficiently low that this limitation is not a concern. However, accumulated damage to the metallic mesh at NTX parameters can cause a weaker signal in portions of a scintillator image, a feature evident in some of the images.

Time-resolved beam images on the scintillator screen are captured with a Roper Scientific gated-intensified CCD camera viewing the scintillator through a vacuum window, and images are processed using the public-domain program ImageJ. Figure 2-10 shows a typical beam image taken on NTX near the focal point.

Whole-beam scintillator images, like those in Figure 2-10, are the primary optical diagnostics reported here, but a scintillator-based imaging technique is also being used now to map the four-dimensional (4-D) phase-space distribution of the NTX [45]. The phase-space distribution $f(x, y, x', y')$ is measured over many shots by scanning the beam cross section with a movable pinhole having a diameter of 20 thousands of an inch. The transmitted beamlet then travels to the nominal focal point, about 1 m, where it strikes the scintillator plate. The position of the pinhole defines the coordinates x and y, and from the image, we can extract the density distribution of x' and y'. Figure 2-11 shows this technique schematically, along with selected images of the individual beamlets that reveal a very detailed phase-space structure. A detailed knowledge of the 4-D phase space is essential both for more realistic initializations of neutralized-transport simulations and for understanding the NTX measurements.

2.4.3 Non-interception charge-density diagnostic

All the NTX diagnostics mentioned above entail inserting apparatus temporarily into the beam line, either blocking or significantly altering the ion beam. Moreover, since characterization is not normally done while experimental data is being recorded, there

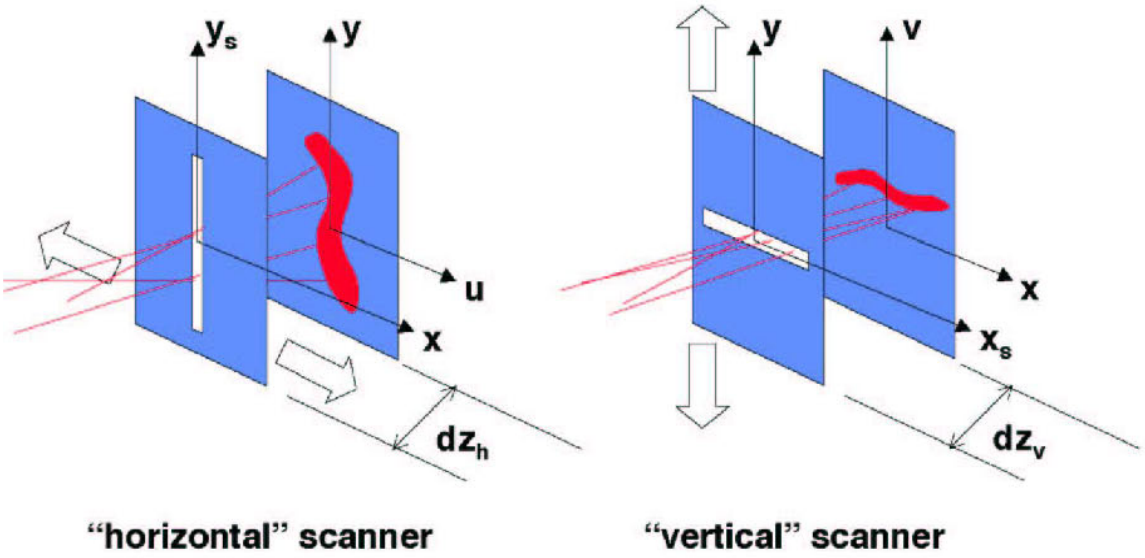

Figure 2-9: Optical slit scanner diagnostics.

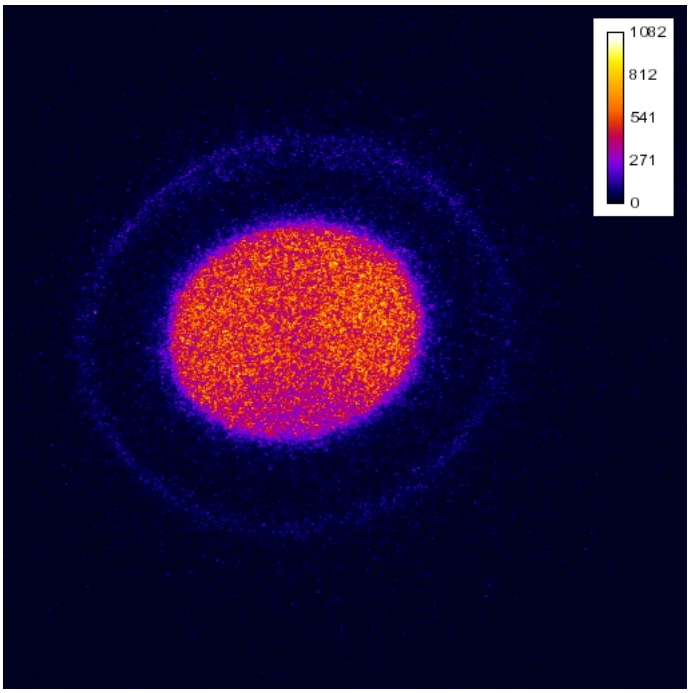

Figure 2-10: Typical image from optical diagnostics.

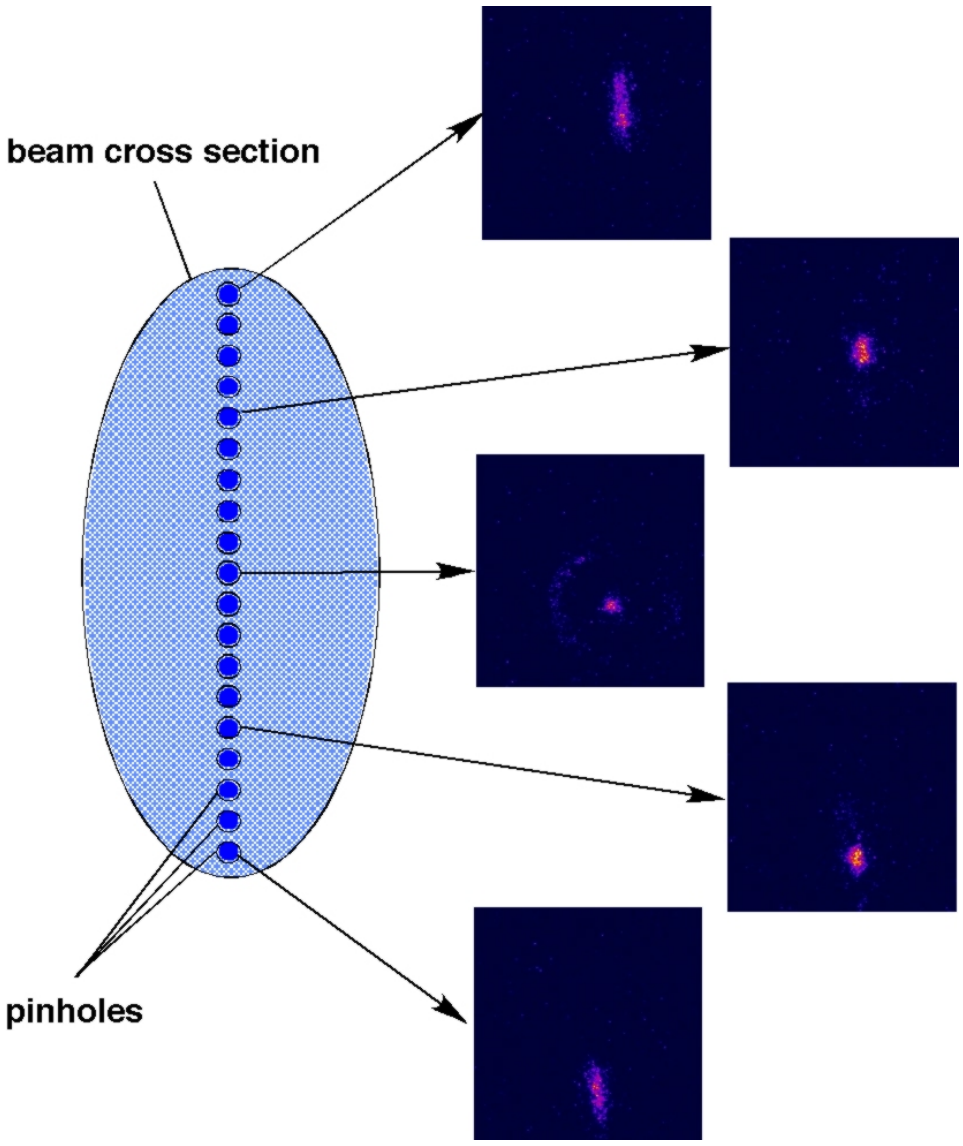

Figure 2-11: Phase space optical scanner.

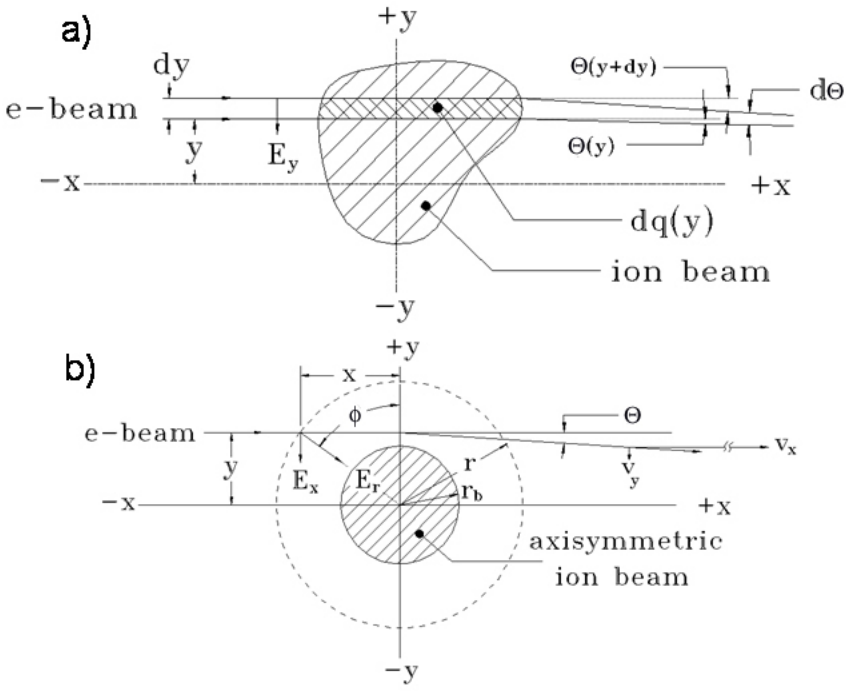

Figure 2-12: Electron beam deflection by ion beam space charge. (a) A transverse cross-sectional view of an arbitrary charge distribution in the x and y directions. Probe electrons of velocity v_x are directed horizontally from left to right ($-x$ to $+x$) at various heights, y, and acquire a velocity v_y orthogonal to v_x, (b) an axisymmetric nonrelativistic charged particle beam which is long relative to its transverse dimensions, and where the charge density is a function of radius only, the electric field E_r at any given radial distance, r, from the beam center will be proportional to the charge enclosed within a concentric cylindrical Gaussian surface of radius r, as shown by the dashed circle.

is a possibility that beam parameters may change after being measured.

As an alternative, we have developed a non-intercepting beam diagnostic to characterize an ion beam during its operation. By repeatedly measuring the deflection of a low-current electron beam propagating across the NTX beam, we can map out the transverse charge density of the ion beam (Figure 2-12).

For non-relativistic ion beams that are long compared with their cross section, an electron injected on a plane perpendicular to the beam motion will remain on that plane, i.e., the $x-y$ plane in Figure 2-12(a). Under the assumption that the electron moves in such a way that $v_x \gg v_y$, the trajectories can be considered straight lines with a small angular deflection after passing near the ion beam. Since the e-beam accelerates when approaching the ion beam, and decelerates when moving away from the ion beam, v_x can be considered constant along the e-beam trajectory.

The deflection angle can be obtained from the equation of motion

$$\frac{dv_y}{dt} = -\frac{e}{m}E_y, \tag{2.5}$$

where e and m are the charge and mass of the electron, and $E_y$is the electric field produced by the ion beam charge distribution on the $x-y$ plane.

Since $v_x = dx/dt$, we have

$$\frac{dv_y}{dx} = -\frac{e}{mv_x}E_y, \tag{2.6}$$

and

$$\frac{d\theta}{dx} = -\frac{e}{mv_x^2}E_y, \tag{2.7}$$

where $\theta = v_y/v_x$. Therefore, the deflection angle is given by integrating E_y along the e-beam trajectory, from the point where the e-beam enters the diagnostic box, to the point where the e-beam hits a measuring device, like a scintillator.

$$\theta = -\frac{e}{mv_x^2}\int E_y dx, \tag{2.8}$$

From Maxwells equation $\nabla \bullet \mathbf{E} = \rho/\varepsilon_0$, and since E_z is zero for the ion beam with uniform density along its direction of motion, we have

$$\frac{\partial E_x}{\partial x} + \frac{\partial E_y}{\partial y} = \frac{\rho(x,y)}{\varepsilon_0}. \tag{2.9}$$

Integrating this equation along an e-beam trajectory (y=constant) we obtain,

$$\int \frac{\partial E_x}{\partial x} dx + \int \frac{\partial E_y}{\partial y} dx = \frac{1}{\varepsilon_0} \int \rho(x,y) dx. \tag{2.10}$$

The first term is zero since E_x vanishes far away from the ion beam.

If we define the current intercepted by a thin wire or a slit at position y and of width dy as $I(y)$, then

$$\frac{d}{dy} \int E_y dx \propto I(y). \tag{2.11}$$

From Eq. (2.8) we obtain

$$I(y) \propto \frac{d\theta}{dy}. \tag{2.12}$$

Therefore a slit- or wire-scan current measurement can be related to an e-beam deflection scan measurement through its derivative. To determine, without making any assumptions of charge distribution shape, the 2D charge density distribution, a full set of deflection measurements over many different electron-beam directions x and offsets, y must be made. This procedure produces the Radon Transform of the 2D density distribution. Once the Radon Transform is obtained, various methods of computing tomography can be used to invert the Radon Transform, yielding the density distribution.

The above method of analysis simplifies when the beam density distribution is axisymmetric. Analytic solutions for various axisymmetric one-dimensional (1D) charge distribution functions can be formulated. For example, Figure 2-12(b) shows an ax-

isymmetric nonrelativistic charged particle beam which is long relative to its transverse dimensions, and where the charge density is a function of radius only, the electric field E_r at any given radial distance, r, from the beam center will be proportional to the charge enclosed within a concentric cylindrical Gaussian surface of radius r, as shown by the dashed circle. For an electron beam passing through an ion beam, the amount of line charge density "seen" by the e-beam will vary as the e-beam travels through. This results in a decrease of the acquired transverse velocity, which has a functional dependence on the e-beam offset y from the ion beam axis, going to zero for zero offset y. By scanning the e-beam through various offsets y, the radial dependence of λ (and thus the volumetric charge density ρ) can be calculated. In particular, for an exponentially decaying density distribution

$$\rho(r) = \rho_0 e^{-r/r_0}, \tag{2.13}$$

the vertical aquired velocity v_y is

$$v_y \propto \int_{-\pi/2}^{\pi/2} \left(1 - e^{-y/r_0 \sec\theta}\right) d\theta, \tag{2.14}$$

where r_0 is the exponential decay radius. Similar formulas can be derived for hard-edged uniform, Gaussian, and Gaussian-hollow axisymmetric beam density distributions. Common to all solutions is the result that deflection angle is invariant with y, once the entire charge distribution is not intercepted. The above analyses assume linear electron trajectories from x=-∞ to x=+∞ with a ground potential at infinity.

The sub-millimeter electron beam has a current of 1–5 μA and an energy of 5–8 kV. A chicane of four magnets, labeled D1–D4 in Figure 2-13, first deflects its trajectory some chosen distance above or below the beam axis, and then on the other side of the NTX beam line, deflects it back approximately to the original plane, where its position is registered on a scintillator for optical analysis. The current and energy

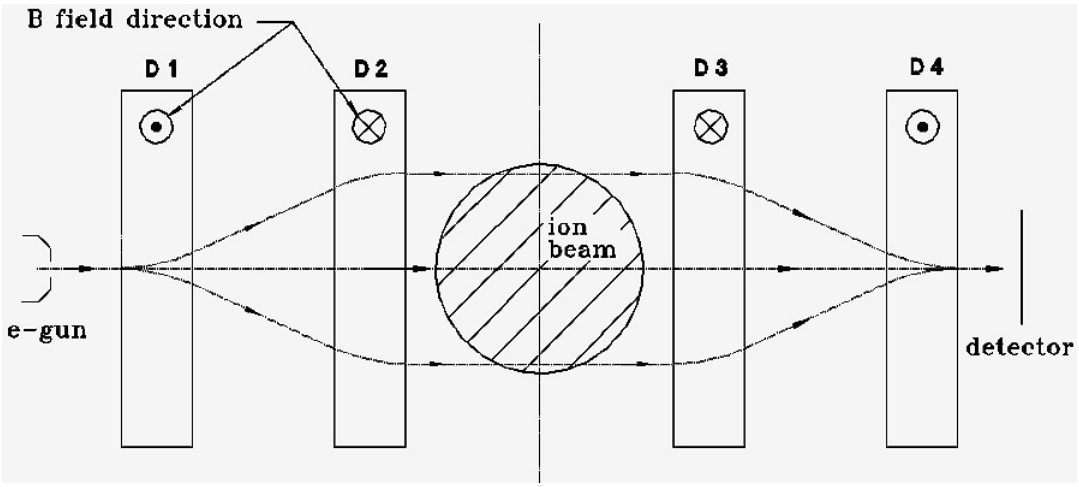

Figure 2-13: Sketch of the NTX non-intercepting beam diagnostics.

of the electron beam are chosen so that it will not significantly perturb the NTX beam but will itself be significantly deflected. Provided that the electron-beam space charge is negligible compared with the NTX beam, the electrons will be deflected at a predictable angle that depends on the charge-density distribution of the NTX beam, integrated along the electron-beam trajectory. By varying the strength of the magnetic fields on a series of NTX shots, the electron beam can pass through every part of the ion beam, and the scintillator detects the resulting deflections as functions of time along each pulse.

Figure 2-14 shows a photograph of the assembled diagnostic box, with the electron gun, magnets, and scintillator all placed inside a vacuum chamber maintained at better than 10^{-7} Torr. The commercial electron gun has a LaB6 cathode that operates at an energy of 5–10 keV and delivers a beam current that meets the requirement of 1–2 μA. The dipoles D1–D4 are iron-dominated to minimize the current requirement and provide high field uniformity, and they are designed to operate inside the vacuum chamber with the cathode. The detector is a Yttrium Aluminum Perovskite (YAP:Ce) scintillator with a 100-nm aluminum coating on the front surface to drain accumulated charge. A CCD camera is focused on the scintillator and is connected to a computer

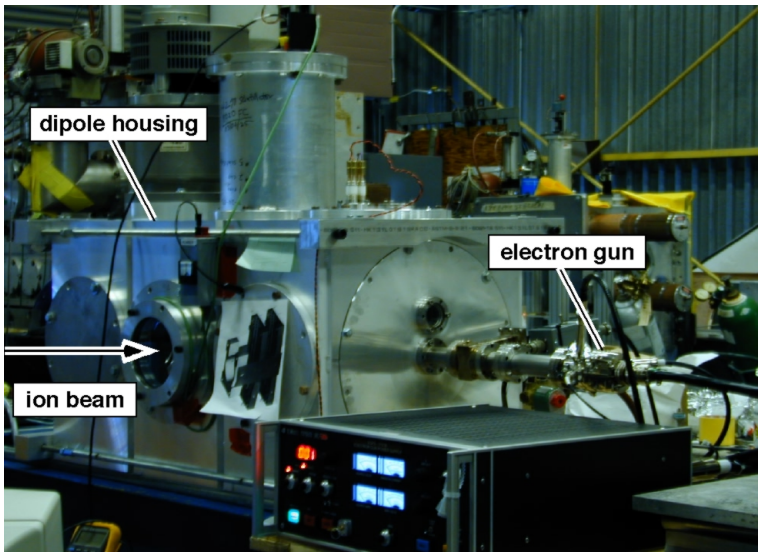

Figure 2-14: Photograph of the NTX non-intercepting beam diagnostics.

to record image data. We measure $\pm$ 3-cm vertical displacement of the electron beam while varying the current through magnets D1 and D2, confirming that this diagnostic can scan an ion beam with a diameter up to 6 cm. Results of this diagnostic and design details are presented elsewhere, along with preliminary experimental findings [50].

The diagnostic system has been installed in the NTX ion beam line to measure the ion beam density profile. The measured profile is compared with a direct scintillator measurement for the same ion beam parameters. Figure 2-15 shows the transverse displacement of the e-beam trajectory by the ion beam as the e-beam scanning height is varied relative to its axis to scan the ion beam radial profile. The lines with solid diamonds and hollow circles show, respectively, the experimental data and theoretical predictions. For the experimental data, the e-beam is vertically translated over a 4 cm height across the ion beam. A Python tracking code is used to model the e-beam deflection assuming an axissymmetric gaussian charge density distribution of 14 mm width and $\lambda = 2 \times 10^{-8}\, C/m$, e-beam energy of 8 keV and 2D (z, x) slab geometry.

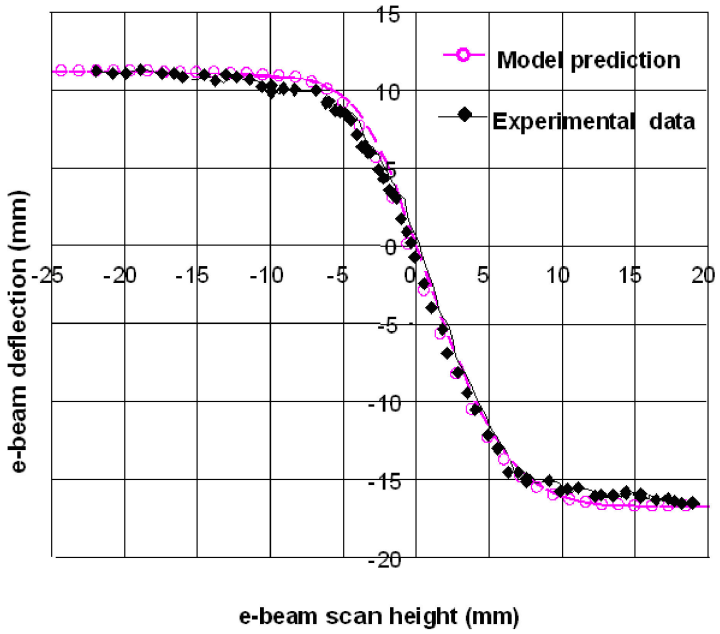

Figure 2-15: Transverse displacement of perturbed e-beam trajectory by an ion beam as a function of unperturbed e- beam trajectory. Experimental (solid diamonds) and calculated (hollow circles).

Figure 2-16 shows a comparison of the integrated ion beam density profiles measured optically by placing a ceramic scintillator in front of the ion beam, and by the e-beam system. The integrated densities are obtained by doing a least-square fit on the data presented in Figure 2-15 to obtain $I(y)$. The derived profiles agreed well for this 1.3 cm ion beam profile. Because of relative insensitivity to background subtraction, inherent in the optical imaging, the e-beam diagnostic has an advantage over the direct measurement of the beam profile with the scintillator. This is important when measuring beam halos.

2.5 Numerical Tools

In the HIF-VNL we have available a suite of computer codes to design the experiments, model details of their performance, and to analyze the data. These codes, which range from zero-dimensional systems codes to 3-D particle-in-cell simulations, are able to

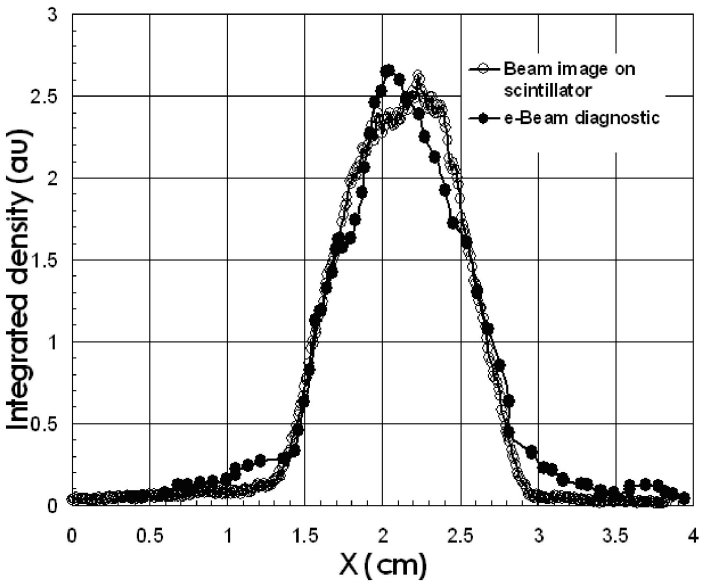

Figure 2-16: A comparison of the integrated ion beam density profile measurements. The lines with hollow and solid circles show, respectively, the ion beam profiles measured destructively by directly placing a ceramic scintillator in front of the ion beam, and nondestructively using the e-beam diagnostic system.

model all parts of an accelerator from source to target at an appropriate level of detail (Figure 2-17). In the accelerator, the areas studied include beam formation (ion source), beam matching, emittance growth, lattice-error tolerances, beam-halo formation, and bunch compression. Beam transport in the reactor chamber is also being examined to determine the best ways to neutralize the beam and to minimize the focal spot. In this thesis, the main computer codes used to run the numerical simulations are the ($r-z$ and $x-y$) particle-trajectory code EGUN for gun design, and the 3-D particle-in-cell code WARP. For the neutralized transport section, WARP is used by neglecting the plasma dynamics and assuming an effective space-charge neutralization for the ion beam. The 3-D electromagnetic code LSP is used for a self-consistent simulation including the ion beam and the neutralized plasma. For data analysis, we have a series of dedicated data reduction programs written in the computer language PYTHON. For image analysis the program of choice is ImageJ.

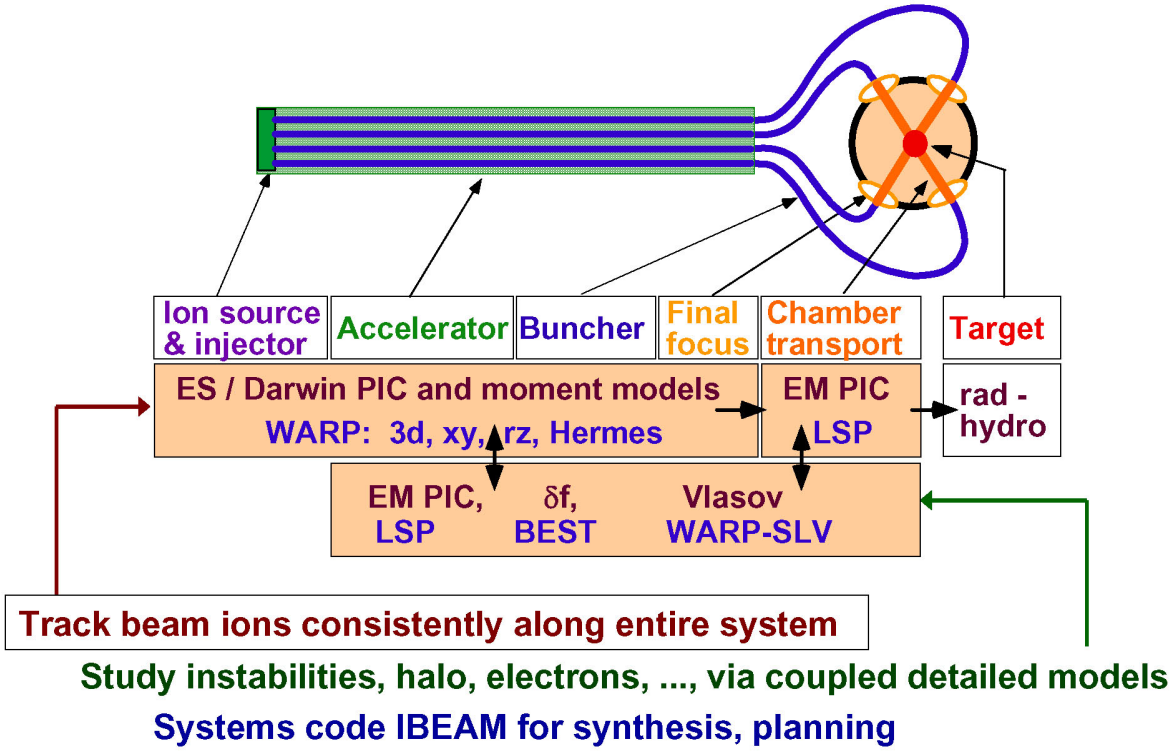

Figure 2-17: Codes for beam dynamics simulations.

2.5.1 EGUN

The ($r - z$ and $x - y$) particle-trajectory code EGUN [51] computes trajectories of charged particles in electrostatic and magnetostatic focusing systems including the effects of space charge and self-magnetic fields. Starting options include Child's Law conditions on emitters of various shapes, user-specified conditions input for each ray, and a combination of Child's Law conditions and user specifications. Either rectangular or cylindrically symmetric geometry may be used. Magnetic fields may be specified using an arbitrary configuration of coils, or the output of a magnet program, such as Poisson, or by an externally calculated array of the axial fields. The program first solves Laplace's equation. Next, the first iteration of particle trajectories is started using one of four starting options. On the first iteration cycle, space charge forces are calculated from the assumption of paraxial flow. As the rays are traced, space charge is computed and stored. After all the particle trajectories have been calculated, the program begins the second cycle by solving the Poisson equation with the space charge from the first iteration. Subsequent iteration cycles follow this pattern. The Poisson equation is solved by an alternate column relaxation technique known as the semi-iterative Chebyshev method. A fourth-order Runge-Kutta method is used to solve the relativistic differential equations of the trajectory calculations.

2.5.2 WARP

WARP [13] is a multidimensional (2-D and 3-D), electrostatic intense beam simulation program developed and used at the Heavy Ion Fusion Virtual National Laboratory. It allows flexible and detailed multi-dimensional modeling of high current beams in a wide range of systems, including bent beam lines using a "warped" coordinate system (from which the code derives its name). It is being designed and optimized for heavy ion fusion accelerator physics studies. At present it can model the beam dynamics

in a 3-D description, an axisymmetric (r, z) description, a transverse slice (x, y) description, a simple envelope model used primarily to obtain a well-matched initial state, and envelope/fluid models used for scoping and design. The discrete-particle models in WARP combine the particle-in-cell (PIC) technique commonly used for plasma modeling with a description of the "lattice" of accelerator elements. WARP is a time-dependent particle code – the particles are advanced in time and the self and applied fields are applied directly to update the particles' momenta. The calculation can follow the time-dependent evolution of beams, or can efficiently be used to study steady-state beam behavior in 3-D or 2-D (r, z) by solving for the self-consistent field only infrequently or by using an iterative method. The transverse-slice model is s-dependent, and is effectively a steady-flow model. The beam can be initially generated from one of several general distributions or from first principles via space-charge-limited injection from an emitting surface. The self-consistent field is assumed electrostatic – Poisson's equation is solved on a Cartesian mesh that moves with the beam. In a bend, the solution is altered to include the curvature of the coordinates. Complex conductor geometry can be included in the field solution using a subgrid-scale, or cut-cell, boundary algorithm to afford a realistic description of the geometry while minimizing the required grid resolution. Regions where the physics or the geometry requires a small spatial scale can be resolved as finely as needed using Adaptive Mesh Refinement, implemented in WARP. In order to accommodate space-charge-limited injection with very fast rise time, a specialized refinement patch is implemented. Near the emitting surface, the self-fields are calculated along independent one-dimensional lines normal to the surface, with increasing refinement towards the surface. Figure 2-18 shows a self consistent calculation of the ESQ Injector using WARP.

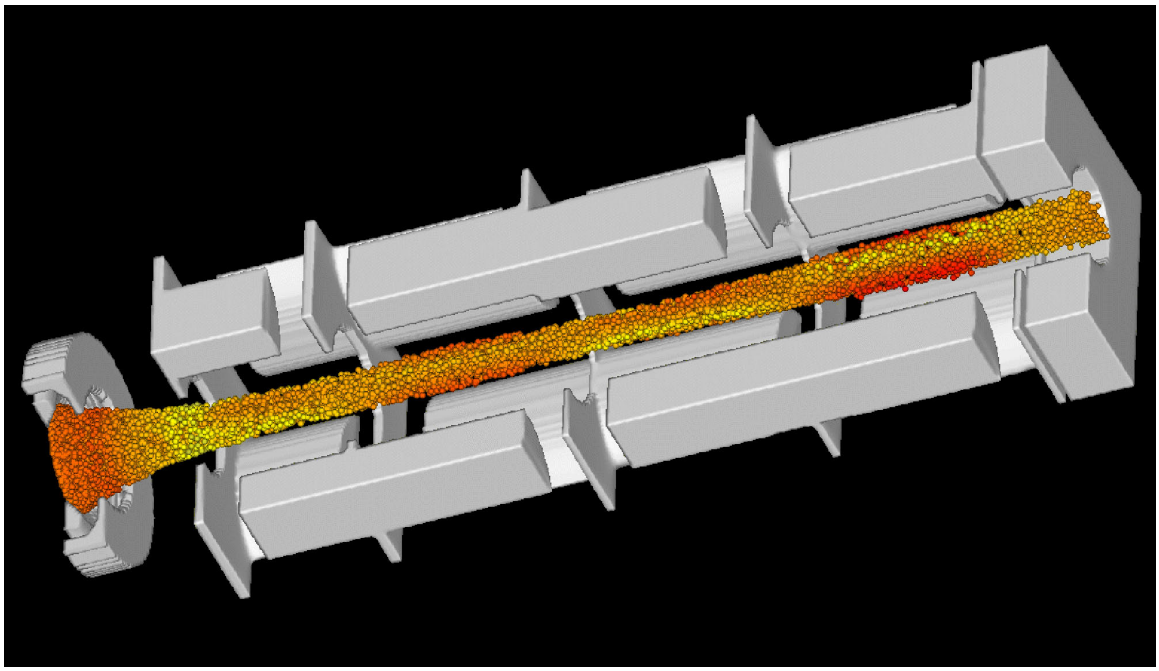

Figure 2-18: WARP simulation of the ESQ Injector.

2.5.3 LSP

LSP [15] is a 3-D (as well as 2-D and 1-D) electromagnetic code for large-scale electromagnetic plasma simulations using the particle-in-cell method. Both explicit and direct-implicit electromagnetic field and particle-advancing algorithms are available. Algorithms are also implemented for field emission, transmission-line boundaries, dielectrics, dispersive magnetic materials, secondary electron generation, multiple scattering, ionization of neutrals, surface heating, and desorption of neutrals from surfaces. A hybrid fluid model for electrons has been implemented, allowing electrons in dense plasmas to be modeled with a kinetic or fluid treatment as appropriate.

2.5.4 ImageJ

ImageJ is a public domain Java image processing program. It runs, either as an online applet or as a downloadable application, on any computer with a Java virtual machine. It can display, edit, analyze, process, save and print 8-bit, 16-bit and 32-

bit images. It can read many image formats including TIFF, GIF, JPEG, BMP, DICOM, FITS and "raw". It supports "stacks", a series of images that share a single window. It is multithreaded, so time-consuming operations such as image file reading can be performed in parallel with other operations. It can calculate area and pixel value statistics of user-defined selections. It can measure distances and angles. It can create density histograms and line profile plots. It supports standard image processing functions such as contrast manipulation, sharpening, smoothing, edge detection and median filtering. It does geometric transformations such as scaling, rotation and flips. Image can be zoomed up and down. All analysis and processing functions are available at any magnification factor. The program supports any number of windows (images) simultaneously, limited only by available memory. Spatial calibration is available to provide real world dimensional measurements in units such as millimeters. Density or gray scale calibration is also available. ImageJ is designed with an open architecture that provides extensibility via Java plugins. Custom acquisition, analysis and processing plugins can be developed using ImageJ's built in editor and Java compiler. User-written plugins make it possible to solve almost any image processing or analysis problem.

THIS PAGE INTENTIONALLY LEFT BLANK

Chapter 3

Ion Source

3.1 Calculation of the Pierce Electrode Shape for Aberration-free Sheet Particle Guns

In order to explore aberrations in magnetic transport and the effects of incomplete neutralization, an ion source with a variable perveance and a very low emittance has been designed and tested. The source characteristics are summarized in Section 3.3. Figure 3-1 shows the schematic of a typical ion diode and Figure 3-2 shows a photograph of the emitter and Pierce (focusing) electrode assembly.

The search for aberration-free diode geometries for the extraction of high-perveance

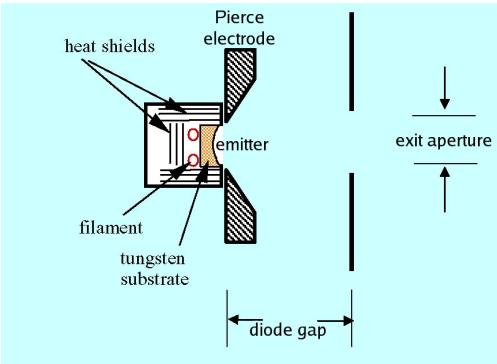

Figure 3-1: Schematic of a typical ion diode.

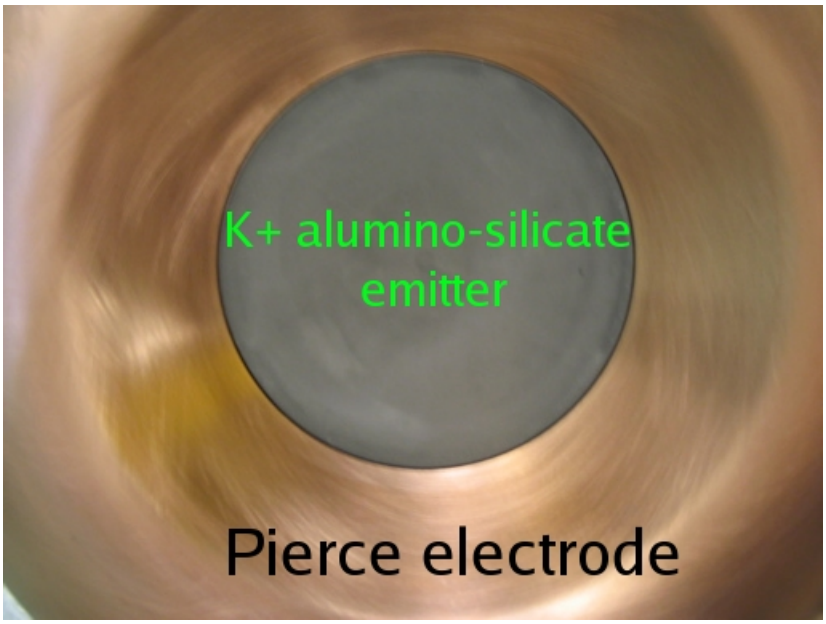

Figure 3-2: Photograph of the emitter and Pierce (focusing) electrode assembly.

beams has been a topic of research for the past 60 years, ever since Pierce [52] found an analytic solution for sheet beams. Pierce's solution can only be used in guns that do not have an aperture, or that have a high transparency mesh placed at the extracting electrode aperture to let the beam out and still define an equipotential. Furthermore his mathematical method, based on analytic functions of a complex variable to solve for the field potential outside the beam region, cannot be used in general geometries. We will describe a procedure to find aberration-free gun geometries for non-relativistic beam diodes in the framework of the cold-fluid description. Discussions are made regarding appropriate boundary conditions, and analytic and numerical methods are introduced in order to solve such a complex diode problem.

3.1.1 Cold fluid description of non-relativistic beams

It is plausible to assume that the beam flow is governed by the cold-fluid equations, because the thermal energy of the particles (i.e., the temperature) is negligibly small compared with the energy associated with the mean flow of the beam in a well-

designed particle gun. In the IS units, the cold-fluid equilibrium equations are:

$$(\mathbf{V}\cdot\nabla)\gamma\mathbf{V} = \frac{q}{m}[\mathbf{E_0}+\mathbf{E^s}+\mathbf{V}\times(\mathbf{B_0}+\mathbf{B^s})], \tag{3.1}$$

$$\nabla\cdot(n\mathbf{V}) = 0, \tag{3.2}$$

$$\nabla\cdot(\mathbf{E_0}+\mathbf{E^s}) = \frac{q}{\varepsilon_0}n, \tag{3.3}$$

$$\nabla\times(\mathbf{E_0}+\mathbf{E^s}) = 0, \tag{3.4}$$

$$\nabla\times(\mathbf{B_0}+\mathbf{B^s}) = \mu_0 q n\mathbf{V}, \tag{3.5}$$

$$\nabla\cdot(\mathbf{B_0}+\mathbf{B^s}) = 0 \tag{3.6}$$

where q and m are the ion charge and rest mass, respectively, $n(\mathbf{x})$ is the ion density and $\mathbf{V}(\mathbf{x})$ is the ion flow velocity,

$$\gamma(\mathbf{x}) = \left[1-\frac{V^2(\mathbf{x})}{c^2}\right]^{-1/2} \tag{3.7}$$

is the relativistic mass factor, which is kept to be non-unity in the present formulation applicable for both electron and ion diodes; c is the speed of light in vacuum, $\mathbf{E_0}(\mathbf{x})$ and $\mathbf{B_0}(\mathbf{x})$ are the externally applied electric and magnetic fields, respectively, $\mathbf{E^s}(\mathbf{x})$and $\mathbf{B^s}(\mathbf{x})$ are the self-electric and self-magnetic fields of the ion beam, respectively.

There are four variables, namely, $n(\mathbf{x})$, $\mathbf{V}(\mathbf{x})$, $\mathbf{E^s}(\mathbf{x})$, and $\mathbf{B^s}(\mathbf{x})$, that must be solved with appropriate boundary conditions discussed below.

For future references, introducing the electrostatic potential $\phi(\mathbf{x})$ and magnetostatic vector potential $\mathbf{A}(\mathbf{x})$ defined by

$$\mathbf{E}(\mathbf{x}) = \mathbf{E_0}(\mathbf{x})+\mathbf{E^s}(\mathbf{x}) = -\nabla\phi(\mathbf{x}), \tag{3.8}$$

$$\mathbf{B}(\mathbf{x}) = \mathbf{B_0}(\mathbf{x}) + \mathbf{B^s}(\mathbf{x}) = \nabla \times \mathbf{A}(\mathbf{x}), \tag{3.9}$$

and the current vector potential $\chi(\mathbf{x})$defined by

$$\mathbf{J}(\mathbf{x}) = qn(\mathbf{x})V(\mathbf{x}) = \nabla \times \chi(x), \tag{3.10}$$

we express the cold-fluid equilibrium equations as

$$(\mathbf{V} \cdot \nabla)\gamma\mathbf{V} = \frac{q}{m}[\mathbf{E} + \mathbf{V} \times \mathbf{B}], \tag{3.11}$$

$$\nabla^2\phi = -\frac{q}{\varepsilon_0}n, \tag{3.12}$$

$$\nabla^2\mathbf{A} = -\mu_0 qn\mathbf{V}, \tag{3.13}$$

where $\mathbf{A}(\mathbf{x})$ has been assumed to satisfy the gauge condition

$$\nabla\cdot\mathbf{A}(\mathbf{x}) = 0. \tag{3.14}$$

Evidently, the cold-fluid equilibrium equations are highly nonlinear.

For a non-relativistic diode, the applied and self-magnetic fields may be negligibly small. Under the approximations

$$\gamma(\mathbf{x}) \cong 1, \tag{3.15}$$

$$\mathbf{B}(\mathbf{x}) = \mathbf{B_0}(\mathbf{x}) + \mathbf{B^s}(\mathbf{x}) = 0, \tag{3.16}$$

we only need to solve Eqs. (3.1)–(3.3). Assuming the laminar flow condition

$$\nabla\times\mathbf{V}(\mathbf{x}) = 0 \tag{3.17}$$

we find from Eq. (3.1) that

$$\nabla \left[\frac{1}{2} m V^2(\mathbf{x}) + q\phi(\mathbf{x}) \right] = 0 \tag{3.18}$$

or

$$\frac{1}{2} m V^2(\mathbf{x}) + q\phi(\mathbf{x}) = const = 0, \tag{3.19}$$

where we have set the constant to be zero so that for a space-charge limited emission gun (zero flow velocity emission) the electrostatic potential is zero at the emitter. Since $\mathbf{J}(\mathbf{x}) = qn(\mathbf{x})V(\mathbf{x})$, then

$$n(\mathbf{x}) = \frac{|\mathbf{J}(\mathbf{x})|}{|q|\,|\mathbf{V}(\mathbf{x})|} = \frac{1}{|q|}\sqrt{\frac{m}{2}}\frac{J(\mathbf{x})}{\sqrt{-q\phi(\mathbf{x})}}, \tag{3.20}$$

where $J(\mathbf{x})$ is the magnitude of the current density vector $\mathbf{J}(\mathbf{x})$.

Therefore, the entire non-relativistic diode problem is reduced to the following two equations

$$\nabla \cdot \mathbf{J}(\mathbf{x}) = 0, \tag{3.21}$$

$$\nabla^2 \phi = \frac{1}{\varepsilon_0}\sqrt{\frac{m}{2q}}\frac{J(\mathbf{x})}{\sqrt{\phi(\mathbf{x})}}, \tag{3.22}$$

which must be solved subject to appropriate boundary conditions. Notice the change of notation in Eq. (3.22) so that these equations describe the flow of negative particles of charge $-q < 0$, and that the potential is non-negative.

3.1.2 Prescription to Find Aberration-Free Gun Geometries

Equations (3.21) and (3.22) form the basis to find the field potential (ϕ) configurations inside the beam region by prescribing a divergence-free current density flow ($\mathbf{J}$) and defining beam boundaries in such a way as to have self-consistent boundary conditions for the electrostatic potential. The potential inside the beam is a solution of the

following system

$$\nabla^2\phi = \frac{1}{\varepsilon_0}\sqrt{\frac{m}{2q}}\frac{J(\mathbf{x})}{\sqrt{\phi(\mathbf{x})}}, \tag{3.23}$$

$$\varphi\,|_{emitter} = 0, \tag{3.24}$$

$$\varphi\,|_{collector} = \phi_0, \tag{3.25}$$

$$\frac{\partial\phi}{\partial n}\,|_{beam-boundary} = f(\mathbf{x}), \tag{3.26}$$

where $f(x)$ must be chosen self consistently.

Once ϕ is found *inside* the beam region we solve for the potential ψ *outside* the beam region by solving Laplace's equation and matching the *inside* and *outside* solutions for the potential and the normal derivative at the *beam boundary*. This is a *Cauchy problem for Laplace equation*,

$$\nabla^2\psi(\mathbf{x}) = 0, \tag{3.27}$$

$$\psi_{beam-boundary} = \phi_{beam-boundary}, \tag{3.28}$$

$$\frac{\partial\psi}{\partial n}\,|_{beam-boundary} = f(\mathbf{x}). \tag{3.29}$$

For the beam interior, the simplest choice for an aberration-free beam flow is to set $\mathbf{J} = J\mathbf{e_z}$, where $J = constant$, i.e., particles follow straight line trajectories from the emitter to the collector. Figure 3-3 describes a generic system for a constant current density flow.

The boundary conditions appropriate for this type of flow are described in Figure 3-4. The emitter and collector are equipotential surfaces and the field must be parallel to the beam boundaries. In this situation $f(\mathbf{x}) = 0$ on the beam boundary, i.e., the electric field normal to the field boundary vanishes.

The boundary conditions to determine the equipotential extensions from the emitter and from the collector are described in Figure 3-5. Notice that the boundary

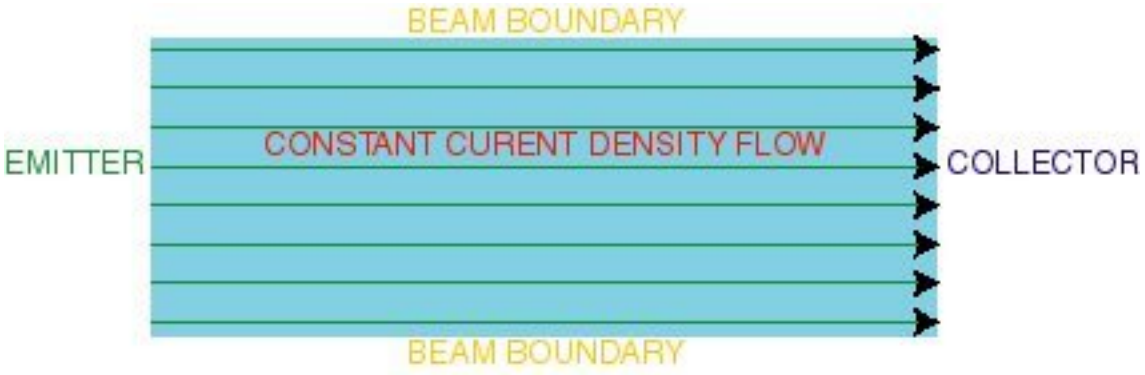

Figure 3-3: Generic Gun System for Constant Current Density Flow.

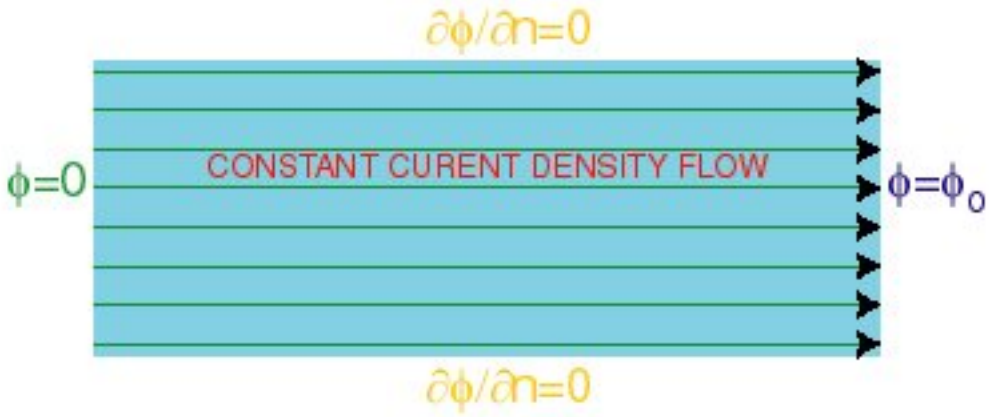

Figure 3-4: Boundary conditions for Generic Gun System for Constant Current Density Flow.

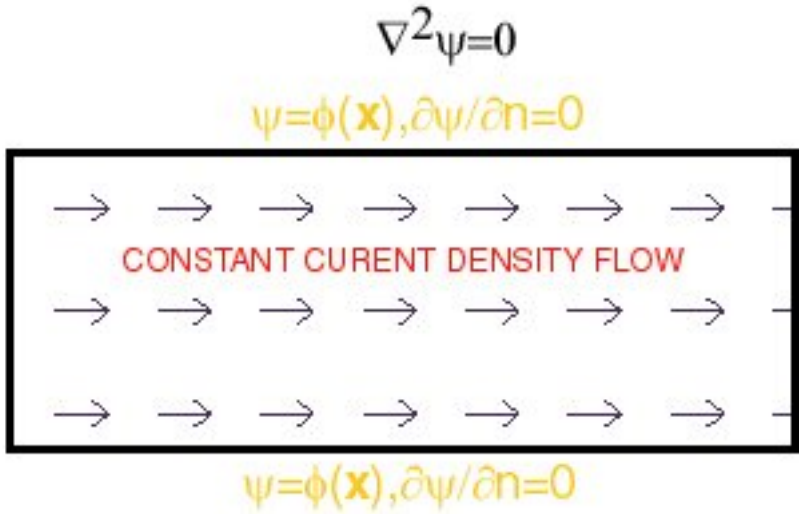

Figure 3-5: Boundary conditions for exterior solution of Generic Gun System for Constant Current Density Flow

conditions are specified *only for the beam boundary.* The potential ψ does not have to match the potential ϕ anywhere else.

More complex flows, like converging axisymmetric flows, can be described by an appropriate choice of the divergence-free current density vector $\mathbf{J}(r,z)$. For example the uniform beam flow between concentric spheres is described by

$$\mathbf{J}(r,z) = \frac{C}{(r^2+z^2)^{3/2}}(r\mathbf{e_r} + z\mathbf{e_z}) \tag{3.30}$$

where C is a constant. The choice

$$\mathbf{J}(r,z) = \frac{C}{r(r^2+z^2)}(r\mathbf{e_r} + z\mathbf{e_z}) \tag{3.31}$$

with C being a constant, will generate a non-uniform flow.

3.1.3 Sheet beams and Pierce diode solution for 2-D flow

For constant current density flow in slab geometry, where the beam is flowing along the z-direction and is infinite along the y-direction, we have from Eq. (3.23),

$$\nabla^2\phi(x,z) = \frac{1}{\varepsilon_0}\sqrt{\frac{m}{2q}}\frac{J}{\sqrt{\phi(x,z)}}, \tag{3.32}$$

where

$$\mathbf{J}(x,z) = -J\mathbf{e_z} \tag{3.33}$$

and $J > 0$ is an *arbitrary* constant. In order to fix the value of J, an additional boundary condition must be imposed on ϕ. We choose the space-charge limited emission condition $\phi'(0) = 0$.

3.1.3.1 Electrostatic potential solution inside the beam.

Equation (3.32) is the equation for the potential inside the beam. Since there are no forces along the x-direction, then

$$\phi''(z) = \frac{1}{\varepsilon_0}\sqrt{\frac{m}{2q}}\frac{J}{\sqrt{\phi(z)}}, \tag{3.34}$$

$$\phi(0) = 0, \tag{3.35}$$

$$\phi(d) = \phi_0, \tag{3.36}$$

$$\phi'(0) = 0, \tag{3.37}$$

where d is the distance from the emitter to the collector. The boundary conditions on the beam boundary are trivially satisfied since the potential does not depend on the x-direction.

The solution to Eq. (3.34) is

$$\phi(z) = \phi_0 \left(\frac{z}{d}\right)^{4/3}. \tag{3.38}$$

The current density J is related to ϕ_0 and d by the Child-Langmuir Law

$$J = \frac{4\varepsilon_0}{9}\sqrt{\frac{2q}{m}}\frac{\phi_0^{3/2}}{d^2}. \tag{3.39}$$

3.1.3.2 Electrostatic potential solution outside the beam.

Outside the beam the electrostatic potential obeys Laplace's equation. In slab geometry the upper and lower regions bounded by the equipotentials from the emitter and the collector are independent and the solution in one region can be obtained from the other by reflection. For simplicity let's define as $x = 0$ the position of the upper beam boundary. Then we have to solve

$$\frac{\partial^2\psi}{\partial x^2} + \frac{\partial^2\psi}{\partial z^2} = 0, \tag{3.40}$$

$$\psi_{beam-boundary} = \phi_0 \left(\frac{z}{d}\right)^{4/3}, \tag{3.41}$$

$$\frac{\partial\psi}{\partial n} \mid_{beam-boundary} = 0. \tag{3.42}$$

It is straightforward to obtain a solution to Eq. (3.40) by working in the complex plane defined by the variable $w = z + ix$, which gives

$$\psi(x,z) = \phi_0 \Re \left(\frac{z+ix}{d}\right)^{4/3}. \tag{3.43}$$

Since the right hand side of Eq. (3.43) is the real part of an analytic function, it is a solution of Laplace's equation; also since it is symmetric about $x = 0$, then $\frac{\partial\psi}{\partial n}(x = 0, z) = 0$. Furthermore $\psi(x = 0, z) = \phi_0 \left(\frac{z}{d}\right)^{4/3}$.

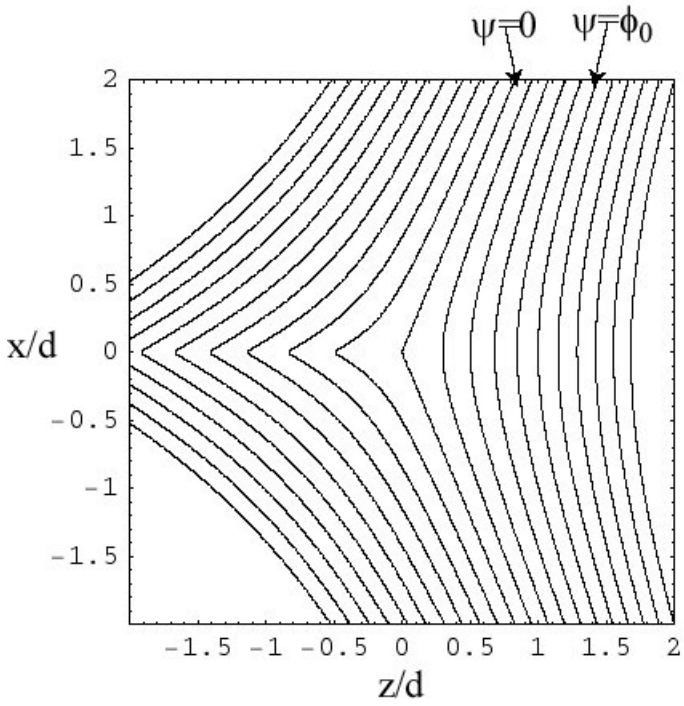

Figure 3-6: Equipotentials of ψ.

In the polar coordinates $z = \rho\cos\theta, x = \rho\sin\theta$, we have

$$\psi(\rho,\theta) = \phi_0 \left(\frac{\rho}{d}\right)^{4/3} \cos(4\theta/3). \tag{3.44}$$

Figure 3-6 shows the equipotentials of ψ. The only region relevant for our analysis is the region bounded by the equipotential that start from the emitter, the equipotential that start from the collector , the $x = 0$ line and the boundary at infinity. Figure 3-7 shows the gun design based on this solution obtained by Pierce in 1940 [52].

Notice that in polar coordinates, the equation for the equipotential that starts at the emitter is given by

$$\theta = 3\pi/8, \tag{3.45}$$

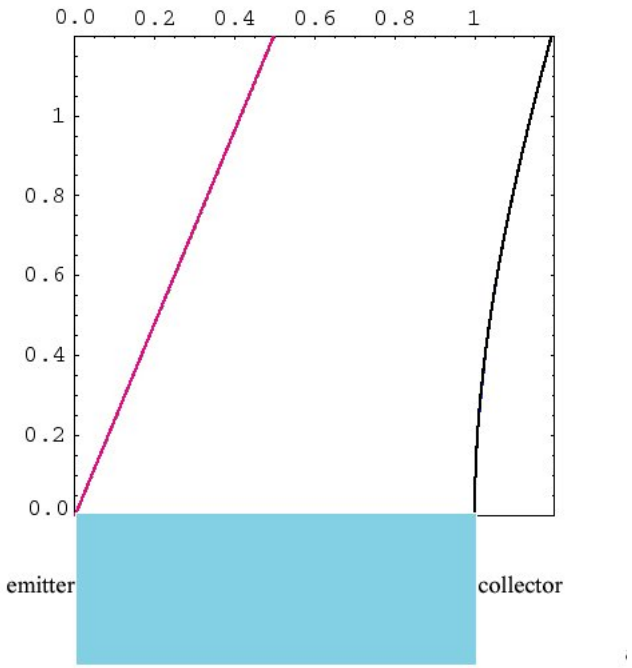

Figure 3-7: Pierce solution for uniform rectilinear space-charge flow in slab geometry.

and the equation of the equipotential that starts at the collector is

$$(\rho/d)^{4/3}\cos(4\theta/3) = 1, \tag{3.46}$$

as illustrated in Figure 3-7.

3.2 Current transient elimination in one-dimensional diodes

Section 3.1, which describes a procedure to obtain an aberration-free ion beam diode design, assumes a time-independent steady-state space-charge-dominated (Child-Langmuir) flow. In practical situations, during beam turn-on the voltage at the source is increased from zero to start extracting the beam; it stays constant for a time comparable to the desired pulse length, and is decreased to zero to turn off the emission.

The transient behavior is dominated by the extraction pulser voltage time profile and the transit time of the ions inside the diode.

The transient longitudinal dynamics, i.e., the relationship between the time-dependent voltage on the "extracting electrode" and the current and energy at the end of the diode is simulated by running particle-in-cell codes like WARP3D in a time-dependent mode.

Figure 3-8 shows the experimental waveforms, from the 2 MeV ESQ Injector at LBNL, of the current and energy transient oscillations, which decay away within a few multiples of the particle transit time across the gun, for the case of a sudden turn-on of the extracting voltage. The elimination of these oscillations is very important for space-charge-dominated beams since such oscillations will lead to envelope variations along the beam which will reduce the dynamic aperture of the accelerator.

In this section we discuss the generalization, to any complex geometry, of a method proposed by Lampel and Tiefenback [53] to eliminate transient oscillations in a one-dimensional planar diode. This generalization has been implementated in WARP3D.

3.2.1 Current transient elimination in a one-dimensional planar diode

In a one-dimensional planar diode it is possible to find an analytic solution for the extracting voltage waveform that will eliminate the current and energy transient oscillations.

Figure 3-9 shows a schematic diagram of a planar diode. Let $\phi(x)$ be the potential corresponding to the steady-state space-charge-dominated flow:

$$\phi(x) = -V(x/L)^{4/3}. \tag{3.47}$$

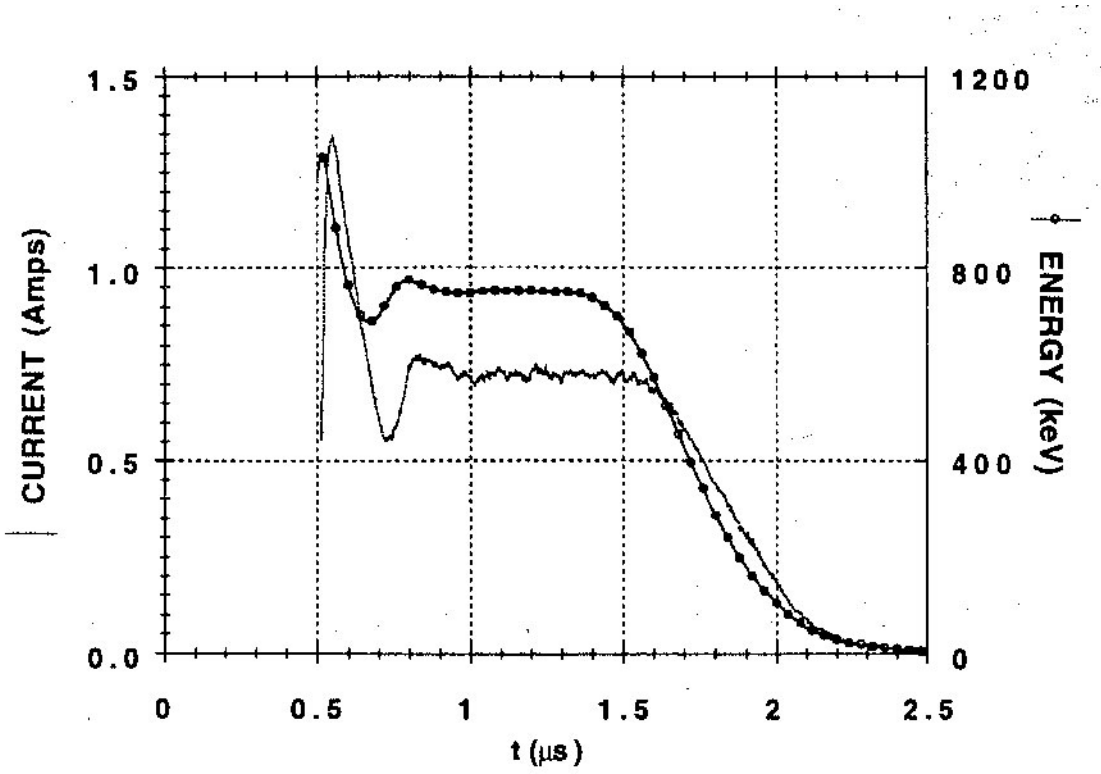

Figure 3-8: Current and energy transient oscillations for the case of a sudden turn-on of the extracting voltage.

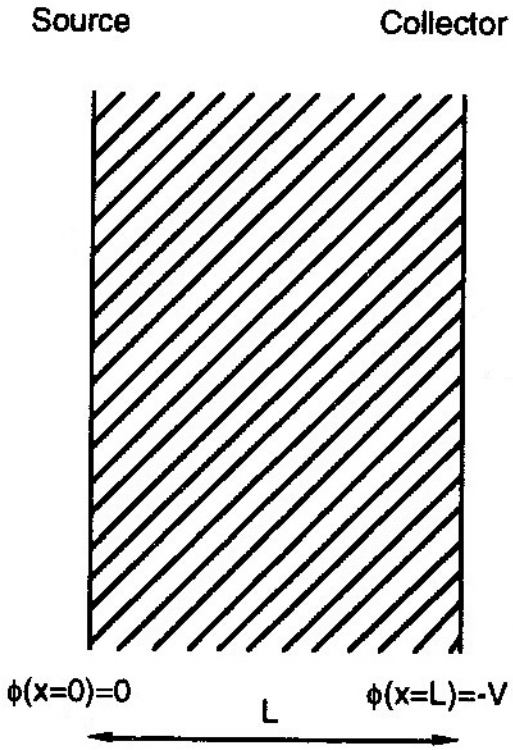

Figure 3-9: Schematic diagram of a planar diode.

3.2.1.1 Correction of beam head oscillations

To calculate the required V(t) we use the following procedure starting from the steady state solution [53].

- Divide the diode into two regions on either side of the plane at $x = \xi$ (Figure 3-10).
- Eliminate the charge for $x > \xi$.
- Keep field solution for $x < \xi$ unchanged by requiring the field at $x = \xi$ to be the same as in the steady-state space-charge-dominated flow.
- Find the potential at the collector to satisfy Laplace's equation for $x > \xi$, and continuity of potential and field at $x = \xi$. The result is

$$\psi_c(\xi) = -V[\frac{4}{3}(\xi/L)^{1/3} - \frac{1}{3}(\xi/L)^{4/3}]. \tag{3.48}$$

- Express the parameter ξ in terms of the time at which the leading particles in the beam are at ξ. From energy conservation we obtain

$$\frac{1}{2}m(d\xi/dt)^2 = qV(\xi/L)^{4/3}. \tag{3.49}$$

By integrating the preceding equation we obtain

$$(\xi/L) = (t/\tau)^3, \tag{3.50}$$

where the transit time factor is defined as

$$\tau = 3\sqrt{mL^2/2qV}. \tag{3.51}$$

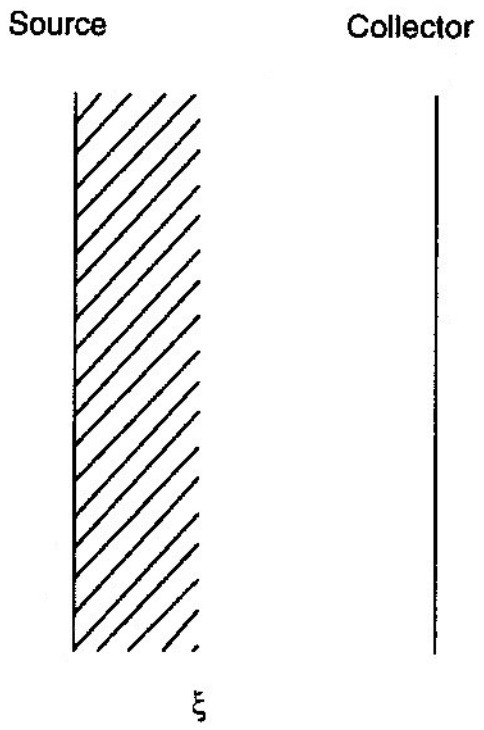

Figure 3-10: Beam head uniform current flow.

Since $V(t) = \psi_c(\xi)$, the beam head oscillations will be corrected by applying the following voltage waveform at the collector

$$V(t) = -V[\frac{4}{3}(t/\tau) - \frac{1}{3}(t/\tau)^4] \text{ for } t < \tau, \tag{3.52}$$

$$V(t) = -V \text{ for } t \geq \tau, \tag{3.53}$$

which is illustrated in Figure 3-15.

3.2.1.2 Correction of beam tail oscillations

The procedure can be extended to eliminate beam tail oscillations by dividing the diode into two regions on either side of the plane at $x = \xi$, eliminating the charge for $x < \xi$ (Figure 3-11), keeping the field solution for $x > \xi$ unchanged by requiring the

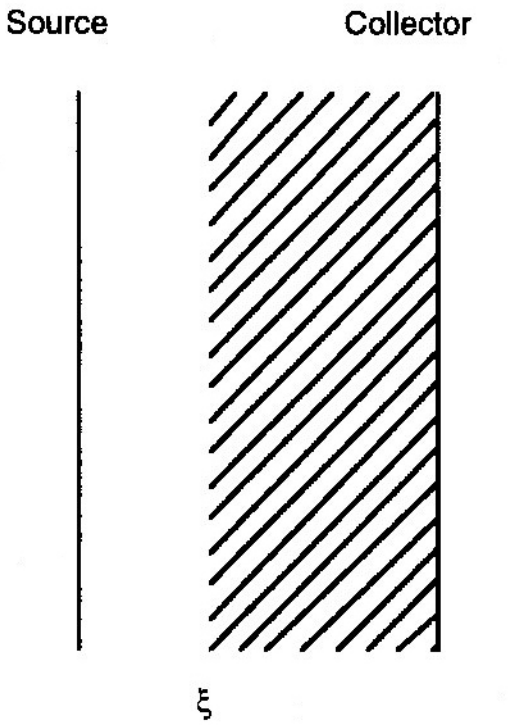

Figure 3-11: Beam tail uniform current flow.

field at $x = \xi$ to be the same as in the steady-state space-charge-dominated flow, and changing the potential at the collector to satisfy Laplace's equation for $x < \xi$, and continuity of potential and field at $x = \xi$. The solution in terms of the parameter ξ is

$$\psi_c(\xi) = -V[1 + \frac{1}{3}(\xi/L)^{4/3}]. \tag{3.54}$$

Setting the time origin as the time when the emission stops, the beam tail oscillations will be corrected by applying the following voltage waveform at the collector:

$$V(t) = -V[1 + \frac{1}{3}(t/\tau)^4] \text{ for } t < \tau. \tag{3.55}$$

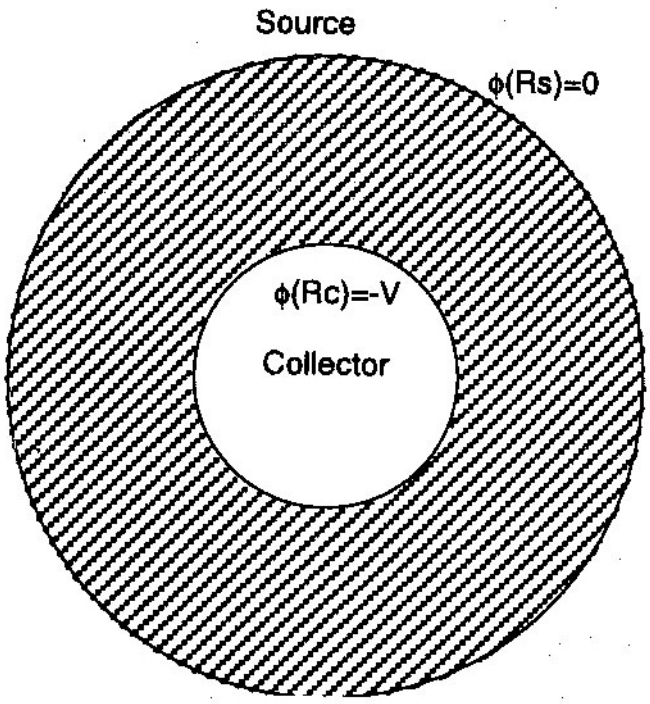

Figure 3-12: Schematic diagram of a concentric-spheres diode.

3.2.2 Current transient elimination between concentric spheres

For the Child-Langmuir flow between concentric spheres (or between infinite coaxial cylinders), the procedure described above provides a set of ordinary differential equations whereby a solution for the extracting voltage waveform can be obtained that will eliminate the current and energy transient oscillations.

Figure 3-12 shows a schematic diagram of a diode formed by two concentric spheres. Let $\phi(r)$ be the potential corresponding to the steady-state space-charge-dominated flow. The Poisson equation is

$$(1/r^2)(d/dr)(r^2 d\phi/dr) = -\rho/\varepsilon_0. \tag{3.56}$$

Since

$$\frac{1}{2}mv^2 = -q\phi \text{ and } \rho = I/4\pi r^2 v, \tag{3.57}$$

we obtain

$$(d/dr)(r^2 d\phi/dr) = -(I/4\pi\varepsilon_0)\sqrt{-m/2q\phi}, \tag{3.58}$$

where v and I are the beam velocity and current respectively.

To correct for the beam head transients we will follow the same procedure described in Section 3.2.1, starting from the steady-state Child-Langmuir flow solution.

- Divide the diode into two regions on either side of the sphere at $r = \xi$ (Figure 3-13).
- Eliminate the charge for $r < \xi$.
- Keep field solution for $r > \xi$ unchanged by requiring the field at $r = \xi$ to be the same as in the steady-state space-charge-dominated flow.
- Find the potential at the collector to satisfy Laplace's equation for $r < \xi$, and continuity of potential and field at $r = \xi$. The result is

$$\psi_c(\xi) = \xi^2(1/\xi - 1/R_c)\phi'(\xi) + \phi(\xi). \tag{3.59}$$

- Express the parameter ξ in terms of the time at which the leading particles in the beam are at ξ. F1rom energy conservation we obtain (inward flow)

$$\frac{1}{2}m(d\xi/dt)^2 = -q\phi. \tag{3.60}$$

Since we do not have a closed form solution for $\phi(r)$, $V(t)$ will be obtained by integrating numerically Poisson's and the velocity equations to obtain $\phi(\xi)$ and $t(\xi)$. The initial conditions are

$$\phi(R_s) = 0, \tag{3.61}$$

$$\phi'(R_s) = 0, \tag{3.62}$$

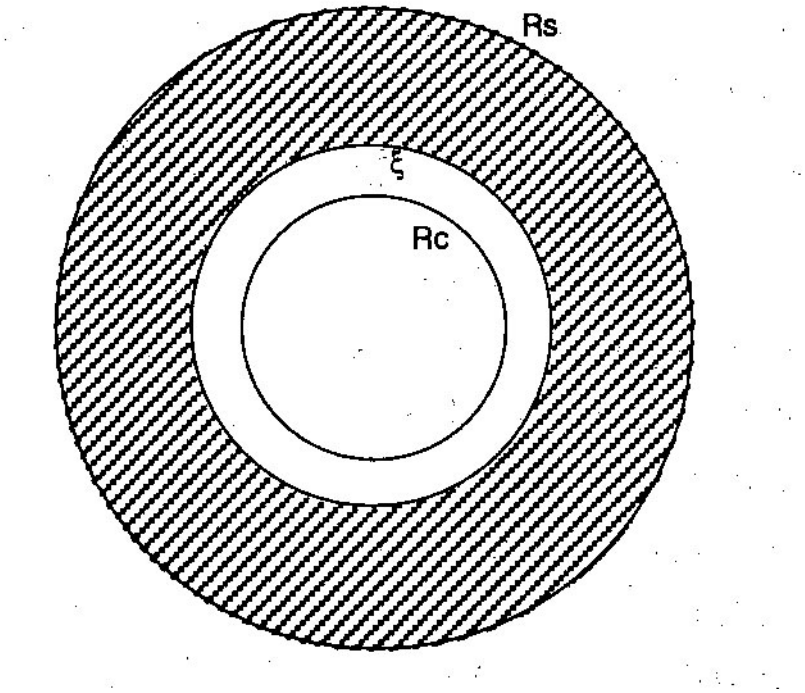

Figure 3-13: Beam head uniform current flow.

$$\tau(R_s) = 0. \tag{3.63}$$

Since $V(t) = \phi_c(\xi)$, we obtain the required voltage waveform by substituting these solutions into the expression for $\phi_c(\xi)$.

A similar analysis, following a different approach, has been reported by Kadish et al. [54]. Particle codes written to study the beam dynamics of one-dimensional diodes have been used to check the validity of the procedure [55-57].

3.2.3 Current transient elimination in general geometries

The essential feature of the described procedure is to force the field solution in the region occupied by the beam, at any given time, to be the same as the steady state solution in the same region. This can be done in one-dimensional structures by prescribing an extracting voltage waveform $V(t)$ since a condition at a single point (the collector) is enough to fulfill the requirement.

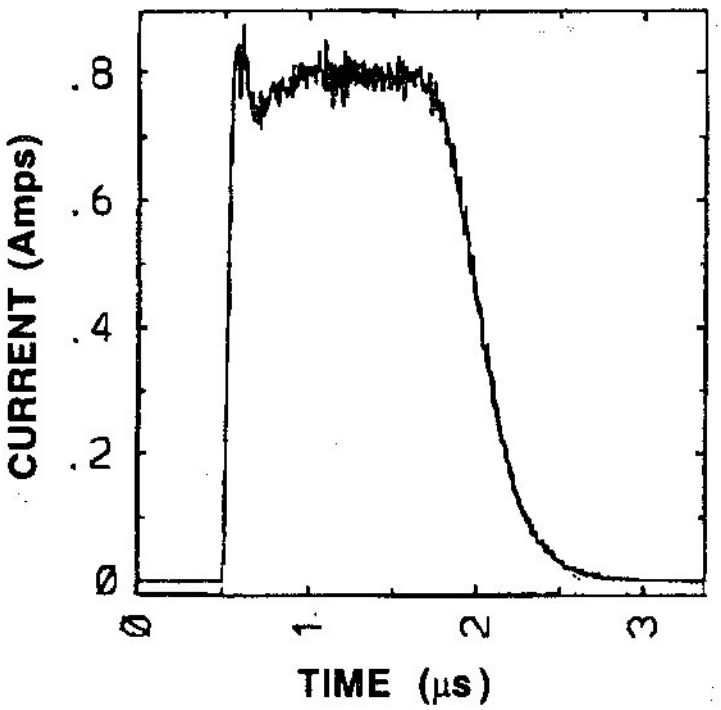

Figure 3-14: Current profile for the 2 MeV injector using the numerically calculated voltage wave form.

For a two- or three-dimensional gun, the procedure requires the prescription of extracting voltage waveforms along a curve or on a surface, respectively. Since this requirement is not attainable we can compensate only partially the transient oscillations. For an axisymmetric structure, for example, one may use as an effective potential the average energy of the particles at a given cross-section and follow the same procedure as that described for one-dimensional structures.

We have implemented the general procedure to eliminate transient oscillations in the three-dimensional particle-in-cell code WARP3D.

We have also implemented it in two injectors, namely, the earlier 2 MeV Injector [58] and the present NTX diode. Figure 3-14 shows the current at the end of the cylindrically symmetric 2 MeV injector using the numerically calculated voltage waveform $V(t)$ applied on the extracting electrode. The resulting current profile exhibits

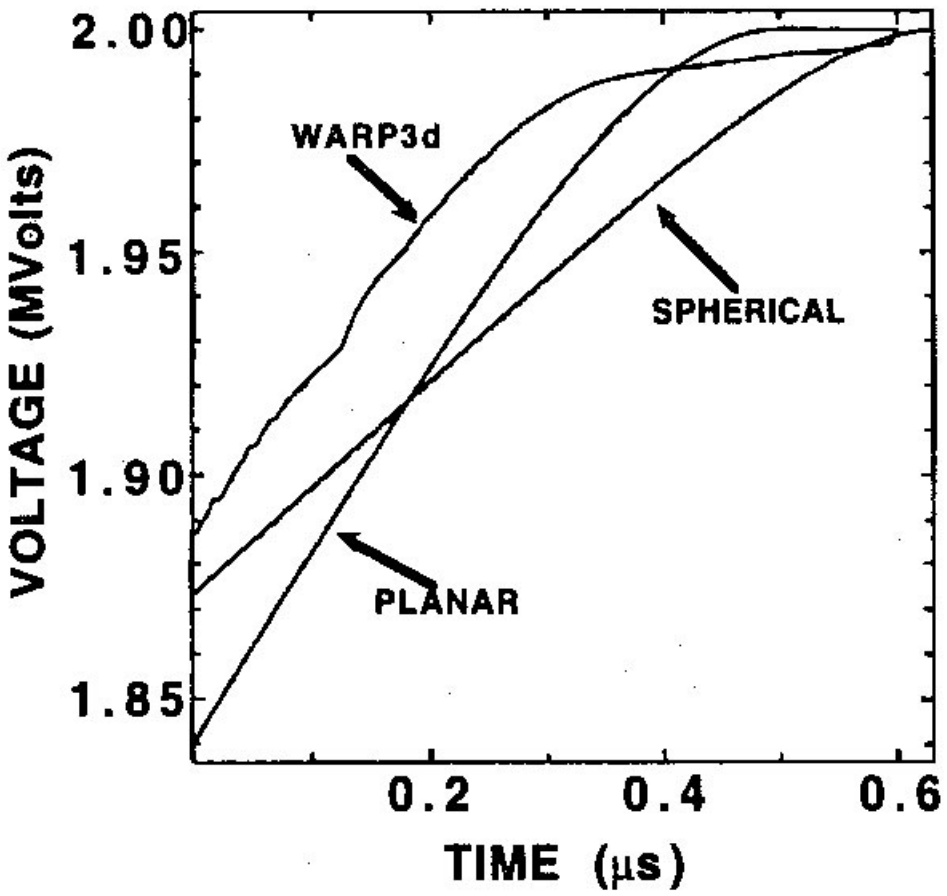

Figure 3-15: Voltage waveform as calculated and used in WARP3D and the corresponding ideal waveforms for the planar, and spherical-equivalent diodes.

a decrease in the beam head transient oscillation. Since the 2 MeV heavy ion fusion injector gun is poorly represented by either a planar diode or a two-concentric-sphere diode, attempts to use the voltage waveforms $V(t)$ calculated for such geometries resulted in a rather small decrease in the transient oscillation. Figure 3-15 compares the waveforms obtained for the planar and spherical diodes.

An attempt to elliminate transient oscillations in the NTX diode will be discussed in Sec. 3.3.3..

3.3 The NTX Variable-perveance Heavy Ion Source

3.3.1 Design and performance of a high brightness ion source

The NTX experiments require a beam current that can be varied by one order of magnitude, up to 75 mA. This variability is needed both to investigate the effects of aberrations in final focus and to test the sensitivity of plasma neutralization to beam current. In addition, neutralization studies also require a high source brightness, a quantity which is proportional to the beam current divided by the square of its emittance [33]. The use of aperturing to vary the perveance simultaneously generates high-brightness beams by removing the edge of the beam after it exits the diode. Beam scraping, however, produces secondary electrons that must be controlled. Stray electrons can introduce nonlinear space-charge forces, which can lead to an increase of the transverse emittance [59] and, in extreme cases, to beam disruption. In NTX, the secondary electrons are controlled by placing electron traps near the beam scraper. Each of these electron traps has a sufficiently large negative potential to confine the electrons even in the presence of the positive ion-beam self field.

The EGUN [51] calculation in Figure 3-16 shows potential contours and steady-state ion trajectories for a nominal case of the ion gun, including the diode and the beam aperture and electron-trapping device. The 75-mA K^+ beam is produced on the surface of a 2.54-cm diameter alumino-silicate source [46] heated to 1060 ^{o}C, and it exits the 12-cm diode gap with an energy of 300–400 keV. A beam aperture plate, with holes of variable diameter, is placed about 8 cm beyond the diode exit plate, sandwiched between two metal rings of 5-cm length and 6.2-cm inner diameter. The nominal 3 kV negative bias on these rings provides adequate trapping of the free electrons produced by ions striking the aperture. Figure 3-17 shows a photograph of the NTX beam scraper system.

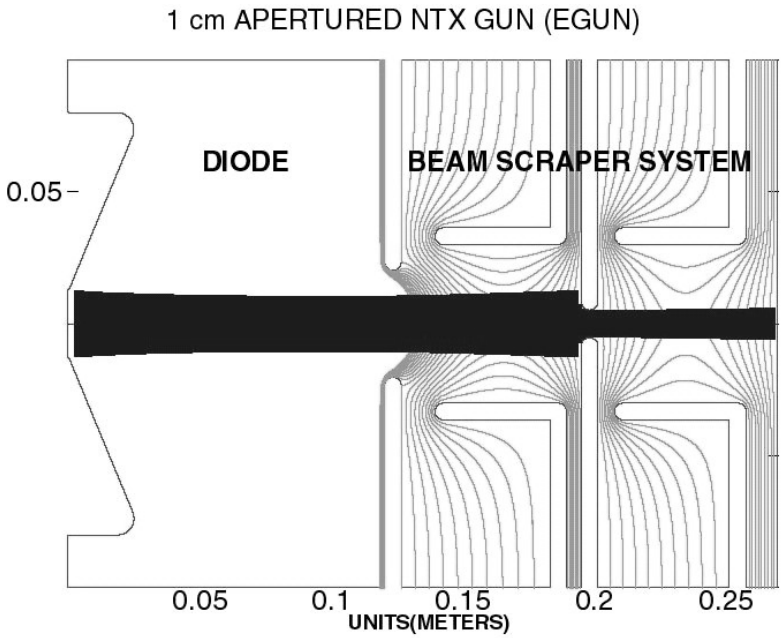

Figure 3-16: EGUN simulation of the NTX diode and beam aperture system.

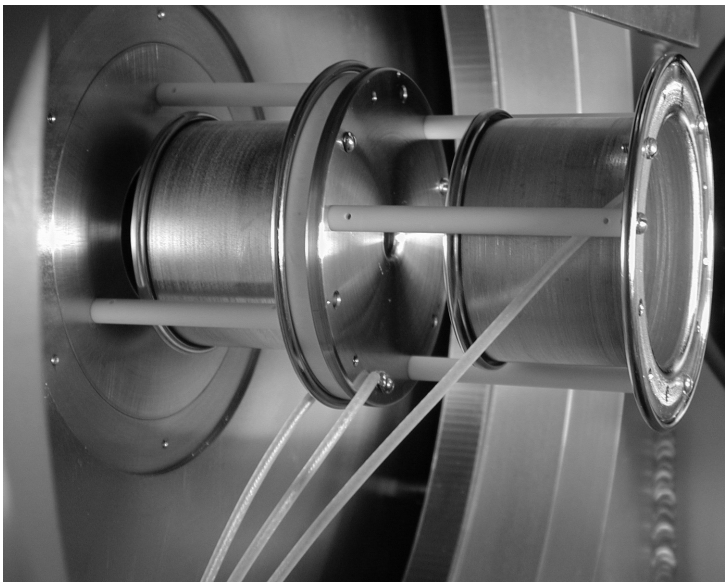

Figure 3-17: Photograph of the NTX beam scraper system.

We first characterize the diode without an aperture plate. At 400 kV, the peak current is 77 mA, which agrees with the 73-mA EGUN calculation within the ±5% uncertainty of the measurement. The measured current follows the familiar Child-Langmuir scaling [33] as the voltage is varied by a factor of three. The measured beam profile and emittance show small deviations from uniformity due to known imperfections in the beam optics. When an aperture of 2-cm diameter is inserted and the nominal electron-trap voltage is applied, the measured current is 55% of the total, again consistent with the EGUN prediction. The density profile of the apertured beam is found to be much more uniform, and the emittance in each of the transverse directions is lower by a factor of two, producing overall a doubling of brightness.

Figure 3-18(a) shows that a smooth uniform bright beam profile is generated by increasing source temperature, smoothing the source surface and positive biasing of the aperture. As the bias potential on the aperture is reduced, electron neutralization leads to enhanced current density on-axis and a highly non-uniform beam profile has been observed (Section 3.3.4).

The line-integrated beam profile is parabolic, indicative of a uniform beam profile, and the normalized edge emittance is measured to be 0.05 π-mm-mr, which is less than a factor of 2 times of source-temperature-imposed value.

When the ion beam is apertured and a negative bias voltage of 3–6 kV is used to capture electrons, the measured beam profile is quite uniform. The slit-integrated density profile shown in Figure 3-19 for a 25-mA beam deviates from the corresponding EGUN calculation by a maximum of 2%, with the average deviation being much smaller. The measured emittance is less than a factor of two above the value expected from the source temperature alone ($\varepsilon \approx 7.5\pi$-mm-mr). The only significant qualitative difference between the experimental phase-space plots in Figure 3-19 and the corresponding computer-generated plots is a slight S-curve deviation in x' result-

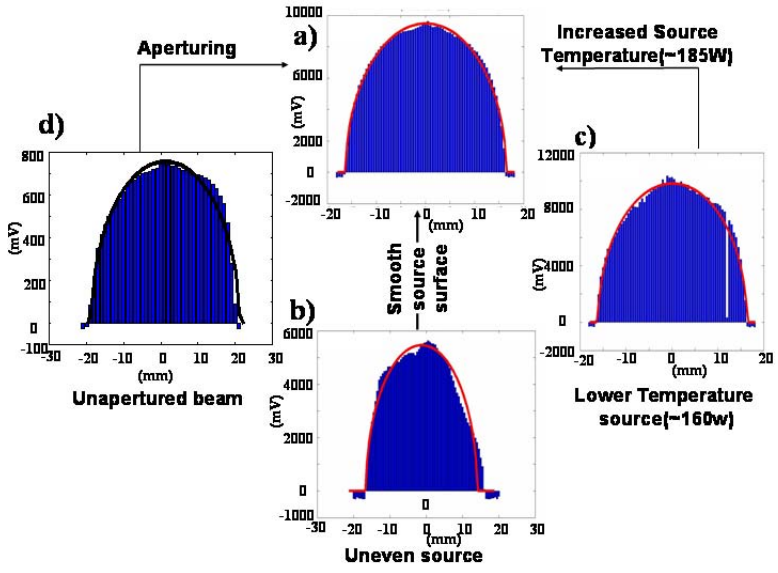

Figure 3-18: Slit integrated NTX ion beam profile. Profile a) is obtained by increasing source temperature, smoothing source surface and biasing aperture.

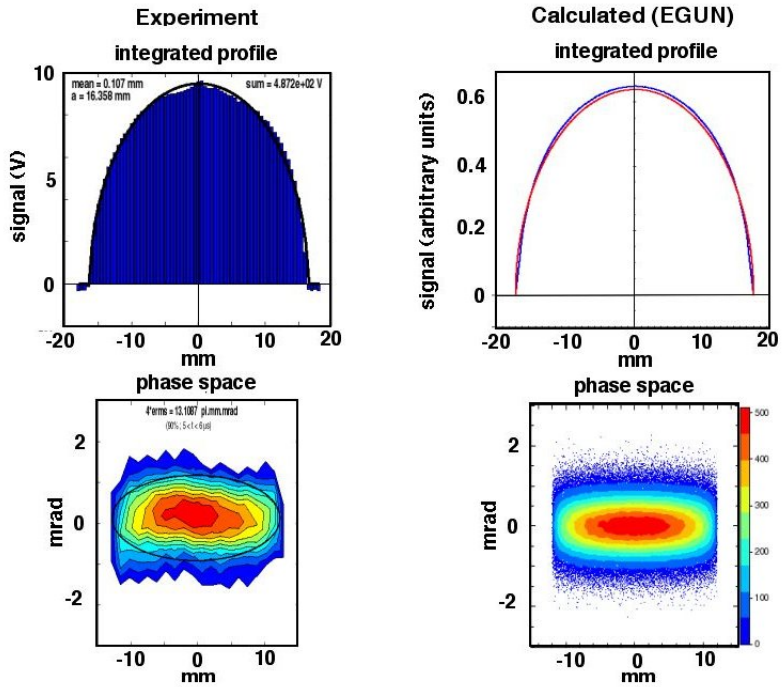

Figure 3-19: Measured slit integrated density profile and (x, x') phase space of a high-brightness apertured beam (300 kV, 25mA, 2-cm aperture). The corresponding EGUN calculations are shown to the right.

ing from a third-order ("spherical") aberration in the NTX focusing system. The K^+ beam in Figure 3-19, with energy of 300 keV and $\varepsilon \approx 12.5\pi$-mm-mr, is used for the neutralized-transport experiments reported here.

3.3.2 Current-voltage relation

The K^+ beam is produced within the source chamber by a standard hot-plate [46] of a 2.54 cm diameter alumino-silicate source across a diode with a 12 cm gap. The pulsed power is provided by a Marx generator and crowbar switch that were used in the Multiple Beam Test Experiment (MBE-4) [42]. This Marx generator produces a pulse with 0.5–1 μs rise time and is crowbared to produce a 5-μs "flat-top". The unapertured beam current follows the Child-Langmuir Law, reaching 80 mA at 400 keV. Figure 3-20 shows the Marx voltage waveform, the extracted ion current waveform and the confirmation of the Child-Langmuir law. With a 2 cm diameter aperture, the current is reduced by approximately one half; a 1 cm diameter aperture reduces the current to 1/4 of the 2 cm aperture value. Most of the detailed experiments have been performed with the 2 cm aperture, where the current is 25 mA at 300 keV.

3.3.3 Current transient in the NTX gun

As described in Section 3.3.2, the NTX diode voltage waveform is provided by a Marx generator and a crowbar switch. The Marx generator produces a rise time between 0.5 and 1 μs and is crowbared to produce a 5-μs "flat-top". The oscilloscope waveform in Figure 3-20 (top-left) shows the Marx voltage profile wit a rise time ~600 ns. The crowbar limits the pulse to a 5-μs "flat-top", and produces a decay time ~500 ns.

Since the transit time of the ions in the diode is ~300 ns, the elimination of the beam head current transient using the prescription described in Section 3.2 is not possible due to the limitations of the Marx generator. A voltage waveform rise time longer than the ion transit time in the diode produces a smooth rise time of the current

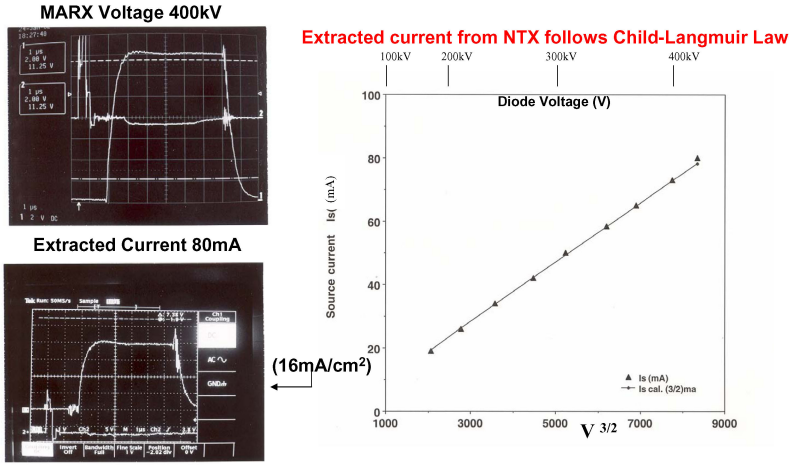

Figure 3-20: Measured voltage and current waveforms and verification of the Child-Langmuir law

at the end of the diode as shown in Figure 3-20 (bottom-left). A modification of the Marx generator to produce a rise time ∼300 ns should produce a sharper current rise time.

In order to correct the beam tail transient effects, a mechanism to stop the emission of ions in the presence of diode voltage is required. There is an ongoing program at the HIFS-VNL to control the ion emission from an alumino-silicate emitter by controlling the emitter temperature with a laser beam; this mechanism is based on the fact that the emission from the alumino-silicate emitter is negligible below temperatures $\lesssim$800 ^{o}C.

3.3.4 Control of secondary electrons

The K^{+} beam is produced by a standard hot-plate source [46], and the perveance and emittance are controlled by passing the beam through a metal aperture after the diode. Negatively biased rings on either side are used to capture electrons liberated by

ions striking the aperture plate. The change in transverse emittance that results from aperturing primarily affects the focal-spot size. For the space-charge-dominated NTX beam, WARP simulations show that dynamics in the final-focus lattice is insensitive to the beam emittance.

A smooth uniform bright beam profile is generated by increasing the source temperature, smoothing the source surface and aperturing the beam [8]. The use of an aperture to vary the perveance also generates a high-brightness beam by removing the edge of the beam after it exits the diode. Beam scraping, however, produces secondary electrons that are controlled by an electron trap.

The control of electrons is very important in this experiment, as stray electrons can introduce nonlinear space charge forces, which could lead to increase of beam emittance, and disruption of beam propagation. Our technique is to confine the electrons generated by the perturbing process to its place of birth by adjacent electron traps. These electron traps have negative potentials sufficiently large to confine the electrons even in the presence of the positive potential (a couple of kilovolts in NTX) from the self-field of the ion beam. Figure 3-16 shows a sketch of the ion gun and the beam scraper system, as designed using the EGUN code, and Figure 3-17 is a photograph of the aperture and electron trap located at the exit of the NTX diode. The trap consists of two metal tubes, each of 5 cm length, and 6.2 cm inner diameter with an aperture plate in between. The upstream and downstream tubes are located 0.8 cm from the aperture plate. A nominal negative 3 kV potential is provided on each of the metal tubes, providing adequate electron trapping in the presence of the ion beam. Another electron trap, 7.5 cm in radius, is located at the downstream end of the beamline, 10.16 cm downstream from the last quadrupole magnet. A nominal negative 7 KV voltage is used across this second trap to make it effective for collection of stray electrons.

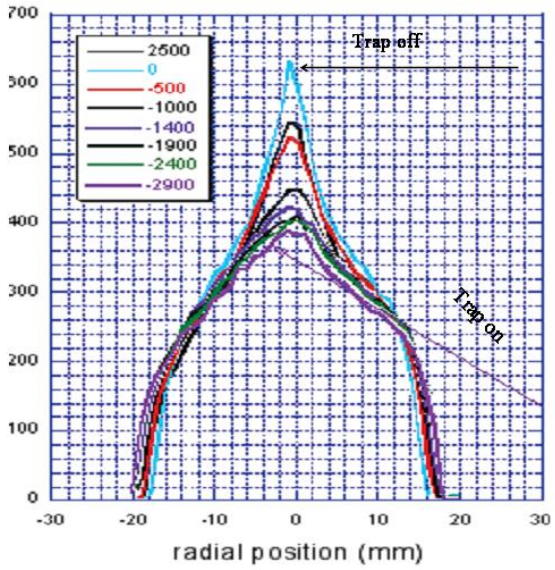

Figure 3-21: Electron effect on density

We run a series of tests in order to prove the effectiveness of the NTX beam scraper system. A Faraday cup is used to measure the total beam current exiting the aperture plate, and a slit/ slit-cup arrangement to measure the line-integrated beam profile (with slit cup only) and emittance (with slit and slit cup). The Faraday cup and the slit cup each consists of a collector and a guard ring/grid with bias voltages that are controlled to collect beam ions only. In addition, we also monitor currents flowing through the aperture plate and each of the two electron traps.

To understand the effect of electrons generated by the beam on the aperture and the diagnostic plates, we vary the bias voltage on the electron trap. The total current measured in the Faraday cup increases as the magnitude of the negative bias is reduced. We also measure the change in beam profile as the bias voltage is varied. We notice that as the bias voltage moves towards zero, the on-axis current is greatly enhanced. Associated with the on-axis enhancement is a slight reduction in the overall radial dimension of the beam as shown in Figure 3-21.

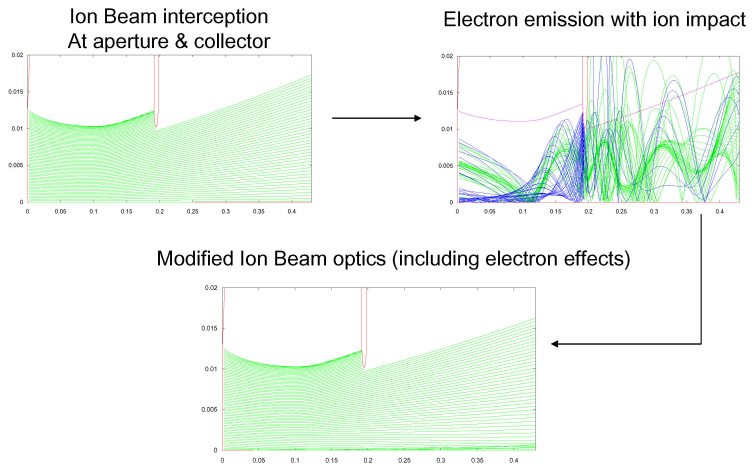

Figure 3-22: EGUN simulation of ions and electrons in the NTX diode and the scraper system.

These observations are consistent with a picture where electrons are trapped within the beam as the electron trap voltage is reduced. To quantitatively evaluate these effects, we have performed a series of simulations; using PIC codes as well as ray-tracing codes. The predicted behaviour of ions and electrons are shown in Figure 3-22. With the qualitative agreement of code and experiment, the following picture emerges: when the negative bias on the electron trap is sufficiently high, the electrons born on the aperture plate and the diagnostic plates are locally trapped. Their effect on the ion beam is minimal. However, as the negative bias is reduced, the electrons are finally able to break through the electrostatic barrier, and will accumulate around the beam axis (the bottom of the potential well). The region of electron population increases with reducing bias voltage. These on-axis electrons cancel the space-charge effect of the ions, causing the overall ion beam envelope to decrease, and the on-axis ion density to increase. The total current through the aperture also increases as a result.

Chapter 4

Matching and Transport in a Magnetic Quadrupole Focusing System

4.1 Final Focus Physics and Scaling Relations

The relevance of NTX to the fusion driver is derived from the observation that the key scaling parameter is perveance, defined in SI units by

$$Q = \frac{1}{4\pi\varepsilon_0}\frac{2ZeI_b}{m_i v_i^3}, \tag{4.1}$$

where I_b is the beam current, and Z, m_i, and v_i are respectively the charge state, mass, and velocity of the beam ions.

The beam dynamics of a low current, low energy beam, as in NTX, is identical to a high current, high energy beam in a fusion driver, as long as the perveance is the same, and the focusing fields are scaled appropriately. In the NTX experiment the injector is designed to generate a very high-brightness, space-charge-dominated potassium beam where the perveance is varied by means of a beam aperturing system

immediately down stream of the ion source and upstream of the first quadrupole as discussed in Chapter 3. By changing the aperture size, we vary the beam current at a fixed energy.

A simple theoretical model for neutralized drift provides us the framework in which we analyze more detailed experiments and simulations. For a beam which is nearly ballistic, the focal length f is given by

$$f = \frac{r_0}{\theta}, \tag{4.2}$$

where r_0 is the beam radius and θ is the angle of convergence at the entrance of the drift section (i.e., at the exit of the quadrupole lattice). The final spot size r_s at the focal point is given by

$$r_s = \frac{\varepsilon}{\theta}, \tag{4.3}$$

where ε is the unnormalized emittance of the beam at target. The first question, addressed with a combination of simulations and experiment, is whether we can achieve the focal spot at target, more specifically, whether we can control the beam in the quadrupole lattice to produce any desired beam size r_0 and convergence angle θ at the entrance to the drift section. As described below, beam control is obtained by changing the magnetic strength of 4 quadrupoles. We have varied the quadrupoles to obtain various values of θ (5 mr, 10 mr, 15 mr and 20 mr) for a given beam energy and current. The agreement between theory and experiment is excellent. We have also varied individual quadrupole strengths, and demonstrated that the beam shape changes in a predictable manner. In addition, the beam energy (and current) is varied, and again, the beam shape varied in a predictable manner. Finally, the perveance is varied, and good agreement between simulations and experiments is obtained.

The ultimate objective for the fusion application is to deliver the entire pulse onto the target with the same small spot. This is a nontrivial task because the beam

energy and current from head to tail is not uniform. The different slices of the beam may have somewhat different beam envelopes through the magnetic lattice, leading to different beam size and convergence angle, and therefore variable focal length from head to tail. We need to know the sensitivity of the beam optics to small changes in beam energy. To evaluate this effect, we have measured the beam size as the energy is varied. We have observed that energy variations of 1% lead to a reduction of current density by 50%. This experimental result is consistent with theory. We have also measured directly the spot size variation from head to tail and significant changes have been observed. The voltage waveform shows a variation of ∼1%, and this energy variation is enough to account for the head-to-tail variation in spot size. For future work, we need to study the energy sensitivity for other lattices (e.g., a 6-quad lattice) to determine if the energy sensitivity could be reduced. Also, time-dependent focusing may be used to correct for the head-to-tail variations.

For a beam with a uniform transverse current density, the description of the beam transverse size along the channel is given to first order by the envelope equations of Kapchinskij and Vladimirskij [60],

$$\frac{d^2a}{dz^2} = Ka + \frac{2Q}{a+b} + \frac{\varepsilon_x^2}{a^3}, \tag{4.4}$$

$$\frac{d^2b}{dz^2} = -Kb + \frac{2Q}{a+b} + \frac{\varepsilon_y^2}{b^3}, \tag{4.5}$$

where a and b are the transverse edge dimensions of the beam, z is the propagation distance along the quadrupole lattice centerline, K is the quadrupole force given by $B'/[B\rho]$, with B' being the magnetic field gradient and $[B\rho]$ being the beam rigidity, and ε_x and ε_y are the unnormalized "edge" emittances defined in Eqs. (2.3) and (2.4). The space-charge force is proportional to the perveance Q and the pressure force is proportional to the square of the unnormalized "edge" emittances ε_x and ε_y. For given perveance and unnormalized "edge" emittances, the beam envelopes do not

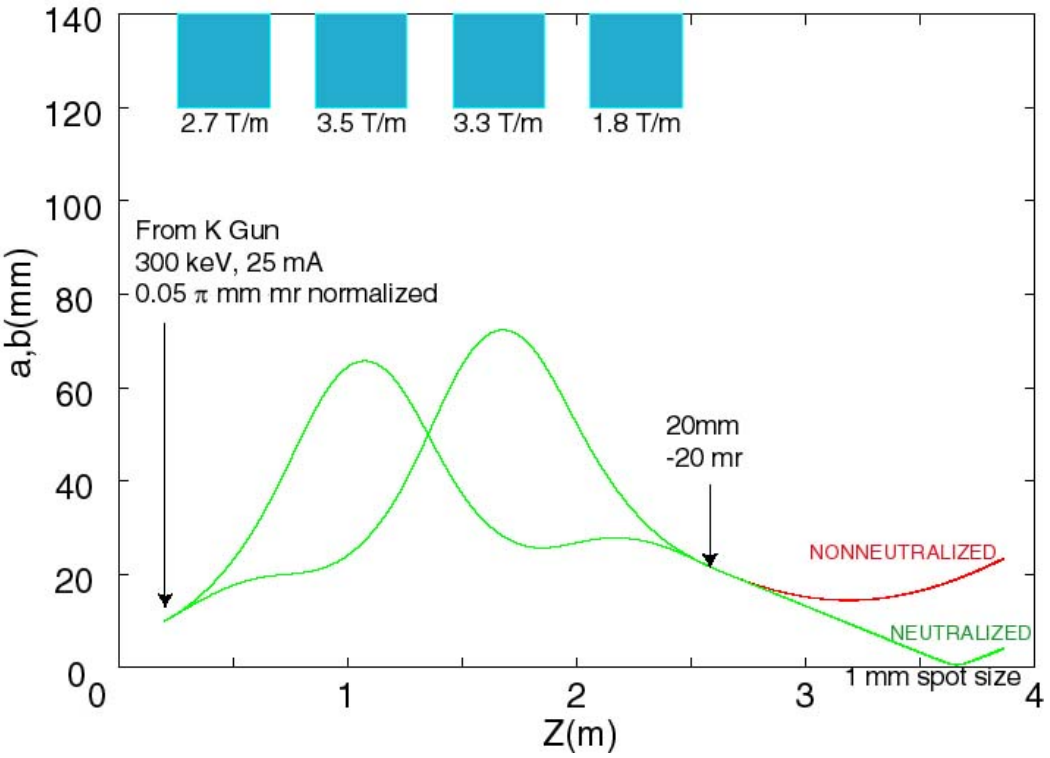

Figure 4-1: Final focus lattice for ballistically neutralized drift.

change when the magnetic field is transformed proportional to the rigidity; and for given perveance and rigidity, the beam envelopes are self-similar when the emittance is proportional to the beam size and simultaneously the magnetic field is inversely proportional to the beam size. For NTX, $Q \sim 0.0006$, corresponding to a 25 mA potassium beam at 300 keV. An equal perveance driver beam will correspond to a 10 kA Xenon beam at 2.5 GeV. It is worth noticing that during the final focus transport the beam dynamics is space-charge dominated at the beginning, and becomes emittance dominated as the beam approaches the focal plane.

Figure 4-1 shows the horizontal and vertical beam envelopes through the NTX system, with and without beam neutralization after the final focus lattice. The quadrupole fields are chosen to obtain a beam of one-meter focal length (20 mm radius, and 20 mr convergence) at the entrance to the neutralization region.

The heavy ion beam is space-charge dominated in the final focus system, where it has a large cross section and is highly non-paraxial. The beam expands in the two center magnets, which determines the amount of nonlinear magnetic fields that the beam samples as well as the degree of the non-paraxial motion. These geometrical aberrations will change the focusing properties calculated by the envelope equations. Therefore, particle tracking simulations require the knowledge of the multipole field content of the magnetic field. It can be shown [16] that to third order the main contributions to the beam dynamics come from the normal quadrupole, the normal sextupole and pseudo-octupole components of the magnetic field. These three components are included in all the numerical simulations performed for the design of the lattice.

Neuffer [16] has shown that the geometric aberrations depend only on the non perturbed (first order) particle trajectories; therefore the scaling properties of the geometric aberrations for a final focus system depend only on the perveance Q, if the scaled field reproduces the multipole components of the original field. He also found a formula to estimate the correction (increase) of the spot size given in Eq. (4.3) due to geometric aberrations:

$$\Delta r_s \simeq 1350 \times \ell_{quad} \times \theta^3, \tag{4.6}$$

where ℓ_{quad} is the length of the last quadrupole magnet and θ is the convergence angle in radians. For NTX, the unnormalized emittance $\varepsilon \sim 20\ \pi$ mm-mr, the convergence angle $\theta \sim 20mr$, and $\ell_{quad} \sim 0.4m$, from which we estimate $r_s \sim 1mm$, and $\Delta r_s \sim 4mm$. In Chapter 5 we will show that experimentally and numerically we obtain $\Delta r_s \sim 0.5mm$, about a factor of 8 less increase in spot size due to geometric aberrations. The discrepancy comes from the fact that the estimate in Eq. (4.6) was obtained by analyzing a specific lattice configuration (a quadrupole doublet) which is very different from the NTX lattice.

For fusion applications we require that the final focus system will deliver the entire beam pulse onto the target with the same small spot size. Chromatic aberrations affect the focal spot radius due to deviations from the nominal ion momentum which result in a variation in the focal length produced by the magnet system. They can be separated into two types. The first kind of chromatic aberrations depends on the velocity and current changes from the beam head to the beam tail. The velocity and current changes result from initial transients in the injector, from voltage errors in the accelerating gaps, and from residual momentum tilt during beam compression. Different slices of the beam may have somewhat different beam envelopes through the magnetic lattice, leading to variations in the beam size and convergence angle, and therefore variable focal length from head to tail. The second kind of chromatic effects depends on the momentum spread at a given beam slice (i.e., the longitudinal emittance). It is produced along the beam line by thermalization of velocity errors. For a driver there is a requirement to keep a small relative momentum spread of $\delta p/p \sim 10^{-3}$, and to remove the velocity tilt by the time the beam reaches the focal plane.

An estimate of the correction (increase) of the spot size [see Eq. (4.3)] due to chromatic aberrations from momentum spread was obtained by Lee [61]:

$$\delta r_s = 6 f \theta \left(\frac{\delta p}{p} \right), \tag{4.7}$$

where f is the focal length of the last quadrupole magnet, θ is the convergence angle in radians and $\delta p/p$ is the beam momentum spread. For NTX, the focal length $f = 1m$, the convergence angle $\theta \sim 20mr$, and $\delta p/p \sim 10^{-3}$, from which we estimate $\Delta r_s \sim 0.1mm$. Hence, spot size increase due to chromatic aberrations from momentum spread is negligible on NTX. Eq. (4.7) includes the partial cancellation of chromatic effects by the space charge of a uniform density beam. The effects of beam space-

charge on the beam dynamics also include nonlinear forces arising from non-uniform charge density distributions as well as image forces from the beam pipe. These effects depend on the length of the lattice and the clearance between the edge of the beam and the walls of the chamber, and are negligible for a short system as NTX.

It is possible to infer the effects of momentum spread by studying the sensitivity of the beam parameters to small changes in energy for a given beam slice. The results can be evaluated by measuring the beam size as the energy is varied for a given beam slice.

4.2 The NTX Final Focus Lattice

The pulsed quadrupoles for final focusing must have excellent field quality so as not to introduce unwanted aberrations due to magnet imperfections. The design, construction, and measurements of these magnets are presented in this section.

4.2.1 Lattice design

The NTX magnetic-transport section is designed to correspond closely to a typical HIF driver final-focus channel. The section consists of four pulsed quadrupole magnets separated by short drift regions, plus the drift regions at the two ends. Optical scintillators imaged by CCD cameras and mechanical slit scanners [8] are used to measure the beam profiles and phase space distributions of the beam at the end of the Final Focus lattice. The three-dimensional (3-D) layout of the magnets and the beam source is shown in Figure 4-2.

Figure 4-1 shows the horizontal and vertical beam envelopes through the system. The trajectory labeled "neutralized" models ideal neutralization by artificially turning off the transverse space-charge field after exiting the final-focus lattice. The quadrupole fields are chosen to produce a beam with 1-m focal length (20-mm radius

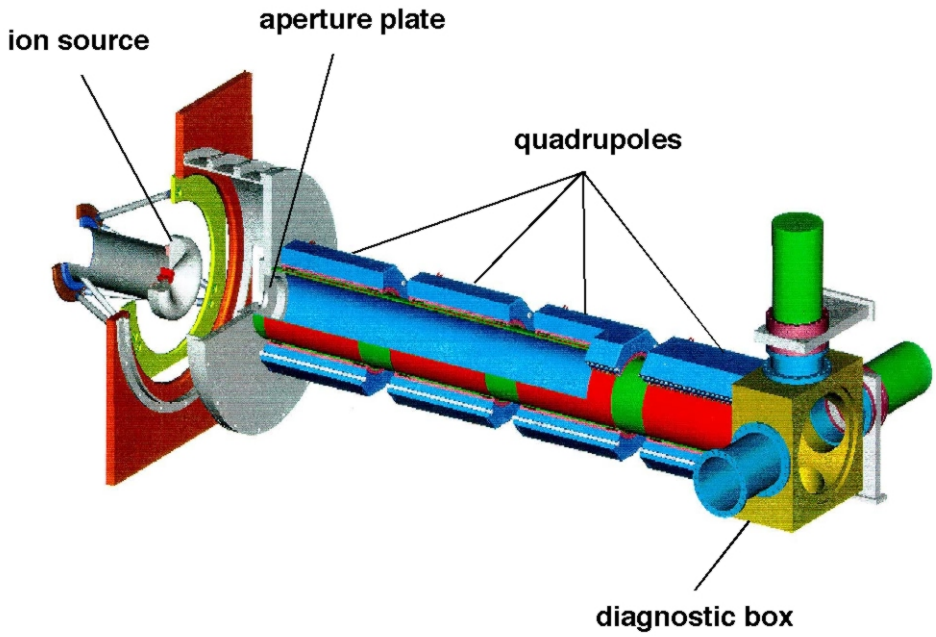

Figure 4-2: NTX final focus transport layout.

and 20-mr convergence angle) at the entrance to the neutralization region. The beam is quite large in the two center magnets, which determines the required bore size and winding radius.

Each magnet has a relatively short center section, and a substantial portion of the magnetic field is contained in the end fringe fields, which have significant axial components. Due to the large radius fluctuations in the focusing magnets, the ion-beam dynamics is highly non-paraxial. Consequently, the usual beam-axis-integrated method of representing fields by normal multipoles of discrete length does not give accurate particle trajectories in simulations, because these hard-edge field approximations omit the axial field components and nonlinear radial gradients that are major sources of particle deflection. Particle-tracking simulations therefore require the knowledge of the full multipole content of the magnetic field. Previous work [16] has shown that, to second order, the main magnetic-field multipoles contributing to beam dynamics are the normal quadrupole, the normal sextupole, and the pseudo-octupole components. These three components are included in all the numerical simulations used in designing the NTX lattice, since 3-D magnetic analysis is essential.

4.2.2 Magnetic field modeling

Each magnet is a current-dominated quadrupole, with eight conductor turns per coil in a single layer, arranged inside a cylindrical laminated-iron return core. A 3-D finite-element model of the magnets is generated using the ANSYS/Emag program and is solved for the 3-D static field. A scalar potential formulation is used, with source current elements used for the coil. The space modeled, a one-eighth section of half a magnet, is shown in Figure 4-3. Far-field (infinite boundary) elements bound the end and the outer radius, 75 cm from the magnet midplane, which extends well past the source and final focus points. A cylindrical Neumann boundary is used to simulate the steel core in order to speed up the analysis when a fine mesh is used.

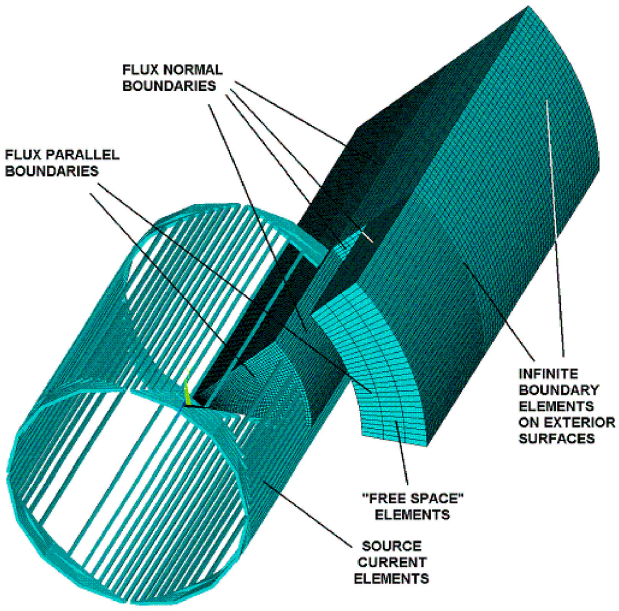

Figure 4-3: Symmetrical magnet model with one-half octant shown.

This choice is acceptable because a coarse-mesh model with steel included shows no significant saturation.

The resulting 3-D field map generated is decomposed into both normal and pseudo multipoles as a function of distance in the axial direction. Figure 4-4 shows these multipoles as a function of longitudinal distance z. Both half-octant models and full-magnet finite-element models, complete with spiral coil geometry, crossovers, and leads, are computed to determine both symmetry-allowed and full-skew (normal and skew) multipoles, respectively. The higher-order normal multipoles are comparatively unimportant. Finally, we have performed beam-tracking simulations through the lattice of focusing elements generated by superposition of these field maps.

4.2.3 Magnet design and fabrication

The NTX magnet design differs from the initial specification [62] in the choice of a larger bore and winding radius, as well as in the simpler coil design. Table 1 gives the final design and operating parameters.

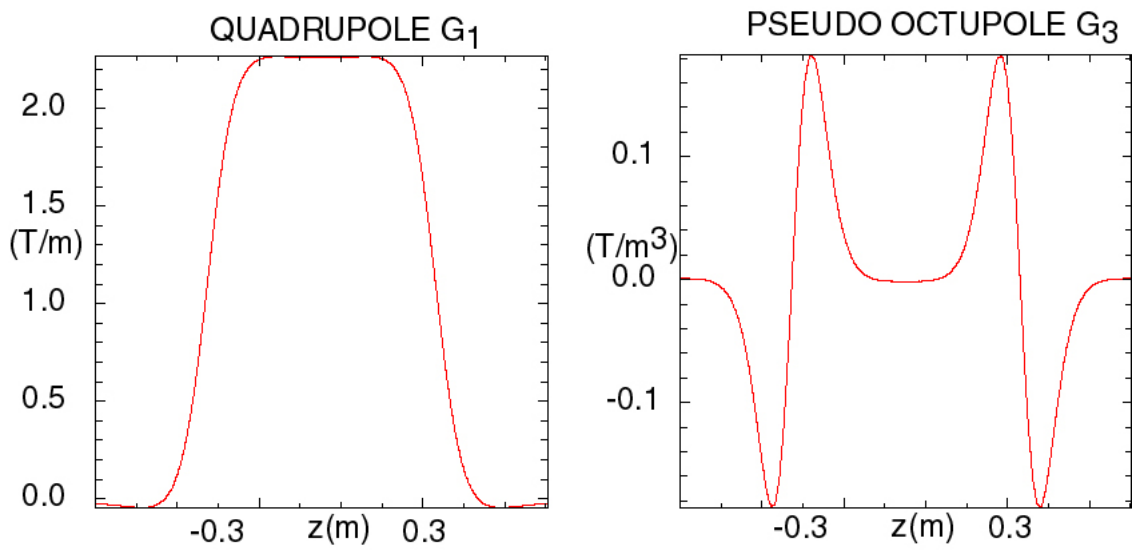

Figure 4-4: Dominant (a) quadrupole and (b) pseudo-octupole coefficients for the multipole decomposition $B_\perp(r,\theta,z) = G_1(z)r\cos(2\theta) + G_3(z)r^3\cos(2\theta) + \ldots$

Parameter	Value	Unit
Beam Aperture Radius, R_b	14.9	cm
Magnet Winding Radius, R_W	17.32	cm
Steel Inner Radius, R_i	18.33	cm
Steel Outer Radius, R_o	25.63	cm
Mag., Total Lengths, L_m, L_0	46, 50	cm
Magnet to Magnet Spacing	60	cm (ctr.-ctr.)
Field Gradient, B'=dBx/dy	2–5	T/m
Maximum Field, B	0.6	T, @ 12 cm
Number of Turns, N	8	Turns/coil
2-D Field Coefficients, B_n	7×10^{-4}	T/T, @ 10 cm
Conductor Diameter, d_c	4.65	mm
Magnet Current, I_{min}-Imax	3.3–8.2	kA
Magnet Resistance, R	0.036	Ω
Magnet Inductance, L	232	μH
Pulse Length (full half sine), t	2.2	ms
Magnet Voltage (Max), V	2.7	kV
Pulse Energy (Max), U	7.8	kJ
Energy Loss/pulse (Max), Q_t	2.7	kJ
Operating Pulse Rates (Max)	0.5, 0.1	Hz
Temperature Rise@Steady State (Max)	25	^{o}C, (0.5 Hz P.R.)

Table 4.1: NTX quadrupole magnet parameters

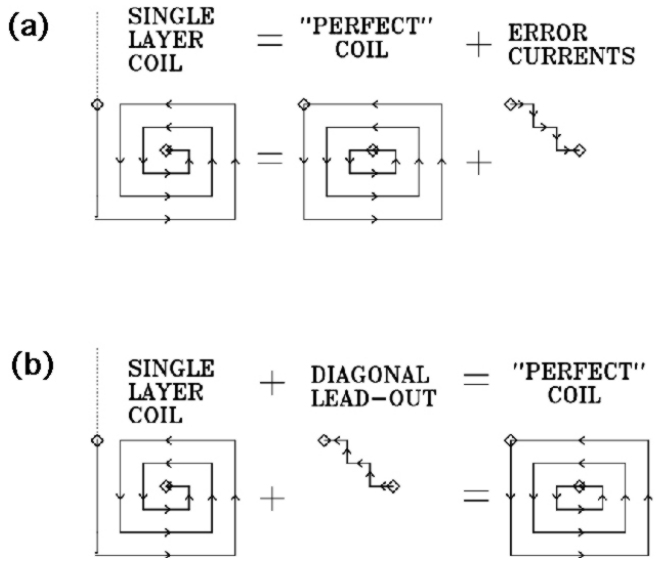

Figure 4-5: Concept for correcting coil winding errors. (a) Single-layer coil normally introduces error currents due to incomplete current loops. (b) Adding a diagonal lead-out can correct this problem and produce nearly perfect fields.

The magnets are fabricated using a simplified, single-layer coil design, featuring a novel diagonal leadout. The diagonal leadout from the inner turn approximates the staircase-pattern of missing currents that are inherently present in any spiral coil. This leadout design allows short coils with a few turns to have relatively high field symmetry. This concept is sketched in Figure 4-5.

Each magnet is driven by a capacitor, which is discharged through a series string of thyristors to produce a half-sine-wave current pulse. A 2-mF capacitor is used to achieve the full current with minimal voltage and to increase the pulse length, thus reducing eddy currents. Bipolar charging of the capacitor is used to decrease the voltage that appears between the magnet and the grounded housing by a factor of two compared to unipolar charging.

We have performed 2-D transient magnetic modeling to determine the effect of eddy currents in surrounding components, such as beam tubes, flanges, diagnostics, and electron traps. Eddy currents in the beam pipe are found to be acceptable, with a 7.4% loss of the peak field and a 0.28 ms field-peak-time lag from the source current

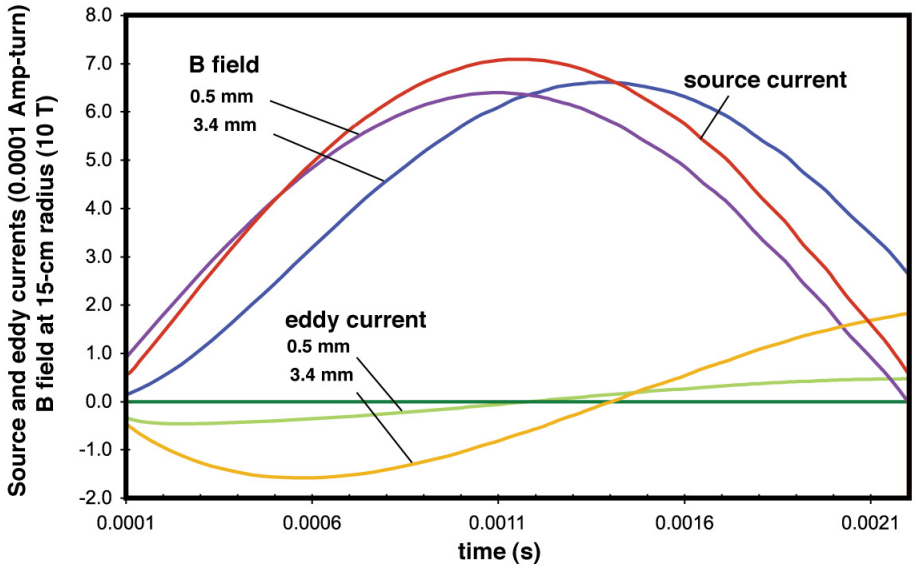

Figure 4-6: NTX beam-pipe eddy currents and magnetic fields from 2-D finite-element analysis. The linear dimensions indicate the beam-pipe thickness.

peak, as shown in Figure 4-6.

Six quadrupoles have been fabricated in order to provide two spares. One quadrupole has been subjected to 10^4 full-current pulses to test reliability, and the others have received 10^3 full-current pulses for acceptance testing. No cooling, other than free air convection, is necessary. Figure 4-7 shows one of the coils during fabrication.

4.2.4 Magnetic field characterization

The choice of a technique to measure the quadrupole magnetic field was constrained by two factors. First, the beam envelope varies significantly within the magnet, making a 3-D map of the field necessary. This requirement rules out techniques, such as rotating (harmonic) coils, that generate an axially integrated field measurement. Second, the magnets are pulsed because cooling requirements prevent the magnets from being operated continuously, except at relatively low fields that would compromise the

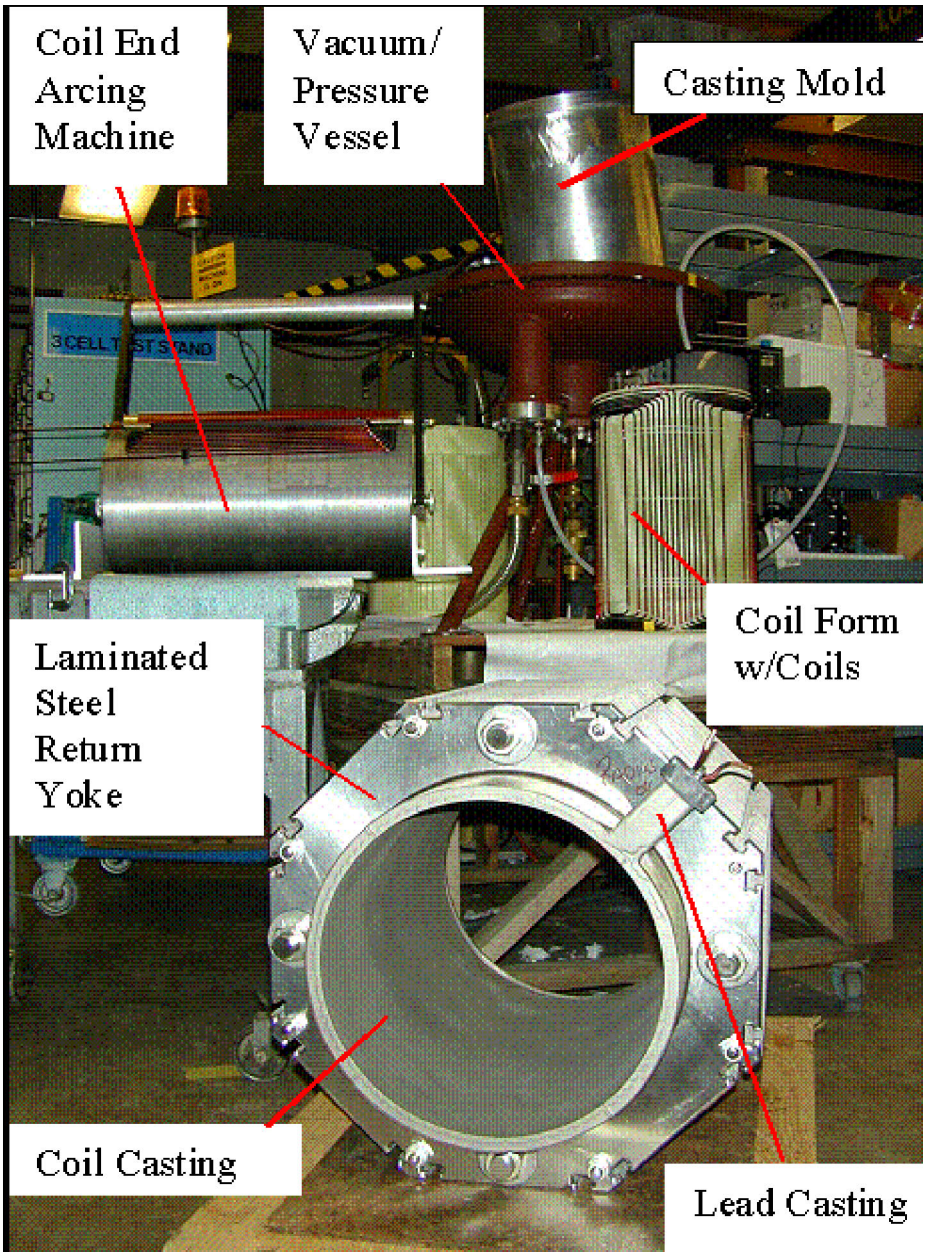

Figure 4-7: Photograph of an NTX magnet during fabrication.

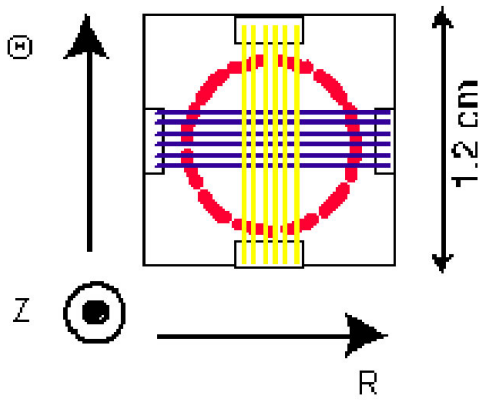

Figure 4-8: Illustration of the orientation of the windings on the magnetic-field probe. All windings have circular cross sections and consist of two layers.

accuracy of the measurement. The time-varying fields preclude the use of Hall probes and many other commercially available probes. Also, such probes do not allow us to study the effect of eddy currents in the beam pipe on the magnetic field.

The quadrupoles are characterized using simple pickup loops to monitor the changing flux as the magnets are pulsed. The probe design, sketched in Figure 4-8, balances the considerations of accuracy, signal strength, and ease of fabrication. Three separate pickup loops are incorporated into each probe to permit the measurements of the magnetic field vector. Each loop has 20 turns (two layers of ten turns) of 0.13-mm (5-mil) copper wire. The three cross sections have slightly different diameters to minimize mechanical interference between the sets of windings. Four of these probes are spaced equally around a disk at a 10-cm radius and mounted on a supporting cylinder inserted into the magnet bore. The cylinder can be rotated about its axis or adjusted vertically and horizontally, and the magnets are moved longitudinally on rails so the probes can sample different axial positions.

We have two different modes of field measurements. For initial characterization, the axis of the supporting cylinder is aligned with the magnet mechanical axis. With the probes positioned lengthwise near the center of the magnet, the cylinder is rotated

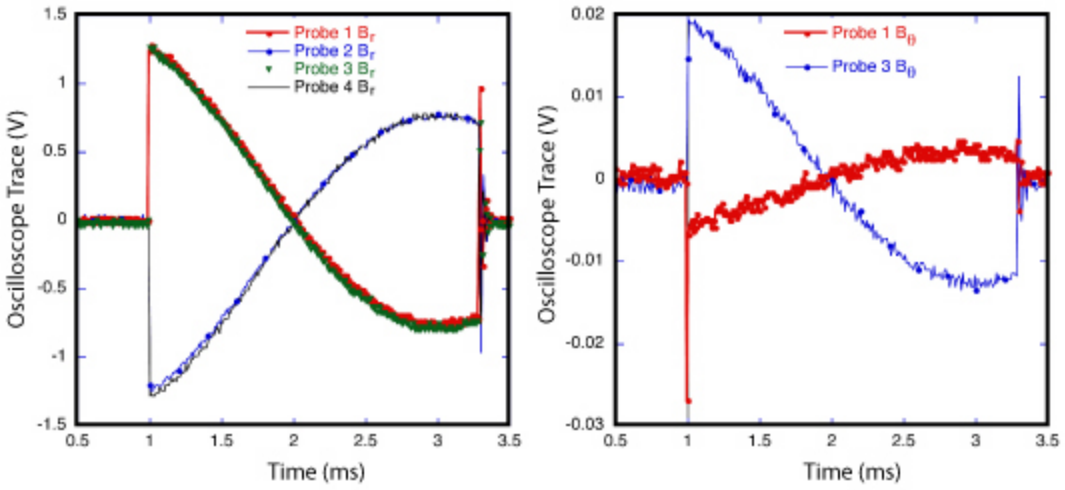

Figure 4-9: Oscilloscope traces of the probe output when the supporting cylinder is rotated to place probes at center of the quadrupole windings. The left traces are from loops oriented to sense the radial flux, and the right traces are from loops sensing the azimuthal flux.

to maximize either the radial or azimuthal field for the four probes. Measurements are then recorded as the cylinder is rotated in 15-degree increments for 90 degrees. The magnet is shifted axially, and measurements are taken again as the cylinder is rotated back in 15-degree steps to the starting angle. This process is repeated with the probes near each end of the magnet. Each measurement records all three components of the field vector at four positions. Although this is a very sparse field mapping, any fabrication problems will stand out. The second mode entails a detailed mapping of the field over a constant radial position relative to the magnet axis. These data are then used both to determine the tilt and offset of the quadrupole field axis with respect to the mechanical axis and to identify higher order modes.

Output from the probes is shown in Figure 4-9. The signal-to-noise ratio is excellent for probe orientations aligned with the field. Careful adjustment of the rotational position of the probes can reduce at least one of signals to the noise level in the other probe orientation. The field components calculated from the signals are shown in Figure 4-10. The applied magnet current is shown with the field plots to demonstrate

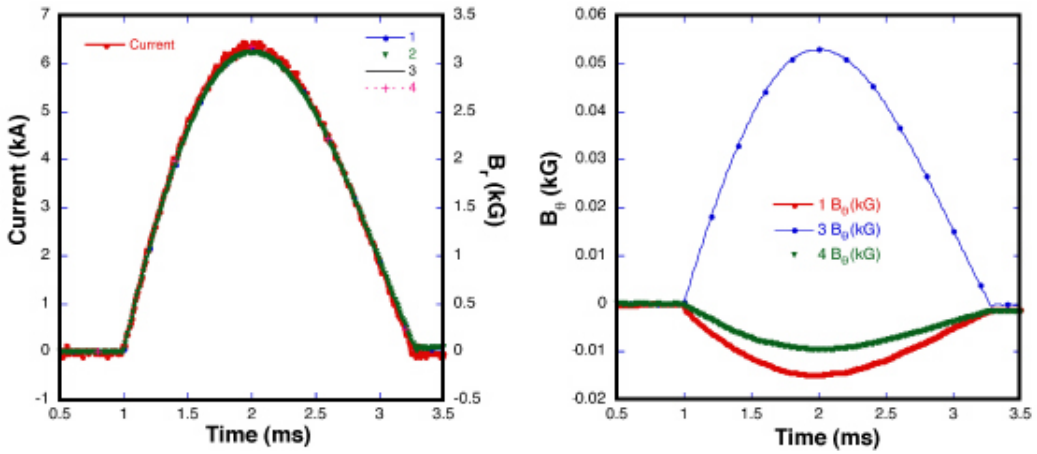

Figure 4-10: Magnet current along with the integrated and calibrated radial field (left), and the corresponding azimuthal field (right).

the fidelity of the system and analysis. Figure 4-11 compares the measured longitudinal profile of the quadrupole field with the computed profile, where the peak fields are normalized for comparison.

4.3 Beam Matching and Transport

The main issue of the magnetic-focusing experiments is the control of emittance growth due to higher-order fields from magnetic multipoles and image fields. In this section, we present experimental results from NTX on beam envelope and phase space distributions, and compare these data with the results of particle simulations by the PIC code WARP.

As discussed in Chapter 3, the K^+ beam is produced within the source chamber by a standard hot-plate [46] of a 2.54 cm diameter alumino-silicate source across a diode with a 12 cm gap. The pulsed power is provided by a Marx generator and crowbar switch that were used in the Multiple Beam Test Experiment (MBE-4) [42]. This Marx generator produces a pulse with 0.5–1 μs rise time and is crowbared to produce a 6-μs "flat-top". A smooth, uniform, bright beam profile is generated by increasing

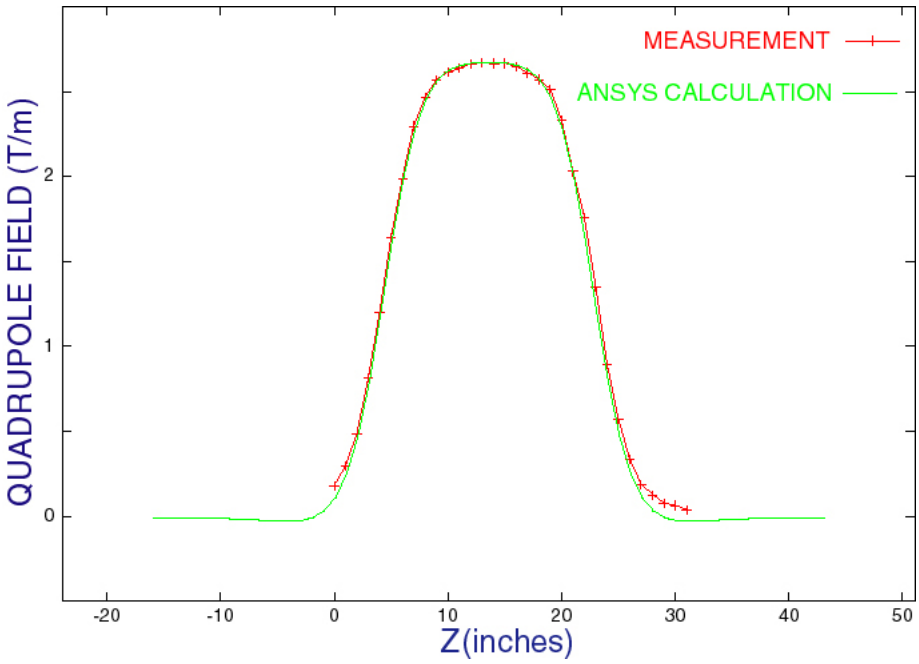

Figure 4-11: Calculated and measured NTX quadrupole gradients.

the source temperature, by smoothing the source surface and by aperturing the beam [8]. The use of an aperture to vary the perveance also generates a high-brightness beam by removing the edge of the beam after it exits the diode. Beam scraping, however, produces secondary electrons that are controlled by an electron trap. Figure 3-16 shows a sketch of the ion gun and the beam scraper system, as designed using the EGUN code, and Figure 3-17 is a photograph of the aperture and electron trap located at the exit of the NTX diode. The trap consists of two metal tubes, each of 5 cm length, and 6.2 cm inner diameter with an aperture plate in between. The upstream and downstream tubes are located 0.8 cm from the aperture plate. A nominal negative 3 kV potential is provided on each of the metal tubes, providing adequate electron trapping in the presence of the ion beam. Another electron trap, 7.5 cm in radius, is located at the downstream end of the beamline, 10.16 cm downstream from the last quadrupole magnet. A nominal negative 7 KV voltage is used across this second trap to make it effective for collection of stray electrons.

The transport section consists of a double FODO channel with very short drift regions, including the drift from the source into the channel, and the drift into the plasma neutralization chamber. Figure 4-1 shows the calculated beam envelope (x and y) through the system. The beam is quite large in the two center magnets, which determines the required bore size and winding radius. The magnet has a relatively short center section and a substantial portion of the magnetic field is contained in the end fringe fields, with significant axial components. The beam is transported through a 2.4 m long path magnetic section. The distance from the beam aperture radius to the center of the first magnet, the quadrupole length, and the quadrupole to quadrupole spacing are 26 cm, 46.50 cm, and 60 cm, respectively. The field gradient and maximum field of a magnet are calculated to be 2–5 T/m and 0.6 T, respectively, with a current range of 3.3 to 8.2 kA. The pulser for each NTX quadrupole magnet consists of a bipolar-charged 2 mF capacitor which is discharged through thyristors to produce a current half-sine wave with a pulse width of 2.3 μs. Bipolar charging and a large capacitance were chosen to minimize the voltage from the magnet leads to the grounded magnet housing for the maximum design current. The pulser output voltage is monitored with a resistive voltage divider and the magnet current is monitored with a current transformer. Inside the magnetic lattice, a thin wall (3.3 mm) stainless steel tube of 13 cm inner radius is installed. Eddy currents are calculated by transient 2-D finite element analysis, and it is found to result in a 7.4 % loss of the peak field, and a 275 μs peak-field-time lag from the source current peak. It is observed that the measured axial field fall-off profile agreed well with the computational model [63]. Our measurements with and without stainless steel tube also agree well with the calculations.

Several diagnostics have been used to characterize the ion beam. The primary diagnostics for this experiment consist of (1) a Faraday cup, (2) a slit /slit-cup system and (3) a scintillator with a gated CCD camera system. The Faraday cup and the

slit cup each consists of a collector and a guard ring (grid) with bias voltages that are controlled to collect beam ions only. In addition, we also monitored currents flowing through the aperture plate and each of the two electron traps. The removable Faraday cup is inserted into the NTX beamline at the exit of the injector and at the end of the magnetic lattice to measure total beam current. The slit/ slit-cup arrangement is used to measure the line-integrated beam profile (with slit cup only) and emittance (with slit and slit cup) at the same locations. Beam profile is measured optically using a glass or ceramic (96% alumina) scintillator with associated camera. Charge neutralization of this scintillator is provided by a high-transparency (80–90% transmission) metallic mesh placed on or near the surface of the scintillator. By applying a negative bias to the mesh, stray external electrons are decelerated and deflected away from the scintillator, limiting their contribution to the optical image to negligible levels. Time-resolved beam-induced images on the scintillator screen are captured with a Roper Scientific gated, intensified CCD camera viewing the scintillator through a vacuum window, and images are processed using the public domain program ImageJ.

We have developed a new technique to measure the 4-dimensional phase space distribution of the beam using the beam imaging diagnostics [8], as discussed in Section 2.4. The phase space distribution $f(x, y, x', y')$ can be measured by scanning the beam with a small pinhole (20 mils in diameter) and letting the transmitted beamlet to travel a long distance ($\sim$1 meter) before striking the scintillator where an image is taken. The position of the pinhole defines the coordinates x and y, and from the image we can extract the density distribution of x' and y'. Due to the fact that the beam at the exit of the final focus system is prepared to focus to a small spot in the absence of space charge, a standard pepperpot technique does not work since all the individual beamlets would fall on a single spot. Figure 2-11 shows schematically this technique along with some images of the individual beamlets that

show a very detailed structure of the phase space distribution. The knowledge of the 4-dimensional phase space is essential in order to run more realistic simulations of the beam focusing to a small spot while drifting through neutralizing plasma.

The primary simulation tool is WARP3D [13]. The code is used to simulate the ion beam from source through the 4-quadrupoles and the neutralized drift section to the target. Details of the experimental setup are incorporated into the code including all electric (electrodes) and magnetic fields (third order non-linear magnetic fields as calculated by ANSYS).

The ion beam extracted from the Pierce-type NTX diode suffers from spherical aberrations, as evidenced by phase-space distortions (high emittance) and non-uniform density profiles. Since the source of these aberrations is the presence of high-order field components, the particles at the edge of the beam are the most affected. A high-brightness beam is produced on NTX by removing the beam edge after the pulse is generated in the diode [43].

A high brightness, low emittance ion beam is an essential component of the Neutralized Transport Experiment (NTX) to obtain the minimal spot size at the focal plane. To study beam transport through the final focus system we have used an apertured, 300 keV, 25 mA, beam with an initial unnormalized edge emittance of 12.5 π-mm-mr and a semigaussian transverse phase-space distribution in the WARP-3D simulations.

4.3.1 Envelope control

A series of measurements have been performed to demonstrate the control that WARP3D has in predicting the quadrupole fields to obtain prescribed beam parameters. The first case is to produce a round beam with the nominal parameters of 20 mm radius and 20 mr convergence (one-meter focal length).

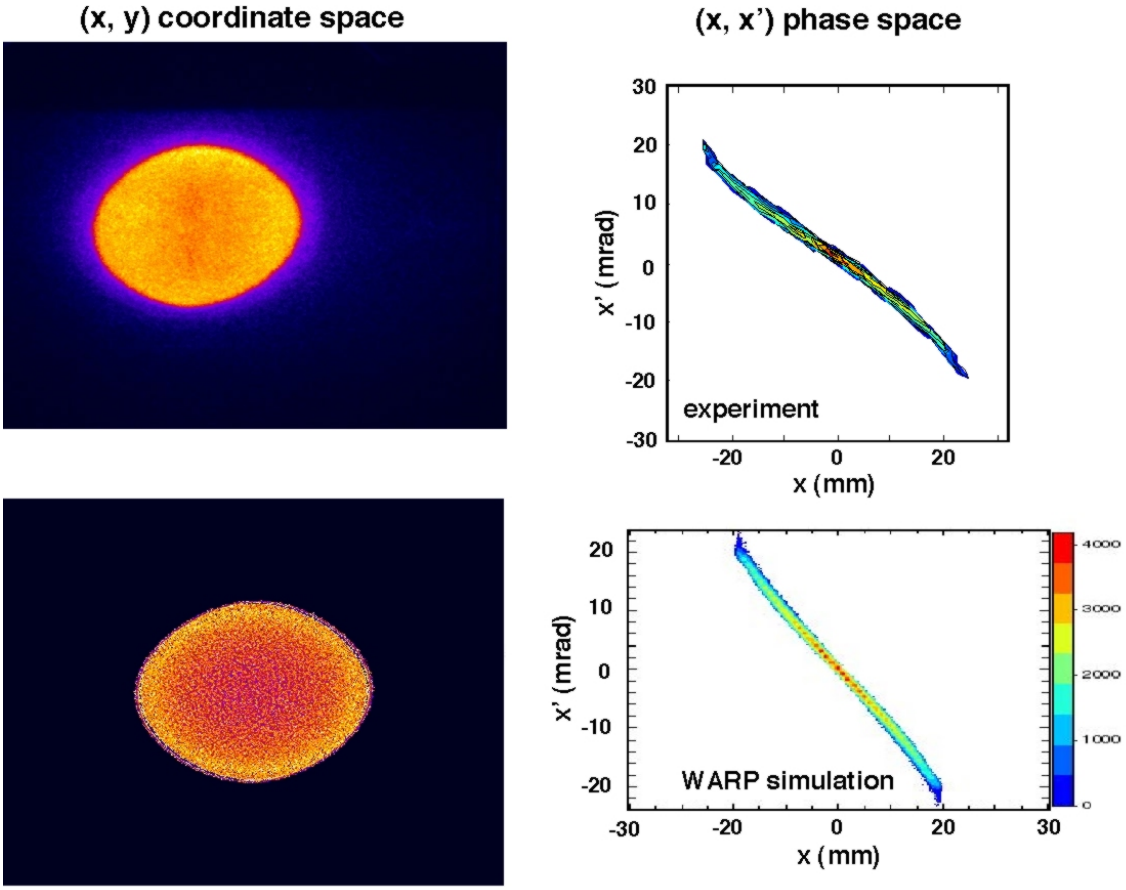

Figure 4-12: Experimental (top) and WARP-3D simulation (bottom) results of the NTX beam profile and phase-space distribution at exit of channel.

Figure 4-12 shows good agreement between the measured (top) and calculated (bottom) beam profile and phase space distribution for the nominal energy (300 keV, 25 mA) and quadrupole field configuration at the entrance to the neutralization region. Figure 4-12 also shows that the final parameters for the nominal case correspond to that of a beam of the required 1-m focal length (20 mm radius and 20 mr convergence).

The slight distortion (asymmetry) of the beam profile has been traced back to a small rotation (5 mr) of one of the quadrupoles. The beam has a uniform core with a narrow rim due to field aberrations and the final beam emittance of the beam is about 25 π-mm-mr, which should allow the beam to be focused to a 1–2 mm

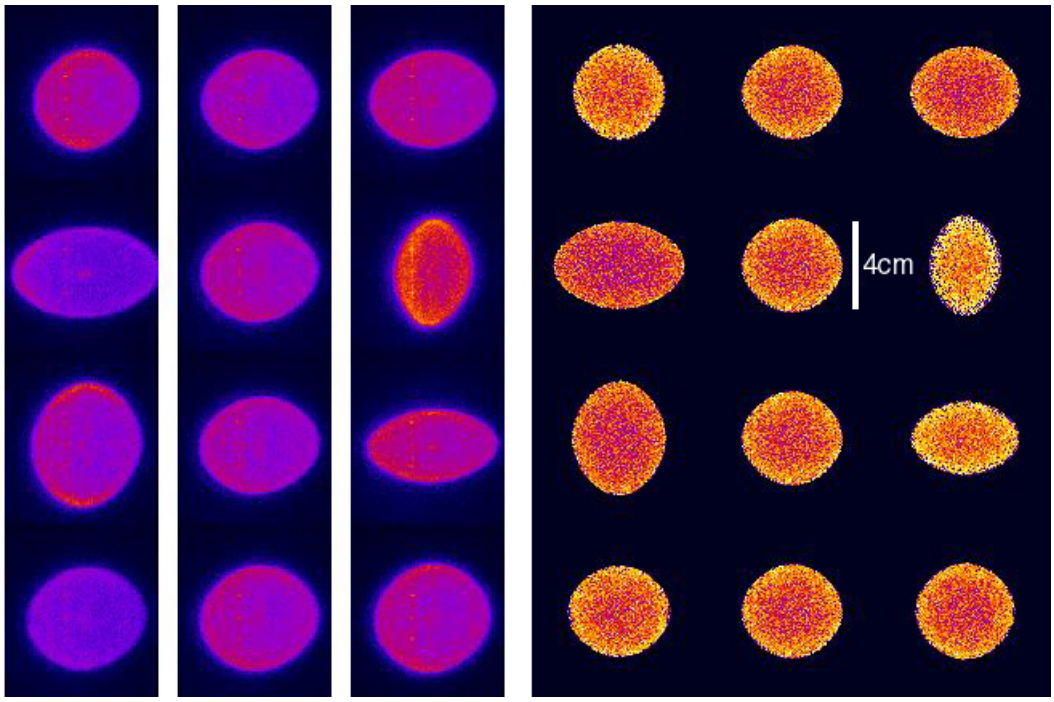

Figure 4-13: Numerical results (right) and camera images (left) of the NTX beam profiles as a function of the quadrupole field configuration.

focal-spot radius in neutralized-transport experiments. Furthermore, the Faraday cup measurements of the beam current at the entrance and exit of the final focus system show insignificant beam loss along the transport channel.

We have also compared the beam profiles for several quadrupole strength configurations as calculated by WARP3D and as measured. In Figure 4-13, for each quadrupole, the corresponding row shows the profiles for a change of -5%, 0% and +5% from the nominal quadrupole strength. This comparison shows good agreement between measurements and simulations.

In order to study the dependence of the spot size on the convergence angle, we have varied the quadrupoles to obtain various values of the convergence angle θ (5 mr, 10 mr, and 20 mr) for a given beam energy and current. Agreement between theory and experiment is excellent. Finally, the perveance is varied, and the same code-experiment agreement is demonstrated.

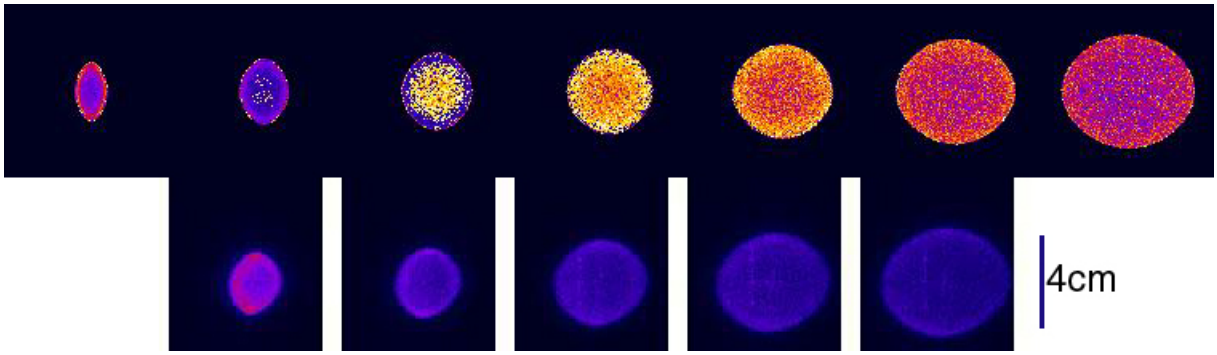

Figure 4-14: Numerical results (above) and camera images (below) of NTX beam profiles as a function of the beam energy.

4.3.2 Energy scan

We have also performed a complete characterization of the quadrupole lattice by comparing experimental results with particle simulations when the beam energy (and current) is varied. Again, the beam shape varied as predicted by WARP3D, when a 3% energy shift correction is applied. Figure 4-14 shows good agreement between the calculated (top) and measured (bottom) beam profiles at the exit of the final focus system as the beam energy is varied in steps of 3% around the nominal energy which corresponds to the image at the center. The numerical simulations track the beam behavior as the beam expands by a large factor as the energy changes from -9% to +9% around the nominal energy (Figure 4-15).

Since the unnormalized "edge" emittances ε_x and ε_y are weakly dependent on the energy, we have also verified a property of Eqs. (4.4) and (4.5), that the envelope parameters a, a', b, and b' do not change when the magnetic field is transformed proportional to the rigidity, i.e., proportional to the momentum of the ions.

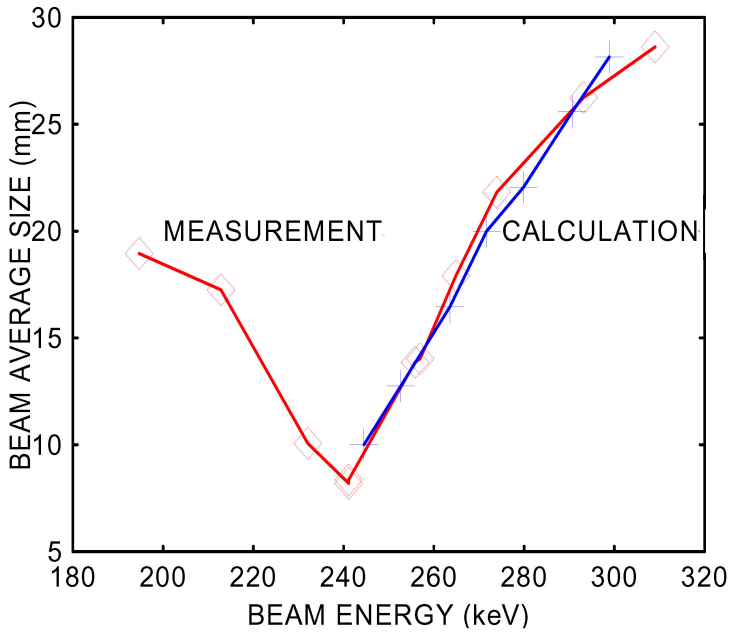

Figure 4-15: Calculated (blue plus sign) and measured (red diamond) beam sizes at the exit of the final focus system as the beam energy is varied. A factor of 3% is subtracted from the energy used in the calculation.

4.4 Sources of Errors

While we have very good agreement between theory and experiment in many aspects, there are several observations, which are not yet well understood. We have mentioned the need for an arbitrary energy calibration factor in order to obtain agreement between theory and code. To refine the energy calibration in the experiment, we have performed a series of time-of-flight (TOF) experiments, as well as careful calibration of resistive and capacitive monitors. Although the three different ways of energy calibration agree within the experimental uncertainties, the discrepancy with theory persists. In pursuit of the explanation of this discrepancy, we suspect that stray electrons might play a role. To ascertain this effect, we have incorporated a mesh liner along the pipe. However, while the currents are clearly collected on the mesh, its net effect on the beam profile is relatively minor.

To quantify these effects, a series of experiments are performed. These include: (a) stray electron effects on the beam inside the quadrupole lattice, (b) calibration of beam energy, (c) measurements of quadrupoles field strength, (d) effectiveness of the diagnostic devices, and (e) beam halo formation.

4.4.1 Stray electron effects inside the quadrupole lattice section

As we mentioned in Sec. 3.3, the NTX magnetic transport section contains an aperturing system for variable perveance, brightness and beam size. This aperturing technique is provided with a sandwich-type electron trap to collect electrons.

Ions from the poorly matched beam head, and halo ions in the main pulse of the beam can strike the outer wall of the final focus system beam tube. A single ion impact can produce thousands of secondary electrons depending on the energy and angle of incidence, with ions of grazing-angle incidence producing the largest secondary electron yields. Only a small fraction of the beam ions striking the wall is needed to provide a space-charge-limited supply of electrons from the wall. If the secondary electrons are not stopped, they are attracted by the beam potential and can provide some degree of beam neutralization. Presence of wall electrons is measured using a long radial metal mesh, which is installed inside the magnetic drift section. Mesh radial diameter, space of wire and mesh length are 23.5 cm, 1.27 cm and 2.28 m, respectively. Figure 4-16 shows the 23.5 cm diameter metal mesh inside the magnetic transport section, which is biased with a $\pm$2kV potential.

The beam profile at the scintillator located at the end of the final focus magnets and the current in the mesh as a function of the mesh voltage are measured. Figure 4-17 shows the measured current in the mesh by varying its bias voltage. As a negative voltage is applied across the mesh, there is no significant current measured in the mesh. It shows that there is insignificant number of ions from the beam halo near the

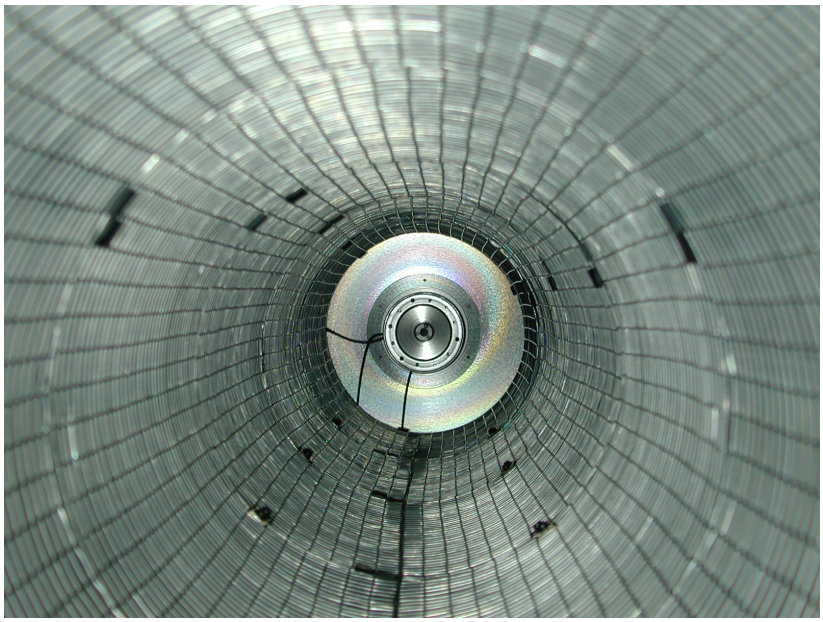

Figure 4-16: A cylindrical metal mesh inside the beam pipe in the magnetic final focus section.

beam pipe wall. When the voltage is switched to positive, significant current in the mesh is measured. It shows that wall electrons are collected in the positive biased mesh. These electrons are generated in the drift tube wall. But the beam is not affected by electrons.

Figure 4-18 shows the beam radii corresponding to several beam energies under the condition of the mesh bias powered to ± 2 kV and without any mesh voltage. By comparing these three cases, we find that the beam radius changes are insignificant. It is inferred that for a large pipe, the wall electrons spend only a small fraction of their time within the beam. The electrons are moving at their greatest velocity while passing through the beam, reducing their net effect of beam neutralization. Though a mesh inside the final focus magnetic section is not necessarily effective due to the large diameter of the beam pipe, it provides good evidence that a positively biased metal mesh can reduce beam neutralization due to stray electrons. This effect can be very significant in a small size drift tube, as we have found in the neutralized drift section with its 3 inch diameter pipe [8].

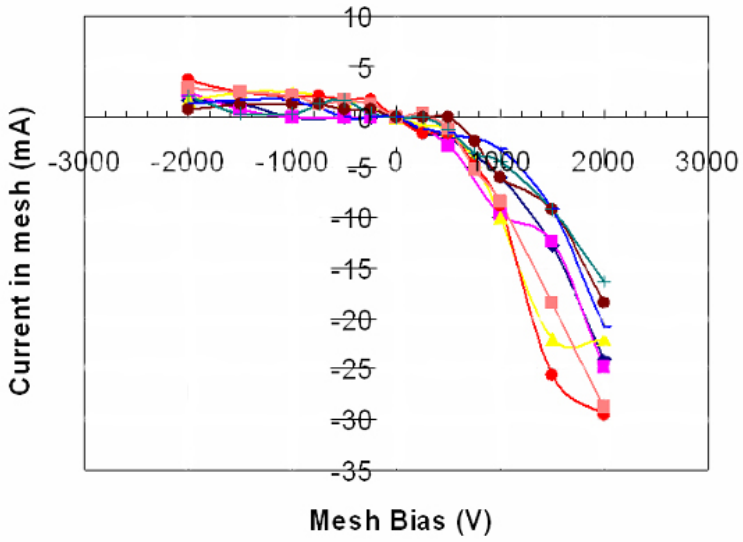

Figure 4-17: Mesh current when applying voltage across the mesh. Different lines correspond to different energies, ranging from 244 keV to 320 keV.

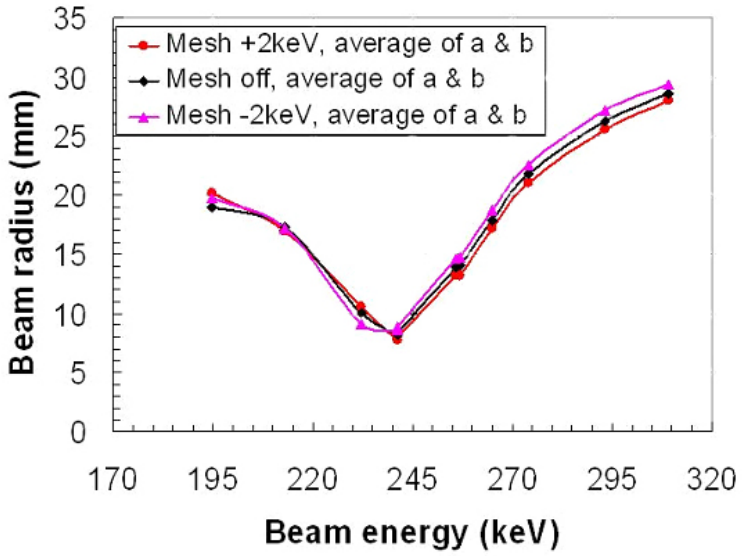

Figure 4-18: Beam radius as a function of beam energy as the mesh bias is turned on at ± 2 kV and is turned off.

4.4.2 Calibration of energy

The NTX source is powered from a Marx generator as mentioned in Chapter 3. The voltage is measured with a capacitive voltage divider. Calibration of beam energy is important because of the sensitivity of beam transport to the beam energy in a quadrupole transport channel as we have shown in Section 4.3. To provide a cross-check of the beam energy measurement, the capacitive system is compared to time-of-flight measurements and a resistive voltage divider system. The ion beams are capable of supporting and transmitting a variety of waves. Longitudinal space-charge waves are longitudinal oscillations of the beam within the conducting boundary of a vacuum wall. These waves have been studied and applied to continuous electron beams in microwave devices, bunched charged particle beams in particle accelerators, and space-charge dominated charged particle beams. The equilibrium and stability of these waves have been explored theoretically. In this subsection, we discuss a diagnostic technique that utilizes longitudinal space charge waves in heavy-ion beams to determine the beam energy using the time-of-flight (TOF) method. In the TOF method we longitudinally perturb a slice of the beam with a fast voltage pulse applied to a kicker near the path of the beam. The kicker may be any cylindrically symmetric mechanical structure near the beam that can rapidly generate a localized longitudinal electric field on the beam. A typical kicker and kick pulses are shown in Figure 4-19.

The voltage pulse applied to the kicker locally perturbs the energy of the beam particles passing near the structure. The perturbation propagates in the form of a wave that travels with the beam. In the long wavelength limit, there is a fast wave traveling toward the front of the beam pulse and a slow wave traveling toward the rear. Measuring the arrival time of the resulting space charge wave at a detector placed a suitable distance downstream provides a measure of the beam energy. The structure utilized as a kicker is a thin aperture which also limits the beam transversely for the final focus experiments. The NTX TOF pulse has a rise time of about 4 ns, a fall time

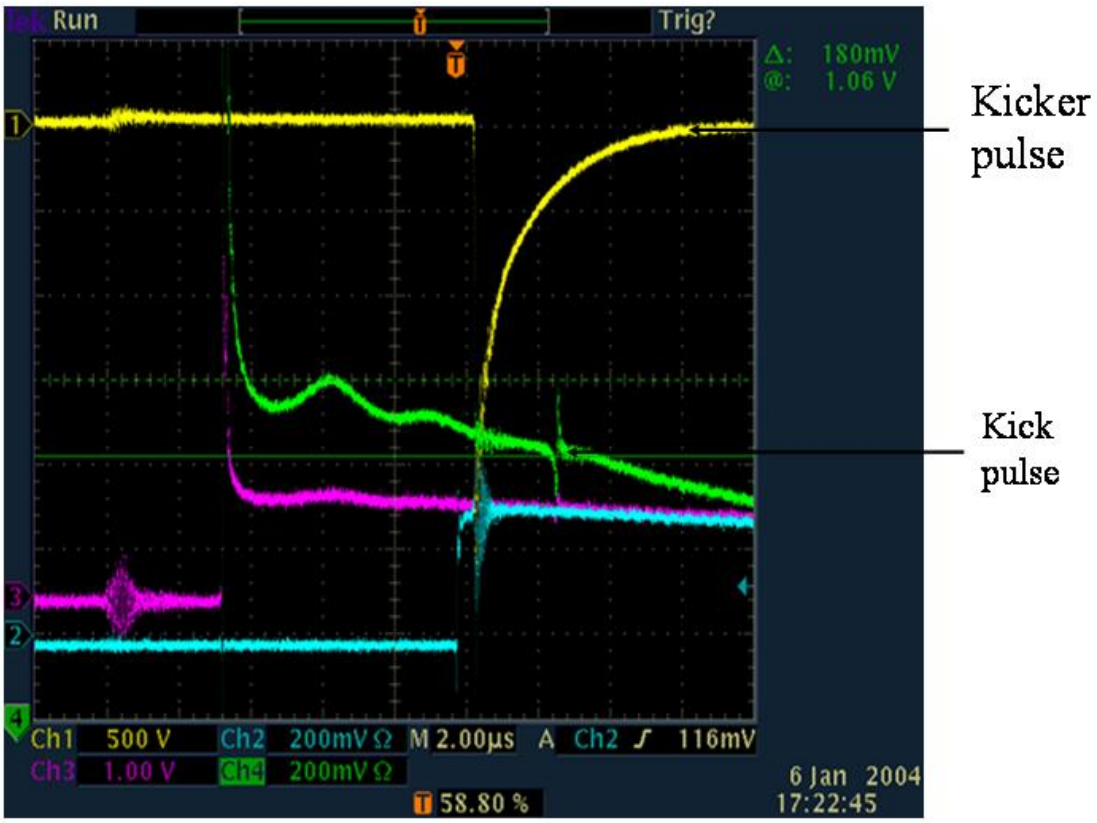

Figure 4-19: Typical waveforms of kicker (yellow trace) and kick (green trace) pulses for time-of-flight measurements. The oscilloscope vertical scale is arbitrary, the horizontal scale is 2 μs per division. The magenta and blue traces are auxiliary traces captured in this image.

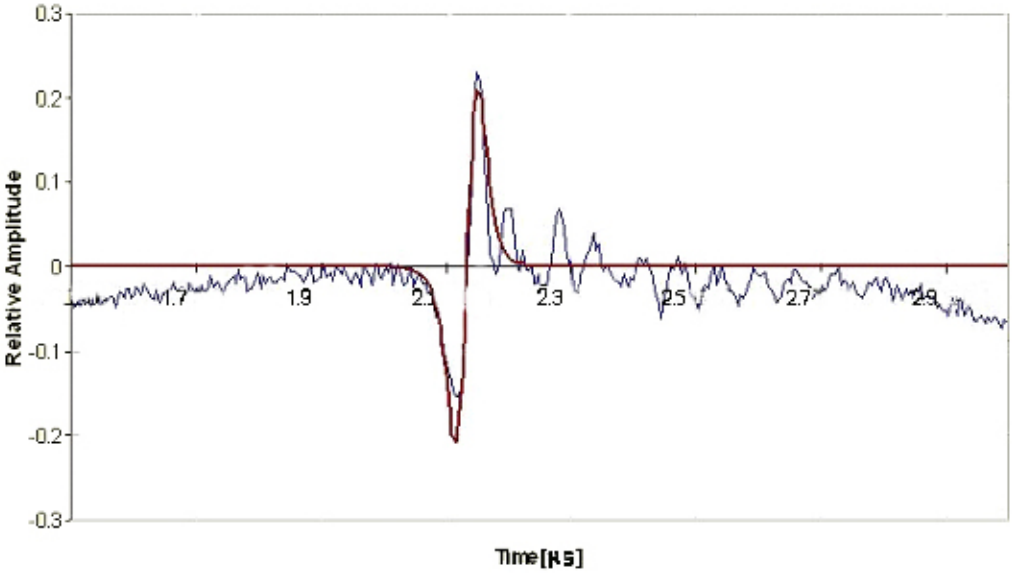

Figure 4-20: Space charge wave in NTX for a low-current beam.

about 1 μs, and a peak output voltage of -2.5 kV. The path length between the kicker and registering beam current at a Faraday cup is 2.48 m. The initial pulse resembles the longitudinal electric field (spatial derivative of the potential perturbation) at the kicker. Beam ions are spread apart at the front of the wave and compressed at the rear. The result is a double pulse which is very well defined in time. The time reference for TOF measurements is the point in which the wave passes through zero. This corresponds to those particles which were at the location of the aperture at the time that the pulser voltage is turned on. The comparison between data and the 1-D model is shown in Figure 4-20 for a small current (1 mA).

Agreement between model and data is good. However, for a large current (25 mA) the discrepancy varies. Figure 4-21 shows relative difference between TOF beam

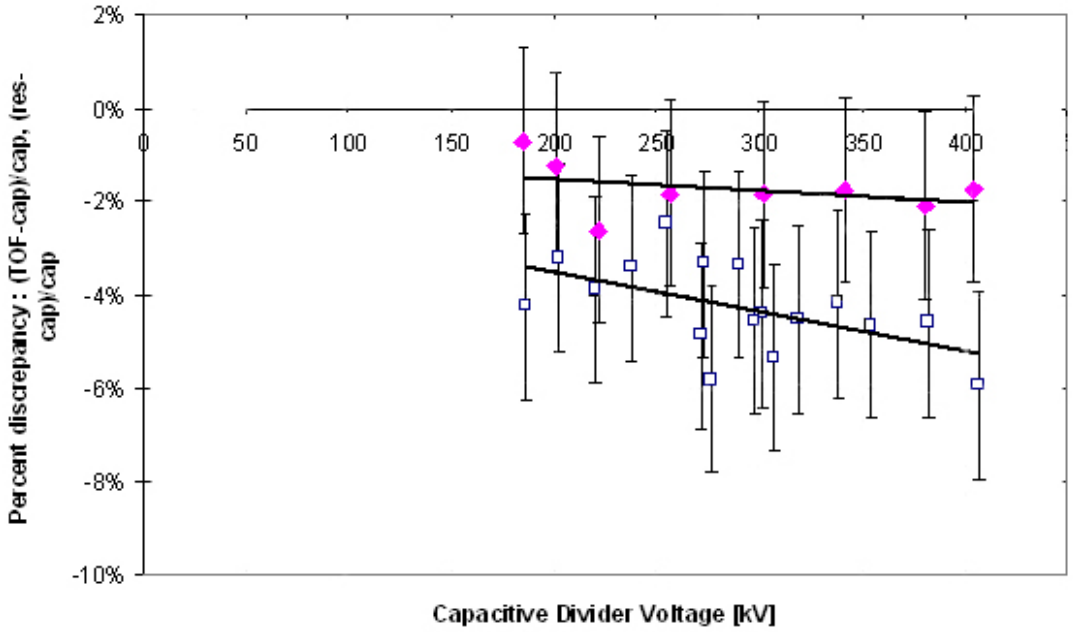

Figure 4-21: The relative difference between TOF beam energy (open squares), resistive divider voltage (diamonds), and capacitive divider voltage readings (0% line) as a function of NTX Marx voltage. Both TOF and resistive divider measurements are shown as a function of capacitive divider voltage. 2% error bars are assumed for both sets of measurements. A linear fit to the data points is also shown for each set of measurements. The voltage indicated by the resistive divider lies between the capacitive divider and the TOF measurements.

energy (open squares), resistive divider voltage (diamonds), and capacitive divider voltage readings as a function of NTX Marx voltage. Both TOF and resistive divider measurements are shown as a function of capacitive divider voltage. 2% error bars are assumed for both sets of measurements. A linear fit to the data points is also shown for each set of measurements. The voltage indicated by the resistive divider lies between the capacitive divider and the TOF measurements.

The strength of the 4 quadrupole magnets is provided by 4 separate power supplies using a pulser. Waveforms of each power supply are monitored on an oscilloscope screen. There is a $\pm 0.5\%$ magnetic field error bar when measured on wave forms displayed on the oscilloscope. Moreover, the magnet current monitor is a current

transformer with an accuracy specification of +1% and -0%. The existing timing setup assumes that the peak quadrupole field occurs at the peak of the monitored magnet current. In reality, there is attenuation and a time shift because of the diffusion of the magnetic field through the 3.3 mm pipe wall. This phase shift is approximately 275 μs based on ANSYS 2-D transient EM finite element modeling. Because of this time shift, the timing of the beam may not be during the peak quadrupole field. By the same modeling, the peak field is attenuated by approximately 7% and has been considered in setting the magnet currents.

4.4.3 Effectiveness of diagnostic devices

As was discussed in Sec. 2.4, the diagnostics that have been used in this experiment are Faraday cups, Slit cups and scintillators associated with electronics and a CCD gated camera. Though slit cups have available an electron guard ring, there exists the possibility of generation of secondary electrons noise by the energetic particles, whose presence can mislead the interpretation of halo particles studies. Moreover, once the energetic particles strike on a scintillator, its effectiveness degrades as a function of the incoming beam particle energy.

4.4.4 Beam halo formation

Finally, we have observed clear evidence of halo formation, i.e., the rings surrounding the central image, in both configuration space (Figure 4-22) and velocity space (Figure 4-23).

We have not been able to account, from numerical simulations, for the origin of the halo particles in configuration space. One source of halo formation could be the unavoidable non-uniform ion emission from the alumino-silicate emitter, due to fabrication tolerances or non-uniform temperature distribution.

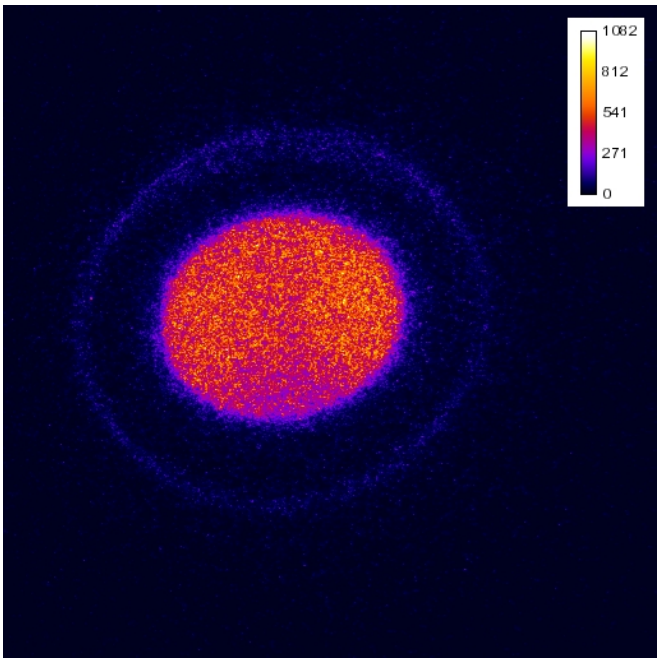

Figure 4-22: Evidence of beam halo formation in the configuration space. Image for a 6% off-energy beam, measured at the end of the final focus system (beam size ~2 cm)

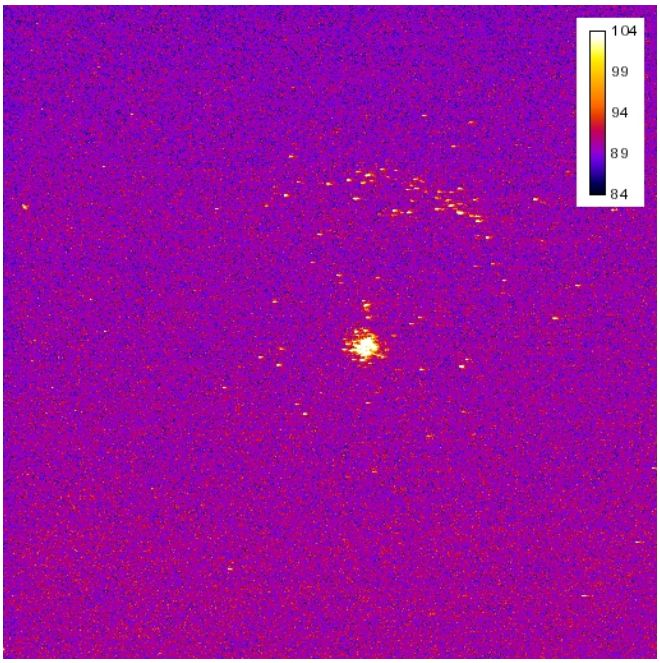

Figure 4-23: Evidence of beam halo formation in the velocity space. Image from a pinhole positioned at the end of the final focus system and at the center of the beam, as measured at the focal plane.

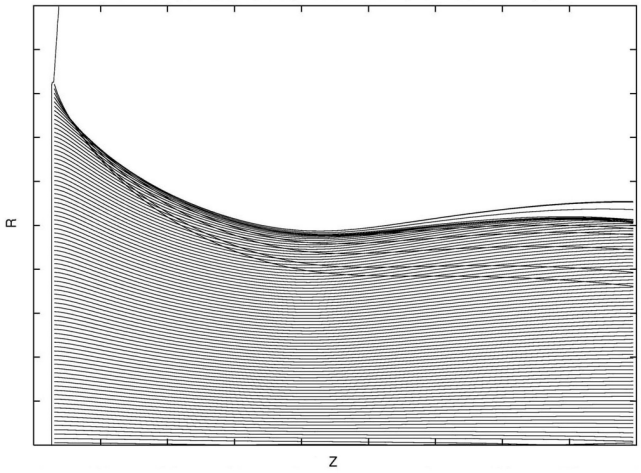

Figure 4-24: Translaminar components originated from non-ideal emitter position with respect to Pierce electrode.

The origin of the halo formation in velocity space has been traced back to a diode geometry property. The emitter is slightly receded from its ideal location with respect to the Pierce electrode. This non-ideal geometry generates ion trajectories which travel at an angle non-similar to the trajectories of the main body of the beam, and generate so-called translaminar components (Figure 4-24). This components appear as a halo when the the beam is intercepted by a pinhole and the transmitted current is imaged on a scintillator as shown in Figure 4-23.

THIS PAGE INTENTIONALLY LEFT BLANK

Chapter 5

Final Neutralized Drift to Target

A crucial aspect of NTX is the validation of neutralized transport in the fusion chamber. As described in Chapter 2, the presently favored concept for neutralization of driver beams involves passing the ion beams through a low-density plasma before they enter the fusion chamber. Because the plasma which is in contact with an emitting surface supplies enough electrons, the neutralizing electrons remain trapped in the beam potential as the beam exits the plasma, providing charge and current neutralization in the chamber. In addition, the main driver beams arrive after the hohlraum exterior has been heated to about 100 eV. As these pulses approach the target, they are photostripped by soft X rays from the target. They also receive further neutralization from the plasma formed around the target by photoionization of the background gas.

5.1 Ballistic Neutralized Transport

The layout of the 1-m NTX plasma neutralization section is shown in Figure 5-1. The upstream plasma, modeling the plasma plug that neutralizes the beam after it exits the final-focus section, consists mainly of electrons and doubly charged aluminum ions from a pulsed cathode-arc source (sometimes called a metal-vapor vacuum arc or

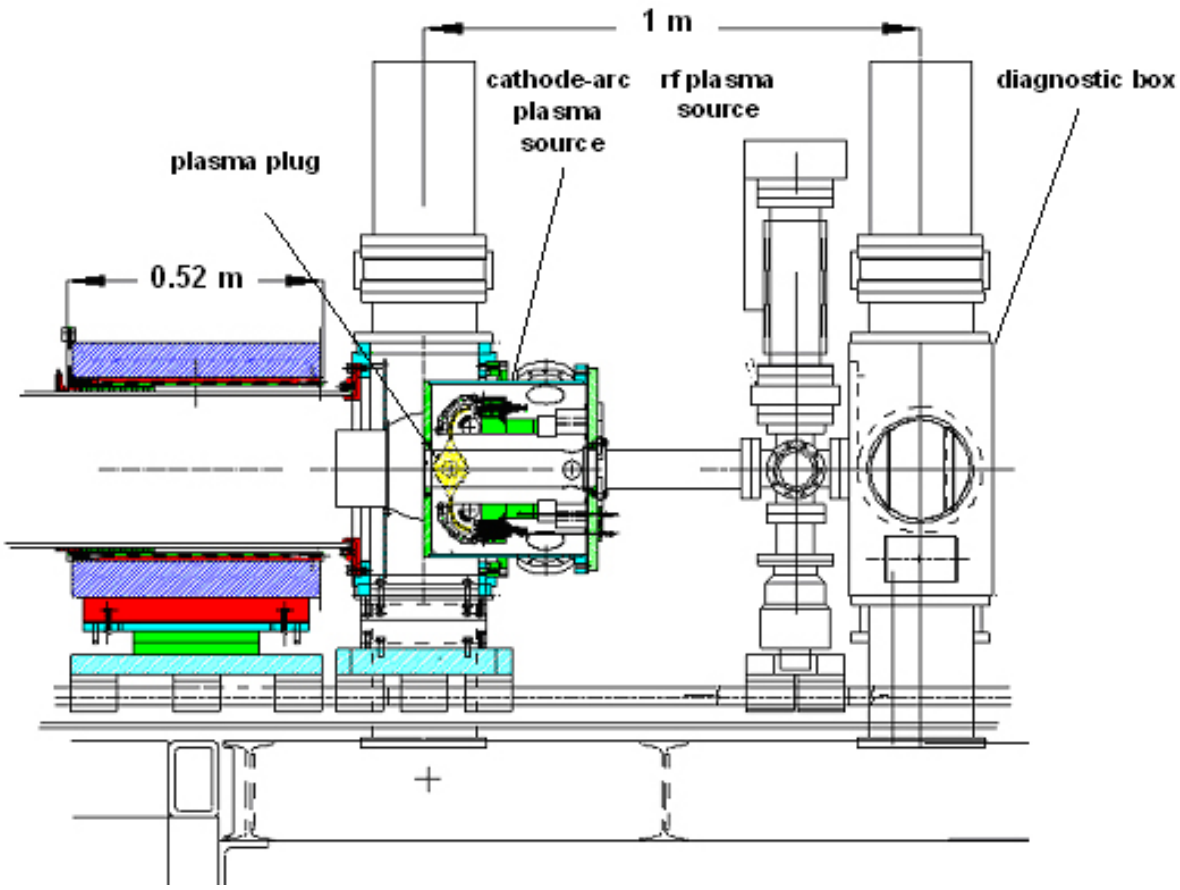

Figure 5-1: NTX neutralization section layout.

MEVVA source). The plasma itself is centered 0.25 m downstream from the end of the last magnet so that it is sufficiently far away from the fringe fields, and it extends about 0.05 m in both directions. After the beam exits this first plasma, it drifts 0.75 m through a 3.5-cm-radius beam pipe into a diagnostic area at the nominal focal point. A second plasma generated at the center of the cross simulates the photoionized gas that will surround a target hohlraum after it has been heated by early low-current "foot" beams. This "target" plasma is generated by a pulsed radio-frequency (rf) source and has a charge density approximating what is expected in a fusion chamber. A diagnostic box is placed at the focal point.

5.2 Plasma Source

NTX uses two plasma sources to demonstrate the effects of beam neutralization. A pulsed cathode-arc source provides an upstream aluminum plasma for the initial neutralization, and a pulsed radio-frequency (rf) source provides a volume plasma near the beam waist. These sources can model the effects of beam neutralization well, even though they obviously cannot duplicate the photoionization or the collisional stripping and scattering that are expected in a driver.

We have used the electromagnetic PIC code LSP [14,15] to determine the requirements for both plasma sources. Numerical simulations indicate that we require a neutralizing plasma with a length in the range of 10–20 cm and an electron density that is 1–100 times the nominal initial NTX beam density of about $3 \times 10^8\, cm^{-3}$. The density of the target plasma, of course, will increase as the beam impinges on the target due to continuing photoionization by X rays from the hohlraum. However, the nominal plasma density around the target is expected to be comparable to the final beam density. For NTX, this value will be around $10^{10}\, cm^{-3}$, depending on the perveance and the focal-spot radius.

5.2.1 Cathode-arc plasma source

The pair of pulsed cathode-arc plasma sources shown in Figure 5-2 have been designed and fabricated at LBNL for the NTX neutralized-transport experiments. The density and duration of the metal plasma can be adjusted over a very wide range. For example, aluminum plasma of density $10^8 - 10^{12}\, cm^{-3}$ can be produced in pulses of 1–1000 μs by selection of suitable arc current and discharge geometry. These sources have a negligible fraction of neutral atoms and molecules in the plasma, making them ideal sources for a neutralizing plasma.

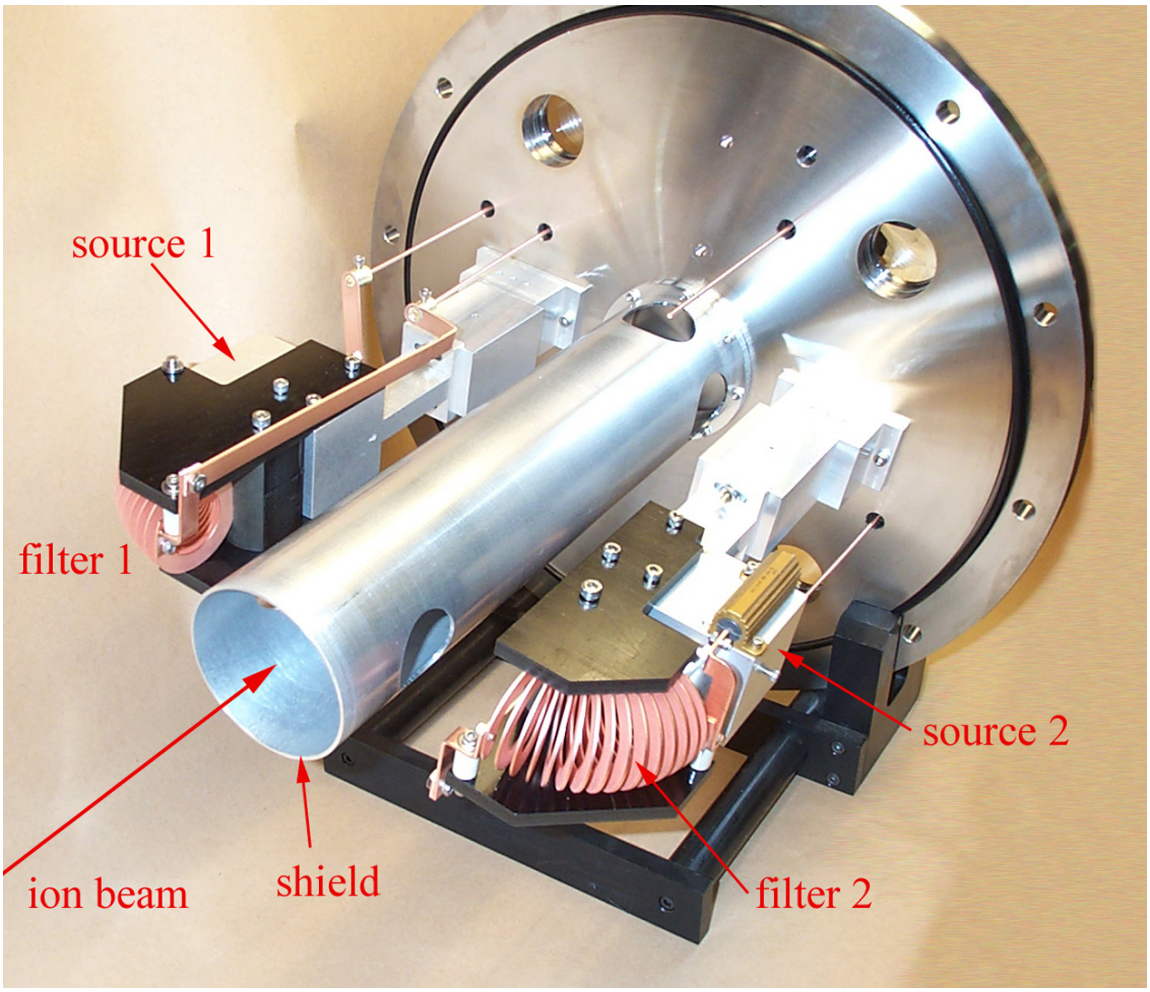

Figure 5-2: NTX cathode-arc plasma sources mounted on beam pipe. Plasma is injected in the path of the ion beam through openings in the aluminum metal shield. The shield is designed to reduce the magnetic field at the location of the ion beam, to limit plasma entering the quadrupole region, and to prevent macroparticles from the source from entering the beam region.

The plasma sources are of the "mini-gun" type, consisting of a replaceable cathode rod of 0.625-cm diameter and about 2.5-cm length, a ceramic insulator as part of the cathode assembly, and a grounded anode body [64]. The source is coupled to an open macroparticle and neutral-atom filter [65], consisting of a copper coil with a 90^{O} bend. The filter removes particles from the plasma stream, allowing only clean, fully ionized metal plasma to reach the NTX beam line. Two of these source/filter assemblies are installed on NTX, injecting plasma from opposing sides to produce a symmetrical plasma distribution. The consumable cathode of each source is made from aluminum, because deposition of aluminum on the beam line components does not introduce foreign material. The lifetime of the cathode before maintenance is estimated to be about 10^5 pulses.

In initial tests, the two source units (plasma gun and filter) are mounted in a high vacuum. A large ion collector, made from a flat, isolated sheet of stainless steel, is positioned between the sources and biased negatively to repel electrons and collect ions. The plasma ion current proves to be noisy, as is typical for cathodic vacuum arcs. We use the plasma at about 250 μs after arc triggering, just before the second maximum of the plasma current, so repeated measurements of the plasma ion current are made at that time to get information on statistical fluctuations. The result is shown in Figure 5-3.

The source units are then mounted on a large flange to be inserted in the beam line. The flange, with sources and the beam shield, is evacuated with a small turbomolecular pump to a base pressure of about 10^{-5} Torr. To demonstrate the shot-to-shot reproducibility, ten successive ion current pulses are overlaid in Figure 5-4. Through the body of the pulse, the ion current on repeated shots is seen to fluctuate by about $\pm 10\%$.

The plasma density can be estimated by noting that the ion current is given generally by $j_i = Zen_iv_i$, where j_i is the ion current density, Z is the average charge

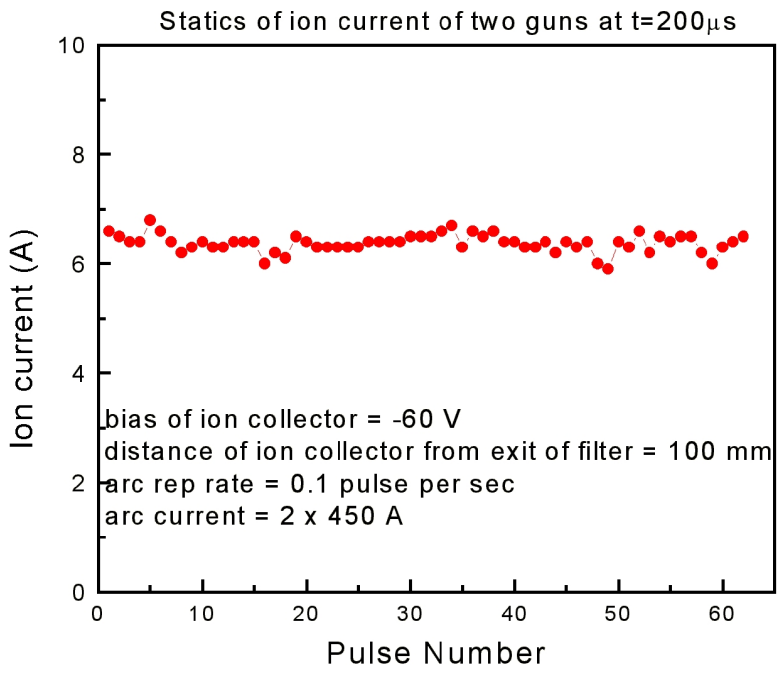

Figure 5-3: Ion current signal from the two cathode-arc plasma sources, each operating with 450 A arc current and fed by the same pulse-forming network.

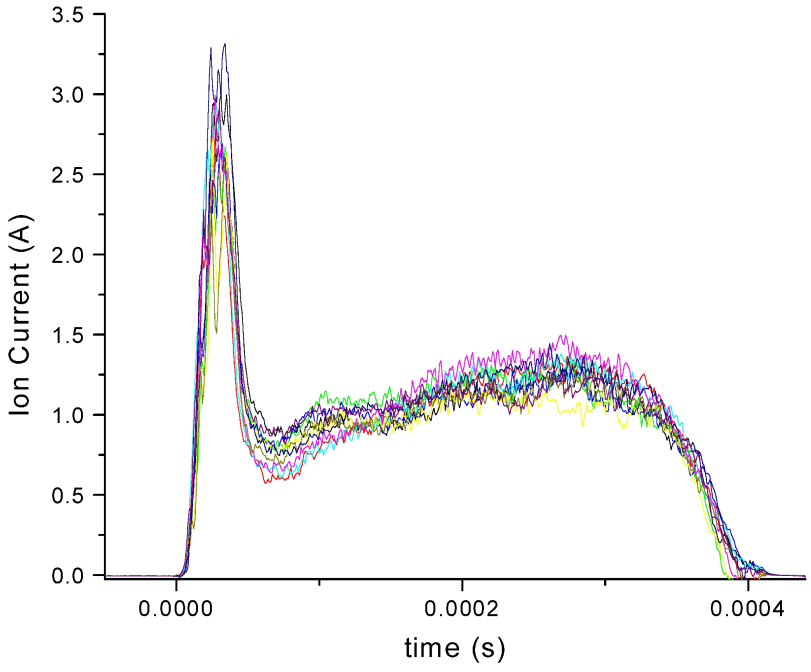

Figure 5-4: Aluminum ion current of ten successive arc pulses collected by an ion collector at the location of the NTX ion beam.

state number, e is the elementary charge, n_i is the ion number density, and v_i is the average ion velocity in the direction of the collector, which is here identical with the plasma flow velocity. From previous work [66], it is known that $Z = 1.7$, $v_i = 1.54{\times}10^5$ m/s, and with an area of collection of about $10^{-2}\ m^2$ we obtain $n_i \simeq 1.8{\times}10^{10}\ cm^{-3}$ for the average plasma density inside the metal shield at about 250 μs after arc triggering, at a pulse-forming network (PFN) charging voltage of 2.0 kV. This density can be controlled either by changing the distance between the filter exit and the beam shield, or by adjusting the arc current through the PFN charging voltage.

A commercial Langmuir probe from Scientific Systems, together with its accompanying SmartSoft software, is used to measure the density of the aluminum plasma produced by the cathode-arc source as a function of space and as a function of discharge voltage. Since the plasma streams into the beam line at supersonic ion velocities, the analysis algorithms contained in the SmartSoft software cannot be used. However, using the ion saturation current from the measured current-voltage (I–V) characteristics and making simplifying assumptions about the aluminum plasma allows us to estimate the plasma density. We find that the NTX cathode-arc source produces plasmas with densities in the $10^{10} - 10^{11}\ cm^{-3}$ range and that the plasma density is proportional to the discharge voltage over the range from 1.5 kV to 2.5 kV. The measurements show that the plasma density along the axis is peaked at the location of the pair of entry ports where the plasma enters the beam line and drops off over a distance of a few centimeters. At the axial location of the entry ports, the density is greatest near the entrances to the two ports, and decreases towards the axis since the plasma expands as it moves away from the ports.

The Langmuir probe requires 5 μs to acquire each data point on the I–V characteristic, and each I–V characteristic is comprised of 200 points. Thus, to obtain the temporal resolution necessary to measure the plasma density at a given instant during the 300 μs cathode-arc discharge, the Langmuir probe is operated in the "box-

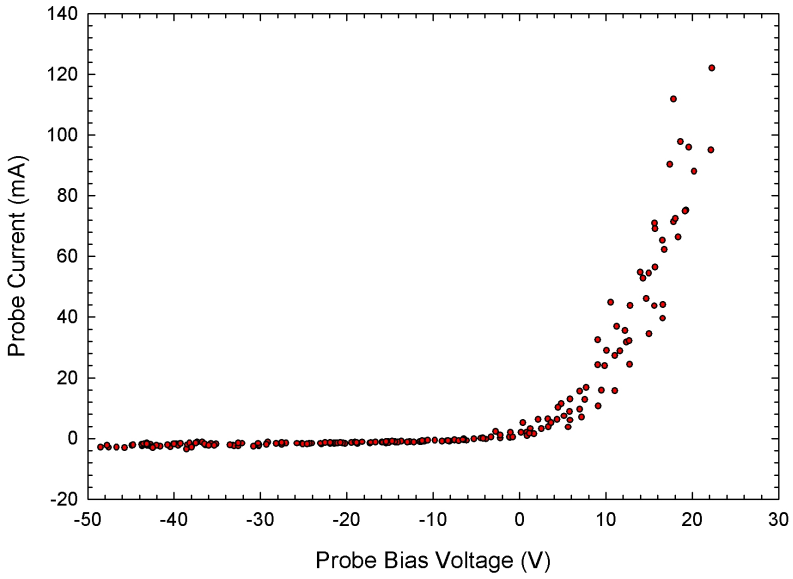

Figure 5-5: Each point on the I–V characteristic is taken from a single shot of the cathode-arc plasma source. The shot-to-shot variability produces a spread in the data. The ion saturation current can be used to determine the plasma density.

car" mode. In the boxcar mode, a trigger pulse generated at the desired time during the discharge triggers the Langmuir probe to take a single I–V measurement. The cathode-arc system must then be triggered 200 times to acquire a complete I–V characteristic. The 10% – 20% shot-to-shot variation of the cathode-arc source is reflected in the scatter of the points in the IV characteristic shown in Figure 5-5. Despite these fluctuations, the ion saturation current I_{sat} can be measured from these data and used to calculate the plasma density.

Figure 5-6 shows the dependence of the ion saturation current on the discharge voltage. Below 1.5 kV, arc triggering does not occur. Operation above 2.5 kV is not possible with the PFN presently in place. The data show that the plasma density can be varied by a factor of four by adjusting the PFN charging voltage.

The axial density profile is shown in Figure 5-7. The axial extent of the plasma is approximately 5 cm and is strongly peaked near the port openings which are located at $z = 144\ mm$. It should be noted that even though the densities plotted in Figure

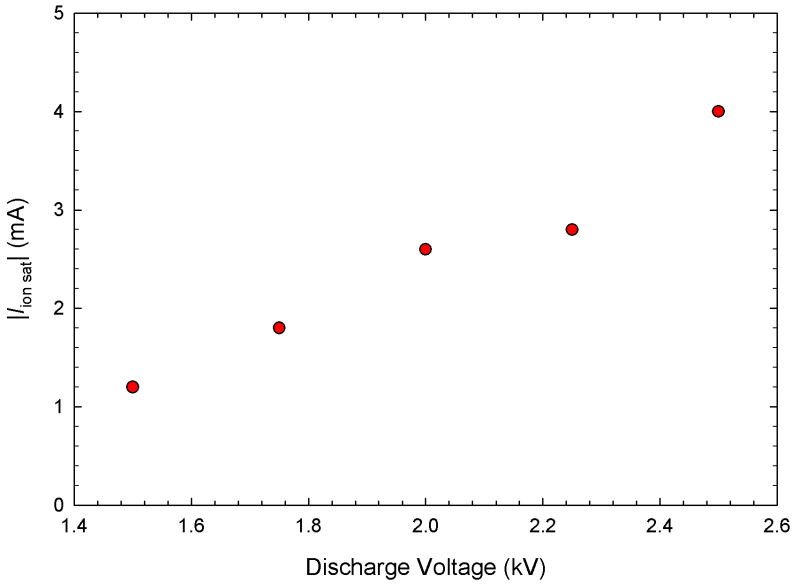

Figure 5-6: Ion saturation current as a function of NTX cathode-arc dischage voltage. The plasma density varies proportionally with this current.

5-7 are those computed by the questionable SmartSoft algorithm, they are very close to the values calculated using the simple model outlined above. Moving the Langmuir probe in the transverse direction allows us to measure the transverse profile of the plasma stream. From the ion saturation current measured at numerous points across the beam path, we find that the plasma expands and the density decreases as the plasma moves away from the ports, and the density is smaller near the top of the beam-line tube.

5.2.2 Radio-frequency plasma source

A radio-frequency (rf) plasma source, shown in Figure 5-8, has been designed and assembled at PPPL to model a target plasma in NTX [67]. The goal is to generate plasmas with electron densities up to $10^{11}\,cm^{-3}$ and a pressure in the range of $10^{-6} - 10^{-5}$ Torr, requiring effectively full ionization. The low pressure is important to prevent neutrals from stripping the beam ions to higher charge states.

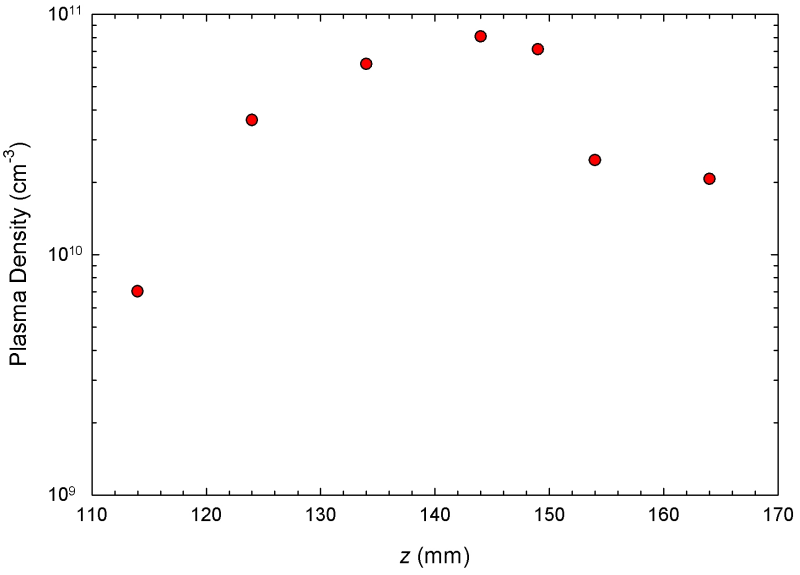

Figure 5-7: Axial profile of the plasma density as a function of longitudinal position near the plasma entry ports.

The pulsed plasma source has a six-way cross at the center of its design. A turbo-pump attached to one face maintains the vacuum, while the gas inlet and the rf quartz window are attached to the opposite face. A three-turn copper spiral antenna is situated inside a shielded box and faces the window. The rf matching network is directly connected to the antenna enclosure and is tuned to match the low impedance antenna to the 50 Ω transmission cable. The drift tube for the ion beam is connected to two flanges on the six-way cross perpendicular to the turbo-pump and antenna. The plasma drifts into the center of the cross, and intersects the propagating ion beam. The source operates by applying a puff of argon gas and a pulse of rf power to the antenna. The potential advantages of pulsed operation are that it can easily operate at high peak rf power levels, and the amount of gas can be limited. The plasma density and the neutral gas pressure are issues primarily while the ion beam is passing through the plasma, an interval of about 100 μs. Consequently, the plasma parameters and neutral-gas pressure are dynamic quantities and need to be measured as a function of time in order to evaluate source operation.

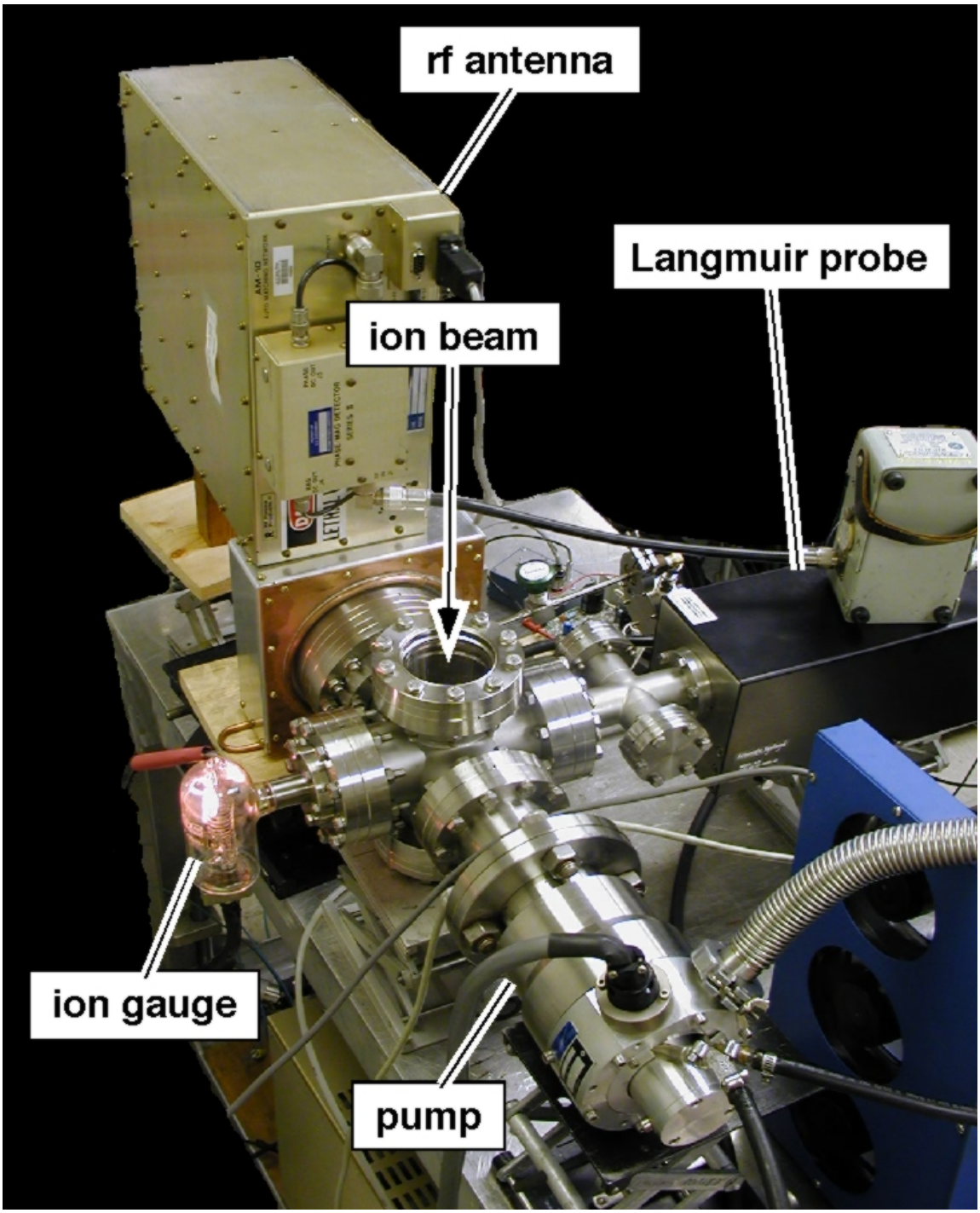

Figure 5-8: PPPL rf Argon plasma source before installation. Plasma is created in the six-way cross along the ion-beam path.

A typical ion-gauge controller does not have the time response to measure the quick pressure bursts when a gas puff is applied to the system. However, by measuring the voltage across a resistor placed in series with the collector current of the gauge, the dynamic absolute pressure in the plasma source can be ascertained. The dynamic pressure measurement is calibrated at a fixed pressure while the pressure gauge is read, and the voltage across the resistor is recorded. To insure that the observed rise time is indicative of the rising gas pressure and not the RC time response of the circuit, the pressure measurement for a given plasma condition was repeated with two different resistors with an order-of-magnitude difference in resistance. The pressure evolutions for the two resistors were in agreement. Applying a 5-ms gas puff to the plasma source, the pressure sharply rises to 2 mTorr and pumps away in about one second. This time scale is appropriate for NTX because the experiment produces a 100-μs ion beam every 15 seconds. The plasma electron density is measured with the Langmuir probe because this device compensates for the effects of rf fields. Also, since the pulsed plasma source is found to have very reproducible breakdown time and plasma parameters, the Langmuir probe can make time-resolved measurements.

To operate the plasma source, the gas valve and the rf power are triggered at the same time (t=0). In this mode, it is easy to deliver more than 2 kW of rf power to the source, compared to only 1 kW for continuous plasma source operation. The power is measured with a directional coupler and calibrated diode. Figure 5-9 shows the source characteristics versus time for a net forward power of $\sim$3.5 kW. Before t=3.75 ms, the plasma density is less than the sensitivity of the Langmuir probe ($\sim 10^7 cm^{-3}$), and the neutral pressure is below the sensitivity of the dynamic pressure measurement (10^{-6} Torr). The onset of breakdown is clearly observed in the forward and reflected rf power versus time. The rf matching network is adjusted so that there is a maximum net power delivered to the plasma. At t=3.75 ms, the electron density is $10^{11}\, cm^{-3}$, and the neutral pressure is simultaneously low. The effective ionization

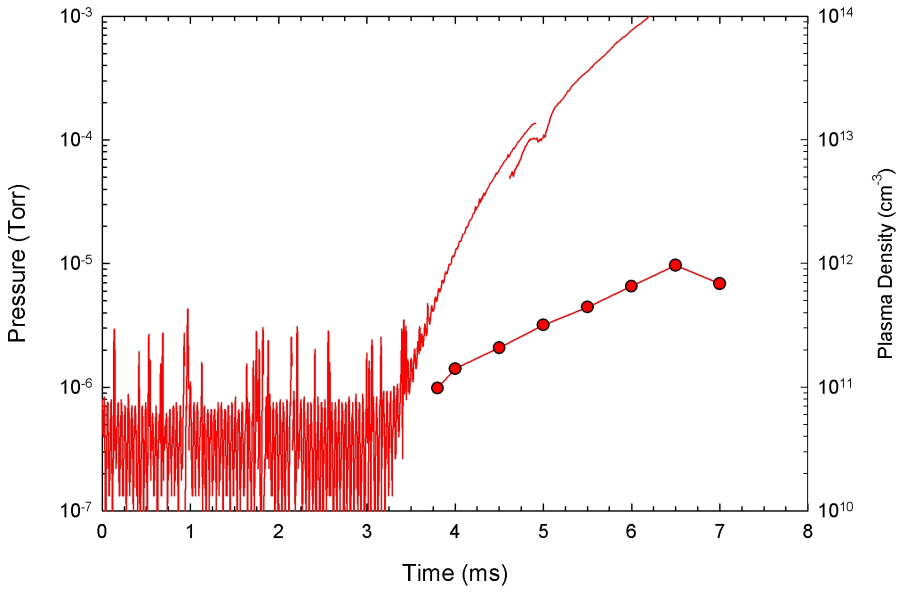

Figure 5-9: Time evolution of neutral gas pressure and plasma electron density (solid circles) in the pulsed plasma source. One upgrade under consideration is replacing the gas valve with a faster one to reduce the length of the gas puff and the total amount of gas into the system. Another upgrade would use a pulsed rf supply to increase the rf power level.

fraction for t=3.75 ms is in the range of 50–100%. At later times, the power density is not sufficient to sustain the ionization fraction, and the neutral density rises faster than the electron density.

One difference between the initial source tests at PPPL and those at LBNL is that the rf generator is unable to provide 3.5 kW of power at LBNL and is limited to 2.5 kW. This lower power limits the maximum plasma density that could be achieved. A number of density measurements are made in the six-way cross with the Langmuir probe. A profile measurement is made transverse to the axis of the plasma source and turbo-pump (Figure 5-10). The density is peaked on axis. There is a factor of two drop near the plasma source wall radius of 5 cm. Distances greater than 5 cm from the center of the cross are hidden from the straight-line path of the plasma out of the source. There, the density decreases by an order-of-magnitude at a distance 5 cm from the wall radius of the plasma source.

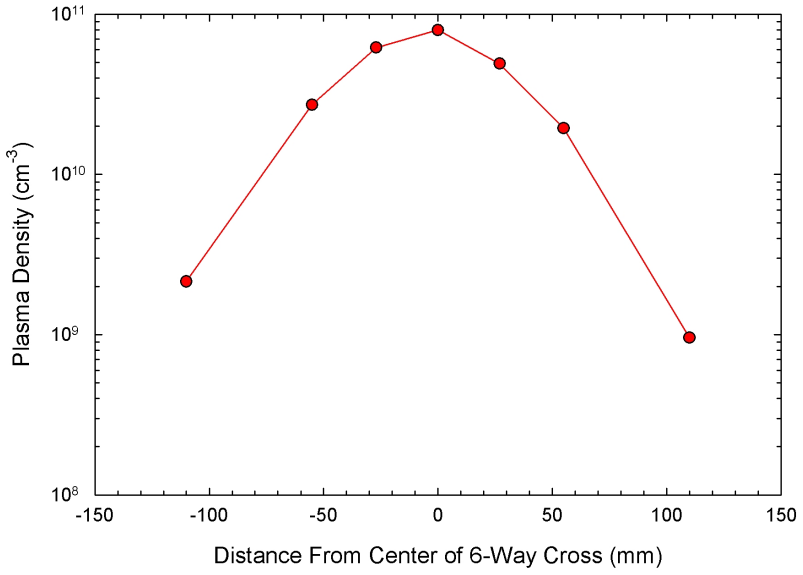

Figure 5-10: Plasma density profile transverse to the plasma source in the six-way cross.

Another profile measurement is made in the six-way cross, but along the axis of the plasma source (Figure 5-11). In this direction, the plasma has a steep gradient away from the antenna because of the short plasma skin depth ($\sim$ 1 cm). Consequently, the plasma density drops by two orders-of-magnitude across the cross diameter in this direction. In future work, a weak magnetic field might be used to reduce the density drop.

Finally, the density at the center of the cross is measured as a function of rf power. The results, ploted in Figure 5-12, show that the electron density increases exponentially with rf power. The data point near 3.5 kW is obtained at PPPL, but since the rf generator at LBNL is limited to 2.5 kW, the highest density presently available from the rf source in NTX is $5 \times 10^{10}\, cm^{-3}$.

In final NTX experiments, the rf generator was brought back to its 4-kW power capability in order to achieve the previously observed densities, and the gas valve was replaced with a faster one to limit the gas introduced to the NTX vacuum system.

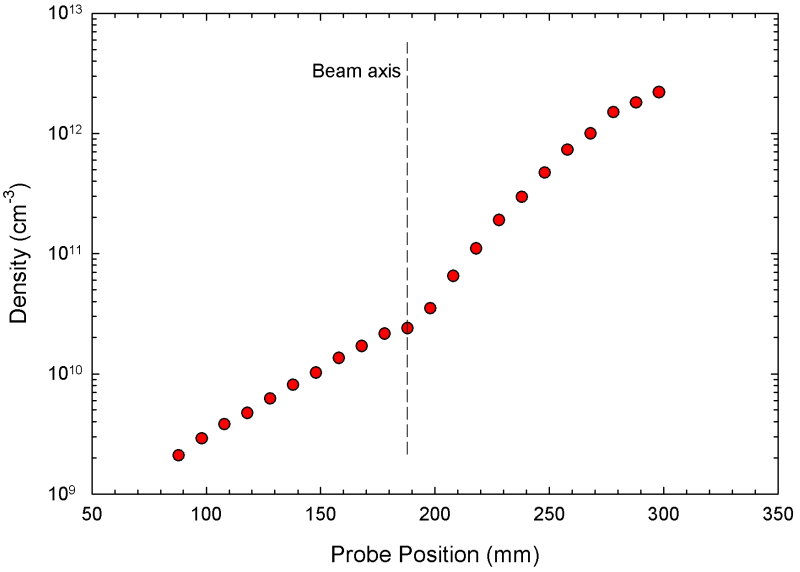

Figure 5-11: Plasma density in the transverse direction, towards the rf power source, showing a steep gradient.

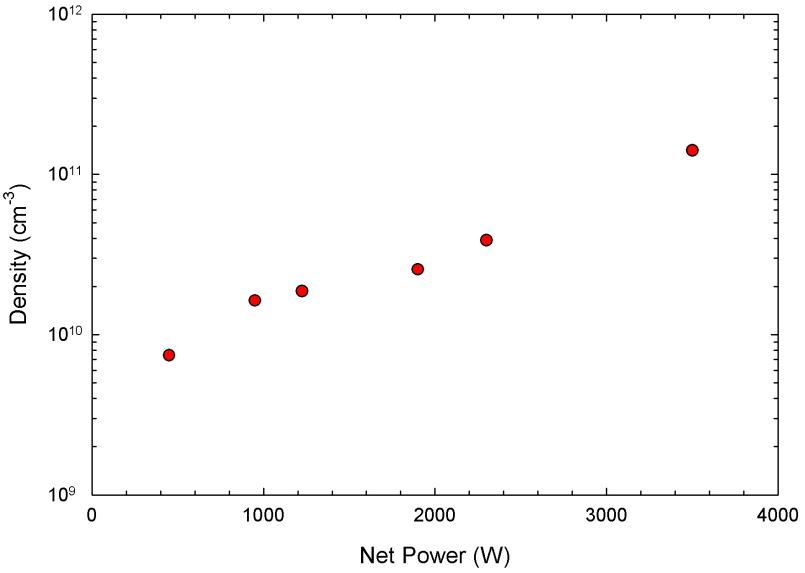

Figure 5-12: Electron density in the center of the cross as a function of rf power.

5.3 Neutralized-drift experiments

An important area of NTX research is studying the effects of beam neutralization on transport. As discussed in Section 5.1, a converging ion beam exiting the final-focus lattice is injected into a 1-m drift section, where neutralization is provided by a plasma from the metal arc source and the rf plasma source. Both sources deliver reproducible plasmas with densities up to ten times greater than the beam density, a sufficient value for a range of neutralization experiments. We have studied the effects of an upstream "plasma plug", where electrons are extracted from a plasma and dragged along by the beam potential, as well as the effects of the "volumetric plasma" nearer the focal point, where neutralization is provided along the beam path just before the focal point.

Experimental findings for both neutralization methods have been compared with the results of LSP [14,15] particle simulations. Using particles extracted from a WARP simulation as input, we simulate the neutralization process of the focusing beam as it passes through a plasma, following the beam past its focal point (Figure 5-13). The simulation domain is 3.8 cm in radius and 130 cm long. The K^+ beam is injected through an open (Neumann) boundary at z =-30 cm and initially has a 2-cm outer radius, a 25-mA current, and a 300-keV energy. At initialization, the plasma has a uniform density of electrons and Al^{+2} ions. It extends radially to the outer wall and occupies a 10-cm longitudinal region beginning 20 cm after the injection plane. The 3-eV plasma temperature is comparable with the critical energy, $\frac{1}{2}m_e v_i^2 = 4\,eV$, a fact that could affect the neutralization process to some extent. Space-charge-limited emission (SCLE) of cold electrons is permitted where the plasma is in contact with the outer wall. This boundary enables the re-supply of low-energy electrons to maintain quasi-neutrality of the plasma during the simulation. Because each impacting beam ion will stimulate the emission of many electrons, we also permit SCLE of electrons at the $z = 100$ cm wall. An electron trap prevents electrons from drifting upstream into

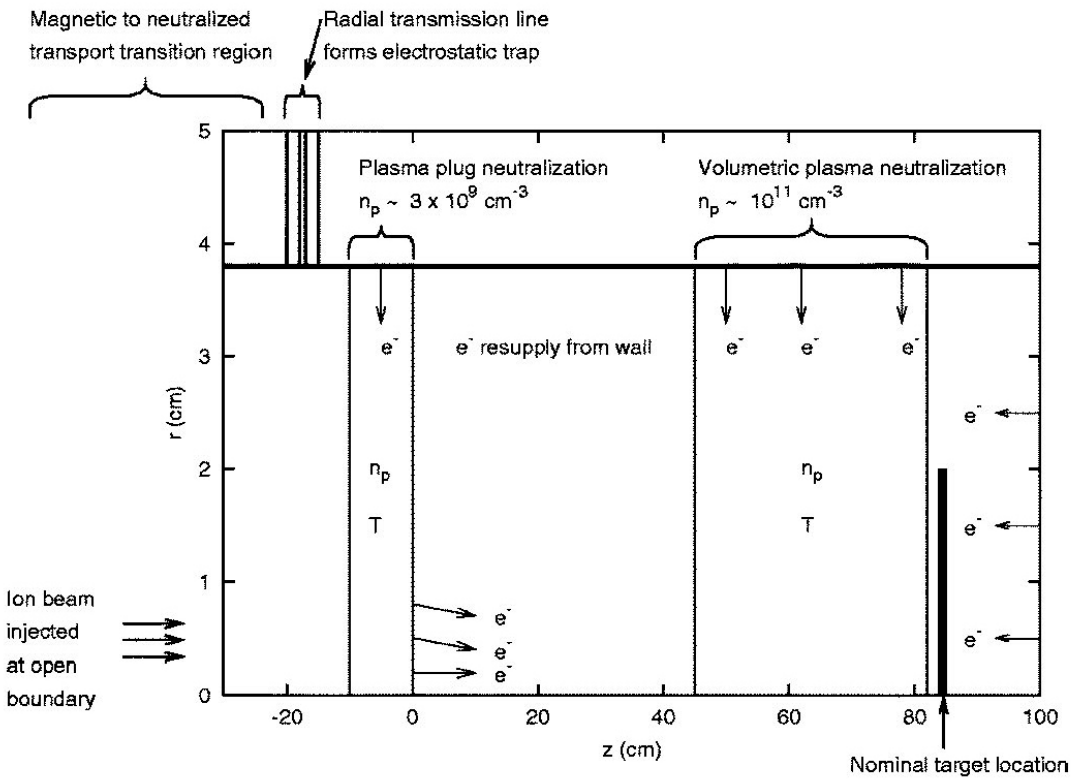

Figure 5-13: LSP simulation schematic.

the magnetic focusing region. The trap consists of a 1-cm-long ring electrode that is centered at z=-18.5 cm and negatively biased at 1 kV in the simulation. Finally, the PIC simulations are collisionless, with no beam stripping or ionization processes.

In the neutralized drift section, WARP3D can be used to model the beam dynamics when a simple approximation is applied in which the space charge forces are uniformly reduced by a neutralization factor, of the order of 95 to 97%, which is a result obtained from a more detailed neutralized beam transport calculation using LSP code [15]. LSP models the plasma-beam interaction in detail, while WARP3D is the code of choice for magnetic lattice beam dynamics. The simplifying approximation allows us to extrapolate the beam dynamics effects in the quadrupole section to the final beam spot.

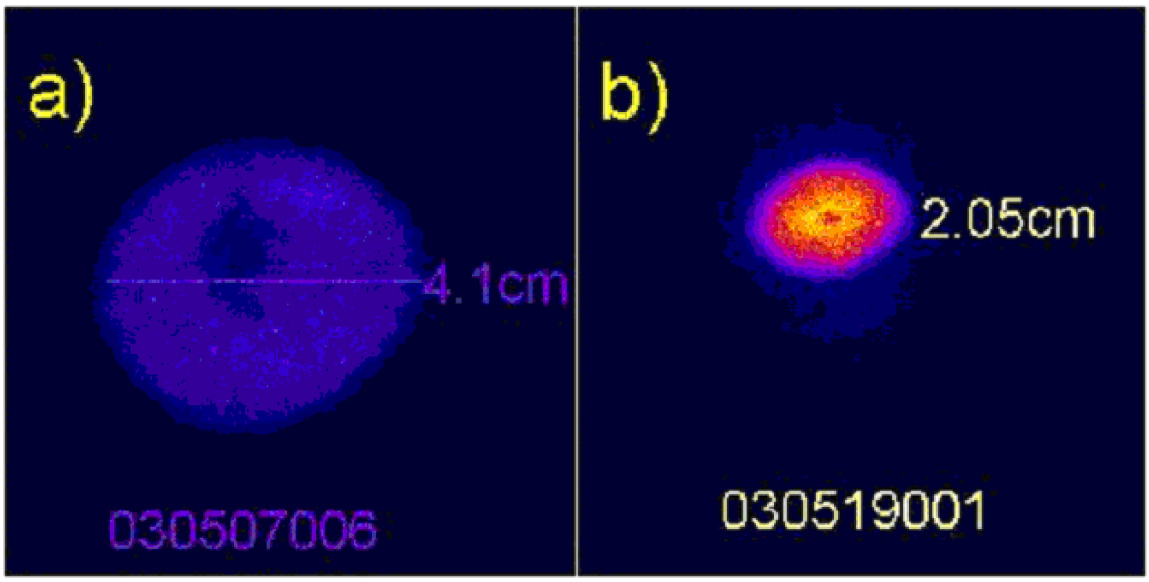

Figure 5-14: Beam images for a 255 keV beam measured 1m downstream, transported through a tube of diameter a) 15 cm and b) 7.6 cm.

5.3.1 Beam transport in vacuum

5.3.1.1 Uncontrolled neutralization

As a preliminary step to characterize beam transport in the NTX final-focus system, a 255-keV beam is injected into a large (15-cm) diameter pipe from the exit of the final focus magnet to a diagnostic box 1 m downstream; a large diameter pipe ensures that electron emission from the walls is negligible. The beam is also transported through a nominal 7.6-cm diameter pipe corresponding to the actual neutralized drift section containing the MEVVA plasma plug system. Figure 5-14 shows beam images for unneutralized beam transported through (a) 15 cm diameter tube and (b) 7.6 cm diameter tube. A smaller spot size, roughly 50% less in diameter, is measured for transport in the 7.6 cm diameter tube, which does not agree well with the calculated beam transport in a vacuum. This smaller beam size is due to the capture by the beam of free electrons from the wall that partially neutralize the beam.

5.3.1.2 Control technique of unwanted neutralization

Ions from the poorly matched beam head and halo ions in the main pulse of the beam can strike the outer wall of the transport tube. A single ion impact can produce thousands of secondary electrons depending on the energy and angle of incidence with ions of grazing-angle incidence producing the largest secondary electron yield. Only a small fraction of the beam ions striking the wall are needed to provide a space-charge limited supply of electrons from the wall. If the secondary electrons are not stopped, they are attracted to the beam potential and can provide some degree of beam neutralization.

Halo scrape off will be drastically reduced using the 15cm pipe. Also for larger wall radius, the wall electrons can spend only a small fraction of their time within the beam. The electrons are moving at their greatest velocity while passing through the beam further decreasing their beam neutralization. Thus, the neutralization fraction from these electrons will scale no better than the ratio of the beam to wall radii. A wall radius comparable to that of the beam will provide some sizable degree of neutralization and prevent the observation of expected vacuum transport. The secondary electrons are produced with mean energy roughly that of the ionization potential of the impacted wall atoms – typically 10 eV. The distribution of electrons in ionization events also has a high energy tail falling off as the square of the energy. Thus, if we place a highly transparent wire mesh sleeve within the drift tube and bias it with potential $\gg$ 10 eV, we can expect to collect these secondary electrons and prevent them from moving into the beam path. Given a positive potential, electrons produced on the mesh itself will tend to be trapped near the mesh. Figure 5-15 shows a high beam transference cylindrical tube shape metal mesh that is inserted into the 7.6 cm beam tube. The thickness and longitudinal length of the mesh are 2.2 mm and 58.2 cm, respectively. Outer and inner diameters of the mesh tube are 6.3 cm and 5.88 cm, respectively, thus maintaining better than a 5 mm radial electrical isolation

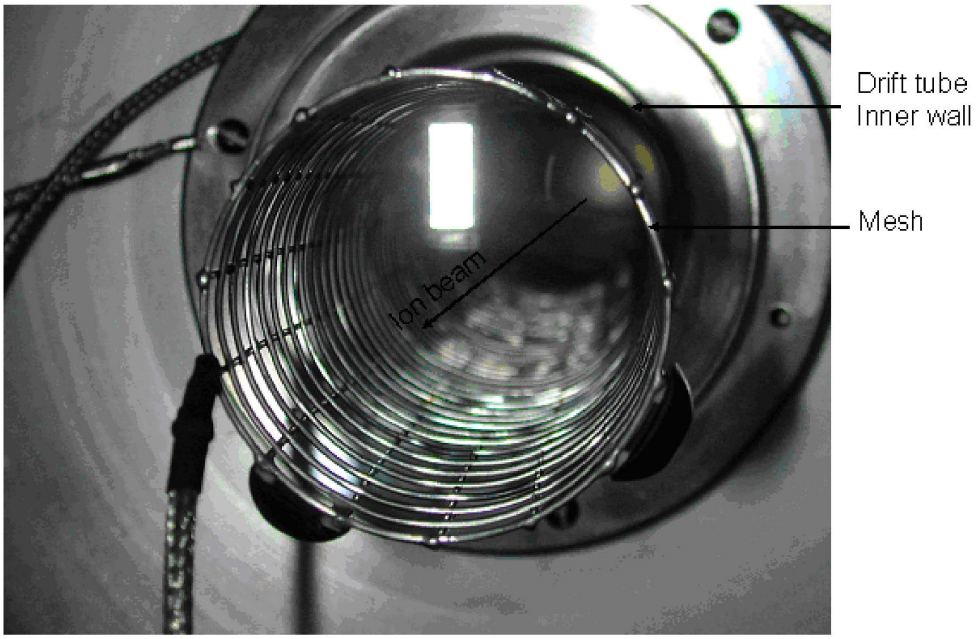

Figure 5-15: Cylindrical metal mesh of outer diameter 6.3 cm is installed inside a 7.6 cm diameter beam drift tube.

from the beam tube wall.

Figure 5-16 shows the measured beam parameters for varying mesh bias. In Figure 5-16(a), the lower line with solid circles shows that a beam diameter of 2.4 cm is measured with 0 V across the mesh bias for 255-keV beam energy. A beam diameter of roughly 3.75 cm is also measured by applying ± 500 V across the mesh for the same beam energy, shown by lines of solid diamonds and cross symbols, respectively. The line with hollow circles shows a measured beam diameter of 3.75 cm using a mesh bias of +250 V. A larger beam diameter of 4 cm is measured with a mesh bias of ± 1 keV for the same 255-keV beam energy, as shown by lines of hollow diamond and solid triangle symbols in the figure. The positive 250 V bias on the mesh provides a smooth trend of beam shape, regardless of beam energies in the range of 245 to 300 keV. Beam diameter measurement by varying beam energies is performed in a 15 cm diameter vacuum tube separately, where the possibility of a wall-electron effect is negligible. There is no mesh or plasma inside the tube that could influence the

measurements of ion beam transport in vacuum conditions. Figure 5-16(c) shows a comparison of beam diameters for transport through the 7.6 cm diameter tube with the mesh inserted with a bias of +250 V, and the 15-cm diameter vacuum tube. The dotted lines with hollow circles and triangles represent beam diameters that are measured in the x and y axis, respectively, for a beam of energies 240 to 310 keV transported through the 15-cm diameter tube. Diameters of 4.53 cm, 4.0 cm, and 2.68 cm are measured in the x-axis for the beam of energies 259 keV, 268 keV and 298 keV, respectively. On the other hand, the lines with solid circles and triangles represent beam diameters that are measured in the x and y axis, respectively, for a beam of energies 244 keV to 290 keV transported through the 7.6 cm diameter tube. Beam diameters of 3.76 cm, 3.15 cm, and 2.41 cm are measured in the x-axis for the beam of 255 keV, 268 keV and 287 keV, respectively. These are the end-to-end measurements of a beam image, without the deduction of any cut off value that is used for statistical error reduction in Section 5.3.2. For a 255-keV beam, a difference of 6 mm in beam diameter is measured between the two cases. This difference is smaller for a more energetic beam. For example, for a 288-keV beam, a difference of 2 mm in diameter is measured for the two cases. For a higher energy beam (say 300 keV), the radial distance of the beam from the wall is larger than the lower energy beam (255 keV) and neutralization is insignificant. By using the mesh and an appropriate voltage across it, we still achieve a slightly smaller size than "expected" for an un-neutralized beam. The difference in the two cases, as we inferred, is due to the fact that the 58.2 cm mesh liner in the 7.6 cm diameter tube is not long enough to cover the entire 1-m long drift tube. As a result, partial neutralization occurrs beyond the ends of the mesh. However, the mesh is a significant development in overcoming uncontrolled neutralization of wall electrons.

Currents corresponding to positive and negative voltages across the mesh are measured during the 255 keV beam pulse. Figure 5-17 shows the experimental data

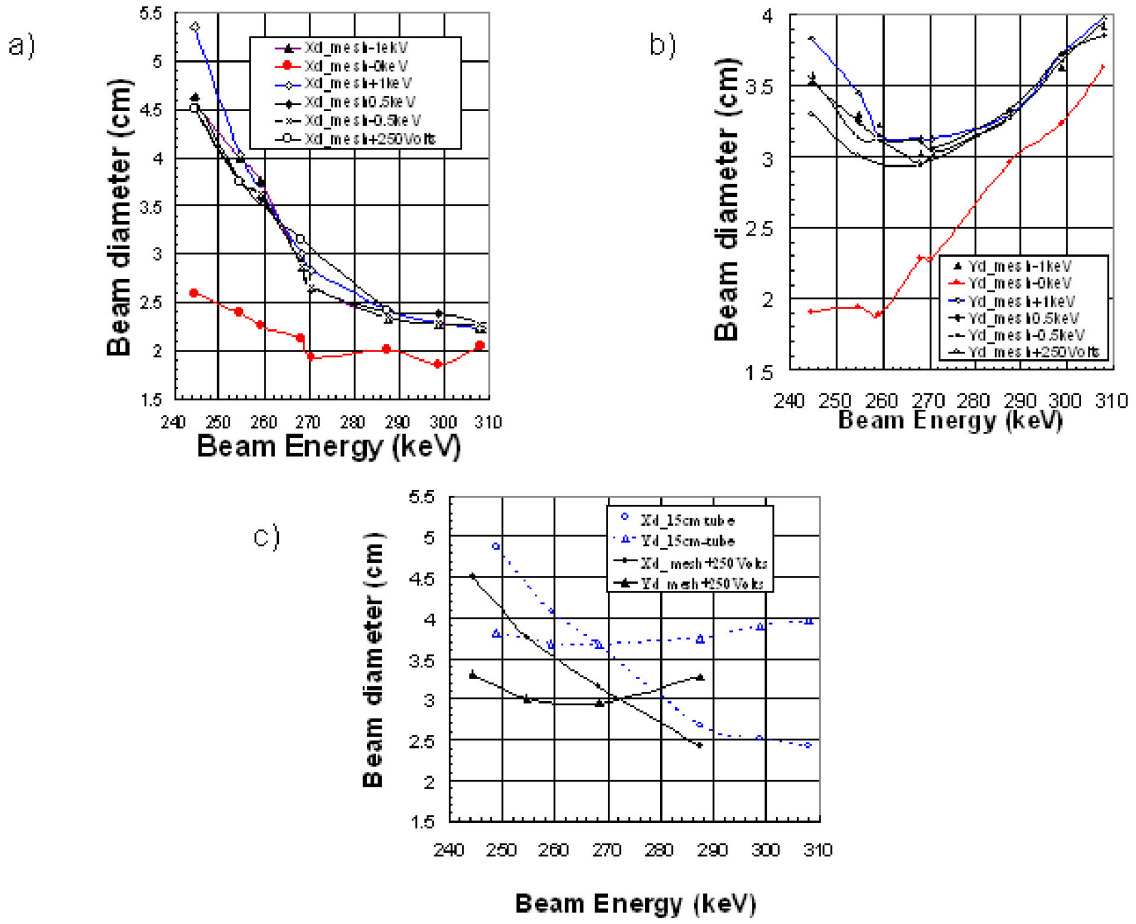

Figure 5-16: Beam diameters corresponding to beam energies as measured in the (a) x-axis and (b) y-axis by varying mesh bias, and (c) a comparison of beam size for a 255-keV beam transported through a 15-cm tube (dotted lines for the x-y axis) and a mesh included 7.6 cm diameter tube (solid lines for the x-y axis) with bias 250 V.

of currents measured in the mesh. A negative current of 6.56 mA is measured at a zero potential across the mesh, which shows that secondary or wall electrons movement is present and only those electrons which directly strike the mesh wire are measured with uncollected electrons remaining around the mesh. A positive 50 V potential is applied across the mesh to collect these all electrons, a current of negative 30.72 mA is measured. Voltages such as negative 250 V and negative 500 V are also applied to the mesh; however, no significant current is measured in these cases. It is inferred that a higher negative potential, like negative 250 V, across the mesh is able to completely stop radial inward and outward motion of electrons, but leaving uncollected electrons. Therefore, collection of all the electrons around the mesh, using a +50 V potential, is a better choice. However, the presence of a higher mesh bias has some effect on the physics of plasma neutralization. For a positive potential, plasma electrons initially accelerated up to the beam velocity as they leave the plasma, are then accelerated up to an energy corresponding the mesh bias. The quiescent co-moving plasma electrons now have a velocity many times that of the beam. As the mesh potential increases, these electrons become inefficient at neutralizing the beam potential and a larger beam focal spot is expected. For a negative potential, the plasma plug electrons are largely excluded from the beam in the region of the mesh yielding no neutralization.

Figure 5-18 shows the measured beam profiles for seven values of energy between 240 and 310 keV, measured 1 m downstream from the exit of the final-focus system. The corresponding profiles from the WARP simulations are also displayed in the figure, and we find good qualitative agreement with the measured profiles. The experimental results are obtained using a sufficiently large beam pipe (15 cm diameter) for final transport to ensure that electron emission from the walls is negligible and a 7.6-cm diameter pipe corresponding to the actual neutralized drift section containing the MEVVA plasma plug system. With the nominal 7-cm diameter beam pipe, the spot sizes initially measured are significantly smaller, due to the capture of free

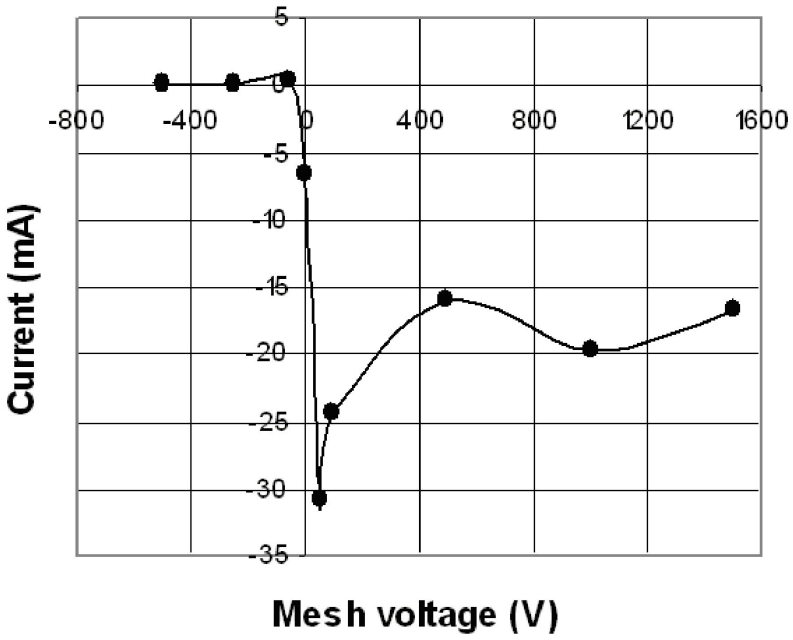

Figure 5-17: Current in the mesh as the mesh bias is varied during a 255-keV beam pulse.

electrons from the wall. This anomalous behavior, however, disappeared when the walls are screened by a negatively charged mesh that trapped these electrons. These profiles show that by using the mesh bias, the measured beam profiles are in general agreement with the WARP calculations for vacuum transport.

5.3.2 Neutralized transport

Non-neutralized and neutralized beams are monitored at the end of a 1 m long neutralization drift section on a glass or ceramic (96% alumina) scintillator. Charge neutralization of this scintillator is provided by a high-transparency (80–90% transmission) metallic mesh placed on or near the surface of the scintillator. By applying a negative bias to the mesh, stray external electrons are decelerated and deflected away from the scintillator, limiting their contribution to the optical image to negligible levels. Time-resolved beam-induced images on the scintillator screen are captured with a Roper Scientific gated intensified CCD camera viewing the scintillator through a

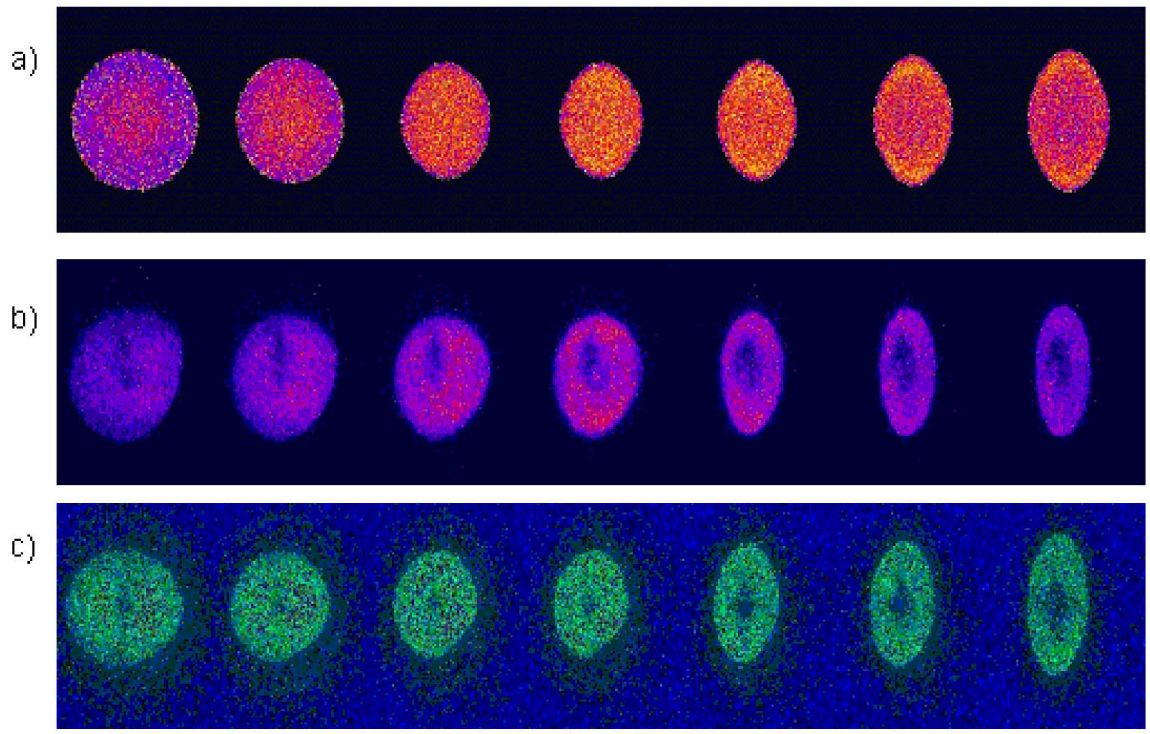

Figure 5-18: Beam profiles for vacuum transport as function of increasing energy (240 keV to 310 keV) from (a) WARP calculations (b) experimental measurements for transport through a 15 cm diameter tube, and (c) experimental measurements for transport through a 7.6 cm diameter tube using mesh bias of +1 keV.

vacuum window, and images are processed using the public-domain program ImageJ.

The low emittance ($\varepsilon \sim 30\pi-$mm-mr) of the beam at the entrance to the neutralization region allows the beam to be focused to a small spot size of 1–2 mm radius at the focal point for neutralized ballistic transport. Figure 5-19 shows beam images of a neutralization experiment: (a) non neutralized, (b) plasma plug, i.e. MEVVA-plasma-neutralized, and (c) plasma plug and RF volume plasma neutralized. A size of 27 mm at Full-Width-Half-Maximum (FWHM) is measured for a non-neutralized condition. The beam radius of 14.7 mm in Figure 5-19(a) is measured using 1/e lower cutoff statistical deduction from the peak fluence of beam imaged with ImageJ. A size of 2.83 mm at FWHM is measured for the MEVVA plug neutralization and its radius of 1.6 mm is measured using the same method. A spot size of 2.14 mm at FWHM and 1.3 mm neutralized beam radius are measured for MEVVA plug and volume plasma neutralization. A better-than-90% beam size reduction is measured using plasma sources. Neutralization with a lower perveance, 6 mA beam current using 1 cm aperture instead of 2 cm diameter aperture, is also performed.

LSP simulations of NTX including plasma plug and volumetric neutralization are performed starting from beam initial conditions at the entrance to the neutralization region. In one series of LSP simulations, shown in Figure 5-20, the initial condition is the final phase-space distribution as calculated by WARP for the transport of the NTX beam from the gun to the exit of the final focus system.

There is qualitative agreement with measured spot sizes, but a detailed measurement of the 4-D phase-space distribution at the exit of the final-focus section is essential in order to initialize more realistic simulations of NTX neutralized beam transport. Figure 5-21(a) shows beam images of experimental data for plasma plug neutralized (Column 1), plasma plug and RF volume plasma neutralized (Column 2), and complete neutralized using 4D phase space from pinhole scan (Column 3). Notice that Column 3 shows the "experimental fully neutralized transport" using the

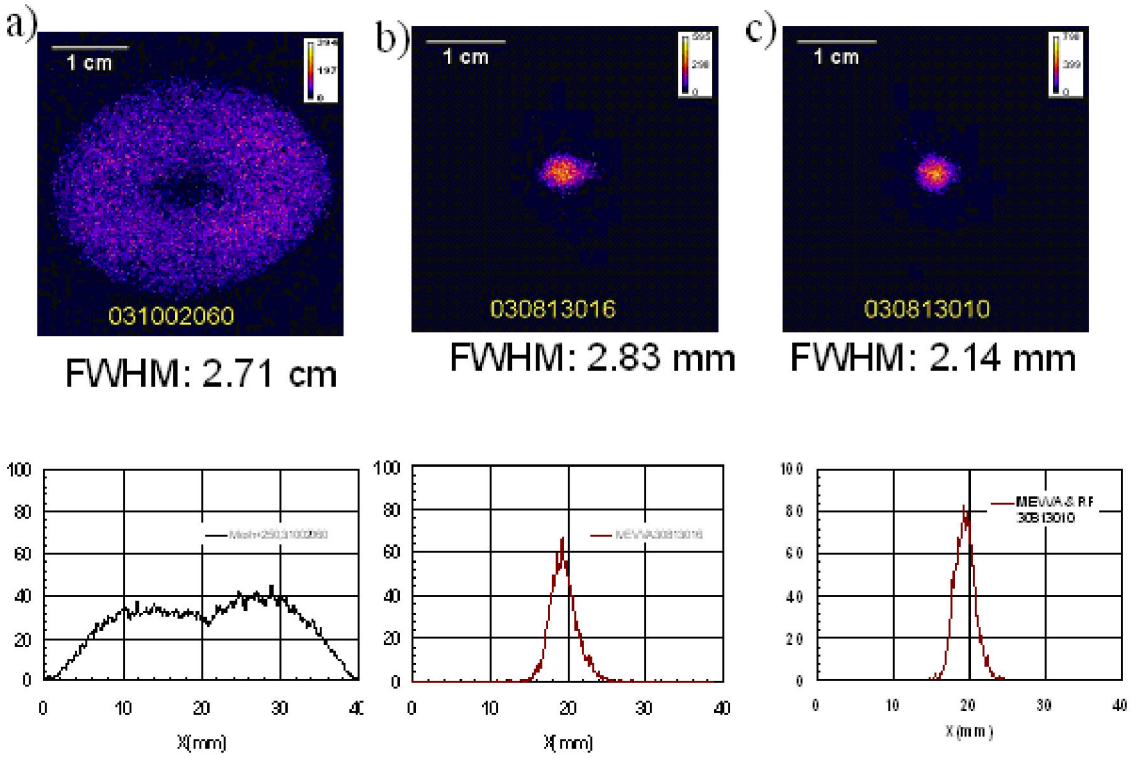

Figure 5-19: NTX spot-size dependence on the neutralization mechanisms. Beam images (top row) and density distribution (bottom row) at the focal plane for three cases of space-charge neutralization for a high perveance (6×10^{-4}) 24 mA, 254 keV K^+ ion beam: a) non-neutralized, b) plasma plug neutralized, and c) plasma plug and RF volume plasma neutralized.

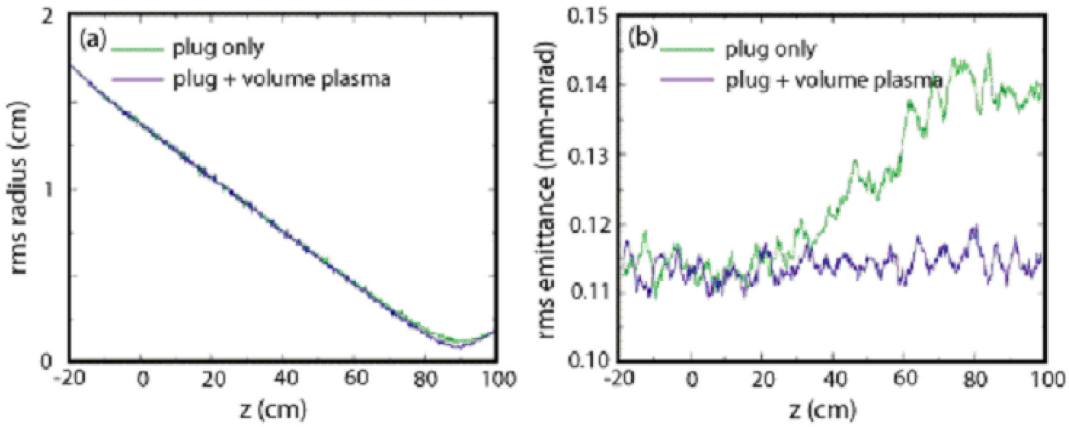

Figure 5-20: Calculated (a) radius and (b) emittance of NTX beam from the WARP-LSP simulations of neutralization by a plasma plug alone and combined with a volume plasma near the focal point. The rms focal-spot radius is 1.3 mm with the plug only and 0.9 mm with both plasmas.

"analog simulation" as discussed in Section 5.3.3. Figure 5-21(b) shows the numerical simulations of all of these cases. Results of 2 different aperture cases (24 mA, and 6 mA) show that neutralized beam sizes did vary significantly with variable perveance.

Although the experimental focal-spot size and shape agree qualitatively with the corresponding simulation results, a careful comparison of the radial density profiles shows qualitative differences. Figure 5-22 shows a comparison of profiles at the nominal focal point, 1 m beyond the last final-focus magnet. The experimental profile is hollow, and there is substantial charge in a halo extending well beyond the calculated 1.5-cm beam edge. In contrast, the LSP simulation gives a profile with negligible halo and a broad density peak at the beam center, providing that we ignore the statistically insignificant values within a 1-mm radius. The calculation uses the same initial emittance, radius, and convergence angle as the experiment, but it is idealized in assuming axisymmetry, neglecting interactions with the background gas, and specifying an initially Gaussian velocity distribution.

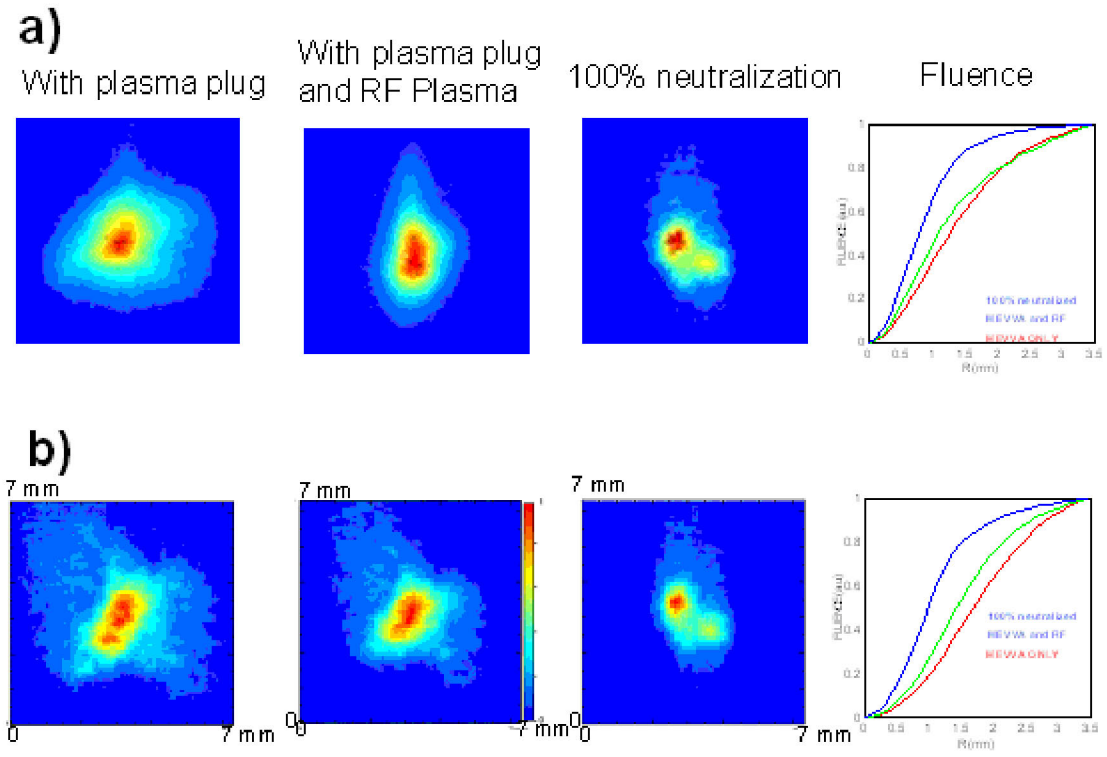

Figure 5-21: Comparison of experimental (top) and numerical (bottom) results of the NTX spot-size dependence on the neutralization mechanisms.

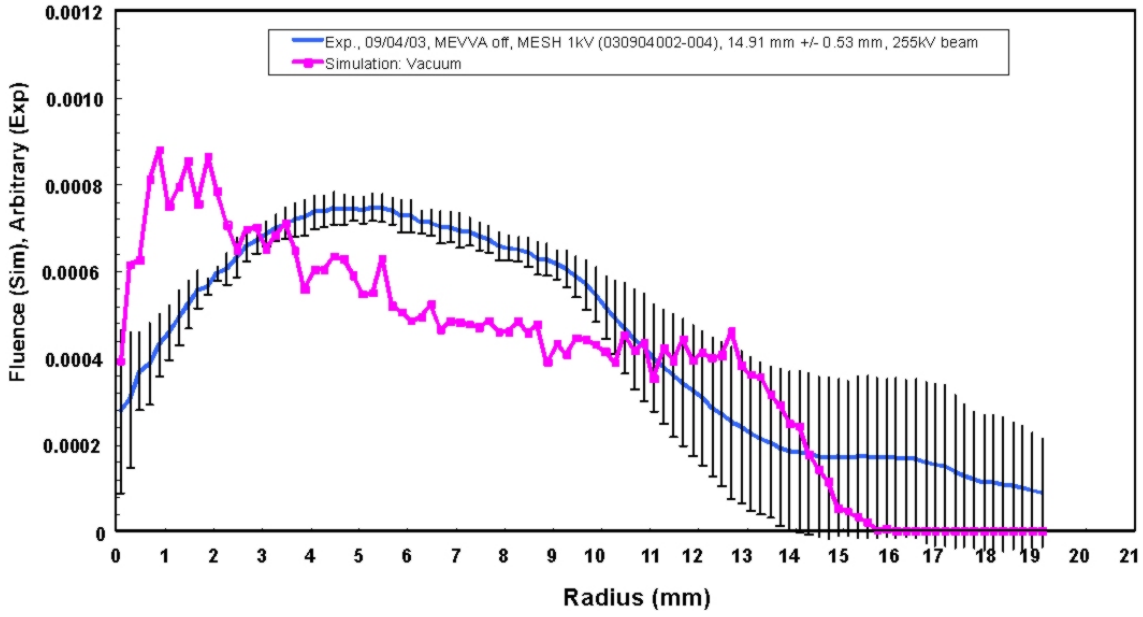

Figure 5-22: Comparison of a radial density profile from an unneutralized NTX shot with a theoretical profile (magenta) from an LSP simulation.

5.3.2.1 Beam current

The beam current is measured at the entrance and at the exit of the final transport system with and without a plasma. It is measured using a Faraday cup; the cup is biased with a +500 V and its internal guard ring is biased with a negative 900 V. An electron trap is installed in front of the Faraday cup. Figure 5-23 shows beam current as a function of energy for beam traveling through the neutralization drift section. All measurements overlap with each other and show 100% beam current transport in the system. There is no significant beam loss in the drift section, and full beam current is transported with and without neutralization.

5.3.2.2 Beam focal plane

Variation of the neutralized beam radius with axial position is measured at the diagnostic box by varying the scintillator position over a range of 15 cm around the

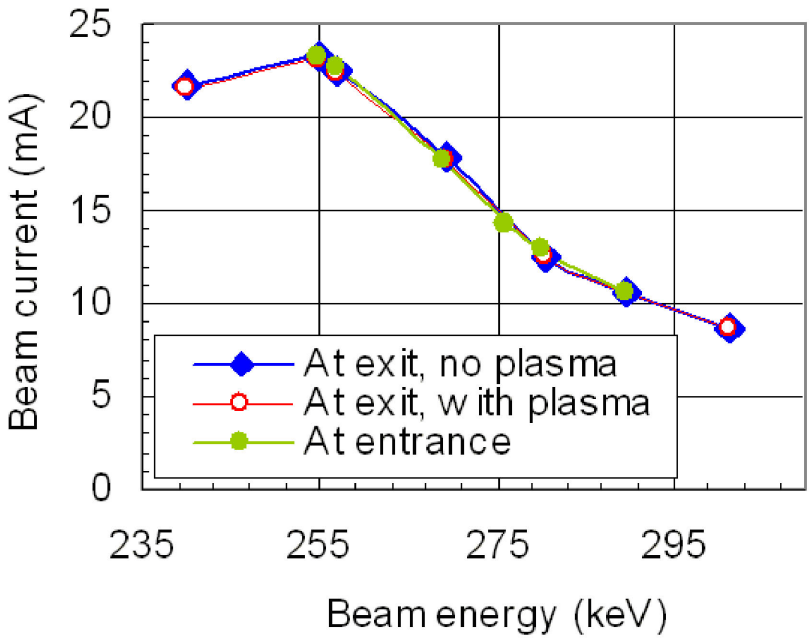

Figure 5-23: Measured beam current. The solid circles represent the currents measured at the entrance of the 1m final transport section; the solid diamonds represent the currents measured at the end of the 1m drift section; and the hollow circles represent the currents measured when beam is neutralized using the MEVVA plasma plug.

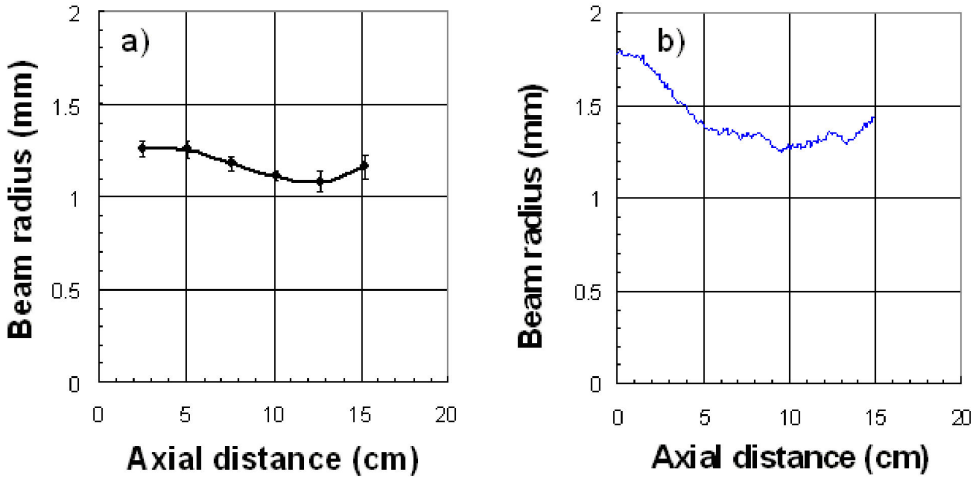

Figure 5-24: Axial beam envelope variations in (a) 7.6cm drift tube (mesh with +250 V bias), and (b) theoretical calculation (without mesh).

predicted focal plane. Figure 5-24 shows the axial beam envelope variations in (a) experiment using the electron supressor mesh with a +250 V bias inside the 7.6 cm drift tube, and (b) theoretical calculation using LSP. Though the discrepancy in beam radius is less than a millimeter, this difference might be due to the absence of mesh in the calculation.

5.3.2.3 Energy dependence and head-to-tail variation

The sensitivity of beam optics to small changes in beam energy is evaluated by measuring the beam size as the energy is varied for a given beam slice (Figure 5-25). We have observed that energy variations of 1% led to reduction of current density by 50%. This experimental result is consistent with numerical simulations.

The beam pattern of the neutralized NTX beam from head-to-tail is also measured by varying the time delay of the image recording system (Figures 5-26 and 5-27). To ascertain the head to tail variation of the pulse, a 255-keV beam is transported through a mesh-less 7.6 cm diameter tube through plasma produced with a 2-keV discharge potential. Time slices of 100-ns width are recorded with delays between 4.6 μsec and

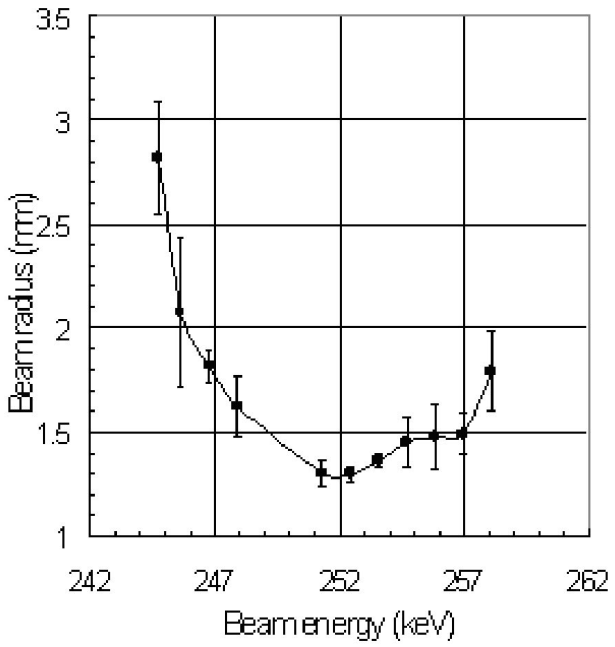

Figure 5-25: Spot size as a function of energy as measured in NTX.

12.8 μsec in intervals of 0.2 μsec. It is observed that the beam head and tail have halos. We infer that the longitudinal forces due to beam space charge increase the velocity of the beam head but slow down the beam tail. Although the beam radius is flat for a time delay of 6 μsec to 11 μsec, closer examination shows that the beam radius variation is of order 0.2 mm; this might be due to shot–to–shot variations of the Marx voltage, or variations of charge accumulation in the capacitor tank of the high voltage system of the MEVVA plasma plug.

5.3.2.4 Spot size dependence on plasma parameters

A series of idealized axisymmetric LSP simulations indicates that plasma neutralization should be fairly insensitive to variations in plasma parameters. These simulations use an idealized Gaussian velocity distribution, with the same emittance used above. A comparison between experiment and theory of the radial distribution profile at focus is shown in Figure 5-28. The basic size of the beam spot is similar in both

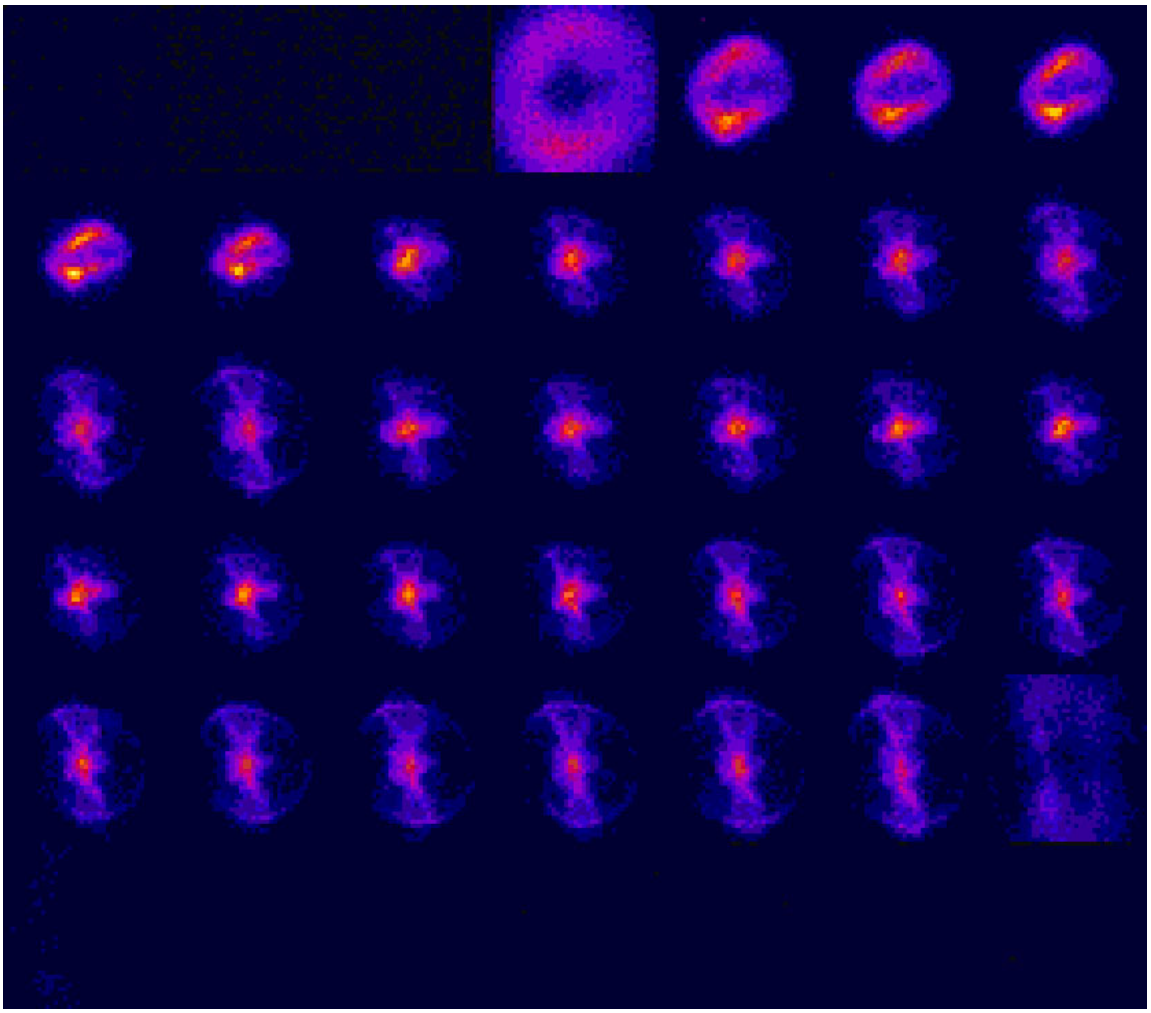

Figure 5-26: Beam images from head-to-tail taken at the focal plane, showing blow up of the beam head and tail.

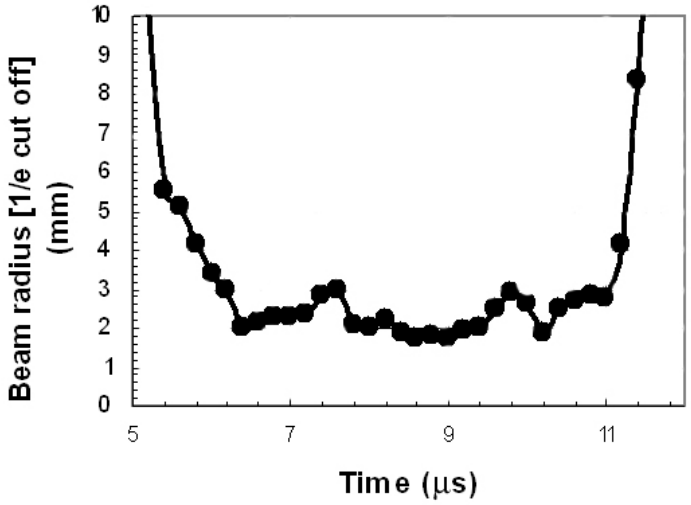

Figure 5-27: Spot size variation from head-to-tail measured at the focal plane, showing blow up of the beam head and tail.

cases with differences attributed to a halo due to nonlinear focusing seen in the experimental curve. Simulations show that if electrical connection is maintained to the chamber wall through electron SCLE, the beam spot shows little variation for plasma densities ranging from 3×10^8–$3 \times 10^{10}\, cm^{-3}$ for an initial plasma temperature of 3 eV. Without electron emission from the wall, the plasma plug charged up due to loss of electrons and the spot size degraded in time, particularly for smaller plasma densities. For a 6-eV initial plasma temperature, which is greater than $\frac{1}{2} m_e v_i^2$, the beam spot size is roughly 50% larger than the case with a 3-eV plasma. The sensitivity of the beam spot to the incoming beam emittance is calculated to be weak, with only a 30% spot-size variation for a factor-of-three change in emittance. This low sensitivity to emittance indicates that charge neutralization in the NTX experiment should be quite close to the 96% value seen in simulations and should not be influenced by details in the emittance.

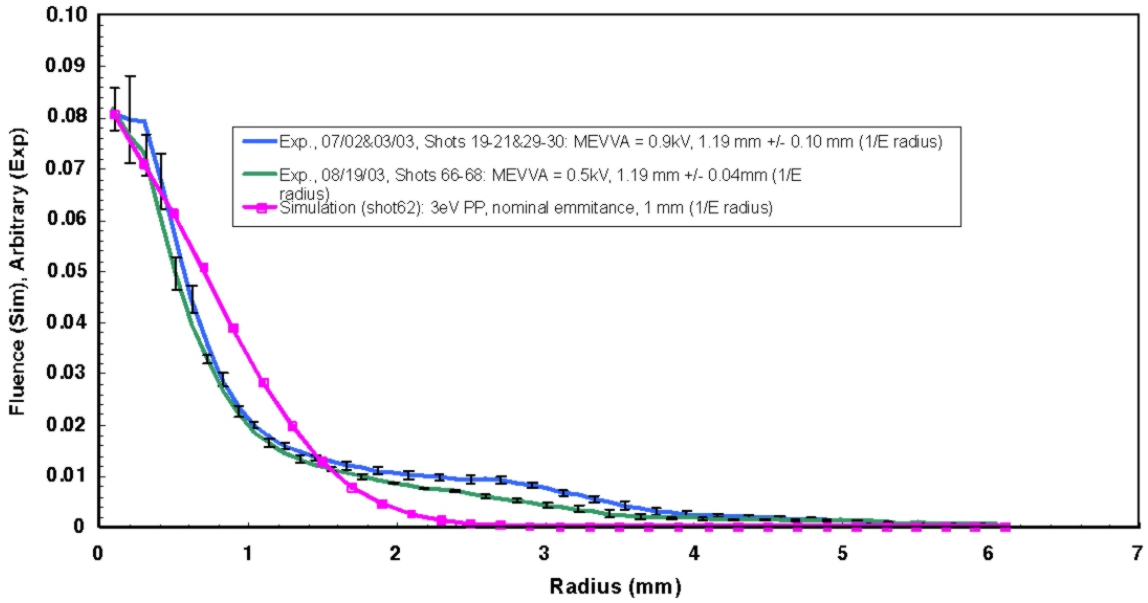

Figure 5-28: Comparison of radial density profiles from two plasma-neutralized NTX shots with a theoretical profile (magenta) from an LSP simulation.

The neutralized beam radius is also measured as a function of the MEVVA plasma discharge voltage. Figure 5-29 shows (a) beam radius vs. plasma discharge voltage, and (b) comparison between the experiment and LSP simulations of the radial distribution profile. The basic size of the beam spot is similar in both cases (experiments and theory) with differences attributed to a halo due to nonlinear focusing seen in the experimental curve. Simulations show that if electrical connection is maintained to the pipe wall through electron space-charge-limited emission (SCLE), the beam spot shows little variation for plasma densities ranging from 3×10^8–$3 \times 10^{10}\, cm^{-3}$ for an initial plasma temperature of 3-eV. For a 6-eV initial plasma temperature, which is greater than $\frac{1}{2} m_e v_i^2$, the beam spot size is roughly 50% larger than the case with 3-eV plasma (Figure 5-29a). The sensitivity of the beam spot to incoming beam emittance is calculated to be weak with only a 30% spot-size variation for a factor of three change in emittance. This low sensitivity to emittance indicates that charge neutralization in the NTX experiment is close to that 96% value seen in simulations, and thereby is not influenced by details in the emittance.

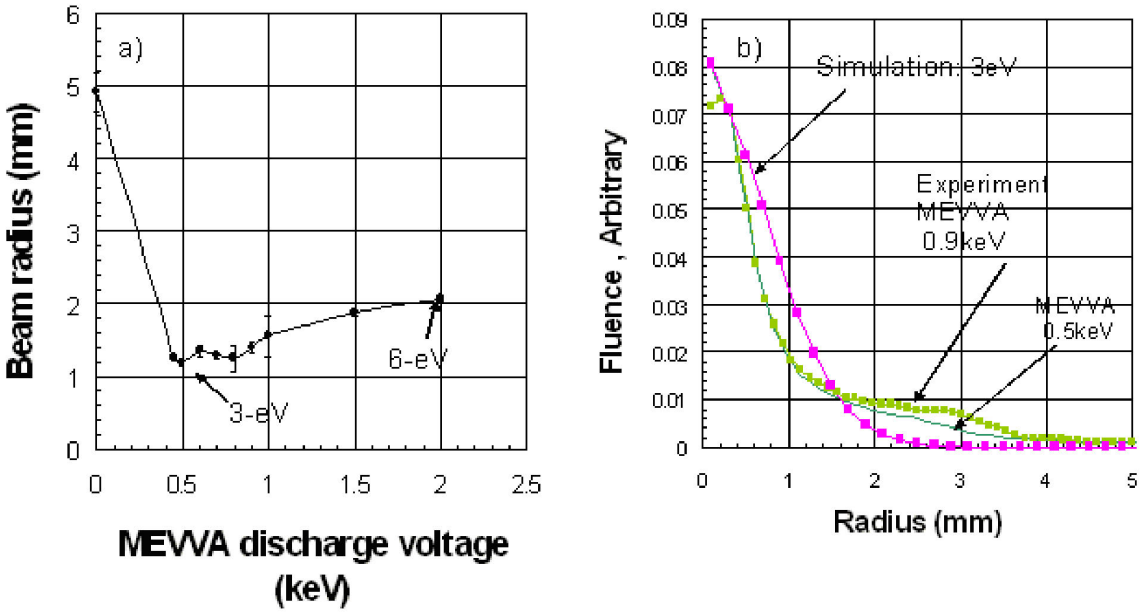

Figure 5-29: (a) Neutralized beam radius vs. plasma discharge voltage, and (b) comparison between experimental and theoretical radial distribution profiles.

5.3.2.5 Geometric aberrations

The goal of a final focus experiment is to obtain the minimal spot radius. Eq. (4.2) suggests that one could reduce the spot size by increasing the convergence angle, provided that the emittance is not significantly increased. In general, as the angle is increased, the beam envelope goes through larger excursions in the magnetic lattice, which in turn leads to increase in emittance through higher order (particularly third order) aberrations. The distortion of phase space due to geometric aberrations has been studied numerically. In our experiment, we see the same phase-space distortions, leading to increased spot size with large angles. Both code and experiment predict minimum spot radius at ~15 mrad (Figure 5-30). Eq. (4.6) predicts a monotonically increasing spot size as the convergence angle is varied. In the experiments, however, the results are complicated by non optimal entrance conditions from the apertured source which is the same for the different magnet tunes. In fact, for the NTX lattice and fixed entrance conditions, the emittance growth along the lattice may be larger

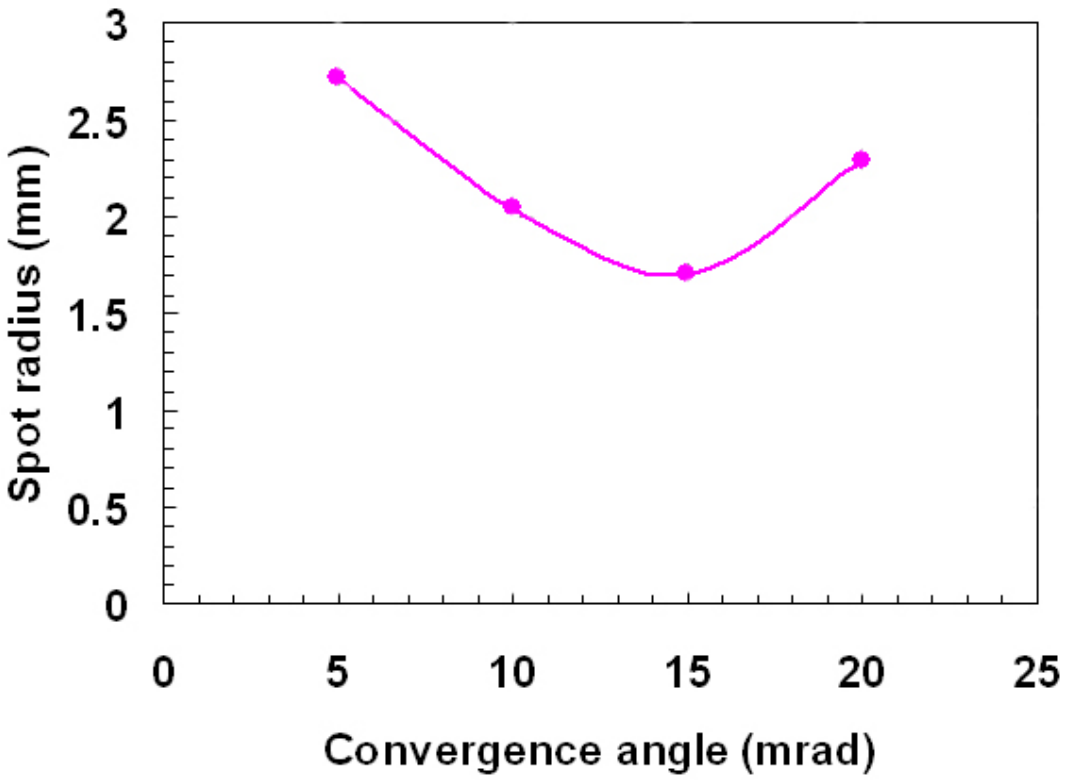

Figure 5-30: Spot size as function of convergence angle as measured in NTX.

for smaller convergence angles.

5.3.2.6 Spot size dependence on perveance.

Finally, we consider variations of perveance. In general, we expect the geometric aberrations to be less significant for lower perveance beams. This is true if the final focus lattice is matched to the beam perveance; it is always possible to design a final focus system for a lower perveance beam that will be less affected by geometric aberrations. The NTX lattice is designed for the 25 mA potassium beam at 300 keV, with perveance Q $\sim$ 0.0006.

Figure 5-31 shows the spot size dependence on perveance by comparing the beam images at the focal plane for a 264 keV beam that has been apertured to 25 mA and 6 mA, respectively, and that are transported through the final focus system using the

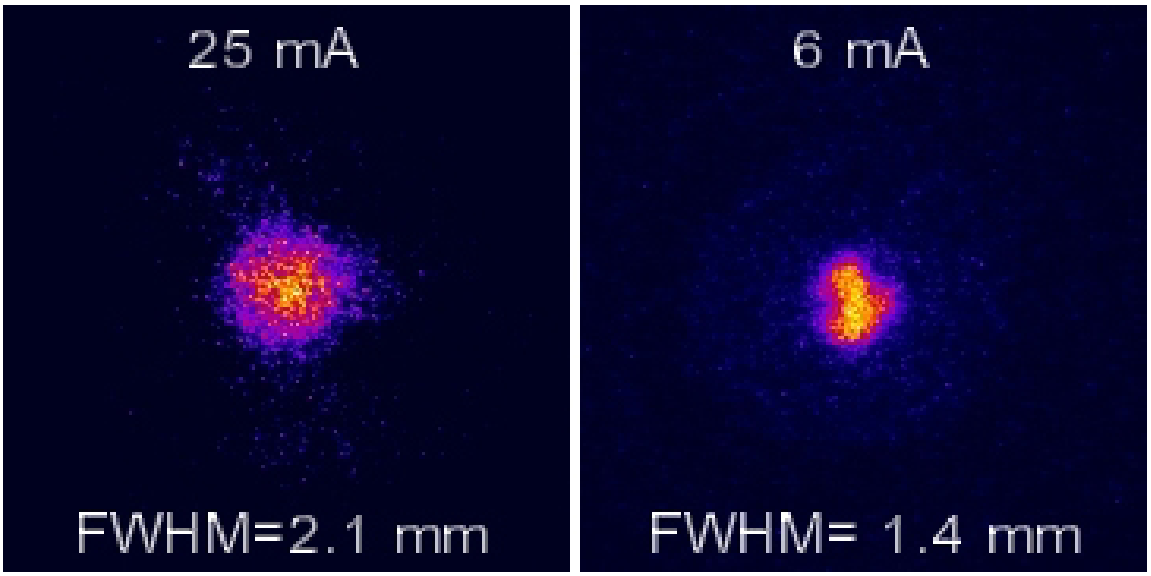

Figure 5-31: Spot size dependence on perveance as measured in NTX.

same quadrupole fields. There is a large reduction in spot size for the lower perveance beam.

It is important to point out that the low emittance ($\sim 25\pi$-mm-mr unnormalized) of the beam at the entrance to the neutralized region allows for the beam to be focused to a small spot size (1–2 mm radius) at the focal plane for neutralized ballistic transport. Furthermore, Faraday cup measurements of the beam current at entrance and exit of the final focus system have shown negligible beam loss along the transport channel.

5.3.3 "Analog simulation" of fully neutralized beam transport

As discussed in Section 2.4.2, we have developed an optical technique to measure the 4-D phase-space distribution of the beam. The phase space distribution $f(x, y, x', y')$ will be measured by scanning the beam with a 0.5-mm diameter pinhole and letting the transmitted beamlet travel about 1 m before striking the scintillator. The pinhole position defines the coordinates x and y, and from the image, we can extract the density distribution of x' and y'. This technique is used to measure the detailed

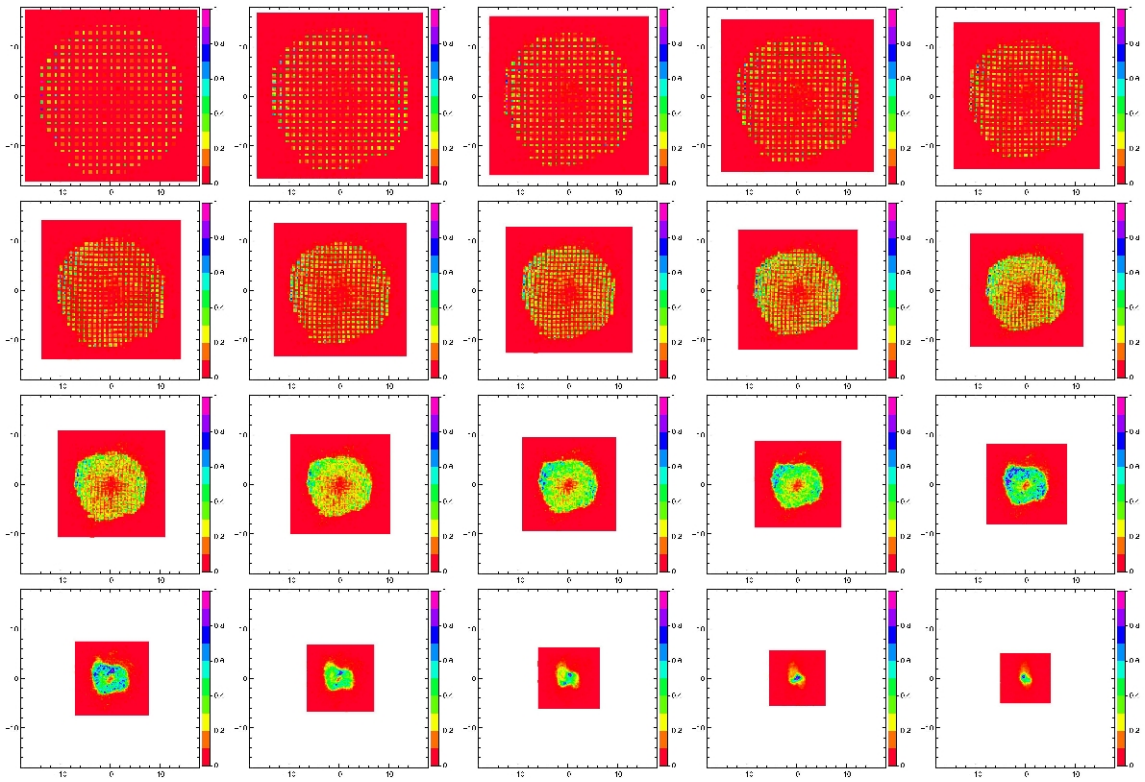

Figure 5-32: Ballistic propagation of the fully neutralized NTX beam by propagating the 4-D phase space down to the focal plane. Images from top left to bottom right correspond to beam profile at 5 cm steps starting from the pinhole plane and ending at the focal plane.

structure of the phase space distribution.

The same diagnostic system can be used to simulate the effect of full neutralization on a beam, since each beamlet going through a pinhole only carries the information about the phase space distribution at a given location without being perturbed by the space charge of the full beam. The superposition of all pinhole images at a given location can be compared with a beam-transport calculation where the space charge is turned off from the pinhole-scan plane to the focal plane (Figure 5-32).

A comparison between this analog simulation and a WARP run with the space-charge field artificially suppressed is shown in Figure 5-33. The agreement of the focal-spot radius is seen to be excellent, despite differences in azimuthal structure. This agreement indicates that the NTX emittance is low enough after focusing to

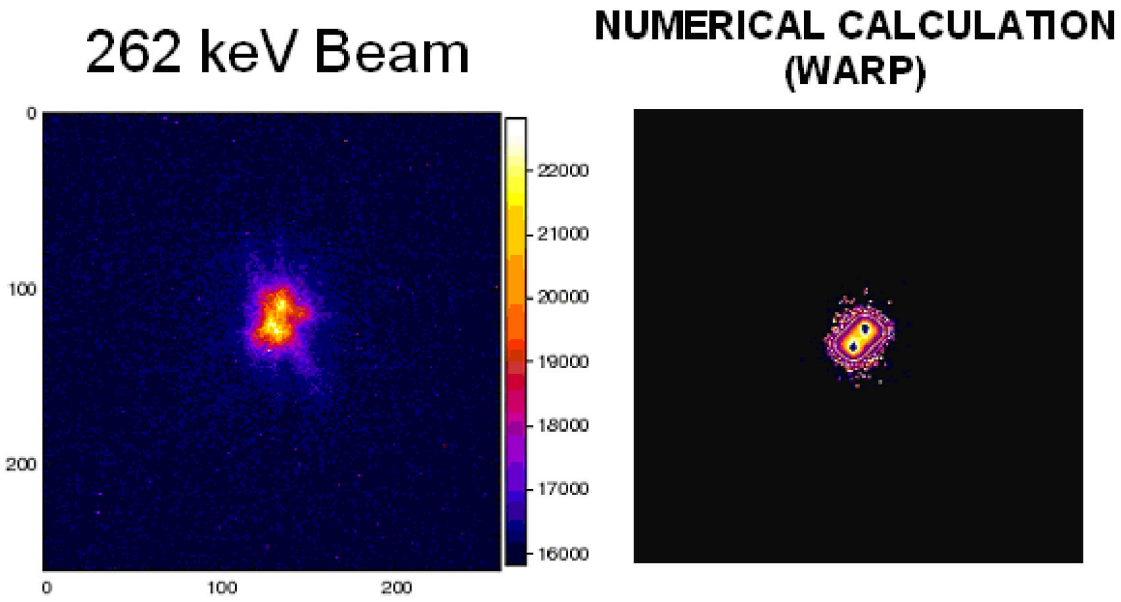

Figure 5-33: Analog (pinhole) simulation (left) and WARP calculation (right) of fully neutralized NTX beam focused to a small spot. Each image box is a 4-cm by 4-cm square.

produce a focal spot of about 1 mm radius, given adequate neutralization.

THIS PAGE INTENTIONALLY LEFT BLANK

Chapter 6

Conclusions

6.1 Summary

The Neutralized Transport Experiment at LBNL provided the first experimental validation of neutralized ballistic transport of a space-charge-dominated beam. Although the experiment used a beam that is orders of magnitude lower in current than a driver for heavy-ion fusion, a careful choice of parameters guarantees that the transport physics closely matches that of a full-scale system. We produced a very small focal spot at the end of an integrated beam system consisting of a high brightness injector, a quadrupole focusing system, and a final neutralized drift section. Using a novel beam aperturing technique we were able to produce a very high brightness ion beam from conventional alumino silicate ion source. The physics of beam transport through a magnetic quadrupole system was studied, and we demostrated excellent agreement between simulations and experiment over a broad parameter regime. The neutralized drift experiments demonstrated dramatically improved focusing by passing the beam through a low-density "plasma plug" produced by a metal-arc source, and a second "volume plasma" near the beam waist. Detailed end–to–end simulations were carried out in parallel with the experiments, and careful comparisons of the experimental

findings with the results of numerical simulations were presented.

The key question of a final focus experiment is what determines the spot size. We showed from both theory and experiment how to prepare the beam envelope for final neutralized drift. We also studied the effects of beam energy variations and demonstrated the importance of head-to-tail energy uniformity. We studied the higher order aberrations, in particular the geometric aberrations and their effects on the spot size. Finally, we considered the dependence of spot size on perveance. Overall, the comparisons between theory and experiment were very good.

In parallel to the transport experiments, two new diagnostic tools were developed. The first, a refinement of the conventional pepper-pot imaging technique, gave a detailed time-resolved view of the 4-D transverse phase space for beams that have good pulse-to-pulse reproducibility. Using this technique to map the 4-D phase-space distribution at the exit of the NTX final-focus system provided the initial conditions for more realistic simulations of the neutralized-transport experiments. The other tool was a non-intercepting diagnostic that uses a low-energy electron beam directed across the NTX beam line to map out the transverse charge distribution of the ion beam. Both diagnostic techniques provided new information about the structure of the NTX beam and facilitated our understanding of neutralization physics.

We discussed some possible factors in the experiment which are not included in the theory, and an attempt to resolve these issues experimentally. In terms of future experimental work, the most important task is an in-situ measurement of the magnetic field, including all the eddy current effects of the pipe and flanges. One additional unexplained observation has to do with halos in both configuration and velocity space. We presented two examples in Figure 4-22 and Figure 4-23, respectively. Numerical simulations have not been able to account for these halos thus far, and will be the subject of future studies.

While we still have a couple of puzzles to resolve, we believe that much has been learned about the final focus magnetic system relevant for a HIF driver. The questions of how to control energy sweep, design constraints on aberrations and perveance, are now much better understood as a result of this work. In particular, we have demonstrated that the close coupling between theory and experiment offers an extremely powerful approach to the study of an integrated beam system.

6.2 Follow-on Experiments and Future research directions

Since the completion of the work associated with this thesis, we have resolved the halo puzzle. The beam halos were traceable to the imperfections of the NTX source, occurring in the detailed geometry of the emitter and the anode shroud. The halo resulting from the imperfections was directly measured at the source exit, which agreed with numerical simulations.

The issue of the calibration of energy and magnetic field has also been resolved. It turned out that the pulsed magnetic field inside the vacuum pipe is reduced by skin-depth effects in the thin stainless vacuum tube. There is also a phase shift between the field in air versus in vacuum. The measured magnetic field reduction is sufficient to account for the energy calibration discrepancy described earlier.

In addition to the transverse beam compression demonstrated in the present work, we have also completed an experiment in longitudinal beam compression in the presence of plasma. Longitudinal compression in excess of a factor of 50 was demonstrated [68].

In the future, we plan to perform experiments to demonstrate simultaneous transverse and longitudinal focusing. The resulting compressed beam will be used for HEDP studies and ultimately for HIF applications.

THIS PAGE INTENTIONALLY LEFT BLANK

Chapter 7

References

[0]

[1] R. Bangerter, W.B. Herrmannsfeldt, D. Judd, L. Smith, ed's, *ERDA Summer Study of Heavy Ions for Inertial Fusion*, LBL-5543 (1976)

[2] Committee on High Energy Density Plasma Physics, National Research Council of the National Academies, *Frontiers in High Energy Density Physics*, The National Academies Press, Washington, D.C. 2003.

[3] Committee on the Physics of the Universe, National Research Council of the National Academies, *Connecting Quarks with the Cosmos: Eleven Science Questions for the New Century*, The National Academies Press, Washington, D.C. 2003.

[4] M.A. Leitner, et al., *Options for integrated beam experiments for inertial fusion energy and high-energy density physics research*, Nuclear Instruments and Methods in Physics research, A 544 (2005), pp. 315-323.

[5] S.S.Yu, et al., *Heavy Ion Fusion (HIF) driver point designs*, Nuclear Instruments and Methods in Physics research, A 544 (2005), pp. 294-299.

[6] M.A. Leitner, C.M. Celata, E.P. Lee, B.G. Logan, G. Sabbi, W.L. Waldron, and J.J. Barnard, *Design choices for the integrated beam experiment (IBX)*, (May 1, 2003). Lawrence Berkeley National Laboratory. Paper LBNL-51799.

[7] R. H. Cohen1, A. Friedman, S. M. Lund, A. W. Molvik, E. P. Lee, T. Azevedo, J.-L. Vay, P. Stoltz, and S. Veitzer, *Electron-cloud simulation and theory for high-current heavy-ion beams*, Phys. Rev. ST Accel. Beams 7, 124201 (2004).

[8] E. Henestroza et al., *Design and characterization of a neutralized-transport experiment for heavy-ion fusion*, Physical Review: Special Topics Accelerators and Beams, 7, 083501 (2004).

[9] P. K. Roy, S. S. Yu, E. Henestroza, A. Anders, F. M. Bieniosek, J. Coleman, S. Eylon, W. G. Greenway, M. Leitner, B. G. Logan and W. L. Waldron, D. R. Welch and C. Thoma, A. B. Sefkow, E. P. Gilson, P. C. Efthimion and R. C. Davidson, *Drift compression of an intense neutralized ion beam*, Physical Review Letters Vol. 95, (2005), pp. 234801.

[10] J.W. Kwan, et al., *Production of a high-brightness beam from a large surface source*, Nuclear Instruments and Methods in Physics research, A 544 (2005), pp. 430-435.

[11] E. Henestroza, C. Peters, S. S. Yu, D.P. Grote, R.J. Briggs, *Extraction Compression and Acceleration of High Line Charge Density Ion Beams*, Proc. 2005 Particle Accel. Conf., 16-20 May 2005, Knoxville, TN , pp. 2032-2034.

[12] R.J. Briggs, *The pulse line ion accelerator concept*, (April 3, 2006). Lawrence Berkeley National Laboratory. Paper LBNL-59492.

[13] D. P. Grote, A. Friedman, I. Haber, and S. S. Yu, Fusion Eng. Design 32-33, 133 (1996).

[14] T. P. Hughes, et al., Phys. Rev. ST Accel. Beams 2, 110401 (1999).

[15] D. R. Welch, et al., Nucl. Instrum. Meth. Phys. Res A 464, 134 (2001).

[16] D. Neuffer, *Geometric Aberrations in Final Focusing for Heavy Ion Fusion*, Proceedings of the Heavy Ion Fusion Workshop Held at Argonne National Laboratory, Sept. 19-26, 1978, ANL-79-41, p. 333 (1978).

[17] E. Colton, *Correction of Chromatic and Geometric Aberrations Using Sextupoles and Octupoles*, Proceedings of the Heavy Ion Fusion Workshop Held at Argonne National Laboratory September 19-26, 1978. ANL-79-41, 1979, pp. 365-378.

[18] A.A. Garren, *Final Focusing of the Ion Beams of a Pellet Fusion Reactor by Quadrupole Doublets*, ERDA Summer Study for Heavy Ions for Inertial Fusion, July 19-30, 1976. Eds. R. O. Bangerter, W. B. Herrmannsfeldt, D. L. Judd, and L. Smith. LBL-5543, 1976, pp. 102-109.

[19] D.D.-M. Ho, I. Haber, and K.R. Crandall, *Octupole Correction of Geometric Aberrations for High-Current Heavy Ion Beams*, Particle Accelerators, 36, 141, (1991).

[20] S. MacLaren, A. Faltens, P. A. Seidel, *Results from a scaled final focus experiment*, Physics of Plasmas, 9, pp. 1712-1720 (2002).

[21] S. S. Yu, W.R. Meier, R.P. Abbott, J.J. Barnard, T. Brown, D.A. Callahan, P. Heitzenroeder, J.F. Latkowski, B.G. Logan, S.J. Pemberton, P.F. Peterson, D.V. Rose, G.-L. Sabbi, W.M. Sharp, and D.R. Welch, *An Updated Point Design for Heavy Ion Fusion*, Proc. 2002 Amer. Nucl. Soc. Fusion Topical Meeting, 17-21 November 2002, Washington, DC

[22] W. B. Herrmannsfeldt, *Final Focusing and Transmission to Target*, ERDA Summer Study for Heavy Ions for Inertial Fusion, LBL-5543 (1976), p. 25.

[23] S. S. Yu, H. L. Buchanan, E. P. Lee, and F. W. Chambers, *Beam Propagation through a Gaseous Reactor*, Proc. 1978 Heavy Ion Fusion Workshop, Argonne National Laboratory Report ANL-79-41 (1979), p. 403.

[24] C. L. Olson, *Final Transport in Gas and Plasma*, Proc. 1979 Heavy Ion Fusion Workshop, Lawrence Berkeley Laboratory Report LBL-10301 (1980), p. 403.

[25] B. Badger, et al., HIBALL-II *An Improved Conceptual Heavy Ion Beam Driven Fusion Reactor Study*, University of Wisconsin Report UWFDM-625 (1984).

[26] W. M. Sharp, D. P. Grote, D. A. Callahan, M. Tabak, E. Henestroza, S. S. Yu, P. F. Peterson, D. R. Welch, and D. V. Rose, *Realistic Modeling of Chamber Transport for Heavy-Ion Fusion*, Proc. 2003 Part. Accel. Conf., 12-16 May 2003, Portland, OR (2004), pp. 2637-2639.

[27] J. Lindl, Plasma Phys. 2, 3933 (1995)

[28] R. W. Moir, R. L. Bieri, X. M. Chen, T. J. Dolan, M. A. Hoffman, P. A. House, R. L. Leber, J. D. Lee, Y. T. Lee, J. C. Shrock, M. T. Tobin, and W. H. Williams, Fusion Technol. 25, 5 (1994).

[29] M. Tabak and D. A. Callahan-Miller, Nucl. Instr. and Meth in Phys. Res. A 415, 75 (1998).

[30] D. A. Callahan-Miller and M. Tabak, Nucl. Fusion 39, 1547 (1999).

[31] W. M. Sharp, D. A. Callahan, M. Tabak, S. S. Yu, and P. F. Peterson, Phys. Plasmas 10, 2457 (2003).

[32] J. D. Lawson, J. Electron. Control 5, 146 (1958).

[33] See, for example, M. Reiser, *Theory and Design of Charged Particle Beams* (John Wiley & Sons, New York, 1994), pp. 57-59.

[34] D. A. Callahan, Fusion Eng. Des. 3233, 441 (1995).

[35] N. Barboza, Fusion Eng. Des. 3233, 453 (1995).

[36] W. M. Sharp, D. A. Callahan-Miller, A. B. Langdon, M. S. Armel, and J.-L. Vay, Nucl. Instrum. Methods Phys. Res. A 464, 284 (2001).

[37] D. V. Rose, D. R. Welch, B. V. Oliver, W. M. Sharp, and A. Friedman, Nucl. Instrum. Methods Phys. Res. A 464, 299 (2001).

[38] I. D. Kaganovich, et al., Phys. Plasmas 8, 4180 (2001).

[39] D. R. Welch, D. V. Rose, W. M. Sharp, and S. S. Yu, Laser Part. Beams 20, 621(2003).

[40] W. M. Sharp, D. A. Callahan, M. Tabak, S. S. Yu, P. F. Peterson, D. V. Rose, and D. R. Welch, Fusion Sci. and Tech. 43, 393 (2003).

[41] W. M. Sharp, D. A. Callahan, M. Tabak, S. S. Yu, P. F. Peterson, D. R. Welch, D. V. Rose, and C. L. Olson, *Simulation of Chamber Transport for Heavy-Ion Fusion Drivers*, Proc. 3rd Internat. Conf. Inert. Fusion Sci. Appl., 7-12 September 2003, Monterey, CA.

[42] W. M. Fawley, T. Garvey, S. Eylon, E. Henestroza, T. J. Fessenden, K. Hahn, L. Smith, and D. P. Grote, Phys. Plasmas 4, 880 (1997).

[43] S. Eylon, E. Henestroza, P. K. Roy, and S. S. Yu, *High brightness potassium source for the HIF neutralized transport experiment*, Proc. 2003 Particle Accel. Conf., 12-16 June 2003, Portland, OR (2004), pp. 2616-2618.

[44] E. Henestroza, F. M. Bieniosek, S. Eylon, P. K. Roy, and S. S. Yu, *Final Focus System for High Intensity Beams*, Proc. 2003 Particle Accel. Conf., 12-16 June 2003, Portland, OR (2004), pp. 2619-2621.

[45] E. Henestroza, F. M. Bieniosek, S. Eylon, P. K. Roy, and S. S. Yu, *Neutralized Transport of High Intensity Beams*, Proc. 2003 Particle Accel. Conf., 12-16 June 2003, Portland, OR (2004), pp. 2622-2624.

[46] D. Baca, J. W. Kwan, J. K. Wu, and E. Chacon-Golcher, *Fabrication of Large Diameter Alumino-Silicate K+ Sources*, Proc. 2003 Particle Accel. Conf., 12-16 June 2003, Portland, OR (2004), pp. 3294-3296.

[47] S. Eylon, *Multiple Heavy Ion Beams Induction Linac Experiment*, AIP Conf. Proc. 252, W. Berry and P. Kloeppel, eds. (New York, American Institute of Physics, 1991), p.225.

[48] M. J. Rhee and R. F. Schneider, Part. Accel. 20, 133 (1986).

[49] L. Ahle and H. S. Hopkins, *Gated Beam Imager for Heavy Ion Beams*, Proc. 1998 Beam Instrumentation Workshop, 4-7 May 1998, Palo Alto, CA (1998).

[50] P.K. Roy, Simon S. Yu, Enrique Henestroza, Shmuel Eylon, Derek B. Shuman, Jozsef Ludvig, Frank M. Bieniosek, William L. Waldron, Wayne G. Greenway, David L. Vanecek, Ryan Hannink, and Monserrat Amezcua, *Electron beam diagnostic for space charge measurement of an ion beam*, Review of Scientific Instruments, Vol. 76, No. 2, (2005), pp 023301-023308.

[51] W. B. Herrmannsfeldt, *EGUN An Electron Optics and Gun Design Program*, SLAC-Report 331 (1988).

[52] J.R. Pierce, *Theory and Design of Electron Beams* , Second Edition, D. Van Nostrand Company, Inc., Princeton, New Jersey, 1954.

[53] M. Lampel and M. Tiefenback, *Elimination of current transients in a one-dimensional heavy-ion diode*, LBL-14416, 1983.

[54] A. Kadish, W. Peter, M.E. Jones, *A generalization of the Child-Langmuir relation for one-dimensional time-dependent diodes*, LA-10207-MS, 1984.

[55] M. Tiefenback, M. Lampel and A. Faltens, *Optimization of current pulse shapes in a one dimensional diode*, HIFAN Note 179, 1982

[56] J.J. Kung, *Current transient elimination in a one-dimensional diode*, B.S. Thesis, University of California, Berkeley, CA, HIFAR Note 344, 1992.

[57] C.A. Friesen, *Modeling the transients of a spherical diode*, B.A. Thesis, University of California, Santa Cruz, CA, HIFAR Note 400, 1993.

[58] F. Bieniosek, C. Celata, E. Henestroza, J.W. Kwan, L. Prost, P.A. Seidl, A. Friedman, D.P. Grote, S.M. Lund, I. Haber, *2-MV electrostatic quadrupole injector for heavy-ion fusion*, Physical Review: Special Topics Accelerators and Beams, 8, 010101 (2005).

[59] C. Lejeune and J. Aubert, *Applied Charged Particle Optics*, Advances in Electronics and Electron Physics, Supplement 13A, A. Septier, ed. (Academic Press, San Diego, 1980), pp. 159-259.

[60] I.M. Kapchinskij, V.V. Vladimirskij., *Limitations of Proton Beam Current in a Strong Focusing Linear Accelerator Associated with the Beam Space Charge*, Proceedings of the 1959 International Conference on High Energy Accelerators. Geneva, Switzerland: CERN, 1959.

[61] E.P. Lee, *Partial cancellation of the second order chromatic aberration of a quadrupole focusing system by space charge forces*, LBL-28463 (abstract), APS DPP meeting, (1991).

[62] D. B. Shuman, E. Henestroza, D.L. Vanecek, W.L. Waldron, S.S. Yu, *A Large Bore Pulsed Quadrupole Magnet for Transport of High Current Beams at Low Energies*, Proc. 2001 Particle Accel. Conf., 18-22 June 2001, Chicago, IL, p. 2935 (2001).

[63] D. Shuman, S. Eylon, E. Henestroza, P.K.Roy, W.Waldron, S.S.Yu, and T. Houck, in Proceedings of the 2003 Particle Accelerator Conference, edited by J. Chew, P. Lucas, and S. Webber (IEEE, USA, 2003), p.2628.

[64] R. A. MacGill, M. R. Dickinson, A. Anders, O. R. Monteiro, and I. G. Brown, *Streaming metal plasma generation by vacuum arc plasma guns*, Rev. Sci. Instrum. 69, 801 (1998).

[65] A. Anders, Surf. Coat. Technol. 120-121, 319 (1999).

[66] A. Anders and G. Y. Yushkov, J. App;. Phys. 92, 4824 (2002).

[67] P. C. Efthimion, E. P. Gilson, L. Grisham, P. Kolchin, R. C. Davidson, S. S. Yu, and B. G. Logan, Laser Part. Beams 21, 37 (2003).

[68] P. K. Roy, S. S. Yu, E. Henestroza, A. Anders, F. M. Bieniosek, J. Coleman, S. Eylon, W. G. Greenway, M. Leitner, B. G. Logan and W. L. Waldron, D. R. Welch and C. Thoma, A. B. Sefkow, E. P. Gilson, P. C. Efthimion and R. C. Davidson, *Drift compression of an intense neutralized ion beam*, Physical Review Letters Vol. 95, (2005), pp. 23480.